

Die approbierte Originalversion dieser Dissertation ist an der Hauptbibliothek  
der Technischen Universität Wien aufgestellt (<http://www.ub.tuwien.ac.at>).

The approved original version of this thesis is available at the main library of  
the Vienna University of Technology (<http://www.ub.tuwien.ac.at/englweb/>).



Diese Dissertation haben begutachtet:

.....

## DISSERTATION

# Surface Soil Moisture Retrieval Using Envisat ASAR Global Mode Data

ausgeführt zum Zwecke der Erlangung des akademischen Grades eines Doktors der  
Naturwissenschaften (Dr. rer. nat.) unter der Leitung von

Univ. Prof. Dipl.-Ing. Dr. techn. Wolfgang Wagner  
Institut für Photogrammetrie und Fernerkundung (E122),  
Technische Universität Wien

eingereicht an der Technischen Universität Wien  
Fakultät für Mathematik und Geoinformation

von  
Dipl.Geogr. Carsten Pathe  
Matr. Nr. 0327644  
Vogtgasse 14/4/12  
A-1140 Wien

Wien, am 5. Februar 2009

.....

This work was realized in the context of the following research projects:

- MISAR (Using multi-incidence ScanSAR data for biomass retrieval and soil moisture monitoring), funded by the Austrian Science Fund FWF (Project Number P16515-N10)
- ScanSAR Mali (The Potential of ENVISAT ScanSAR Data for Soil Moisture Retrieval over Mali), funded by the European Space Agency (ESA Project Number AO 356)
- SHARE (Soil Moisture For Hydrometeorological Applications In The SADC Region), a project of the Data User Element Innovator Tiger Initiative of the European Space Agency (ESA ESRIN Contract No. 19420/05/I-EC)

# Acknowledgements

---

First of all I would like to thank my mentor Prof. Wolfgang Wagner for giving me the opportunity to realize the dissertation at the Institute of Photogrammetry and Remote Sensing and for supporting the work with his time and efforts and many fruitful discussions.

I also would like to thank my second supervisor Prof. Volker Hochschild from the Institute of Geography at the Eberhard-Karls-University Tübingen, Germany, for his comments and review of the dissertation.

Many thanks go to the members of the radar group at the Institute of Photogrammetry and Remote Sensing for helping me with the processing of the huge data amounts and for their contributions through lots of discussions. Thanks go also to Dr. Daniela Knorr for a first proof reading of the work and her comments on improving the understandability of the text.

I am very grateful to all my colleagues at the Institute of Photogrammetry and Remote Sensing for contributing to the realization of my dissertation with creating a positive work atmosphere at the institute.

For supporting my way I made so far I finally want to thank my parents.

# Kurzfassung

---

Bodenfeuchte als wichtige Größe in den globalen Kreisläufen von Wasser, Energie und Kohlenstoff, ist räumlich und zeitlich hoch variabel. Mit Hilfe von in-situ-Messungen kann die Bodenfeuchte sehr genau bestimmt werden. Allerdings kann sie auf diese Weise aufgrund organisatorischer und finanzieller Gründe nicht auf kontinentalen bis hin zur globalen Ebene gemessen werden. Hierfür können alternativ Radarfernkundungsmethoden genutzt werden, die Daten auf unterschiedlichen zeitlichen und räumlichen Skalen zur Verfügung stellen. Prinzipiell kann die Radarrückstreuung mit Hilfe der Maxwell-Gleichungen beschrieben werden um so Bodenfeuchte aus den Radarsignalen zu extrahieren. Aufgrund der Komplexität natürlicher Oberflächen ist dies aber kaum durchführbar. Daher stehen nur Näherungslösungen zur Verfügung, die eng mit den ihnen zugrundeliegenden Gültigkeitsbedingungen verknüpft sind. Die Anwendbarkeit theoretischer Modelle zur Modellierung der Rückstreuung von unbedeckten Bodenoberflächen und Vegetationsbeständen wurde in zahlreichen Studien kritisch hinterfragt, die keine zufriedenstellenden Übereinstimmungen zwischen modellierten und gemessenen Bodenfeuchtewerten finden konnten. Mit Hilfe sogenannter Change-Detection-Methoden wird versucht, diese Probleme zu umgehen, indem lediglich die Änderungen in der Radarrückstreuung über die Zeit ohne Beschreibung der absoluten Rückstreuung beobachtet wird.

Wagner et al. (1999a-c) entwickelten ein Change-Detection-Modell für C-Band-Scatterometerdaten. Dabei wird die Radarrückstreuung mit Hilfe empirischer Rückstreuparameter zur Ableitung relativer Bodenfeuchtewerte modelliert. Die empirischen Rückstreuparameter beschreiben die Variation der Rückstreuwerte über die Zeit zwischen einem Niedrigstwert typisch für trockene Bodenfeuchtebedingungen und einem Höchstwert typisch für gesättigte Bodenfeuchtebedingungen. Drei unabhängige Radarrückstremessungen pro Aufnahmezeitpunkt unter verschiedenen Einfallswinkeln stehen im Fall es ERS Scatterometers zur Verfügung und werden zur Modellierung saisonaler Rückstreueffekte benutzt, welche auf dem radartypischen Einfallswinkelverhalten basieren. Das invertierte

Rückstreumodell kann dann benutzt werden, um einzelne Radarmessungen zwischen Trockenbedingungen (0%) und Feuchtbedingungen (100%) zu skalieren.

Im Fall des Envisat ASAR steht lediglich nur eine Radarrückstreumessungen bei einem Einfallswinkel zur Verfügung. Daher kann der Bodenfeuchtealgorithmus, der saisonale Änderungen in den Radardaten berücksichtigt, nicht direkt vom ERS-Scatterometer auf die ASAR GM Daten übertragen werden. Die Datenanalyse hat gezeigt, dass Änderungen in der Radarrückstreuung im Zusammenhang mit der zeitlichen Änderung der Vegetation im Allgemeinen schwächer ausgeprägt sind als die durch Bodenfeuchteänderungen hervorgerufenen Signaländerungen. Da außerdem die ASAR GM Daten in HH-Polarisation vorliegen, wird Vegetation von den Radarsignalen besser durchdrungen als im Fall des in VV-Polarisation arbeitenden ERS Scatterometers. Daher wird zur Vereinfachung angenommen, angenommen, dass die Parameter des Rückstreumodells zeitlich konstant sind und saisonale Effekte durch Änderungen der Vegetation vernachlässigt werden können. Mit Hilfe des angepassten Rückstreumodells werden ebenfalls Radareinzelmessungen zwischen den Referenzwerten für trockene und gesättigte Bodenfeuchtebedingungen skaliert.

Die Ergebnisse wurden mit Hilfe von in-situ Bodenfeuchtemessungen des Oklahoma Mesonets und Bodenfeuchtwerten aus ERS Scatterometerdaten validiert. Gute Übereinstimmungen zwischen der relativen oberflächennahen Bodenfeuchte aus ASAR GM-Daten und den Validierungsdaten wurden beobachtet. Beim direkten Vergleich der Ergebnisse zeigt sich, dass die Bodenfeuchte aus ERS-Scatterometerdaten etwas bessere Ergebnisse liefert als der ASAR GM Sensor. Als Hauptfehlerquelle wurde die radiometrische Genauigkeit von 1.2 dB identifiziert. Das ist ein im Vergleich zum ERS Scatterometer mit einer radiometrischen Genauigkeit von 0.3 dB relativ hoher Wert. Trotzdem können aus ASAR GM Daten Bodenfeuchtwerte mit wesentlich mehr räumlichen Details als für den ERS Scatterometer abgeleitet werden, die ebenso die zeitliche Dynamik der Bodenfeuchte abbilden wie im Fall des Scatterometers. Die Validierung hat gezeigt, dass die Vernachlässigung saisonaler Vegetationseffekte auf die Radarrückstreuung eine haltbare Vereinfachung darstellt und das ASAR GM Daten für ein operationelles Bodenfeuchtemonitoring mit Hilfe von Change-Detection-Modellen genutzt werden können.

# Abstract

---

Soil moisture, highly variable in space and time, is a key element in the global hydrologic, energy and carbon cycle. Soil moisture can be measured accurately in the field using *in-situ* measurement techniques. Measuring soil moisture at continental to global scales using *in-situ* techniques is not feasible. Alternatively, soil moisture can be measured using radar remote sensing at different temporal and spatial scales. ScanSAR modes as the Envisat ASAR GM offer medium spatial and temporal resolution. Theoretically, modeling the radar backscattering process for inverting soil moisture information could be obtained by an exact solution of Maxwell's equations. Due to the complexity of natural surfaces, this is not feasible. Only approximate solutions that are critically dependent on the validity of the underlying assumptions can be derived analytically. The applicability of theoretical models for describing scattering by natural soil surfaces and vegetation has increasingly been questioned and many experimental studies did not find a satisfactory match between modeled and measured bare soil backscatter. Change detection methods try to circumvent these difficulties by solely interpreting backscatter changes at fixed locations over time, without attempting to explain the absolute backscatter level.

A change detection model has been developed for C-band scatterometer data by Wagner et al. (1999a-c). It describes radar backscatter in terms of empirical backscatter parameters and the relative surface soil moisture content. The empirical backscatter parameters define the variation of radar backscatter between dry surface soil moisture conditions at wilting level and saturated conditions at field capacity. Three individual backscatter measurements at different incidence angles are available from the ERS scatterometer per acquisition and can be used to model seasonal vegetation cover effects by exploiting the local incidence angle behavior. The inverted model can be used to scale individual radar backscatter measurements between dry (0%) and wet (100%) surface soil moisture conditions.

In the case of ASAR GM only one backscatter measurement at some incidence angle is being made during each overpass. Therefore the algorithm developed for the ERS scatterometer

to account for seasonal vegetation effects can not be applied directly. Data analysis showed that changes in backscatter due to vegetation growth are in general much smaller than changes due to soil moisture. Additionally, ASAR GM is commonly operated in HH polarization which penetrates vegetation better than VV polarization as used by the ERS scatterometer. Therefore, a simplified change detection model is adapted for ASAR GM. It is assumed that, in a first approximation, the backscatter model parameters are constant in time because seasonal vegetation effects are expected to be weak for ASAR GM. This assumption may lead to a seasonally varying error of the retrieval. The adapted change detection backscatter model also scales individual backscatter measurements between a lower backscatter threshold related to dry surface soil moisture conditions and an upper backscatter threshold related to saturated conditions.

The results were validated using *in-situ* soil moisture data from the Oklahoma Mesonet and ERS-1/2 scatterometer derived relative surface soil moisture. Good agreement between ASAR GM relative surface soil moisture and both *in-situ* soil moisture measurements and ERS-1/2 scatterometer derived soil moisture was observed. The direct comparison of the results shows that the surface soil moisture extracted from ERS-1/2 scatterometer data performs slightly better than the data derived from ASAR GM. As the main source of error, the noise of the ASAR GM data with a value of 1.2 dB has been identified which is relatively high when compared to radiometric resolution of at least 0.3 dB of the ERS scatterometer. Nevertheless, the ASAR GM data offer surface soil moisture data with much more details than the ERS-1/2 scatterometer data and still keeping the capability of the scatterometer data to map temporal surface soil moisture trends. The validation of the remotely sensed soil moisture extracted from ASAR GM data has proven that neglecting seasonal vegetation cover effects can be regarded as a valid assumption and operational use of ASAR GM data for soil moisture retrieval using change detection is possible.

# Table of Contents

---

Acknowledgements .....	III
Kurzfassung .....	IV
Abstract .....	VI
Contents .....	VIII
List of Figures .....	X
List of Tables .....	XIII
<b>1. INTRODUCTION</b>	<b>1</b>
1.1. The need for soil moisture data	1
1.2. Scope of Work and Objectives	3
<b>2. SOIL MOISTURE</b>	<b>7</b>
2.1. Definition of Soil Moisture	7
2.2. In-situ Soil Moisture Measurement Techniques	9
2.3. Spatio-Temporal Properties of Soil Moisture	10
<b>3. REMOTE SENSING OF SOIL MOISTURE</b>	<b>15</b>
3.1. Overview of Remote Sensing Techniques for Soil Moisture Retrieval	15
3.2. Basic principles of active remote sensing	18
3.2.1. Sensor Parameters	19
3.2.2. Target Parameters	21
3.3. Scattering from Bare and Vegetated Surfaces	24
3.4. Radar Equation	27
3.5. Soil moisture retrieval from active radar data	28
3.5.1. Theoretical Models	29
3.5.2. Empirical and Semi-Empirical Models	32
3.5.3. Change Detection	33
3.6. Hypothesis of the study	36
<b>4. TEST SITE AND DATA</b>	<b>37</b>
4.1. Test Site	37
4.2. Remote Sensing Data	42
4.2.1. Envisat ASAR Global Mode	42
4.2.2. DORIS Orbit Information	47

4.3. Validation Data	48
4.3.1. <i>In-situ</i> soil moisture	48
4.3.2. ERS Scatterometer Soil Moisture	49
4.3.3. Meteorological Data	51
4.3.4. Land Cover	52
<b>5. METHOD</b>	<b>54</b>
5.1. Data Pre-Processing	55
5.1.1. Geocoding	55
5.1.2. Radiometric Calibration	60
5.1.3. Resampling of ASAR GM Data	64
5.1.4. Local Incidence Angle Normalization	66
5.2. Change Detection Surface Soil Moisture Retrieval Algorithm	71
5.2.1. Original ERS-1/2 Change Detection Soil Moisture Retrieval Algorithm	71
5.2.2. Adapted Change Detection Soil Moisture Retrieval Algorithm for Envisat ASAR GM Data	75
5.2.2.1. <i>Estimation of Dry and Wet Reference</i>	76
5.2.2.2. <i>Surface Soil Moisture Retrieval</i>	78
5.2.3. Calculation of the Retrieval Error	80
<b>6. RESULTS AND DISCUSSION</b>	<b>83</b>
6.1. Estimated Noise Level of ASAR GM Data	83
6.2. Spatial Patterns	84
6.2.1. Model Parameters	84
6.2.2. Relative Surface Soil Moisture	90
6.3. Temporal Patterns	92
6.4. Retrieval Error	100
<b>7. CONCLUSIONS AND OUTLOOK</b>	<b>104</b>
7.1. Conclusions	104
7.2. Outlook	107
<b>References</b>	<b>110</b>
<b>Appendix: Tables</b>	<b>125</b>
<b>Appendix: Figures</b>	<b>141</b>
<b>Curriculum Vitae</b>	<b>180</b>

# List of Figures

---

<i>Figure 1: Cross-section of a soil sample with solid soil particles (a), a liquid phase (b) and a gaseous phase (c) (after Koorevaar et al. 1983)</i>	8
<i>Figure 2: Temporal and spatial process scales in hydrology (Blöschl &amp; Sivapalan 1995)</i>	12
<i>Figure 3: Electromagnetic wave, E – sinusoidal electric wave, M – sinusoidal magnetic wave (Lillesand &amp; Kiefer 2000)</i>	18
<i>Figure 4: Main parameters controlling radar backscatter</i>	19
<i>Figure 5: Illustration of the Incidence angle and the local incidence angle for SAR systems (after Lewis et al. 1998)</i>	20
<i>Figure 6: RMS height s as standard deviation from a mean reference height</i>	22
<i>Figure 7: Schematic illustration of scattering from surfaces with different roughness conditions at increasing (from a to c) incidence angles (after Woodhouse 2006)</i>	25
<i>Figure 8: Backscatter from vegetation: 1) direct backscattering from plants, 2)direct backscattering from underlying soil, 3)multiple scattering between plants and soil, 4) multiple scattering between plants, leaves, stalks ect. (after Ulaby et al. 1986; Chiu &amp; Sarabandi 2000)</i>	26
<i>Figure 9: Schematic illustration of the dependency of radar backscatter from local incidence angle at a given for vegetation canopies</i>	27
<i>Figure 10: Oklahoma/USA</i>	37
<i>Figure 11: Level I Ecoregions of Oklahoma (Commission for Environmental Cooperation 1997)</i>	38
<i>Figure 12: Perspective view of Oklahoma's Topography (SRTM improved GTOPO30 DEM, <a href="ftp://e0srp01u.ecs.nasa.gov/srtm/version2/SRTM30/">ftp://e0srp01u.ecs.nasa.gov/srtm/version2/SRTM30/</a>)</i>	38
<i>Figure 13: Normal annual precipitation, normal annual temperature and average length of frost free period for Oklahoma (Oklahoma Climatological Survey, <a href="http://climate.mesonet.org/normals_extremes.html">http://climate.mesonet.org/normals_extremes.html</a>)</i>	39
<i>Figure 14: Oklahoma Land Cover according to generalized National Land Cover Data (NLCD) classes (North American Land Cover Characteristics – 1 Kilometer Resolution, <a href="http://nationalatlas.gov/mld/landcvi.html">http://nationalatlas.gov/mld/landcvi.html</a>)</i>	41
<i>Figure 15: Envisat with an overview of the major instruments (Attema et al. 2000)</i>	42
<i>Figure 16: Illustration of the ScanSAR imaging principle. © ESA.</i>	45
<i>Figure 17: Potential daily global coverage offered by different ASAR acquisition modes</i>	46
<i>Figure 18: The Oklahoma Mesonet: Location of Measurement Stations in the Counties (<a href="http://www.mesonet.org/sites/">http://www.mesonet.org/sites/</a>)</i>	49
<i>Figure 19: Example of DGG distribution over Austria</i>	50

<i>Figure 20: Three-day surface soil degree of saturation for North America (white – no data, light green – snow cover)</i>	51
<i>Figure 21: Meteorological Measurement Stations from the DS512 data set</i>	51
<i>Figure 22: Reclassified USGS GLCC land cover of Oklahoma</i>	53
<i>Figure 23: Percentages of main land cover classes</i>	53
<i>Figure 24: Processing chain for data pre-processing and surface soil moisture retrieval</i>	54
<i>Figure 25: Earth centred reference coordinate system (Liu et al. 2006)</i>	57
<i>Figure 26: Example of image features used for assessing the geolocation accuracy. Left: detail of radar image with feature 1 (an industrial facility site in Saudi Arabia) encircled. Right: feature 2; branching of the river Kwa in Democratic Republic of the Congo.</i>	59
<i>Figure 27: ASAR Global Monitoring mode backscatter observed over two tropical forest sites: 20.925°E, -2.525°S (left), 20.69°E, -3.79°S (right).</i>	62
<i>Figure 28: Tropical forest areas used for determining the noise and natural signal fluctuations of ASAR GM backscatter measurements.</i>	64
<i>Figure 29: Illustration of the resampling procedure</i>	66
<i>Figure 30: Change in image brightness due to angular dependency of Envisat ASAR GM data before normalization</i>	67
<i>Figure 31: Angular dependency of radar backscatter before normalization Envisat ASAR GM for a grassland site in Oklahoma</i>	67
<i>Figure 32: Angular dependency of radar backscatter before normalization of Envisat ASAR GM for a coniferous forest site in Oklahoma</i>	68
<i>Figure 33: Multi-temporal pixel-by-pixel normalization procedure</i>	68
<i>Figure 34: Removed change in image brightness due to angular dependency after normalization</i>	69
<i>Figure 35: Angular dependency of radar backscatter after normalization of Envisat ASAR GM for a grassland site in Oklahoma</i>	70
<i>Figure 36: Angular dependency of radar backscatter after normalization of Envisat ASAR GM for a coniferous forest site in Oklahoma</i>	70
<i>Figure 37: Dry (red) and wet (blue) backscatter reference curves for winter (solid line) and summer (dashed line) conditions. The model parameters were estimated from ERS scatterometer measurements (1991-2007) of a grassland region in Oklahoma (36.86°N, 102.7°W). The two vertical lines indicate the incidence angle range of the ASAR GM (20-40°)</i>	73
<i>Figure 38: Backscatter model parameter dry reference <math>\sigma^0_{dry}</math> extracted from ASAR GM time series</i>	85
<i>Figure 39: Backscatter model parameter slope <math>\beta</math> (in dB/deg) extracted from ASAR GM time series</i>	85
<i>Figure 40: Backscatter model parameter sensitivity <math>S</math> (in dB) extracted from ASAR GM time series</i>	85
<i>Figure 41: Box plot showing the dry reference <math>\sigma^0_{dry}</math> for main land cover classes</i>	87
<i>Figure 42: Box plot showing the slope <math>\beta</math> for main land cover classes</i>	87

<i>Figure 43: Box plot showing sensitivity S for main land cover classes</i>	88
<i>Figure 44: Slope <math>\beta</math> vs. Dry Reference <math>\sigma^0_{wet}</math></i>	89
<i>Figure 45: Sensitivity S vs. Dry Reference <math>\sigma^0_{wet}</math></i>	89
<i>Figure 46: Sensitivity S vs. Slope <math>\beta</math></i>	90
<i>Figure 47: Relative surface soil moisture maps of Oklahoma extracted from ERS-1/2 scatterometer (left) and ASAR GM data (right) for three different dates in Spring 2005</i>	91
<i>Figure 48: Soil moisture time series from ASAR GM (solid line) and ERS scatterometer (dashed line) (top) and in-situ measurements (bottom) at the MESONET station LAHO for the period January 2005 to July 2006.</i>	94
<i>Figure 49: Correlation R between remotely sensed soil moisture derived from ERS scatterometer and ASAR GM backscatter measurements for 75 Oklahoma Mesonet stations: <math>m_s</math>-ERS vs. in-situ, <math>m_s</math>-ASAR at 3 km vs. in-situ, <math>m_s</math>-ASAR at 50 km vs. in-situ, <math>m_s</math>-ERS at 50 km vs. <math>m_s</math>-ASAR at 3 km and <math>m_s</math>-ERS at 50 km vs. <math>m_s</math>-ASAR at 50 km</i>	96
<i>Figure 50: BIAS between remotely sensed soil moisture derived from ERS scatterometer and ASAR GM backscatter measurements for 75 Oklahoma Mesonet stations: <math>m_s</math>-ERS vs. in-situ, <math>m_s</math>-ASAR at 3 km vs. in-situ, <math>m_s</math>-ASAR at 50 km vs. in-situ, <math>m_s</math>-ERS at 50 km vs. <math>m_s</math>-ASAR at 3 km and <math>m_s</math>-ERS at 50 km vs. <math>m_s</math>-ASAR at 50 km</i>	97
<i>Figure 51: Standard deviation between remotely sensed soil moisture derived from ERS scatterometer and ASAR GM backscatter measurements for 75 Oklahoma Mesonet stations: <math>m_s</math>-ERS vs. in-situ, <math>m_s</math>-ASAR at 3 km vs. in-situ, <math>m_s</math>-ASAR at 50 km vs. in-situ, <math>m_s</math>-ERS at 50 km vs. <math>m_s</math>-ASAR at 3 km and <math>m_s</math>-ERS at 50 km vs. <math>m_s</math>-ASAR at 50 km</i>	97
<i>Figure 52: Spatial distribution of correlation R between <math>m_s</math>-ASAR at 3 km and in-situ soil moisture for 75 Oklahoma Mesonet stations</i>	99
<i>Figure 53: Spatial distribution of BIAS between <math>m_s</math>-ASAR at 3 km and in-situ soil moisture for 75 Oklahoma Mesonet stations</i>	99
<i>Figure 54: Spatial distribution of Standard Deviation between <math>m_s</math>-ASAR at 3 km and in-situ soil moisture for 75 Oklahoma Mesonet stations</i>	99
<i>Figure 55: Soil moisture retrieval error <math>\Delta m_s</math> [%]</i>	101
<i>Figure 56: Retrieval error <math>\Delta m_s</math> as a function of the sensitivity S for given noise <math>\Delta \sigma^0</math> in radar backscatter</i>	101
<i>Figure 57: Model uncertainty <math>\Delta m_s</math> in relation to the sensitivity S for different values of <math>\Delta \sigma^0</math></i>	102
<i>Figure 58: Selected current and planned Earth observation missions related to soil moisture (ESA 2008)</i>	108

# List of Tables

---

---

<i>Table 1: Radar bands used in remote sensing (modified after Lewis et al. 1998)</i> .....	19
<i>Table 2: ASAR sensor characteristics (after Desnos et al. 2000)</i> .....	43
<i>Table 3: Reclassification of USGS GLCC data</i> .....	52
<i>Table 4: Geolocation accuracy for exemplary features.</i> .....	59
<i>Table 5: Standard deviations of natural backscatter variation <math>s_{Signal}</math> and noise <math>s_{Noise}</math></i> .....	84
<i>Table 6: Settings for calculating model uncertainty</i> .....	100

# **CHAPTER 1**

## **Introduction**

---

Soil moisture retrieval from active remote sensing data is one of the main applications of radar remote sensing. Since the 1970's, the search for operational soil moisture retrievals was one of the driving forces within the radar remote sensing community. This introduction highlights of the relevance of soil moisture as an important variable and process in different geo-physical disciplines and fields of application. Based on this, the scope of work and a brief overview of the organization of the thesis will be given.

### **1.1. The need for soil moisture data**

---

Knowledge about the spatial and temporal distribution of soil moisture is an essential prerequisite for many applications in the Earth sciences. The water contained in the soils, the thin layer forming the boundary between the Earths crust and the atmosphere, makes up only a very small proportion of the global water resources. Only 0.05% of global fresh water is contained in the soils (Gleick 1996). Therefore soil moisture seems to be a negligible quantity when compared to global water and fresh water resources. Nevertheless, soil moisture is a key variable in the Earths hydrologic, energy and carbon cycle. Soil moisture controls the partitioning of precipitation into runoff and infiltration as well as the separation of incoming solar radiation into sensible and latent heat fluxes (Entekhabi et al. 1996; Berger et al. 2003). Anomalies of soil moisture can be used as an indicator for upcoming drought or flood events (Douville & Chauvin 2000). The heatwave of 2003 in Europe was preceded by a dry spring with low soil moisture, which led to decreasing evaporation and cooling from soils. This resulted in increased summer temperatures (Titz 2005). There are other feedback loops connected to the state of soil moisture including soil erosion, surface runoff or cloud formation. Future climate models at finer spatial scales will use spatially extended, regular soil moisture observations, which can be provided by remote sensing techniques

(Schiermeier 2008). Soils also play an important role in the global carbon cycle. Decomposition of organic matter and microbiological activity are controlled by moisture and temperature conditions in the soil layer (Melillo et al. 2002; Porporato et al. 2003). And of course, soil moisture is the limiting factor for plant growth and directly influences crop yields and food production (Wild 1993; Entekhabi et al. 1995; Walker 1999; Berger et al. 2003; Huete 2004).

Information on the actual state of soil moisture also is of socio-economic interest. At the moment more than one billion people do not have access to safe drinking water and two billion people have no proper sanitation. It is expected, that two-third of the world's population will be affected by fresh water shortages by the year 2025. Water demand of agriculture is expected to double in the next decades. The global energy demand is projected to rise by 57% and consequently more water, e.g. for cooling, is required. These intensifying demands of fresh water can be addressed to global population growth, further rapid economic development and climate change (Arnell 1999; IPCC 2001; Shannon et al. 2008). To handle the projected shortages of fresh water as a finite and vulnerable resource, an integrated water resource management is mandatory to secure fresh water supply for people, food production, economy, the protection of ecosystems, to deal with the spatial and temporal variability of water availability and to predict and manage extreme events like droughts and floods. Every water resource management system involves hydrologic modelling, which is based on a variety of geophysical parameters. Remote sensing methods can provide information of fundamental importance in catchment hydrology (Bastiaanssen 1999; Grayson & Blöschl 2001). Hydrologically relevant data, which can be derived from remote sensing data, comprise land cover, digital elevation models, vegetation indices, precipitation, evapotranspiration, snow cover and soil moisture (Pietroniro & Prowse 2002). Furthermore, remote sensing methods can help in closing an information gap caused by the globally decreasing number of reporting runoff measurement stations. During the 1990's the number of reporting stations in Africa decreased tremendously (Vörösmarty 2002).

Given the importance of soil moisture in various fields it is amazing to realize, that soil moisture is not being measured regularly like other important geo-physical and climate relevant variables like precipitation, air temperature, air pressure, humidity, incoming solar radiation or sea surface temperature. The reasons for this may arise from

the fact, that soil moisture is temporal and spatially highly variable and the set up and maintenance of soil moisture measuring networks as well as the measurement process itself is time-consuming and costly.

Remote sensing methods working in the microwave region of the electromagnetic spectrum are commonly regarded to be the optimum remote sensing tool for soil moisture monitoring, as microwaves show a unique sensitivity to water contained in the soil layer. Since more than 30 years the extraction of soil moisture information is a research topic in the field of active remote sensing. The fact that there exist no operational soil moisture retrieval algorithms at medium spatial and temporal scales does not mean that operational soil moisture extraction from radar imagery is impossible at all. Numerous experimental studies proved the relation between radar backscatter and soil moisture content. One reason for the non-existence of operational methods can be found in the limited temporal resolution of spatial high resolution SAR data. Most studies on soil moisture retrieval are based only on a few images usually with a temporal distance of one month. This only provides isolated snapshots of the soil moisture conditions for one region. Given the spatial and temporal variability of soil moisture, temporal resolution is at least as important as spatial resolution. The main advantage of remote sensing is the fact, that it provides spatial extended data on routine basis. Nevertheless, extracting soil moisture information from remote sensing data is not straightforward. No near real-time soil moisture product from remote sensing data at medium temporal and spatial scales is available so far (Chauhan et al. 2003).

---

## 1.2. Scope of Work and Objectives

---

This dissertation is intended to answer the question whether or not Envisat ASAR Global Monitoring Mode data can be used for an operational soil moisture monitoring. What are the advantages of these kinds of data, what are the challenges to deal with when employing ASAR Global Monitoring Mode data?

This dissertation is embedded in the research activities at the Institute of Photogrammetry and Remote Sensing (I.P.F.) at the Vienna University of Technology. The institute's remote sensing group is mainly concerned with the retrieval of geo-physical variables from different active Earth observation (EO) sensors such as the ERS-1/2 scatterometer, the MetOp ASCAT, QikSCAT or the Envisat ASAR. Former

studies at I.P.F. explored the potential of scatterometer data for land applications such as soil moisture retrieval or detection of freeze-thaw-cycles. Algorithms for soil moisture retrieval on global scales have been developed, implemented and successfully validated (Wagner et al. 2003). With the launch of Envisat, a new sensor, the Advanced Synthetic Aperture Radar (ASAR), capable of acquiring data in different imaging modes became available. ASAR's Global Monitoring Mode (GM), which is one of its ScanSAR (Scanning Synthetic Aperture Radar) modes, offers time series data at medium spatial and temporal resolutions. Hence the idea emerged to use and transfer I.P.F.'s experience and knowledge gained with soil moisture retrieval from scatterometer data to GM time series data acquired with the ASAR sensor.

Using ASAR GM time series data for soil moisture retrieval may add another aspect in the search for operational soil moisture algorithms from active remote sensing data. This has been one of the central issues in the active remote sensing community for the last 30 years.

Different modelling approaches have been developed to retrieve soil moisture information from active remote sensing data. The simple empirical models showed, that there exists a fundamental relation between radar backscatter and soil moisture, even though these models are site dependent and not applicable for operational soil moisture monitoring. Sophisticated theoretical models with a physical basis allowed some insight into the processes governing the radar backscattering process. Also these models can not be used within an operational environment, because they require comprehensive data sets comprising SAR data at different frequencies and polarizations together with parameters describing surface roughness. Moreover, models describe vegetation layers in a very general way, which did not yield successful results. Given the number of publications, research projects together with the attention paid to this issue at scientific conferences, it can be stated, that soil moisture retrieval from SAR still stands high on the research agenda.

A completely different approach is represented by change detection models. Here, radar backscatter is assumed to be controlled by some static and some dynamic parameters. Based on time series data, the variation of radar backscatter between an upper and a lower limited is related to variations in surface soil moisture. This idea has been used successfully for scatterometer data, providing backscatter at low spatial but

high temporal resolutions. With the launch of Envisat, the ASAR ScanSAR data at medium temporal and spatial resolutions became available.

With this dissertation, a concept originally developed for ERS scatterometer data is transferred and adapted to ASAR GM data. The main objective of this work is to answer the question, whether or not ASAR GM time series data can be used for operational soil moisture retrieval using a change detection approach. What are the advantages of this method? What are the limits of this method and which constraints need to be considered?

For answering these questions, a fully automatic processing chain including geocoding, radiometric correction, data base management, local incidence angle correction and the actual soil moisture retrieval is set up and implemented. Results are validated using *in-situ* soil moisture data from a state-wide measurement network in Oklahoma (USA) as well as other remotely sensed soil moisture data.

The thesis is organized as follows:

**Chapter 1** introduces the subject of the thesis and gives an overview of the thesis structure.

**Chapter 2** describes soil moisture as a geo-physical variable including definitions, methods for measuring *in-situ* soil moisture and its spatial and temporal scale properties.

**Chapter 3** first gives an overview of different remote sensing techniques for soil moisture retrieval. Then background information on active remote sensing necessary for soil moisture mapping are presented. An overview of methods for retrieving soil moisture from active remote sensing data will be given including theoretical models, empirical models and change detection methods.

**Chapter 4** describes the test site and the data used for this study. A physio-geographical overview will introduce the test site. Then the Envisat ASAR sensor and the ScanSAR technique are described. Validation data sets including

the *in-situ* soil moisture measurements, the ERS Scatterometer soil moisture and other auxiliary data sets are presented.

**Chapter 5** contains a detailed description of the methods used to derive the remotely sensed soil moisture products. This comprises the processing chain including geometric correction, radiometric calibration, resampling to time-series format, local incidence correction and the actual change detection soil moisture retrieval algorithm.

**Chapter 6** presents the results and the validation of the soil moisture retrieved from the ASAR GM time series data for the test site. Results are discussed with respect to the initial research question and the relevant literature.

**Chapter 7** gives the conclusions and an outlook to possible further research activities in this field.

# **CHAPTER 2**

## **Soil Moisture**

---

In this chapter the soil moisture as a geo-physical variable is introduced. Definitions of soil moisture will be given. Different methods for *in-situ* soil moisture measurements are described. Finally, the spatial and temporal scale properties of soil moisture are discussed.

### **2.1. Definition of Soil Moisture**

---

A definition of soil moisture is given by Hillel (1982). He defines soil moisture as the volume fraction of water held in the soil against gravity. Another pragmatic definition describes soil moisture as the amount of water which evaporates within 24 hours when drying soil samples at 105°C (Koorevaar et al. 1999).

To understand, how soil moisture influences radar backscatter, it is necessary to take a closer look at the water containing medium – the soil. The term soil refers to the complex medium at the interface between the atmosphere and the lithosphere. It is also called the pedosphere and covers large parts of the Earth's land surfaces. Soils are the result of physical and chemical weathering. They are a mixture of solid, liquid and gaseous constituents, namely minerals and organic matter, water and air (see Figure 1). Under natural conditions, nearly every soil contains water. This water is mainly derived from precipitation via the process of infiltration or from the water table via capillary rise (Ellis & Mellor 1995). The ability of a soil to contain water is caused by attractive forces between the liquid and the solid phase of a soil. Due to these matric forces soils can hold water against forces caused by gravity, evaporation and suction by plant roots. The binding of water in capillaries formed by the soil particles is the result of adhesive forces between water molecules and the surfaces of the solid soil particles and cohesive forces between individual water molecules. Adhesion caused by van-der-Waals forces (intra-molecular forces between atoms or molecules) decreases with the sixth power of the distance to the solid soil particle. The thickness of the water layer bound by

adhesive forces is about 1 nm (Scheffer & Schachtschabel 1998; Koorevaar et al. 1999). Water bound by adhesion can not move freely within the soil. All water, which is not under the effect of this force is able to move within the soil and therefore is called free water (Hillel 1982; Hallikainen et al. 1985; Ulaby et al. 1996).

The water content of a soil can vary between a minimum value at oven dryness and a maximum value at pore space saturation. For agronomic and hydrological applications, two intermediate states are more important: field capacity and permanent wilting point. The field capacity (FC) describes the maximum amount of water, which a soil can hold against gravity. It is reached usually after an already wetted soil has been drained with water for at least two days. The permanent wilting point (PWP) refers to a water content from which plant roots are unable to retrieve water from the soil, because the forces attracting water to the soil particles exceeds the plant roots suction (Hillel 1982).

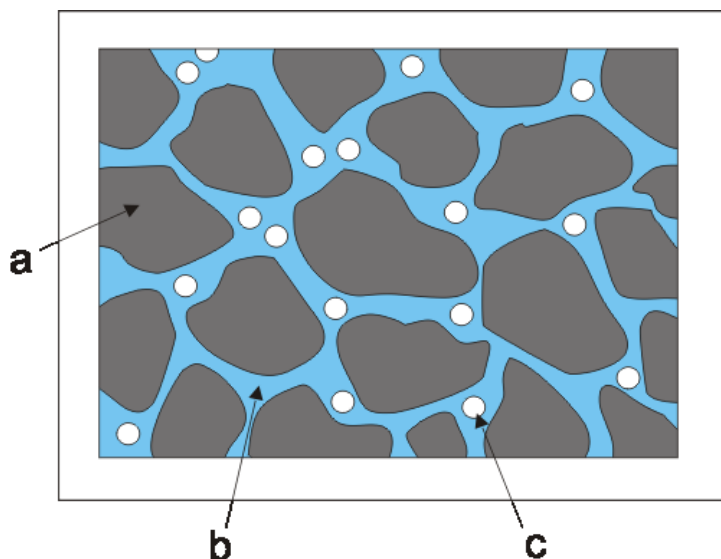


*Figure 1: Cross-section of a soil sample with solid soil particles (a), a liquid phase (b) and a gaseous phase (c) (after Koorevaar et al. 1983)*

The water content of a soil is directly related to its dielectric properties, which have a strong influence on the backscattering process of microwaves. The relation between the dielectric properties of soils and radar backscatter will be described in Chapter 3.2.2.

## 2.2. In-situ Soil Moisture Measurement Techniques

---

Reliable and exact measurements of the soil moisture content are of great importance for different disciplines of the Earth sciences as well as for agronomy. Soil moisture can be measured either *in-situ*, which means measuring soil moisture in the field, or using remote sensing techniques. In-situ measurements can be direct or indirect. The standard method for measuring the soil moisture content is the gravitational measurement technique. With this direct method the soil moisture content is calculated from the mass difference of a soil sample taken in the field before and after oven drying. This method is inexpensive, soil moisture is easy to calculate and it is independent of soil type and salinity. On the other hand it is a destructive test; it is time consuming and does not allow automatic control. Furthermore, the dry bulk density must be known to transfer the mass water content to the volumetric water content (Brady & Weil 1996; Barsch et al. 2000). Indirect measurement techniques estimate the soil moisture content from parameters, which allow conclusions on the actual soil moisture content. An easy and widespread method is the Time Domain Reflectrometry (TDR). A TDR sensor consists of two or three parallel waveguides, a linear structure made of conducting materials, which are placed in the soil material. The moisture content of the soil is estimated from the travel time of an electromagnetic impulse which is passed along the waveguides. The speed of the electromagnetic wave estimated from the travel time allows conclusions about the dielectric constant of the soil. With increasing soil moisture content and increasing dielectric constant of the soil, the speed of the electromagnetic wave is decreasing. For most soils, this method does not require calibration, it can be easily automated and allows long term monitoring of soil moisture (Jones et al. 2002; Walker et al. 2004b).

Another indirect measurement technique is utilizing the force which binds water in the soil for the estimation of the soil moisture content. Tensiometers are placed in the soil and consist of a cup filled with a porous material and water, connected to a manometer. Water from the tensiometer is drawn into the surrounding soil. This causes a negative pressure in the cup which is measured using a manometer. Soil moisture retention curves describe the relation between the measured negative pressure and the water content of the soil. The comparably inexpensive sensors are easy to install and

most irrigation recommendations rely on tensiometer measurements. On the other hand, tensiometers require regular maintenance and their limited measurement range does not allow the measurement of very low moisture contents (Zazueta & Xin 1994; Koorevaar et al. 1999). Other indirect *in-situ* measurement techniques are neutron scattering, gamma ray attenuation and soil electrical conductivity. Further information on these techniques can be found in Schmugge et al. (1980), Topp (2003) and Zegelin (1996).

The main disadvantage of all *in-situ* measurement techniques is the fact, that they only provide point measurements. This makes the regular, automated long term monitoring of soil moisture over larger areas very expensive if not impossible. Here, remote sensing techniques, which give areal estimates of soil moisture, can be used for monitoring from local to global spatial scales. Before describing active soil moisture remote sensing, an introductory overview of passive remote sensing technique is given in Chapter 3.

### **2.3. Spatio-Temporal Properties of Soil Moisture**

---

Characterizing the temporal and spatial distribution of soil moisture, either using *in-situ* techniques or by means of remote sensing is always connected to scale issues. Soil moisture measurements using *in-situ* techniques are usually carried out to describe the soil moisture conditions of an area, e.g. a field, a slope or even an entire catchment. Therefore it is important to know, what kind of relations between point measurements and areal estimates of soil moisture does exist. In case of remotely sensed soil moisture, the opposite case is of interest: How does an areal estimate - remote sensing sensors always acquire information over a certain area of the Earth's surface - of soil moisture relate to smaller spatial entities? For validating modelled or remotely sensed soil moisture products, it is important to know at which time remote sensing data and at which time *in-situ* soil moisture measurements were acquired. The larger the time difference between generated and measured soil moisture, the less confidence can be given to validation results. Therefore the spatio-temporal scale properties are described in the following.

Soil moisture as a property and a process occurring at the interface between the atmosphere and the land surface of the Earth is highly variable in space and time. Within a few meters soil moisture can vary as much as within a distance of kilometres

(Dubayah et al. 1997; Buttafuoco et al. 2005). Spatial soil moisture patterns usually follow topography, vegetation cover, land use or geological substrates, which are closely connected to the soil texture and water holding capacity (Western & Blöschl 1999). In the temporal domain the moisture content in the uppermost centimetres of a soil profile, which is directly exposed to the influences of the atmosphere, can vary in the order of a few hours (Raju et al. 1995). The moisture content at a specific point in space and time is the result of the preceding precipitation events, soil properties (texture, content of organic matter and porosity affecting water holding capacity, soil colour affects evaporative drying), topography (slope and aspect affects runoff, infiltration and evapotranspiration), vegetation cover (interception of precipitation, evaporation from plant surfaces, transpiration of plants, causing turbulence and enhancing evapotranspiration) and climatic conditions (solar radiation, humidity, air temperature affecting evaporation from soil) (Dubayah et al. 1997; Famiglietti et al. 1998; Mohanty & Skaggs 2001).

Precipitation as the main driving force for spatio-temporal soil moisture patterns occurs at different space and time scales. Figure 2 shows typical spatial and temporal scales of hydrological processes. Convective precipitation is a small scale phenomenon in the range of minutes to one hour, whereas precipitation caused by frontal systems affects much wider areas, comprising scale lengths up to 1000 km and range from hours to one day. According to Grayson & Blöschl (2000), there is a link between processes and spatio-temporal patterns. Processes with small space and time scales will lead to temporal more variable small-scale patterns, whereas processes with large spatial and temporal scale lengths will cause spatially more coherent, slowly varying patterns.

Several studies showed that soil moisture variations in time and space can be addressed to two different scale components – a small scale and a large scale component. The small scale component leads to local variations in soil moisture due to soil properties, land cover attributes and local topography. This small scale component acts in the range of tens of meters spatially and in the range of a few days temporally (Entin et al. 1999; Robock et al. 2000). A connection between soil moisture and topography has been found by Grayson et al. (1997). During dry summer conditions no distinct spatial patterns were recognizable due to a maximum of vertical fluxes (evapotranspiration). In winter, during wet conditions, lateral surface and subsurface flow dominated. The large scale component is addressed to atmospheric forcing due to

precipitation and evaporation processes (Robock et al. 2000). Based on extensive *in-situ* data sets in Russia, Vinnikov et al. (1996) observed spatial correlation lengths of soil moisture in the order of 400 – 800 km caused by atmospheric forcing. These findings are supported by Entin et al. (2000). They report spatial correlation lengths in the order of several hundred kilometres for test sites in Russia, Mongolia, China and Illinois (USA).

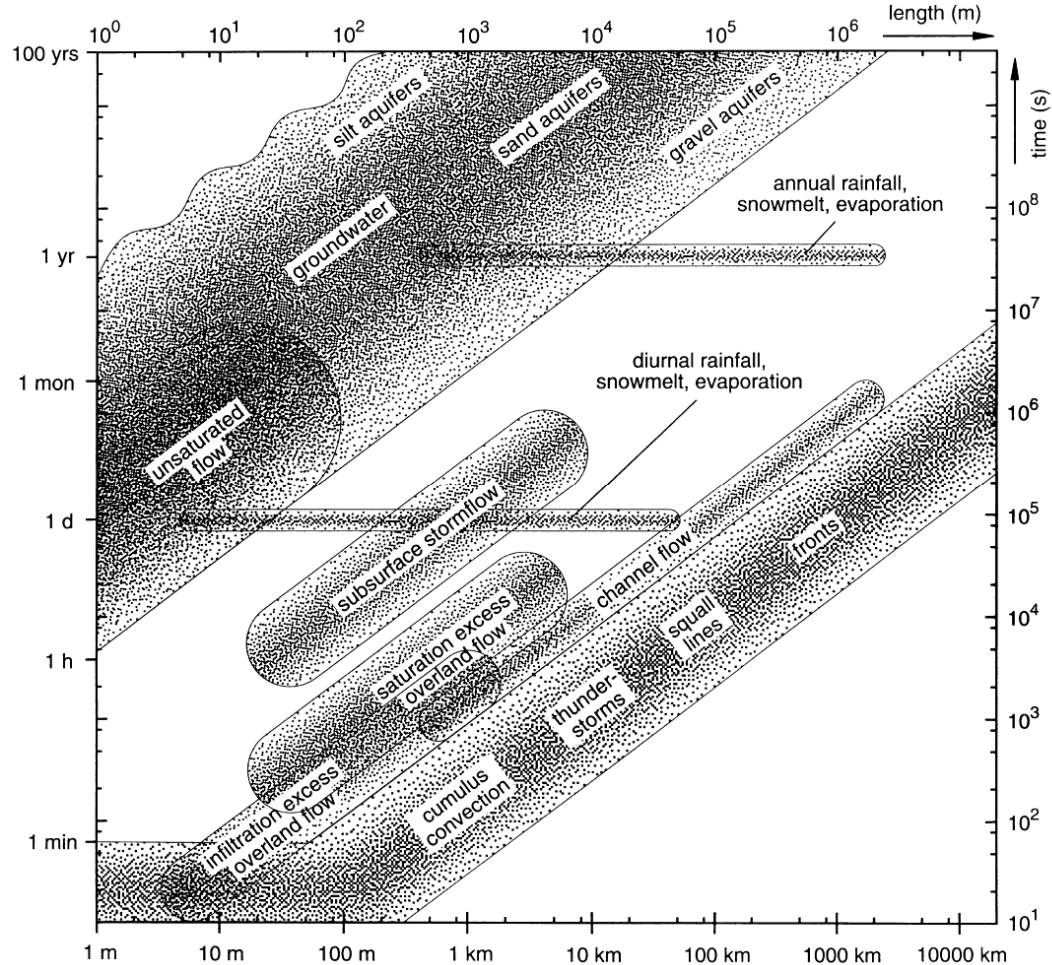


Figure 2: Temporal and spatial process scales in hydrology (Blöschl & Sivapalan 1995)

These findings are important for comparisons of *in-situ* data and remotely sensed soil moisture products. Because of their different spatial scales, a correlation between *in-situ* data and remotely sensed soil moisture products seems to be unlikely. Nevertheless, comparisons of coarse resolution soil moisture time series (i.e. ERS Scatterometer) representing areas  $\geq 1000 \text{ km}^2$  with *in-situ* measurements of soil moisture, typically representing areas  $\leq 0.01 \text{ km}^2$ , showed good agreements between data of such significantly different spatial scales. Bindlish et al. (2003) derived soil

moisture estimates from the SSM/I space-borne microwave radiometer over the Southern United States. With a standard error of 2.5%, *in-situ* measurements of soil moisture agreed well with the daily averaged soil moisture products. Comparisons of relative soil moisture values extracted from SSM/I radiometer data to *in-situ* soil moisture measurements showed, that these coarse resolution products are capable of explaining the temporal behaviour of the soil moisture with a RMSE of 7.18 %. Wen & Su (2003) found a high correlations of  $r = 0.63$  between ERS scatterometer derived relative surface soil moisture time series and *in-situ* top horizon soil moisture in Tibet. Wagner et al. (2003) compared ERS scatterometer retrieved soil moisture with model and precipitation data. High correlations between precipitation data and soil moisture data were found especially for regions with a dense station network. Modelled and remotely sensed soil moisture agreed well over tropical and temperate climates. Based on ERS scatterometer time series data, Ceballos et al. (2005) validated modelled profile soil moisture using *in-situ* soil moisture from a measurement network in the Duero Basin in Spain. Mean profile soil moisture from 20 measurement stations within the test site were compared to the soil moisture retrieved from the ERS Scatterometer with a footprint size corresponding to the test site area. Comparisons of the averaged soil moisture profiles showed a good agreement with  $R^2 = 0.75$  and RMSE = 2.2 vol.%. Agreements between point data and area averaged data in the temporal domain were subject of a study by Wagner et al. (2008). Here the temporal stability concept introduced by Vauchaud et al. (1985) for identifying area representative *in-situ* soil moisture measurement stations was transferred to Envisat ASAR Wide Swath data over a test site in Spain. It was found that temporal stable soil moisture patterns lead to temporal stable radar backscatter patterns. A simple time-invariant linear model to predict soil moisture and radar backscatter at point scale from regional observation was developed. Modelled scaling coefficients and scaling coefficients derived from observations showed good agreement with  $R^2 = 0.86$ .

Knowledge of the scaling properties of soil moisture is important because within the next few years only coarse resolution (25-50 km) soil moisture data derived from spaceborne radiometer and scatterometer systems can be expected to be operationally available (Wagner et al. 2007a). On the other hand, scientific and technological breakthroughs are still needed for operational soil moisture retrieval at finer scales using Synthetic Aperture Radar (SAR) (Wagner et al. 2007b). Global soil moisture products

are already available from the Advanced Microwave Scanning Radiometer (AMSR-E) (Njoku et al. 2003) and from the Advanced Scatterometer (ASCAT) onboard of the Meteorological Operational (METOP) satellite series (Bartalis et al. 2007). The Soil Moisture and Ocean Salinity (SMOS) satellite is planned to be launched in 2008 (Kerr 2007). The spatial resolution is 25 km for ASCAT, 43 km for SMOS, and 56 km for AMSR-E (C-band).

# **CHAPTER 3**

## **Remote Sensing of Soil Moisture**

---

Remote sensing is the term for all techniques which give information on distant objects or geo-physical phenomena without direct physical contact. Remote Sensing of the Earth is also referred to as Earth Observation (EO). This includes observation, mapping/monitoring of objects or phenomena and manual or automated interpretation of the acquired data under the aspect of different geo-physical applications. Common to all remote sensing techniques is the fact that electromagnetic radiation is used as the information carrier. Air-borne or space-borne sensors are used as measuring devices. Different remote sensing techniques utilize different regions of the electromagnetic spectrum. Remote sensing can be either passive or active. Passive remote sensing instruments measure natural radiation, e.g. the solar radiation reflected by objects at the Earth's surface. Active remote sensing sensors carry their own source of electromagnetic radiation. Examples of active remote sensing sensors are space-borne SAR systems or air-borne laser scanners (Löffler 1994; Lillesand & Kiefer 2000).

This thesis only concentrates on space-borne active remote sensing sensors operating in the microwave region of the electromagnetic spectrum. Nevertheless, a very brief overview is given of other remote sensing techniques for soil moisture retrieval is given in the following section.

### **3.1. Overview of Remote Sensing Techniques for Soil Moisture Retrieval**

---

In Chapter 2, the spatial and temporal variability of soil moisture together with the time and effort necessary for precise in-situ soil moisture measurements has been pointed out. Under the aspect of financial costs, manpower and time, it is not feasible to set up an in-situ soil moisture monitoring at continental or global scales. One alternative is the use of remote sensing. The big advantage of remote sensing methods is their capability to repeatedly deliver extended spatial data at different temporal and spatial

scales (Engman & Chauhan 1995). In the following section, different passive remote sensing methods utilizing different regions of the electromagnetic spectrum for soil moisture retrieval are introduced very briefly. All methods deliver indirect estimates of soil moisture. They measure a parameter accessible to remote sensing, which allows indirect conclusions on the soil moisture content (Curran 2001).

Techniques operating in the region of visible light ( $\lambda = 0.3 - 0.7 \mu\text{m}$ ) and the near-infrared ( $\lambda = 0.7 - 1.4 \mu\text{m}$ ) observe the soil surface albedo, the ratio of reflected to incoming solar radiation. An increase in soil moisture leads to a decrease of the albedo. This technique does not give precise values, as there is only a weak relation to soil moisture. The albedo also depends on soil texture, surface roughness, organic matter content, soil color, angle of incidence and vegetation cover. Different dry soil types may be characterized by a variety of different albedos. Reflectance measurements only represent signals from the top millimetres of the soil. Furthermore atmospheric influences cause attenuation of the reflected signals (Walker 1999; Engman 2000).

Thermal infra-red remote sensing methods operate at wavelengths between 8 and 15  $\mu\text{m}$  (Curran 1985). Soil moisture is estimated indirectly via the measurement of the soil surface temperature. This technique is based on the assumption that areas with high soil moisture emit less thermal radiation than areas with low soil moisture contents. However, soil surface temperature also depends on solar radiation, humidity, air temperature and wind causing a diurnal variation of soil surface temperatures. The presence of a vegetation cover can reduce the sensitivity to soil moisture substantially. The soil moisture information is only representative for the top millimetres of a soil profile and atmospheric effects need to be taken into account (Walker 1999).

Measurements of water mass changes affecting the gravitational field of the Earth can give soil moisture information at large catchment scales. With the GRACE double-satellite mission it was possible to map changes in surface hydrology at continental scales and large scale river basins. A summary is given in Crowley et al. (2007). The ability of GRACE to estimate the soil moisture distribution is limited by its temporal resolution of one month and the fact that mass changes less than 2.8 billion tonnes can not be detected (Adam 2002).

Microwaves show a unique sensitivity to the moisture content of natural media due to the pronounced increase of their dielectric constant with increasing moisture content (Ulaby et al. 1982). In the microwave region of the electromagnetic spectrum (see

Chapter 3.2.2.), soil moisture retrieval is also possible using passive remote sensing techniques. This is based on the fact, that every object with a temperature above 0 K emits microwaves due to the motion of the charged particles of its atoms or molecules. Therefore the emissivity changes with the physical temperature of the imaged objects. The quantity measured by the sensor is the brightness temperature TB. With models it is possible to relate changes in the brightness temperature to changes in the soil moisture content. Vegetation layers reduce the sensitivity of the sensor to soil moisture. Therefore longer wavelengths like L-band are preferred. Unfortunately, the energy content of radiation is inversely proportional to its wavelength (Jackson et al. 1996). To obtain detectable signals, passive microwave sensors have to view large areas which results in a poor spatial resolution in the order of around 50 km (Lillesand & Kiefer 2000). Although passive microwave systems offer high temporal resolutions, the poor spatial resolution is seen as the big disadvantage of this technique.

Active microwave remote sensing methods can provide data with much higher spatial resolutions. They are generally capable of delivering soil moisture information at various spatial and temporal scales. Together with their all-weather and all-day sensing capabilities, active microwave remote sensing is superior to optical methods (Engman & Chauhan 1995). Active remote sensing techniques are regarded to hold the largest potential for the retrieval of soil moisture at spatial and temporal scales required by the potential user community (Moran et al. 2004).

The following sections of Chapter 3 only concentrate on active microwave remote sensing techniques. First, the basic principles of active microwave remote sensing will be presented. Then an overview of different techniques for retrieving soil moisture information from the remotely sensed data based on the relevant literature is given. Finally, a brief summary of the different existing retrieval methods is given as a conclusion that lead to the soil moisture retrieval method presented with this study.

## 3.2. Basic principles of active remote sensing

As pointed out in the introduction to Chapter 3, active remote sensing is using electromagnetic radiation as information carrier between the object or phenomenon of interest and the air- or space-borne EO sensor. Electromagnetic radiation is emitted by accelerated electric charges or by electrons in transition from a level of high energy to a level of lower energy. This radiation can be either a natural phenomenon or generated by technical devices (Tipler & Mosca 2004). Electromagnetic radiation can be understood as a form of energy propagation, moving through space as a harmonic sinusoidal wave (Figure 3) at the speed of light ( $c$ ), where the electric and magnetic field vectors are perpendicular to each other and to the direction of wave propagation (Kraus & Schneider 1988). Electromagnetic waves are characterized by the two parameters wavelength ( $\lambda$ ) and frequency ( $f$ ), interrelated via the speed of light ( $c$ ) (Lillesand & Kiefer 2000):

$$c = \lambda \cdot f; \lambda = \frac{c}{f}; f = \frac{c}{\lambda} \quad (\text{Eq. 3.1, 3.2, 3.3})$$

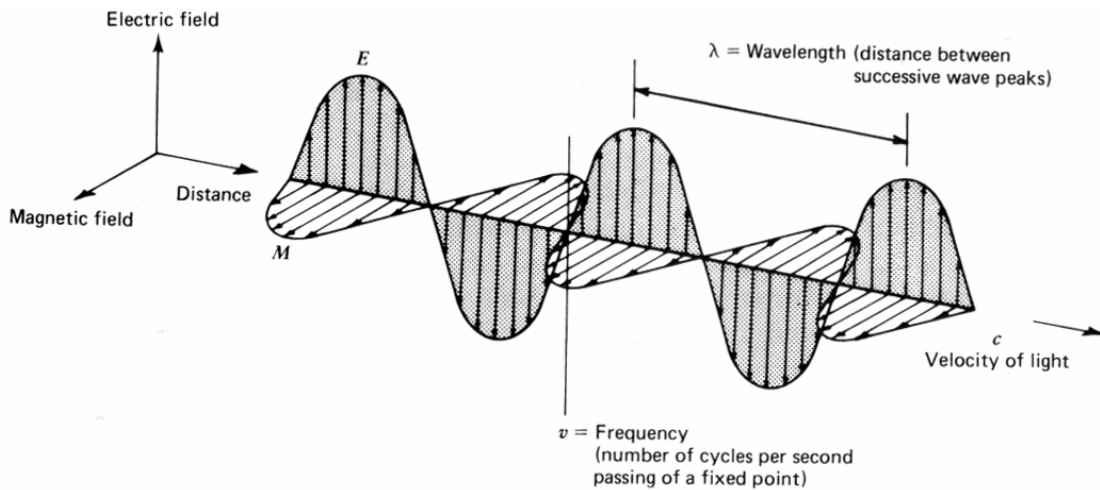


Figure 3: Electromagnetic wave,  $E$  – sinusoidal electric wave,  $M$  – sinusoidal magnetic wave (Lillesand & Kiefer 2000)

Electromagnetic radiation exists at different wavelengths or frequencies, integrated in the electromagnetic spectrum. Active remote sensing techniques using the microwave region of the electromagnetic spectrum cover a wide range of wavelengths  $\lambda$  or frequencies  $f$ . The microwave region of the electromagnetic spectrum is ranging from wavelengths of 1 mm (300 GHz) to 1 m (0.3 GHz). The microwave range is divided

into a number of so called radar bands (Table 1). Microwaves can also be called radar waves, but both terms can be used synonymously as they refer to the same range of wavelengths/frequencies (Lewis et al. 1998).

Band	Wavelength $\lambda$ [cm]	Frequency $f$ [MHz]
X	2.4 – 3.75	12,500 – 8,000
C	3.75 – 7.5	8,000 – 4,000
L	15 – 30	2,000 – 1,000
P	30 – 100	1,000 – 300

Table 1: Radar bands used in remote sensing (modified after Lewis et al. 1998)

In contrast to natural visible light, microwaves generated by radar sensors are monochromatic coherent waves. They are characterized by a known and temporal constant phase difference between the wave fronts. Monochromatic coherent waves are able to cause interference effects. Active microwave sensors are sending out short pulses of radar waves towards the Earth's surface and receive the signals scattered back towards the sensor. The backscattering process is governed by a number of sensor (wavelength/frequency, polarization, incidence angle) and target (dielectric constant, surface roughness) parameters, illustrated in Figure 4 (Dobson et al. 1995).

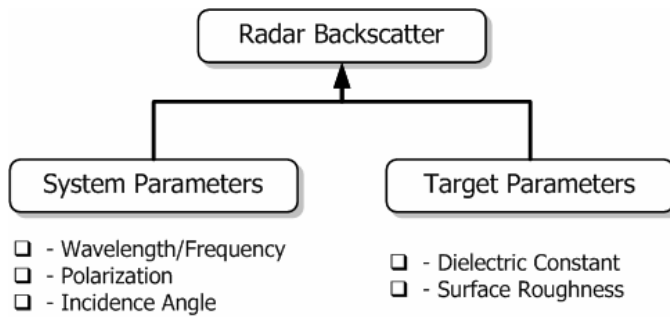
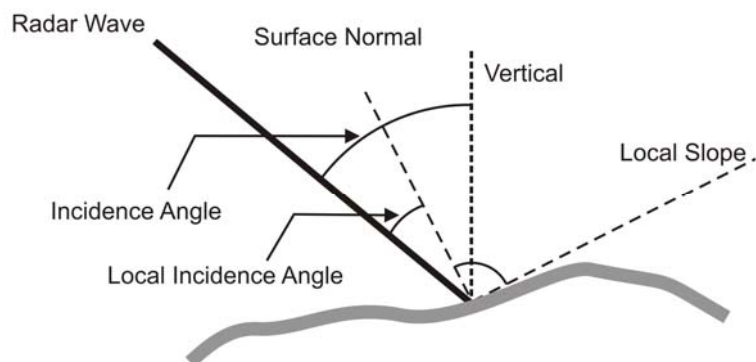


Figure 4: Main parameters controlling radar backscatter

### 3.2.1. Sensor Parameters

The sensor parameters wavelength  $\lambda$ /frequency  $f$ , incidence angle  $\theta$ , polarization, antenna characteristics and transmitted signal power are defined by the sensor's technical configuration. The wavelength/frequency together with the polarization of an active radar sensor controls the ability of the signals to penetrate into the soil layer and/or vegetation canopies. For a given soil moisture content, the penetration depth is

directly proportional to the wavelength (or indirectly proportional to the frequency) of the radar waves used for sensing. According to Ulaby et al. (1982), the penetration depth  $\delta_p$  is the depth below the air/soil boundary at which the signal power of an incident radar wave is reduced to an amount of  $1/e$  or  $\sim 37\%$ . For C-band, the penetration depth for dry mineral soils is approx. 5 cm. The penetration depth decreases with increasing soil moisture content for a given wavelength (Ulaby et al. 1996). Polarization of the radar wave refers to the direction of the electric field vector of the radar waves transmitted by the SAR antenna. It can be either horizontal or vertical. Active SAR sensors can be configured as single-, multi- or full-polarimetric systems. The possible sent-receive (first letter indicates sent-polarization, second letter indicates receive-polarization) combinations of a full-polarimetric system are: HH, VV, HV/VH (HV and VH responses are theoretically identical). Phase differences calculated from the scattering matrix allow conclusions about the dominating scattering processes (Ulaby et al. 1996). The geometrical properties of objects at the Earth's surface are able to cause depolarization. Depolarization can be caused by quasi-specular reflection from corner reflectors, multiple scattering from rough surfaces or multiple volume scattering (Lewis et al. 1998). The incidence angle of the radar waves is controlled by the antenna elevation beam pattern and is defined as the angle between the vertical and the impinging radar waves are (Figure 5). The local topography determines the local incidence angle  $\theta_{loc}$  which is defined with respect to the surface normal. Radar backscatter is influenced by the local incidence angle. For a surface with a given roughness, radar backscatter decreases with increasing incidence angle. For smooth



**Figure 5:** Illustration of the Incidence angle and the local incidence angle for SAR systems (after Lewis et al. 1998)

surfaces, radar backscatter drops off much faster than for rough surfaces. The concept of surface roughness is discussed in the next section. Radar acquisitions covering a large range of incidence angles show a decrease in radar backscatter from near range to far range. This is typical for airborne SAR or space borne ScanSAR systems, as they cover large incidence angle ranges (Dobson et al. 1995; Raney 1998). These influences on the backscattered signals need to be corrected before further analysis of the radar data (see Chapter 5.1.4.).

### 3.2.2. Target Parameters

---

Radar backscatter from the bare soil surfaces is controlled by two important target parameters - the dielectric constant  $\epsilon$  and the surface roughness R (Ulaby et al. 1996). Microwave remote sensing of soil moisture is based on the large differences of the dielectric properties of soil particles and water (Lewis et al. 1998). The dielectric properties are characterized by the complex permittivity or dielectric constant  $\epsilon$ . It is a complex number consisting of a real  $\epsilon'$  and an imaginary  $\epsilon''$  part:

$$\epsilon = \epsilon' + \epsilon'' \quad (\text{Eq. 3.4})$$

The dielectric constant  $\epsilon$  determines the reflection and attenuation characteristics of an electromagnetic wave incident upon a soil surface. For a soil, regarded as a mixture of soil particles, free and bound water and air, the dielectric constant  $\epsilon$  is an average value of the dielectric constants of its constituents and depends on the applied electromagnetic frequency, the physical temperature, the salinity, the volumetric water content and the fractions of bound and free water (Hallikainen et al. 1985; Jackson et al. 1996). At a given wavelength, dry soil has a dielectric constant  $\epsilon$  of 2 – 4. Water at the other hand has a much higher dielectric constant. At a frequency of 5 GHz, which corresponds to C-band, the dielectric constant of fresh water at 20°C is  $\approx 73$ . Adding water to a dry soil will increase the overall dielectric constant of the soil as a mixture of the solid soil particles, air and liquid water tremendously (Curlander & McDonough 1991; Ulaby et al. 1996). This remarkable change of the dielectric constant  $\epsilon$  of the soil material is caused by the special properties of water. The H<sub>2</sub>O molecule forms a permanent dipole, which aligns to an applied electric field (Schanda 1986; Engman & Chauhan 1995). Only the molecules of free water react on an applied electric field, whereas the molecules of the bound water are adsorbed to the surfaces of the soil

particles and thus their dipoles are immobilized (Njoku & Entekhabi 1996). With increasing dielectric constant, the penetration depth decreases and radar backscatter increases. A high dielectric constant of a soil causes a high radar backscatter and indicates a high soil moisture content (Curlander & McDonough 1991; Lewis et al. 1998). If the soil is frozen, than the water molecules and with it the dipoles can not align to an applied electric field any longer and show a very low radar backscatter (Woodhouse 2006).

The quantification of surface roughness always depends on the used wave-length. A surface may appear smooth in L-band but rough in X-band (Engman & Chauhan 1995). Radar backscatter increases with surface roughness. A radar wave impinging on a perfectly smooth surface will experience specular reflection, where the angle of reflection is the same as the angle of incidence. With increasing roughness backscatter becomes more diffuse approaching Lambertian reflectance (Lewis et al. 1998). Surface roughness is usually described using the RMS height  $s$  (see Figure 6) together with its correlation function  $\rho(\xi)$  to describe the vertical roughness component and correlation length  $l$  for the horizontal roughness component. The RMS height  $s$  is defined as the standard deviation of random surface components from a mean reference surface:

$$s = \sqrt{\frac{1}{N} \left[ \left( \sum_{i=1}^N z_i^2 \right) - N \bar{z}^2 \right]} \quad (\text{Eq. 3.5})$$

with

$$\bar{z} = \frac{1}{N} \sum_{i=1}^N z_i \quad (\text{Eq. 3.6})$$

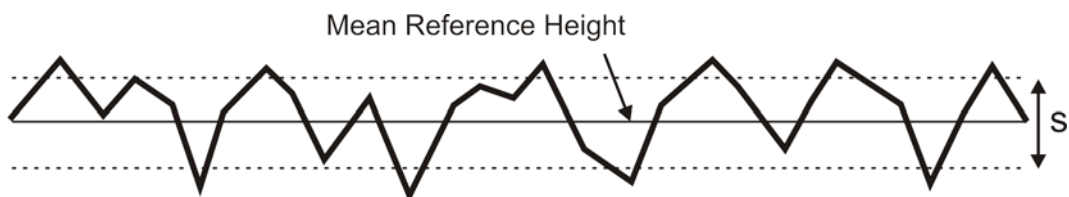


Figure 6: RMS height  $s$  as standard deviation from a mean reference height

The correlation functions describe the degree of correlation between a single roughness components  $z$  at a distances  $\xi$ . Two commonly used autocorrelation functions are:

$$\rho(\zeta) = \exp\left(-\frac{\zeta^2}{l^2}\right) \text{ (Gaussian)} \quad (\text{Eq. 3.7})$$

$$\rho(\zeta) = \exp\left(-\sqrt{2} \frac{\zeta}{l}\right) \text{ (Exponential)} \quad (\text{Eq. 3.8})$$

The correlation length  $l$  describes the distance, at which the random surface components are statistically independent. This is the case where  $l < e^{-1}$ . For perfectly smooth surfaces  $l$  becomes  $\infty$  (Verhoest et al. 2008).

To characterize the surface roughness in relation to the wavelength  $\lambda$ , two criteria can be used, which both are based on the phase difference  $\Delta\varphi$ . Single rays of a wave front impinging on a rough surface are scattered back with a certain phase difference  $\Delta\varphi$  (Raney 1998):

$$\Delta\varphi = 4\pi \frac{\Delta h}{\lambda} \cos \theta \quad (\text{Eq. 3.9})$$

with  $\Delta h$  being the mean height variations of the surface. To define, if a surface is smooth or rough, the Rayleigh criterion can be used, which is true if the phase difference is less than  $\pi/2$  (Raney 1998):

$$h > \frac{\lambda}{8 \cos \theta} \quad (\text{Eq. 3.10})$$

According to Ulaby et al. (1982) the Rayleigh criterion is inappropriate in the microwave domain. Therefore the Fraunhofer criterion is proposed, where the phase difference must be less than  $\pi/8$  for smooth surface conditions (Ulaby et al. 1982):

$$h > \frac{\lambda}{32 \cos \theta} \quad (\text{Eq. 3.11})$$

Surface roughness is often measured in the field using one dimensional surface profiles. Different devices for surface roughness estimation have been developed. Needle profilers consist of a large number of thin metal sticks with a fixed horizontal distance placed at the soil surface. Another method uses special plates with a measurement grid. They are placed on the surface and the profile is photographed and then digitized. A non-contacting device has been developed by Davidson et al. (2000) using a laser profiler, which can perform measurements over a length of 25 m.

It has turned out that the commonly used statistical descriptors of surface roughness, the RMS height and the correlation length, are not well suited for describing natural surfaces. They describe a single-scale process assuming that this adequately

describes the roughness within one SAR resolution cell. Research has shown that a multi-scale process would be a better representation of the surface roughness. Furthermore, theoretical backscatter models rely on the roughness descriptors RMS height and correlation length (Satalino et al. 2002; Manninen 2003). The one dimensional surface representation neglects the three-dimensional character of natural soil surfaces and also the fact that within the resolution cell of a SAR the small scale surface roughness is embedded in a larger scale related to the topography. Furthermore, the surface roughness of agricultural fields also depends on the direction. A ploughed field will have different surface roughness characteristics in the row and the direction perpendicular to it and so the row direction relative to the satellite track needs to be considered when doing surface roughness measurements (Verhoest et al. 2008).

### **3.3. Scattering from Bare and Vegetated Soil Surfaces**

---

Scattering can be described as random redirection of electromagnetic radiation impinging on an object or a surface (Woodhouse 2006). Radar waves impinging at the boundary of two semi-infinite media, which are two bordering media with a defined finite boundary but extending to infinity away from that boundary, are partially scattered back towards the sensor and partially penetrate into the medium. Backscatter from bare natural surfaces can be separated into surface scattering and volume scattering. Admittedly, both scattering mechanisms are present, but for reasons of simplifying the description and modeling of bare surface scattering, one of the two may be neglected (Ulaby et al. 1982). Surface scattering occurs if the lower medium is dielectrically homogeneous or if the radar waves penetrate only little into the medium. The scattering pattern is controlled by the incidence angle of the radar waves and the surface roughness. An illustration of this relation is given in Figure 7. In the case of surface scattering, the incident radar waves are partially reflected in the specular direction (reflected/coherent component) and partially scatter back towards the sensor (scattered/incoherent component). For a fixed incidence angle, the signal strength of the reflected component decreases and the strength of the scattered component increases with increasing surface roughness. The scattered component shows a diffuse scattering pattern which comprises backscatter in all directions. With increasing surface roughness the strength of the scattered component becomes much larger than that of the reflected

component, which becomes negligible. Natural surfaces showing surface scattering are very wet soil, water and wet snow (Ulaby et al. 1982; Rees 2001; Woodhouse 2006).

Volume scattering occurs, if the lower medium is an inhomogeneous medium with a high penetration depth. Here, incoming radar waves cross the boundary between the two media, are scattered back by randomly distributed elements, so called dielectric inhomogeneities, and cross the boundary into the upper medium again. Thus, the backscattering process takes place within the lower medium itself. The intensity of the backscattered signals depends on the roughness of the boundary between the two media as well as on the dielectric and geometric (size, distribution) properties of the discontinuities within the lower medium. Volume scattering can be observed for vegetation canopies, dry soil/sand and dry snow. Even though the scattering from bare soil surfaces occurs at dielectric inhomogeneities within the upper parts of a soil profile, the penetration depth at short wavelengths is very small and volume scattering occurs only in a small soil surface layer. Therefore the volume scattering part becomes negligible and backscatter is treated as surface scattering. Only if the soil becomes very dry, also short wavelengths like C-band are able to penetrate into the soil medium (Ulaby et al. 1982; Woodhouse 2006).

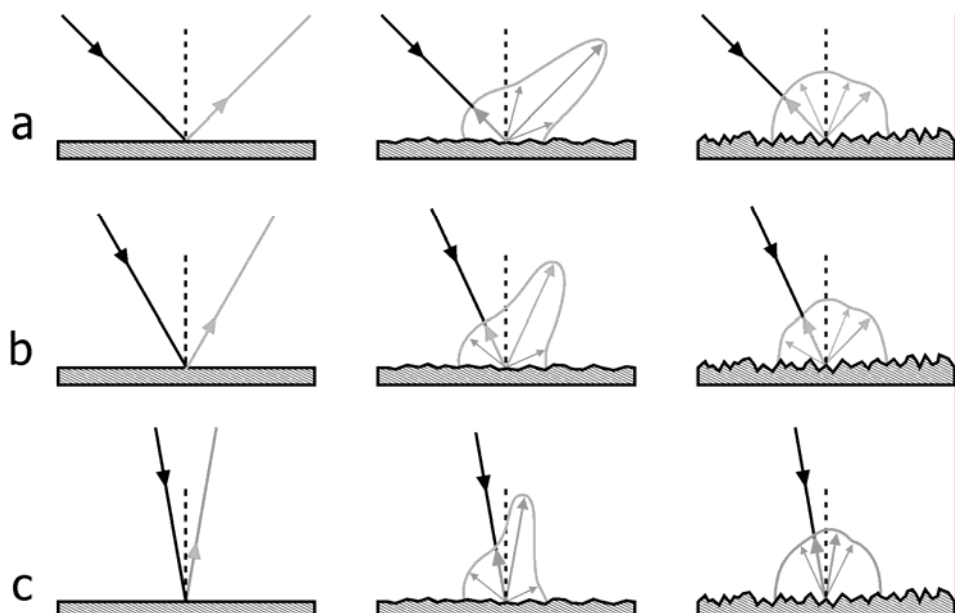


*Figure 7: Schematic illustration of scattering from surfaces with different roughness conditions at increasing (from a to c) incidence angles (after Woodhouse 2006)*

Backscattering from vegetated surfaces is a much more complex process than backscattering from bare soil surfaces. Backscatter from vegetated surfaces consists of surface scattering from the underlying soil surface and volume scattering caused by dielectric discontinuities within the vegetation canopy and their vegetation elements such as stems, branches and leaves (Figure 8).

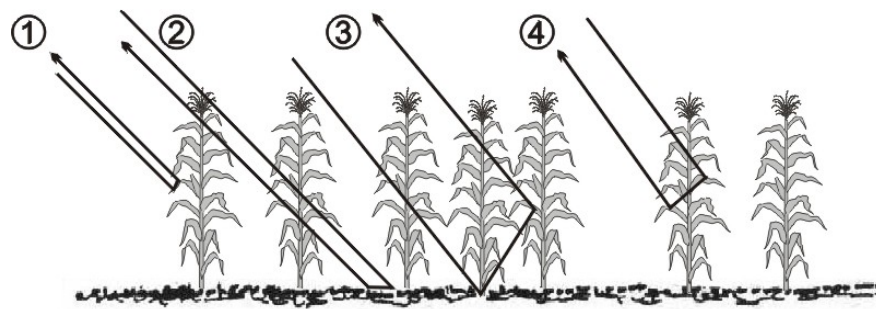


*Figure 8: Backscatter from vegetation: 1) direct backscattering from plants, 2) direct backscattering from underlying soil, 3) multiple scattering between plants and soil, 4) multiple scattering between plants, leaves, stalks ect. (after Ulaby et al. 1986; Chiu & Sarabandi 2000)*

Depending on the incidence angle, frequency and polarization, microwaves are able to penetrate vegetation layers to some degree (Dobson & Ulaby 1998). For a short dry canopy layer, the backscatter contribution from the underlying soil at a given wavelength depends on the incidence angle. For shallow incidence angles, the path length is much longer than for steeper incidence angles. Therefore much more vegetation elements may potentially interact with the impinging incidence angles and surface backscattering will decrease in favour of volume scattering. Thus, soil moisture from areas covered by grass or crops might be possible when using steeper incidence angles (Daughtry et al. 1991; Brisco & Brown 1998). Besides the incidence angle, also the wavelength of the incident radar waves is of importance. Longer wavelengths penetrate deeper into a vegetation layer than short wavelengths. The dependency of radar backscatter from the incidence angle over vegetated surfaces is closely connected to the above ground biomass. For high biomass, the ability to penetrate the canopy layer decreases and the volume scattering contribution becomes larger. Volume scattering from dense randomly distributed vegetation is almost uniformly distributed over a wide range of incidence angles. The influence of the incidence angle on radar backscatter diminishes; radar backscatter decreases very slowly with increasing incidence angle

(Figure 9). This is the case for forests and here especially for tropical rain forest. Soil moisture retrieval from soils under forest is hardly feasible (Ulaby et al. 1982).

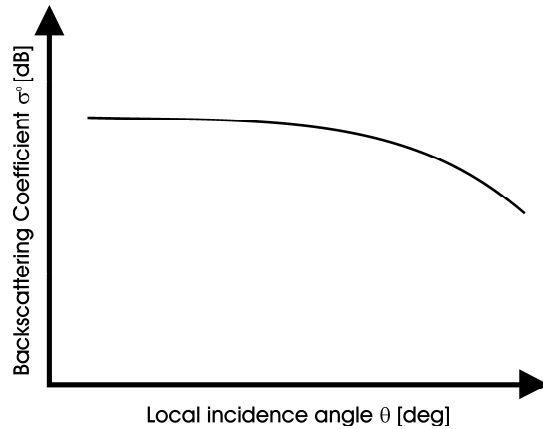


*Figure 9: Schematic illustration of the dependency of radar backscatter from local incidence angle at a given for vegetation canopies*

Additionally, the dielectric properties of the vegetation which are directly linked with their water content, also controls the penetration depth. Depending on phenological stage and time of day, vegetation can hold large amounts of water. The higher the water content, the lower the signal penetration. Depending on the polarization of the microwaves, the vegetation elements will have different effects on impinging microwaves. Horizontally polarized microwaves are scattered more by horizontally oriented vegetation elements and vertically polarized microwaves are scattered more by vertically oriented vegetation elements. Generally, HH polarization is preferred for soil moisture studies under vegetation (Leckie & Ranson 1998). As a general conclusion it can be stated that the presence of a vegetation layer attenuates the sensitivity of radar waves to the moisture content of the underlying soil (Ulaby et al. 1986; Lewis et al. 1998).

### 3.4. Radar Equation

The radar equation (Eq. 3.12) relates the received signal power  $P_R$  to the transmitted signal power  $P_T$  and the sensor parameters wavelength  $\lambda$ , range distance  $R$ , antenna gain  $G$ , illuminated area  $A$  and the target parameters subsumed in the radar backscattering coefficient  $\sigma^0$  (Ulaby et al. 1982):

$$P_R = \frac{\lambda^2}{(4\pi)^3} \cdot \int \frac{P_T G^2 \sigma^0 \Delta A}{R^4} \quad (\text{Eq. 3.12})$$

where:

$P_R, P_T$  - Received and transmitted signal power

$\lambda$  - Wave length

$\sigma^0$  - Radar backscattering coefficient

$\Delta A$  - Illuminated area

$R$  - Range distance

$G$  - Antenna gain

The radar backscattering  $\sigma^0$  coefficient contains information on the physical characteristics of the observed target and relates the emitted power to the received power of the backscattered signals (Woodhouse 2006). For distributed targets, the radar backscattering coefficient  $\sigma^0$  integrates the response of all scattering elements within the resolution cell illuminated by the sensors radar pulse with respect to a unit area on the horizontal ground plane (Eq. 3.13) (Curlander & McDonough 1991):

$$\sigma^0 = \frac{\sigma}{A} \left[ \frac{m^2}{m^2} \right] \quad (\text{Eq. 3.13})$$

Because  $\sigma^0$  can cover a large range of values, this dimensionless parameter is usually transferred to the logarithmic domain using (Ulaby et al. 1996):

$$\sigma^0 [\text{dB}] = 10 \cdot \log 10 \cdot \sigma^0 \left[ \frac{m^2}{m^2} \right] \quad (\text{Eq. 3.14})$$

### 3.5. Soil moisture retrieval from active radar data

---

All attempts to retrieve soil moisture from active radar data rely on the basic assumption, that radar backscatter is a function of a soil's moisture content. A simple formulation of the relation between radar backscatter and soil moisture for bare soil conditions can be written as (Moran et al. 2004):

$$\sigma^0 = f(m_s, R) \quad (\text{Eq. 3.15})$$

This formula reveals the “dilemma” of soil moisture retrieval from radar backscatter: the radar signals contain ambiguous information. The backscattered radar signals contain both soil moisture ( $m_s$ ) and surface roughness ( $R$ ) information (Ulaby et al. 1996). Research has shown that the influence of surface roughness on the

backscattered signal is in the same order or larger than the influence of soil moisture (Satalino et al. 2002). If a vegetation layer is present, the soil moisture retrieval becomes very complex if not impossible. Vegetation, which may contain large amounts of water, has also dielectrical and geometrical properties, which influence the radar waves twice. First, vegetation interacts with the radar waves before they reach the soil surface and second, they also interact with the backscattered signal portions, before they are received by the sensor. In this context, radar backscatter is still a function of soil moisture and surface roughness expressed as  $\sigma_s^0$  plus the two-way-attenuation of the vegetation layer  $\tau^2$ , the direct backscatter contribution of the vegetation layer  $\sigma_{veg}^0$  and multiple backscattering effects within the vegetation layer and between the vegetation and the underlying soil surface  $\sigma_{multi}^0$  (Ulaby et al. 1996):

$$\sigma^0 = \tau^2 \cdot \sigma_s^0 + \sigma_{veg}^0 + \sigma_{multi}^0 \quad (\text{Eq. 3.16})$$

Therefore it is necessary to remove all non-soil moisture related signal components to isolate the soil moisture information in the backscattered signals. The decomposition of the soil moisture signal from other signal components is done using backscatter models. A large number of backscatter models can be found in the literature. They range from simple empirical regression models to sophisticated theoretical models describing the interaction of radar waves with bare soil surfaces and vegetation layers. The next sections try to give a short overview of the basic modeling concepts.

### 3.5.1. Theoretical Models

---

Theoretical models have been developed to provide a mathematical-physical description of radar backscatter. A radar wave impinging on the boundary of two dielectrical homogeneous media will be partly transmitted into the medium and partly scattered back. The boundary is assumed to be a planar surface with height variations smaller than the wavelength of the impinging wave (Jackson et al. 1996). The Maxwell's equations provide an explanation on how electromagnetic waves interact with matter. The amount of energy which is scattered back from the boundary is described by the Fresnel reflectivity, which is derived from the wave equation – a derivate from the Maxwell's equations (Curlander & McDonough 1991; Tipler & Mosca 2004).

Unfortunately, initial assumptions on the geometric properties of the boundary (planar surface with height variations smaller than the wavelength of the impinging radiation) together with the dielectrical properties of the two media do not correspond to natural media. Soil surfaces are randomly rough surfaces which can have roughnesses much larger than the wavelength. Due to dielectrical discontinuities soils are inhomogeneous media behaving like volume scatterers. Given the complexity of natural media, an exact description of scattering of electromagnetic radiation by soil surfaces is not feasible. Therefore theoretical models are based on simplifying assumptions and are only valid within a certain validity ranges expressed in terms of surface roughness. Theoretical models only use amplitude information at one or more wavelengths and of one or more polarizations; phase information remains unconsidered (Dubois et al. 1995).

The standard theoretical models are the Kirchhoff models which are the Geometrical Optics Model (GOM) for rough and the Physical Optics Model (POM) for surfaces with medium roughnesses. The Small Perturbation Model (SPM) has been developed for smooth surfaces (Ulaby et al. 1982; Jackson et al. 1996). But the ranges of validity of these theoretical models expressed in terms of surface roughness do not reflect the roughness conditions usually found in the field. Therefore another theoretical backscatter model, the Integral Equation Model (IEM), has been developed by Fung (1994). The IEM combines the Kirchhoff models with the Small Perturbation Model and covers a much wider range of surface roughnesses and therefore has become the most widely used theoretical backscattering model (Moran et al. 2004). The potential of the IEM to retrieve soil moisture from SAR data has been demonstrated in a large number of studies. Compared to the Kirchhoff models or the SPM, the wider range of possible surface roughnesses of the IEM lead to results that show a better agreement between model simulations using adapted versions of the IEM and observational data (Altese et al. 1996; Su et al. 1997; Macelloni et al. 2000). Improvements of the model results have been achieved by using so called *a priori* information in the retrieval algorithm (Mattia et al. 2006). Bindlish & Barros (2000) applied the IEM over a watershed in Oklahoma and found an overall retrieval error of 3.4%, a value which was expected due to the inherent noise in the SAR data. An extension of the IEM with a semi-empirical vegetation parameterization was tested by Bindlish & Barros (2001). With this method, it was possible to improve the correlation coefficient for an

experimental data set from 0.84 to 0.95. Additionally, several simplifying adaptations of the IEM have been introduced in the literature.

Due to their restrictive validity conditions and simplifying representation of the real world, radar backscatter simulated using theoretical models often show only medium to poor agreements with observations (Dubois et al. 1995; Walker et al. 2004a). Although theoretical models like the IEM can yield soil moisture data, their applicability is mostly restricted to field experiments. Radar backscatter data at different frequencies and polarizations are required together with additional parameters describing the surface roughness. Such data are only available in experimental settings over relatively small areas. Furthermore, the surface roughness description has often been criticized for being too simplistic and not representing the three-dimensional character of natural surfaces (Oh et al. 1992; Macelloni et al. 2000). For practical use with operational space-borne SAR sensors, theoretical models are too data demanding (Thoma et al. 2006). Theoretical backscatter models are not suited for soil moisture retrieval from single-frequency and single-polarization mono-temporal SAR data without auxiliary field data (Moran et al. 2004).

The presence of a vegetation layer adds even more complexity to the modeling of radar backscattering. Due to absorption and scattering within the vegetation layer, the sensitivity of a SAR to the soil moisture of the underlying soil is reduced. A number of theoretical models have been introduced for predicting the backscattering from vegetated soil surfaces. A simple vegetation backscatter model has been introduced by Ulaby & Attema (1978). Here, the vegetation layer is modeled as a randomly distributed cloud of small dipoles. In more sophisticated vegetation backscatter models, leaves are described as dielectrical thin discs, stems and branches are modeled as cylinders (Chiu & Sarabandi 2000; Bindlish & Barros 2001). One example for such a theoretical vegetation model is the Michigan Microwave Canopy Scattering Model (MIMICS). Here a tree canopy is represented as three layers: crown layer, trunk layer and rough surface layer. The interaction of the impinging microwaves with the vegetation uses radiative transfer theory (Ulaby et al. 1990). This is also a major criticism of the model. It neglects the coherent nature of microwaves and applies a method originally developed for non-coherent light. Although vegetation models with their necessary abstractions may help in getting a better understanding of backscatter from vegetated surfaces, experimental results often do not agree with field data. Using a 3D indoor

SAR measurement device, the backscatter within a vegetation layer was analyzed by Brown et al. (2003). They showed, that within a wheat canopy of nearly 60 cm height, the backscatter contribution at X- and C-band from the underlying soil layer was higher than simulated using common radiative transfer vegetation models. This was attributed to an inadequate description of the attenuation by radiative transfer approach in the theoretical vegetation models.

### 3.5.2. Empirical and Semi-Empirical Models

---

Empirical models try to provide a description of the influences of surface roughness and soil moisture on the backscattering coefficient by means of regression analysis. Simple empirical linear regression models are given in the form

$$\sigma^0 = a \cdot m_s + b \quad (\text{Eq. 3.17})$$

where  $a$  and  $b$  are regression coefficients and  $m_s$  represents surface soil moisture. This requires a large number of in-situ observations to establish robust statistical relationships. Regression models proved their ability to describe radar backscatter as a function of soil moisture in a large number of studies (Weimann et al. 1998; Shoshany et al. 2000; Oldak et al. 2003; Sahebi et al. 2003; Zribi et al. 2005). Using empirical models it was demonstrated, that there exists a fundamental relation between the backscattered radar signals and the soil moisture (Rombach et al. 1993; Moeremans & Dautrebande 1998; Weimann et al. 1998). But they do not provide any kind of explanation of the processes involved in the backscattering process and thus can be regarded as black-box-model. Empirical models are site dependent. Linear regression models developed for a specific data set can not be applied to other test sites. With empirical models it is not possible to develop a widely applicable method for operational soil moisture retrieval for large and diverse regions.

Besides purely empirical models, also semi-empirical models have been developed, which are intermediate between theoretical and empirical models. They are based on theoretical models, but have been simplified by taking into account observational data. Two widely known semi-empirical models are the Oh-model and the Dubois-model.

The Oh-model was developed by Oh et al. (1992) for multi-polarized and multi-frequency radar data acquired using a truck-mounted scatterometer for an incidence

angle range of  $10^\circ$  to  $70^\circ$ . To retrieve soil moisture or surface roughness estimates, a co- and a cross-polarized polarization ratio p and q is calculated:

$$p = \frac{\sigma_{HH}^0}{\sigma_{VV}^0} = \left[ 1 - \left( \frac{\theta}{90^\circ} \right)^{3\Gamma_0} e^{-k rms} \right] \quad (\text{Eq. 3.18})$$

$$q = \frac{\sigma_{HV}^0}{\sigma_{VV}^0} = 0.23\sqrt{\Gamma_0}(1 - e^{-k rms}) \quad (\text{Eq. 3.19})$$

Also based on scatterometer data, Dubois et al. (1995) proposed a semi-empirical model for estimating  $\sigma_{HH}^0$  and  $\sigma_{VV}^0$  for bare soil surfaces. Backscatter is expressed as a function of system parameters (incidence angle, wavelength) and soil properties (RMS height, dielectric constant):

$$\sigma_{HH}^0 = 10^{-2.75} \left( \frac{\cos^{1.5} \theta}{\sin^5 \theta} \right) 10^{0.028 \epsilon_r \tan \theta} (k rms \sin \theta)^{1.4} \lambda^{0.7} \quad (\text{Eq. 3.20})$$

$$\sigma_{VV}^0 = 10^{-2.35} \left( \frac{\cos^3 \theta}{\sin^3 \theta} \right) 10^{0.046 \epsilon_r \tan \theta} (k rms \sin \theta)^{1.1} \lambda^{0.7} \quad (\text{Eq. 3.21})$$

Baghdadi & Zribi (2006) evaluated the IEM, Oh- and Dubois-model using ERS-2, Radarsat-1 and ASAR C-band data and observational data. They found, that the Oh-model overestimated the cross-polarized ratio q. For the Dubois-model overestimations as well as underestimations of the backscattering coefficient have been observed, depending on the surface roughness conditions. D'Urso & Minacapilli (2006) also found differences of  $\pm 20\%$  between measured soil moisture data and simulated data using the Oh-model.

### 3.5.3. Change Detection

A general definition of change detection is given by Singh (1989), who describes it as a process or method for identifying changes in the state of an object or a phenomenon by observing it at different times. Change detection techniques have been used for various applications in the field of remote sensing. In an review of change detection techniques, Li et al. (2004) are listing important application fields of remote sensing change detection methods. They comprise studies on land-use and land-cover changes,

forest or vegetation changes, wetland changes, landscape changes, urban change, crop monitoring or environmental change studies. For these kinds of studies, mostly optical air- or space-borne remote sensing data were used.

Given the methodological and practical limitations of the theoretical, empirical and semi-empirical backscatter models described in the previous sections, change detection methods also for soil moisture retrieval emerged in recent years. The main advantage of change detection methods lies in the possibility to use single frequency and single polarization data like they are typically offered by past and current space-borne SAR sensors (Moran et al. 2006). Change detection methods for soil moisture retrieval are based on the assumption that changes in surface roughness and vegetation acts on much longer time scales than changes in soil moisture. Therefore changes in radar backscatter between consecutive radar acquisitions of the Earth's surface are primarily addressed to soil moisture changes (Engman 1994; Entekhabi et al. 2004). Change detection methods do not interpret pixels in relation to other pixels of the same data set, but perform a comparison of pixel values for a specific location over time. The interpretation of radar backscatter on a purely physical basis is replaced with the interpretation of temporal changes of radar backscatter. In these cases, surface roughness and vegetation cover are treated as stable parameters described by some kind of reference values, extracted from long-term backscatter measurements (Engman 1995; Verstraeten et al. 2006).

A number of successful demonstrations of the potential of change detection methods have been published so far. Quesney et al. (2000) used 32 ERS C-band SAR images over the Orgeval catchment in France and proposed a change detection soil moisture retrieval algorithm based on so called sensitive targets. For these targets it was possible to estimate and remove vegetation and surface roughness effects. They showed that with this method soil moisture could be retrieved with an accuracy of  $0.05 \text{ cm}^3/\text{cm}^3$ . Furthermore it was demonstrated, that the surface roughness induced effects can be regarded constant over the year. Six tandem pairs of ERS-1/2 data were analysed by Moeremans & Dautrebande (2000). Using field-averaged backscatter values, a very high correlation with  $R^2=0.99$  between backscatter data and observational data was found. Wickel et al. (2001) applied a change detection approach to a set of 10 Radarsat-1 images. Day-to-day backscatter differences are related to in-situ soil moisture measurements for stubble fields. A strong correlation with  $R^2=0.89$  was found

indicating a linear relation. Wagner et al. (2003) applied a change detection approach to global long-term backscatter data of the ERS scatterometer with a spatial resolution of 50 km. A detailed description of the methods used for this study is given in Chapter 5.2., as this forms the basis at which a change detection approach for ASAR GM data is derived. The soil moisture products derived from the ERS scatterometer were subject of a number of validation studies and proved their applicability at continental to regional spatial scales. In an assessment of different operational soil moisture data sets obtained for the Great Plains, the ERS scatterometer soil moisture performed well when compared to *in-situ* soil moisture and to soil moisture products extracted from the polarimetric scanning radiometer (PSR) and ERA40 atmospheric reanalysis data sets, which comprises assimilated satellite and ground-based measurements of various geo-physical variables. It was shown, that the ERS scatterometer soil moisture is able to capture the temporal evolution of soil moisture as accurate as the ERA40 data set with RMS errors of 5.6% and 5.7% respectively when compared to field observations (Drusch et al. 2004). Pellarin et al. (2006) compared ERS scatterometer surface soil moisture over a test site of 1600 km<sup>2</sup> in southwestern France to area-averaged modeled root zone soil moisture values. A RMS error of 0.061 m<sup>3</sup>·m<sup>-3</sup> was found. A global comparison of ERS scatterometer profile soil moisture with modeled soil moisture and rainfall data by Wagner et al. (2003) showed good agreements especially for tropical and temperate climates with values of R ranging between 0.6 and 0.9. Ceballos et al. (2005) evaluated plant available water derived from ERS scatterometer profile soil moisture using *in-situ* soil moisture values from a test site, equipped with a dense TDR station network, in the Duero Basin in Spain. The study revealed a good agreement between field measurements and remotely sensed data with R<sup>2</sup>=0.75 and an RMS error of 2.2 vol. %.

### **3.6. Hypothesis of the study**

---

From the previous discussion of the various possibilities to derive soil moisture from SAR data it is learned that different retrieval approaches data have been developed and published in the last three decades. So far, no operational method for soil moisture retrieval from spatial high resolution SAR data is available. On the other hand, the experiences gathered with extensive multi-temporal scatterometer data sets at low spatial resolutions show the potential of change detection methods for soil moisture retrieval. With the Envisat ASAR ScanSAR data such as obtained in Global Mode, microwave data at medium temporal and spatial resolutions have become available. This study is based on the hypothesis, that multi-temporal Envisat ASAR Global Mode data can be used for soil moisture retrieval using a change detection approach. It is assumed that, based on a change detection approach originally developed for ERS-1/2 scatterometer data developed by Wagner et al. (1999a-c), a change detection model can be adapted for use with ASAR GM data to infer relative surface soil moisture.

The specific goals of the study are:

- 1) to develop an automatic processing chain for ASAR GM data
- 2) to adapt an existing change detection approach developed for ERS-1/2 scatterometer data for use with multi-temporal ASAR GM data
- 3) to show, that necessary adaptations of the model, e.g. neglecting seasonal vegetation cover effects, does not substantially affect the quality of the retrieved relative surface soil moisture
- 4) to show that surface soil moisture derived from ASAR GM using the change detection model is capable of representing spatial and temporal soil moisture patterns with more detail than it is possible for ERS-1/2 scatterometer data with a distinctively lower spatial resolution

# Chapter 4

## Test Site and Data

---

In this dissertation, a surface soil moisture retrieval algorithm based on a change detection approach is proposed. The algorithm is developed using a comprehensive archive of Envisat ASAR GM data. The validation of the derived soil moisture product uses *in-situ* soil moisture data from a measurement network in Oklahoma/USA. This chapter provides an overview of the test site, the remote sensing data, *in-situ* soil moisture data and other auxiliary data.

### 4.1. Test Site

---

Oklahoma has been selected as test site for this work, because a comprehensive archive of *in-situ* soil moisture data has been made available by the Oklahoma Climatological Survey (OCS).

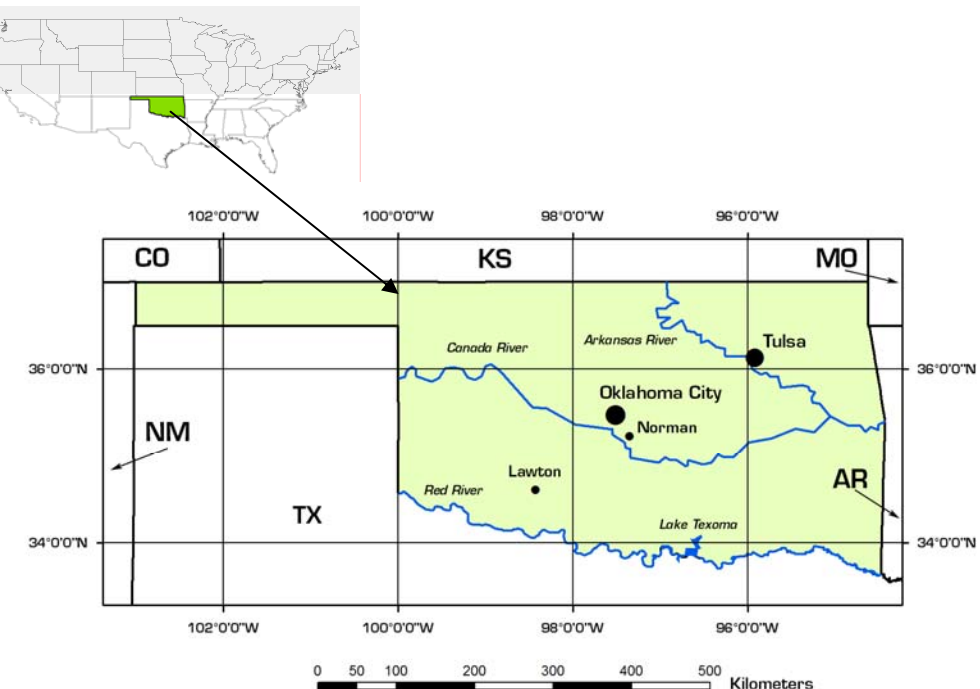


**Figure 10:** Oklahoma/USA

Oklahoma is a federal state in the south-western part of the United States of America (USA) (Figure 10). It covers an area of 181.182 km<sup>2</sup> has a population of 3.5 million people (U.S. Census Bureau Population Division 2007).

The state is situated mainly in the Great Plains, the broad band of prairie and steppe covering the inner continental parts of the United States (Figure 11). Oklahoma's topography is characterized by vast plains, karst plateaus, hills and folded low mountains. The area is generally sloping towards the east. The mean regional slope in the Great Plains is about 1.9 m per kilometer. The highest point of Oklahoma with an altitude of 1,516 m is to be found in the Black Mesa mountain range in the northwestern corner of the Panhandle (McKnight 1992). Surface geology is formed mainly by eolian, fluvial and glacial sediments. Due to the topography of Oklahoma, the basic stream-flow pattern is oriented from west to east and belongs to the Mississippi River basin. The main rivers are the Arkansas River, the Canadian River and the Red River, which forms the border to Texas (Commission for Environmental Cooperation 1997; Woods et al. 2005).



**Figure 11:** Level I Ecoregions of Oklahoma (Commission for Environmental Cooperation 1997)

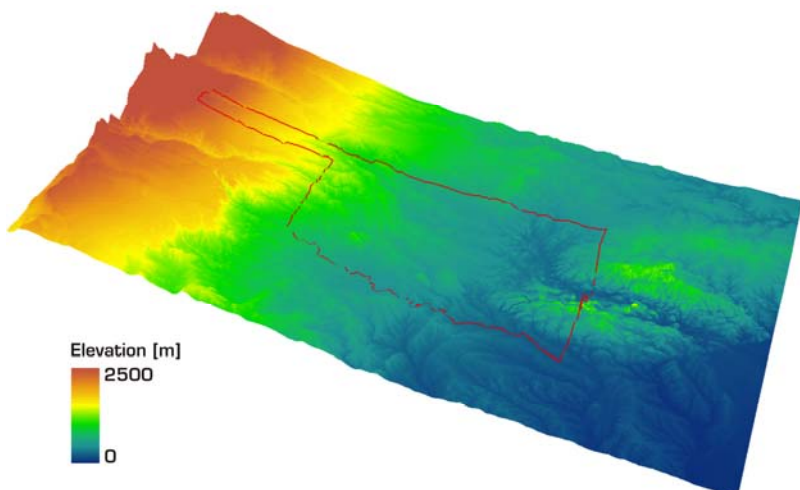


**Figure 12:** Perspective view of Oklahoma's Topography (SRTM improved GTOPO30 DEM, <ftp://e0srp01u.ecs.nasa.gov/srtm/version2/SRTM30/>)

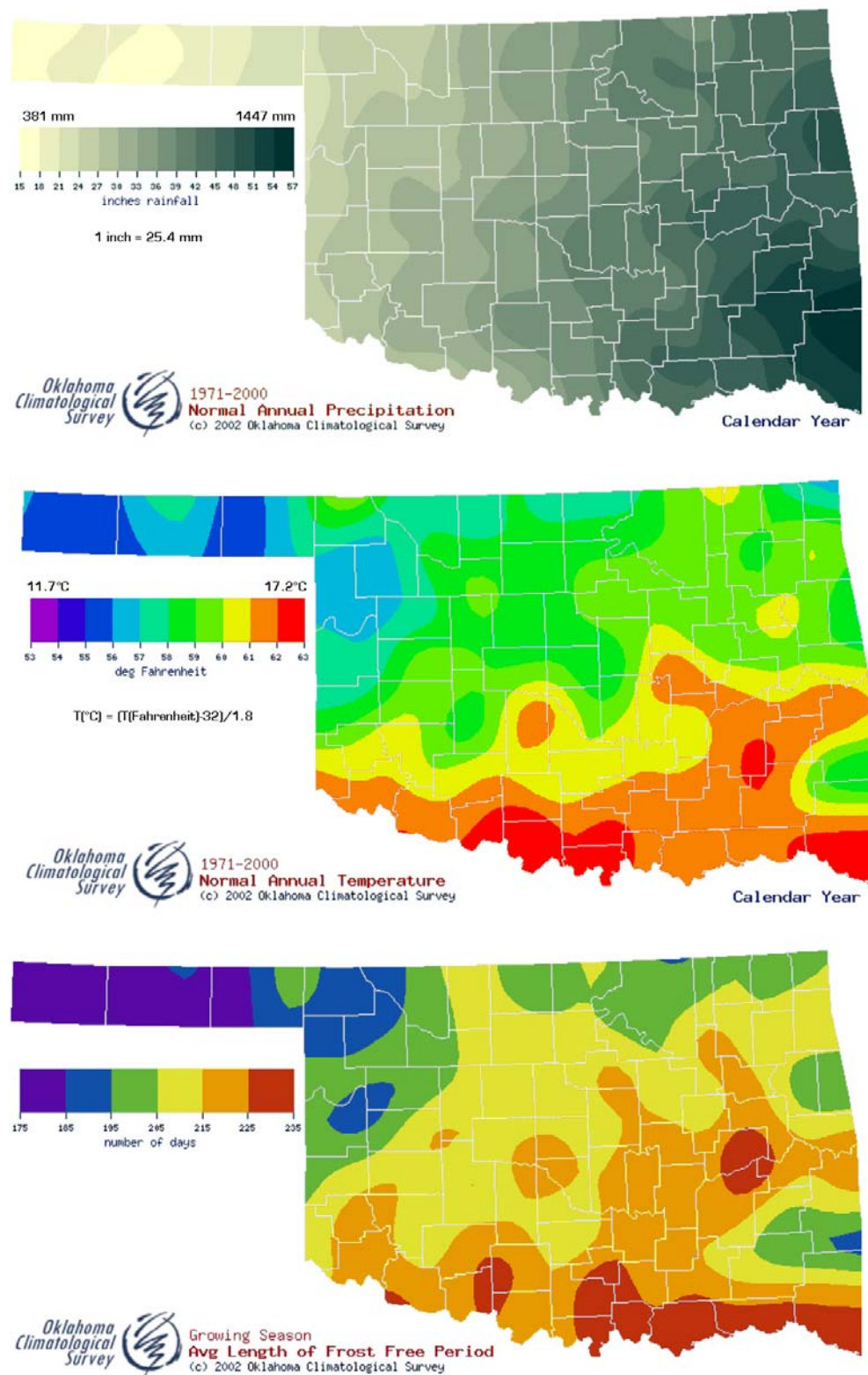


**Figure 13:** Normal annual precipitation, normal annual temperature and average length of frost free period for Oklahoma (Oklahoma Climatological Survey,  
[http://climate.mesonet.org/normals\\_extremes.html](http://climate.mesonet.org/normals_extremes.html))

The climate of Oklahoma is of continental type with a humid subtropical belt in the south. The Rocky Mountains west of the Great Plains block longitudinal movement of air masses. Therefore precipitation in the Great Plains depends mainly on the northward intrusion of moist air from the Gulf of Mexico. These air masses move usually in a northeastern direction. As a result, the western parts of the Great Plains receive less precipitation than the eastern parts (Birdsall & Florin 1992). Consequently, precipitation patterns of Oklahoma are characterized by a decrease from southeast to northwest (Figure 13). In the Ouachita Mountains mean annual precipitation is about 1,440 mm. The driest part of the state is the western part of the Panhandle with an annual mean precipitation of around 400 mm. Precipitation in Oklahoma is characterized by a great variability in rainfall from year to year with a mean annual variation of about 25% of the annual precipitation. Droughts are a recurring pattern of Oklahoma's climate caused by subnormal rainfall, which can last for several years. Since recordkeeping began in Oklahoma, five multi-year periods with subnormal rainfall have been reported for the late 1890s, from 1909-18, 1930-40, 1952-58 and, 1962-72 (Paterson 1994).

The length of the frost free period as well as the mean annual temperature increases from northwest to southeast (Figure 13). The mean annual temperature for Oklahoma is 15.5°C. Together with sudden rises and falls of temperature, Oklahoma experiences severe winds, thunderstorms, blizzards and tornadoes. The persistent winds typical for the Great Plains combined with high summer temperatures cause high evapotranspiration rates of 9 – 11 cm/month for the summer months (Birdsall & Florin 1992; Ropelewski & Yarosh 1998).

Soils are commonly deep and fertile and belong to the order of Mollisols (USDA Soil Taxonomy) or Kastanozems (FAO Soil Units). These soils are typical for semi-arid to semi-humid areas under grasslands. Like temperature and precipitation, also the distribution of suborders of Mollisols shows a general east-west trend. They range from Udolls in the wetter east to Ustolls in the drier west. The leaching of minerals in the soils decreases with decreasing mean annual precipitation towards the west. Under prairie, the soils of the Mollisol order are characterized by a layer of calcium carbonate, which hasn't been leached due to low rainfall rates. These soils show a high amount of organic matter and are well supplied with chemical bases. Consequently, they are very fertile, which makes them to the most productive soils within the United States (McKnight 1992; USDA United States Department of Agriculture 1999).

Reflecting the climatic and topographic conditions, Oklahoma is a transitional zone for vegetation. The eastern part of the state, namely the Ozarks Plateau and the Ouachita Mountains, is covered by deciduous forests, which become more open towards the west. Continuing to the west, this region is followed by vast grasslands – the prairie. The natural vegetation of the wetter eastern part of the prairie is long-grass prairie, followed by mixed-grass prairie in the central part of Oklahoma and short-grass prairie in the dry west. Following the non-Indian settlement of the Great Plains after the 1850's, much of Oklahoma's natural vegetation was lost due to overgrazing, burning, logging, erosion and cultivation. Due to drought conditions and extensive farming a series of dust storms known as the "Dust Bowl" lead to severe soil erosion in the 1930's and forced thousands of people to leave the Great Plains. Besides urban areas, Oklahoma's present land cover is characterized mainly by grazing land, non-irrigated and irrigated cropland (Figure 14). Main crops are wheat and alfalfa. Fruits and cotton are grown in the south. Due to soil depletion and droughts the importance of corn has declined (Woods et al. 2005).

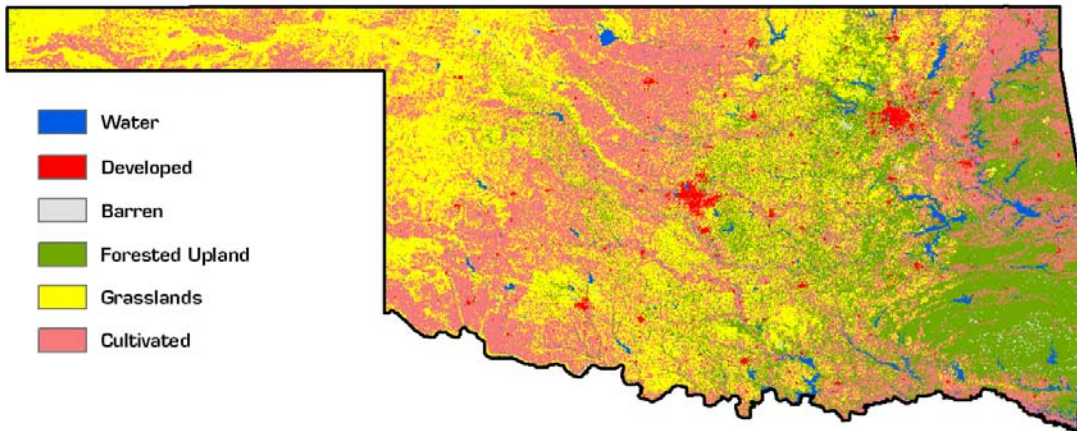


**Figure 14:** Oklahoma Land Cover according to generalized National Land Cover Data (NLCD) classes  
(North American Land Cover Characteristics – 1 Kilometer Resolution,  
<http://nationalatlas.gov/mld/landcvi.html>)

## 4.2. Remote Sensing Data

### 4.2.1. Envisat ASAR Global Mode

This study employs so called Global Monitoring (GM) Mode data acquired by the ASAR sensor onboard of the Envisat satellite. Envisat is the acronym for the European Environment Satellite, the largest earth observation satellite ever built by the European Space Agency (ESA). The Envisat satellite was launched with the Ariane 5 rocket on March 1<sup>st</sup> 2002 from the European spaceport in Kourou, French Guyana. It circles the Earth in a sun-synchronous, near-polar orbit with an inclination angle of 98.55° at an altitude of 795 km. Envisat performs 14 orbits per day and, like its predecessors ERS-1/2, has a nominal repeat rate of 35 days.

The ENVISAT satellite carries a number of different sensors: three spectrometers, two radiometers, two ranging instruments, a high-resolution interferometer and two radar sensors. An overview of ENVISAT with the major instruments is given in Figure 15.

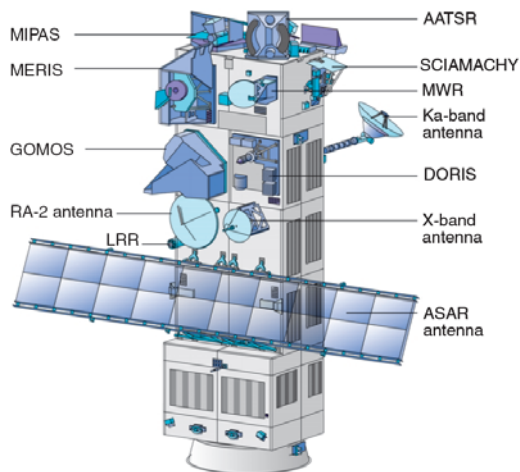


*Figure 15: Envisat with an overview of the major instruments (Attema et al. 2000)*

For developing the surface soil moisture retrieval algorithm, proposed in this dissertation, active remote sensing data acquired with the ASAR sensor have been used. The Advanced Synthetic Aperture Radar (ASAR) is a further development of the ERS-1/2 Active Microwave Instrument - Synthetic Aperture Radar (AMI-SAR). The ASAR sensor is an active radar instrument operated in C-band at a frequency of 5.331 GHz. Compared to the SAR sensor of the ERS-1/2 satellites, the ASAR instrument on

ENVISAT is characterized by a number of technological improvements. The ASAR sensor now offers five exclusive operation modes: Image Mode, Wave Mode, Wide Swath Mode, Global Monitoring Mode and Alternating Polarization. The different imaging modes of the ASAR sensor are characterized by different duty cycles. Due to limited power supply and on-board data storage capacity, the high resolution Imaging Mode can be operated only up to 30 minutes per orbit. Furthermore, exclusive modes can not be operated at the same time. Except from Global Monitoring Mode, the other ASAR sensor modes are operated only on user request. The Global Monitoring Mode has been designed as background mission. This is possible due to a reduced power consumption and data rate at the cost of spatial resolution.

Mode	Global Monitoring (GM)
<b>Polarization</b>	VV or HH
<b>Spatial Resolution</b>	1000 x 1000 m
<b>Temporal Resolution</b>	≤ 3 days (desc. & asc. orbits)
<b>Radiometric Resolution</b>	1.6 dB
<b>Swath Width</b>	≤ 400 km (5 sub-swaths)
<b>Incidence Angle Range</b>	15 – 45°
<b>Center Frequency</b>	5.331 GHz ( $\lambda = 5.67$ cm)
<b>Antenna Size</b>	10 m x 1.3 m
<b>Pulse repetition frequency</b>	1650 – 2100 Hz
<b>Chirp bandwidth</b>	≤ 16 MHz
<b>Power con-sumption</b>	713 W
<b>Duty cycle</b>	100%
<b>Data rate</b>	≤ 0.9 Mbit/s

*Table 2: ASAR sensor characteristics (Desnos et al. 2000)*

The ASAR sensor is capable of acquiring radar data in two different SAR sensing techniques. The radar instrument can be used as a conventional continuous strip-map SAR like the AMI-SAR of the preceding ERS missions or it can acquire radar data

utilizing the ScanSAR technique, which allows the imaging of much wider ground swaths. Therefore the passive antenna concept of the ERS SAR was replaced by an active phased array antenna with a dimension of  $1.3\text{ m} \times 10\text{ m}$  and 320 transmit/receive modules. Each module features two transmit chains (V and H polarization) and a common receive chain. The ASAR antenna allows active beam steering and the operation of the ASAR sensor using the ScanSAR technique. The technical specifications of the ASAR instrument operated in Global Mode can be found in Table 4 (ESA 1998b; Zink et al. 2001).

The ScanSAR technique is a SAR imaging technique, which allows acquiring data over swaths, which are much wider than swaths covered by conventional strip-map SAR sensors. Conventional strip-map SAR sensors like the ERS SAR or the ASAR sensor operated in Image Mode are imaging strips on the earth's surface with a potentially unlimited extent in azimuth direction. In the range direction, the achievable swath width is limited. The antenna of a strip-map mode SAR is characterized by a two-dimensional beam pattern defined by the antenna length and antenna width. The achievable swath width corresponds with the ground range extent covered by the elevation beam width of the SAR antenna. Besides the restrictions in swath width due to the antenna pattern, also restrictions due to sampling requirements to avoid ambiguities in the received signals, beam-forming requirements as well as data rate limitations are controlling the achievable swath width of a conventional SAR (Moore et al. 1981; Tomiyasu 1981; Currie & Brown 1991).

SAR sensors using the ScanSAR technique are based on rapid steering of the antenna beam and rely on the principle of sharing the radar operational time between two or more sub-swaths. The actual imaging process is divided into several blocks of pulses. Operating in continuous respectively conventional mode the SAR is imaging only one swath with a predefined width on the ground, while operating in ScanSAR mode, the sensor scans through adjacent subswaths. The SAR is illuminating one subswath for certain period of time, and then jumps to the next subswath until all subswaths are scanned (Figure 16). The cost of having a much wider swath is the degradation of the spatial resolution and radiometric accuracy. This is due to the fact, that the raw data for the subswaths per imaging period are covering only a fraction of that from conventional imaging. Furthermore, the wide range of incidence angles causes a wide variation in ground range resolution. Therefore the raw ScanSAR processor is

using a greater number of looks to produce images with a nearly constant ground range resolution (Luscombe 1988; Currie & Brown 1991; Raney 1998).

The main advantage of the two ScanSAR modes offered by the Envisat ASAR sensor is the improvement of the temporal resolution of the acquired SAR data (Figure 17). Earth observation satellites like the Landsat satellites, ERS-1/2 or Envisat are circling the earth in low earth polar orbits. One orbit is completed every 90 to 110 minutes. This results in approximately 14 orbits per day. Earth Observation satellites with swath widths in the order of 100 km cover a region at the Earth's surface only every 35 days. This is the case for Envisat Image Mode data. If one is interested in temporal highly variable geo-physical processes like soil moisture, this repeat rate is not satisfactory. Here, temporal resolution becomes more important than spatial resolution. The Envisat ScanSAR modes provide SAR data at medium temporal and spatial scales. The lower daily coverage of the Wide Swath mode compared to the Global Monitoring Mode is caused by electrical power and data storage limitations. When operated in Global Mode and combining ascending and descending orbits, acquisitions of a region at the Earth's surface are possible every 2 to 3 days. These SAR data have been acquired under varying incidence angles. This needs to be corrected before any further quantitative or qualitative analysis and comparisons between data sets.

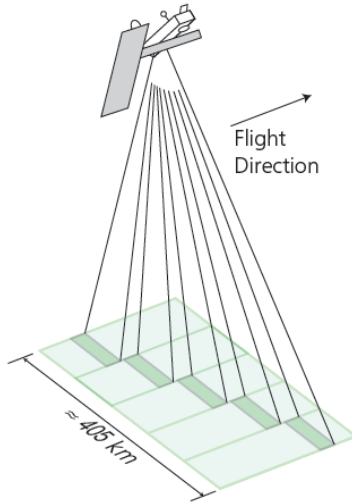


**Figure 16:** Illustration of the ScanSAR imaging principle. © ESA.

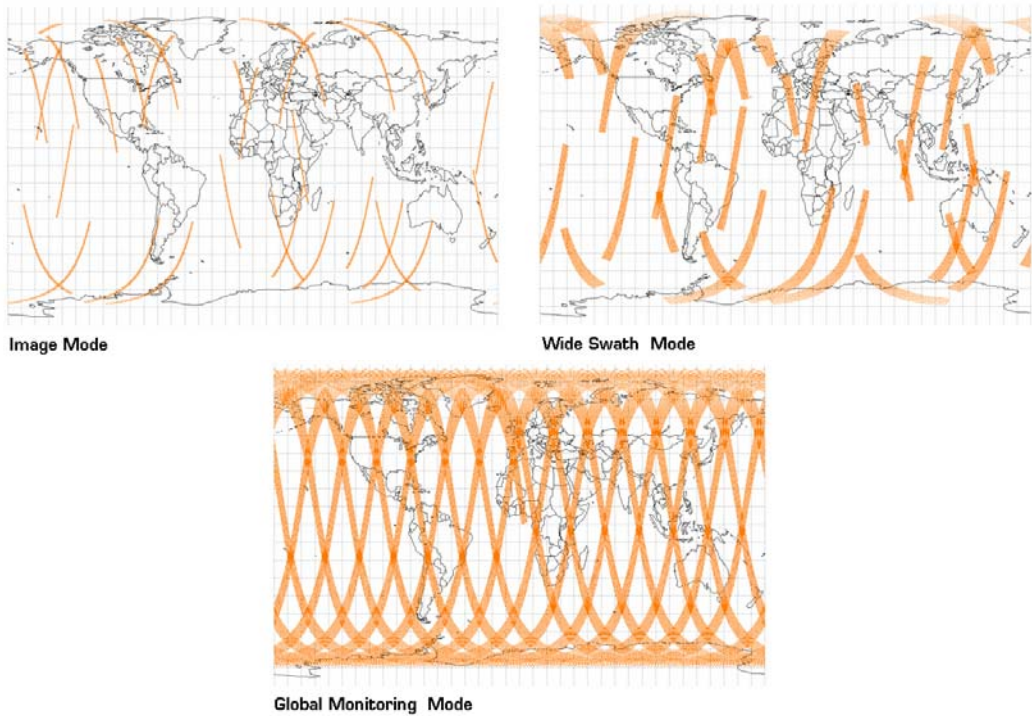


**Figure 17:** Potential daily global coverage offered by different ASAR acquisition modes

The development of the ASAR ScanSAR capabilities and the implementation of a ScanSAR processor are using experiences gathered with the first operational spaceborne ScanSAR system, which was part of the Radarsat-1 mission. Although the application potential could be demonstrated with this sensor, the ScanSAR data did not find a wide field of application. This was due to problems with the radiometric quality of the data. Due to the ScanSAR principle and inappropriate processing, some artifacts were present in the data. Martyn et al. (1999) and Srivastava (2001) are reporting so called “scalloping” effects, which refers to artifacts found in RADARSAT-1 imagery. These errors occur due to periodic amplitude variations along track, where they can appear and disappear. The extent in range may span the whole swath or just parts of it, while the periodicity of scalloping coincides with the period of bursts along track during operation in ScanSAR mode. According to Martyn et al. (1999) the cause for this problem is found in incorrect radiometric compensation for the antenna elevation pattern in azimuth direction. While processing ScanSAR data “natural” coordinates, slant range and Doppler, are used. The generated image amplitude will have the range and azimuth antenna patterns overlayed on it using these coordinates. Good compensation requires exact determination of the Doppler frequency of the centre of the antenna beam. To achieve a radiometric accuracy of 1 dB the Doppler frequency must

be known accurate to a 100 Hz. Because of the large spatial extend in swath width, the scalloping artifacts are visible, even when there are amplitude variations of only 0.1 dB. To overcome this problem completely, the Doppler frequency must be known with an accuracy of up to 25 Hz. Srivasata et al. (2001) are reporting a radiometric accuracy of ScanSAR images showing these scalloping effects of 1.5 dB from amplitude peak to amplitude peak in best case. Depending on the observed terrain features also worse radiometric accuracies can be expected. Furthermore, Martyn et al. (1999) are describing still visible boundaries between adjacent beams in the image data. The reason for this is similar to scalloping and is addressed in badly aligned antenna pattern compensation in range direction, caused by roll movements of the satellite. Roll angle errors of 0.1 degree can produce radiometric errors of 1 dB or even more.

ScanSAR processors for converting raw data to image data were developed mainly for radiometric imaging purposes. Officially, there are no complex Radarsat-1 ScanSAR image data available. But to use ScanSAR data for interferometry, amplitude as well as phase information are needed (Holzner & Bamler 2002). For this reason, a number of complex ScanSAR processing algorithms were proposed in the scientific literature. A good overview of different phase-preserving algorithms for processing ScanSAR data is given in Cumming et al. (1997). In the paper of Bamler & Eineder (1996) a possibility to apply the Range/Doppler (RD) algorithm, developed for traditional continuous mode data, to burst mode data is described, while Wong et al. (1997) are presenting an adapted processing algorithm based on that RD algorithm, to consider the special properties of complex ScanSAR data.

### **4.2.2. DORIS Orbit Information**

---

For geocoding, additional information on the sensor's orbit is required. They are provided in separate ASCII text files, downloadable free of charge from ESA FTP servers. DORIS is an acronym and stands for **Doppler Orbitography and Radiopositioning Integrated by Satellite**. The DORIS instrument is a microwave tracking system for precise orbit determination with an accuracy in the order of centimeters. Based on the Doppler frequency shift, the instrument measures the relative velocity between the Envisat satellite, circling the Earth in its orbit, and a dense network of beacons for precise orbit determination (Guizarro et al. 2000).

The orbit information, necessary for precise automated geocoding, is provided with the DORIS Precise Orbit State Vector files (DOR\_VOR\_AX). This is a level-2 product, updated once per day covering 26 hours of operational time of the Envisat ASAR sensor. Using this kind additional orbit information, the satellite orbit can be reconstructed with an radial accuracy of 0.1 m, an along-track accuracy of 0.3 m and an cross-track accuracy 0.3 m (ESA 1998; Minier 2005).

## 4.3. Validation Data

---

### 4.3.1. *In-situ* soil moisture

---

For validating the generated soil moisture products, *in-situ* soil moisture collected within the Oklahoma Mesonet (Figure 18) is used. The Oklahoma Mesonet is a state-wide meteorological measurement network operated by the Oklahoma Climatological Survey (OCS). It consists of 115 measurement stations, at least one in each county. Standard meteorological data (e.g. air temperature, precipitation, wind speed) are measured automatically every 5 minutes. During 1996 and 1997, 100 soil moisture measurement devices, which estimate the soil water potential, were installed. Soil moisture is estimated using heat dissipation matric water potential sensors for indirect estimation of *in-situ* soil moisture (Illston et al. 2004a). The sensor itself consists of a temperature sensor and a heating element, which are placed in the soil profile. To get an indirect estimate of the *in-situ* soil moisture content, the temperature of the heating element is measured before electric current is sent to the heating element, and after heating. The temperature difference allows conclusions on the moisture content of the surrounding soil via the soil water potential. For wet soils, the temperature difference is lower than for dry soils, because the heat is conducted more effectively away from the sensor. Sensors are installed at four depths (5, 25, 60, 75 cm) and are connected via different communication networks to a central base station, where data are stored, quality checked, processed and distributed (Brock et al. 1995; Basara & Crawford 2000).

To estimate the volumetric water content from the temperature differences, the soil texture at each measurement station must be known. Thus, for each measurement site soil samples were taken for laboratory analysis. Using a empirical relationship

introduced by Arya and Paris (1981), the volumetric water content is derived from the matric potential. For statewide comparisons, an alternative measure of soil moisture was introduced by Schneider et al. (2003), which is independent of soil texture. This measure is called fractional water index (FWI). It is a unitless measure and ranges from 0 to unity (Illston et al. 2004b).

For validating the remotely sensed soil moisture, daily averaged data files were compiled from 5-minute measurements. They contain *in-situ* soil measurements at the four depths and were provided by the OCS.

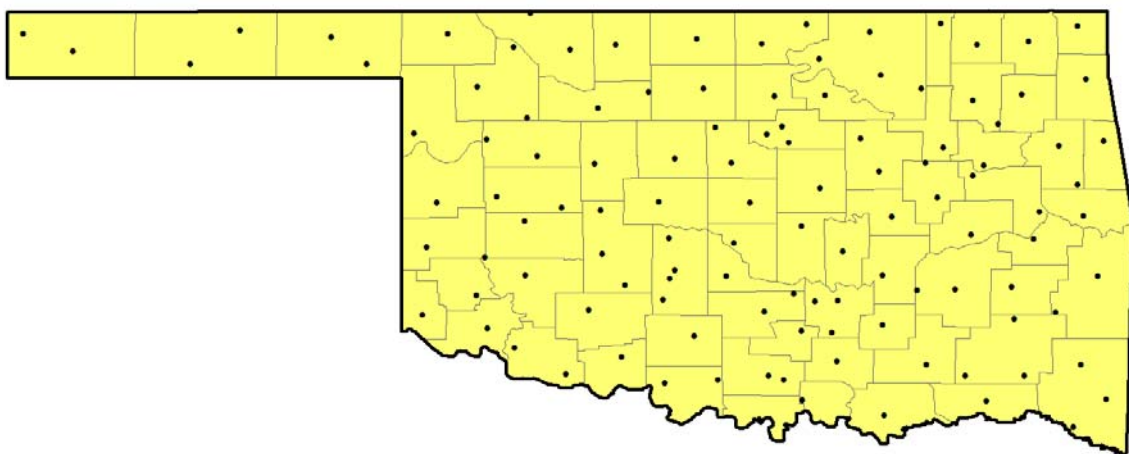


**Figure 18:** The Oklahoma Mesonet: Location of Measurement Stations in the Counties  
(<http://www.mesonet.org/sites/>)

#### 4.3.2. ERS Scatterometer Soil Moisture

---

A multi-year global soil moisture data set derived from ERS-1/2 scatterometer measurements is available. Like the ASAR sensor on Envisat, the scatterometer installed on the ERS-1 and 2 satellites is an active remote sensing device operating in C-band at VV polarization. ERS-1 was operational from 1999 to 2000; ERS-2 is in operation since 1995. Different from the ASAR sensor, the ERS scatterometer is a non-imaging radar device which gives backscatter measurements for a footprint of 25 km with high radiometric accuracy. The scatterometer consist of three antennas oriented 45° forward, perpendicular and 45° backwards relative to the satellite orbit. They obtain backscatter measurements simultaneously over a ground swath of 500 km. The scatterometer can achieve a global coverage every three to four days. Three independent

backscatter measurements at two different incidence and azimuth angles are acquired for each pixel with a spatial resolution of 50 km (KNMI EARS Team 2007). A detailed description of the soil moisture retrieval algorithm is given in Chapter 5.2.

For validating the surface soil moisture derived from the ASAR GM data, surface soil moisture values are used. These surface soil moisture values are relative soil moisture values ranging from 0% at permanent wilting level to 100% at field capacity. They are available globally from 1<sup>st</sup> August 1991 until 31<sup>st</sup> May 2007 with a data gap for the period from 1<sup>st</sup> January 2001 to 12<sup>th</sup> August 2003. This was caused by the loss of the last one of six gyroscopes, which stabilize the satellite in its orbit. Precise orbit estimation was not possible until adapted algorithms for raw data processing were implemented. Furthermore two on-board tape recorders failed. This limits the spatial coverage substantially as data can not be stored on-board when outside the proximity of a ground receiving station (Crapolicchio & Lecomte 2005). The irregular temporal resolution depends on the operation of the scatterometer, but usually acquisitions are available every 2 days. Over land areas surface soil moisture data are to a discrete global grid with a spatial resolution of 50 km and a spacing of 12.5 km (Figure 19). Along with the surface soil moisture values, different data quality flags are provided. A visualization of surface soil moisture over North America is shown in Figure 20.

The scatterometer derived surface soil moisture data are available free of charge for scientific purposes from the website <http://www.ipf.tuwien.ac.at/radar>.

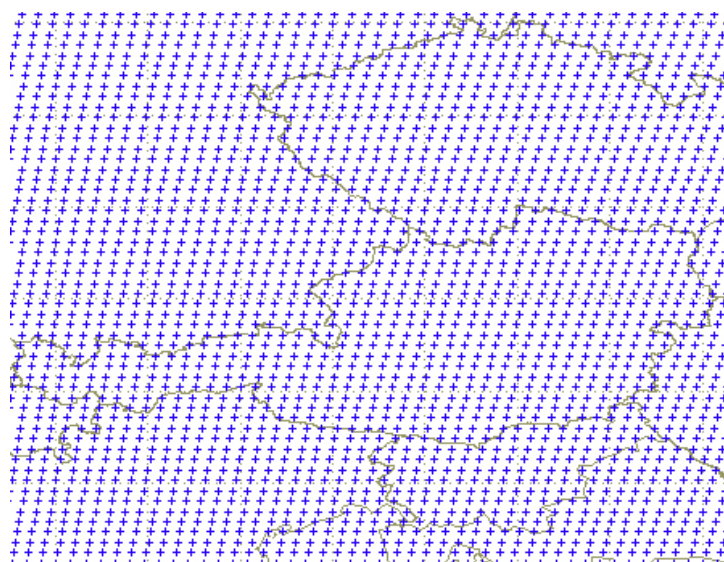


**Figure 19:** Example of DGG distribution over Austria

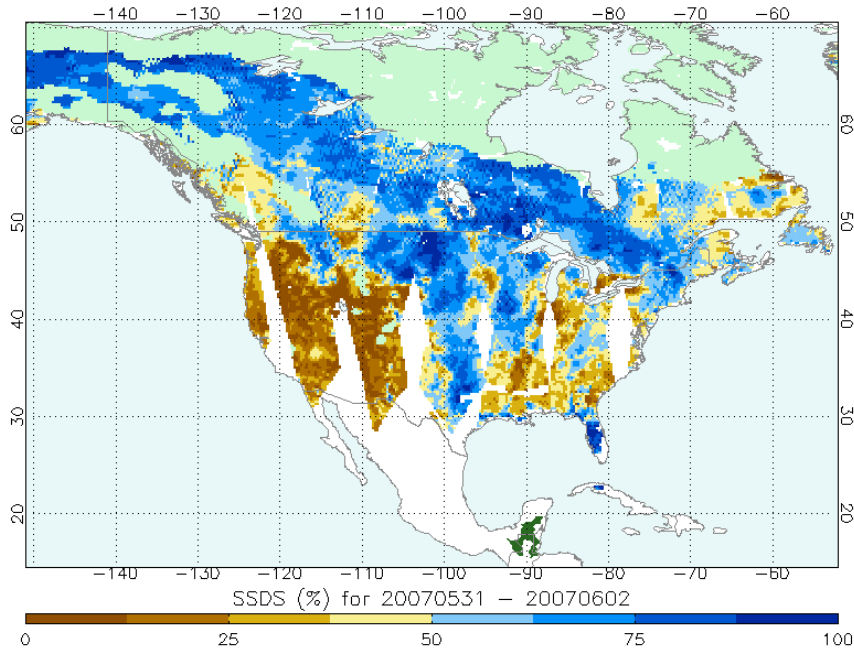


**Figure 20:** Three-day surface soil degree of saturation for North America (white – no data, light green – snow cover)

### 4.3.3. Meteorological Data

For the interpretation of the remote sensing observations and for validation of remotely sensed soil moisture, daily synoptic meteorological data from the DS512 data set have been used. The data were purchased from the Data Support Section of the Computational and Information Systems Laboratory at the National Center for Atmospheric Research. NCAR is supported by grants from the National Science Foundation (USA).

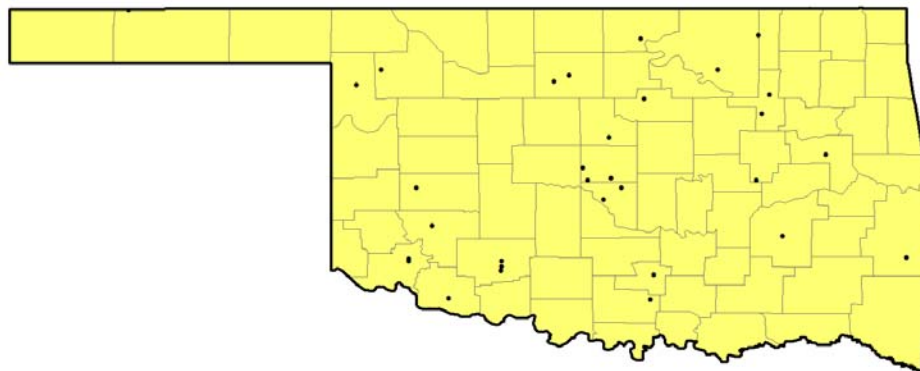


**Figure 21:** Meteorological Measurement Stations from the DS512 data set

The data set is based on a global network of meteorological stations with currently approx. 8900 active stations. Data of all reporting stations are collected, and after basic validation procedures they are summarized on a daily basis. The data sets are provided as ASCII data and comprise basic climate data measurements such as minimum and maximum air temperature, precipitation, solar radiation, humidity, wind speed and sea level pressure (Shea et al. 1994).

#### 4.3.4. Land Cover

For characterization of the land cover over Oklahoma, the United States Geological Survey Global Land Cover Characterization data (USGS GLCC) are used. These data are available for free as a geocoded raster data set from <http://edcsns17.cr.usgs.gov/glcc/>.

The USGS GLCC was derived from optical data acquired with the 1 km resolution NOAA Advanced Very High Resolution Radiometer (AVHRR) in 1992 and 1993 on a global scale. The land cover has been classified into 24 global land cover classes. Based on Anderson et al. (1976), the detailed classification scheme of the USGS GLCC data were reclassified to a smaller number of basic classes (Table 3).

USGS Code	GLCC Description	Re-classified	Description
100	Urban and Built-Up Land	1	Settlement
211	Dryland Cropland and Pasture	2	
212	Irrigated Cropland and Pasture	2	
213	Mixed Dryland/Irrigated Cropland and Pasture	2	Agriculture
280	Cropland/Grassland Mosaic	2	
290	Cropland/Woodland Mosaic	2	
311	Grassland	3	
321	Shrubland	3	
330	Mixed Shrubland/Grassland	3	Gassland
332	Savanna	3	
411	Deciduous Broadleaf Forest	4	
412	Deciduous Needleleaf Forest	4	
421	Evergreen Broadleaf Forest	4	Forest
422	Evergreen Needleleaf Forest	4	
430	Mixed Forest	4	
500	Water Bodies	5	Water bodies
770	Barren or Sparsely Vegetated	6	Barren

*Table 3: Reclassification of USGS GLCC data*

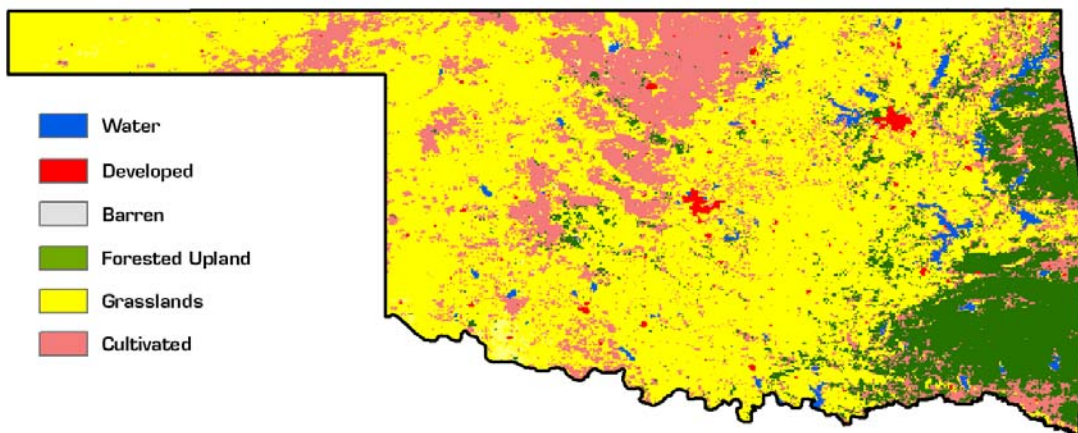


**Figure 22:** Reclassified USGS GLCC land cover of Oklahoma

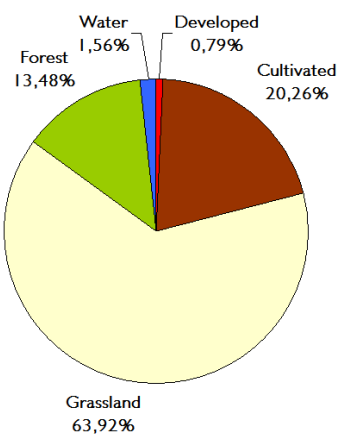


**Figure 23:** Percentages of main land cover classes

# Chapter 5

## Method

With this dissertation an algorithm for surface soil moisture retrieval from multi-temporal ASAR GM data is proposed (section 5.2). This approach is based on an adaptation of a change detection model proposed by Wagner et al. (1999a; 1999b; 1999c) for a global multi-year ERS-1/2 scatterometer data set. The application of the proposed surface soil moisture retrieval algorithm requires a number of pre-processing steps comprising geocoding, radiometric correction, resampling, local incidence angle normalization, and derivation of dry and wet references. An overview of the pre-processing steps is given in Figure 24.

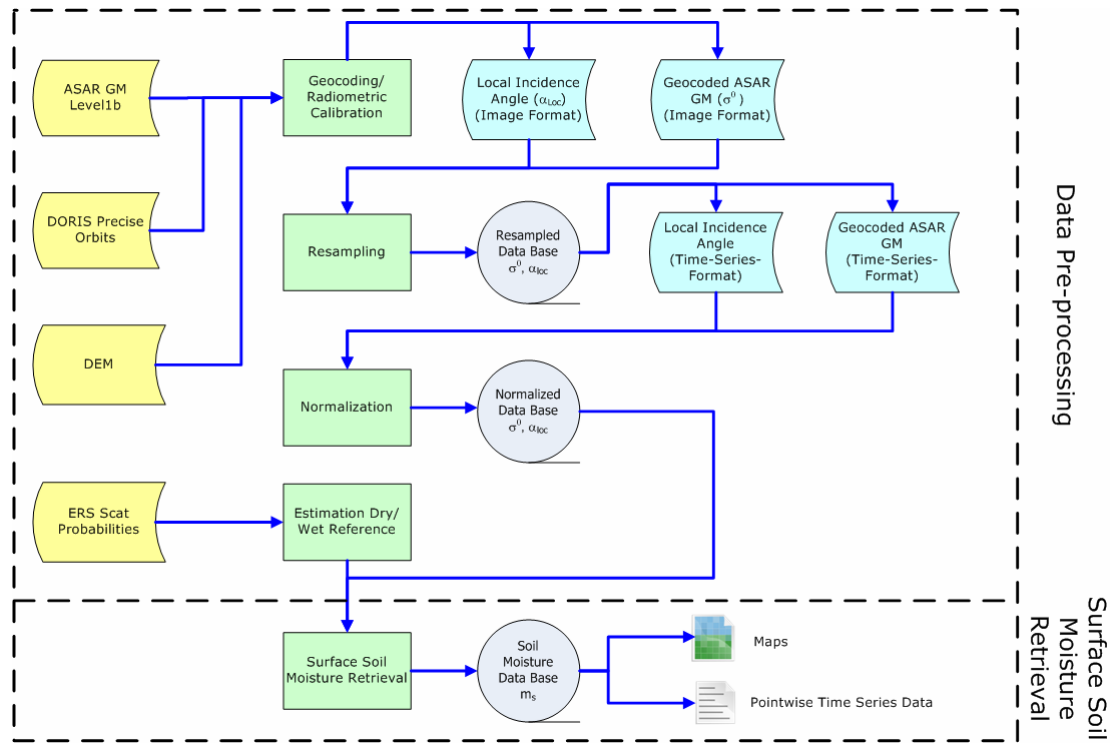


**Figure 24:** Processing chain for data pre-processing and surface soil moisture retrieval

Geocoding runs fully automatic without any user interaction. Two files are generated: the geocoded ASAR GM image and a map showing the local incidence angles for each pixel of the geocoded ASAR GM image. After geocoding, a radiometric

correction is performed to account for the effective scattering area, antenna gain and the range spreading loss. For geocoding and radiometric correction the commercial software package SARscape® developed by the Swiss company SARmap® is used. In the next step, data are transferred from an image format into a time-series-format, stored in a data base with equally spaced grid cells. Each grid cell contains a discrete number of points for which information on acquisition date and time, radar backscattering coefficient and local incidence angle are stored in binary files. ASAR GM backscatter not only depends on dielectrical and geometric properties of the image terrain but also on the influence of the local incidence angle. Therefore a correction of the local incidence angle effect on radar backscatter is mandatory before any further analysis of the data. In the last data pre-processing step, the dry and wet references for each grid point in the data base are estimated. Due to the limited temporal coverage of the ASAR GM data, the reference values for the change detection approach are derived from ERS-1/2 scatterometer time series data. Finally, the surface soil moisture is derived by scaling individual backscatter values between the dry and wet reference for each data base grid point. These steps will be described in detail in the following sections.

---

## 5.1. Data Pre-Processing

---

The proposed surface soil moisture retrieval algorithm exploits a comprehensive archive of ASAR GM data. Before further analysis, the remote sensing data require geocoding, geometric correction and transfer of the data from an image format into a time-series-format.

---

### 5.1.1. Geocoding

---

The geometry of radar images is completely different from that of satellite images acquired by sensors operating in the optical domain of the electromagnetic spectrum. Basically, a SAR measures distances calculated from the signal travel time between the Earth's surface and the sensor. Due to the side looking geometry of SAR sensors, specific geometric distortions like foreshortening, layover or radar shadow areas can be found in SAR images, especially when acquired over mountainous terrain. The radar antenna of space-borne SAR systems is oriented parallel to the flight direction and

sends out radar waves perpendicular to the flight path. In the case of ENVISAT, it is right-looking when flying from the South Pole to the North Pole (ascending pass) and is left-looking when flying from the North Pole to the South Pole (descending pass). The displacement of imaged objects is a function of the height difference between neighboring objects. In case of the ENVISAT and ERS SAR systems, these distortions can be significant, causing shifts of several pixels (Lichtenegger 1996; Lewis et al. 1998).

The proposed surface soil moisture retrieval approach is based on a large number of SAR images. One point at the Earth's surface may be imaged between 50 and 150 times. Therefore an automatic geocoding procedure is required, which is able to work without manually selected tie points and to produce highly accurate images ideally at sub-pixel level.

The Range Doppler approach is a common method for geocoding of SAR imagery. For each ASAR GM image pixel, the range distance estimated from the signal travel time and the Doppler frequency are known. Based on these two parameters, the absolute position of the image pixel in a certain cartographic system can be estimated. The azimuth can be determined by the Doppler shift history in frequency caused by the sensor's forward motion in its orbit and the Earth's rotation. If precise sensor position parameters are available (DORIS orbit files) the location of each image pixel on the ground can be estimated even without knowledge of tie points. The accuracy of this location procedure depends on the accuracy of the sensor position and velocity vectors, the measurement accuracy of the pulse delay time, and knowledge of the target height relative to the assumed Earth model. In case of ERS the accuracy was in the range of about 5 pixels if an accurate DEM was available (Roth et al. 1993). It could be improved to sub pixel accuracy with the availability of only one additional tie point. The approach is also called backward geocoding, as it proceeds backwards from image coordinates to radar or more precisely slant-range geometry, even though the aim of this process is the transformation from SAR geometry to a defined map geometry (Olmstedt 1993).

Given are the platforms position vector  $\vec{S}$  with  $S=\{S_x, S_y, S_z\}$ , also called the state vector, and its velocity vector  $\vec{v}_s$ , together with a point on the ground  $\vec{P}$  with  $P=\{P_x, P_y, P_z\}$  (Figure 25). Due to the Earth's rotation, also this point on the ground has

an velocity vector  $\vec{v}_p$ . If no DEM is used,  $P_z$  will refer to the surface of a predefined ellipsoid and the resulting images are ellipsoid corrected. If a DEM is used,  $P_z$  refers to the DEM's height information and the geocoding result will be a terrain corrected image, in which also the geometrical distortions caused by the relief are corrected. For exact restoration of the Doppler frequency shift of each image pixel, the coordinates of the vectors  $\vec{S}$  and  $\vec{P}$  are given in a geocentric Cartesian coordinate system with its origin at the gravitational centre of the Earth (Figure 25). Precise orbit information provided in the DORIS orbit files (see Chapter 4.2.2.) are used for exact reconstruction of the sensors flight path. Furthermore, the Doppler centroid  $fDC$ , a parameter describing the Doppler shift when the center of the radar beam crosses the target, is required to determine the azimuth position. This parameter has been calculated for each image pixel during ASAR GM raw data processing at the ESA Processing and Archiving Facilities (PAC's) and is attached to each ASAR GM image scene in the line headers (Meier et al. 1993).

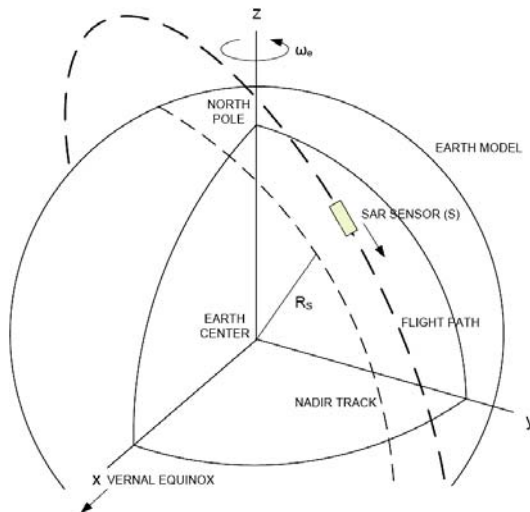


**Figure 25:** Earth centred reference coordinate system (Liu et al. 2006)

The geocoding of an ASAR GM scene based on the Range-Doppler approach is an iterative process. For each image pixel, the slant range  $RS$  using Eq. 5.1 and the Doppler frequency shift  $fD$  using Eq. 5.2 are calculated:

$$R_s = \sqrt{(\vec{S} - \vec{P}) \cdot (\vec{S} - \vec{P})} \quad (\text{Eq. 5.1})$$

$$f_D = \frac{2f_0}{c} \frac{(\vec{v}_p - \vec{v}_s) \vec{R}_S}{|\vec{R}_S|} \quad (\text{Eq. 5.2})$$

where:

$\vec{P}$	=	backscatter element position with $P=\{P_x, P_y, P_z\}$
$\vec{v}_p$	=	point velocity
$\vec{S}$	=	antenna position with $S=\{S_x, S_y, S_z\}$
$\vec{v}_s$	=	platform velocity
$R_S$	=	slant range position
$\lambda$	=	wavelength
$f_D$	=	Doppler frequency
$f_0$	=	Carrier frequency

The estimated frequency shift  $fD$  for the current image pixel is compared to the Doppler centroid  $fDC$ . If  $fD > fDC$ , the estimated sensor position related to the flight direction of the sensor is situated behind the correct position. In this case, the value of  $P_x$  is increased by one and the calculation procedure is performed in a loop until the condition  $fD = fDC$  is fulfilled. The initial value for the  $P_x$  component is given by the estimated orbit range position of the previous pixel. As an anchor point, the corner coordinates of the ASAR GM image scenes, specified in the ASAR GM image file header, are used (Meier et al. 1993; Holecz et al. 1995).

If the azimuth and range positions for each input image pixel are known, the geometrically corrected image matrix can be generated by applying an appropriate transfer function to transform from Cartesian coordinates in the desired output map projection. Finally, the assignment of the new pixel values is done by a common two-dimensional resampling method like nearest neighbor, bilinear or cubic convolution.

The Range Doppler approach was implemented using the libraries of the commercial GAMNMA© software package. To run a fully automatic geocoding, a script using the programming language IDL was written. Other software tools developed at I.P.F., TU Wien, collect all necessary input data, submit them to the libraries of the commercial geocoding software packages and generate ENVI header files for the geocoded ScanSAR image scenes. To achieve the required sub-pixel

accuracy initial testing showed that DORIS Precise Orbit State Vectors are needed in the geocoding process.

The quality of the geocoding was assessed by manually recording the geographical locations of features, which could be easily identified due to their distinct backscatter patterns in a large number of images. As an example, two features are presented. The first feature is an industrial facility site in Saudi Arabia, surrounded by desert. It is located at  $24^{\circ}42'2''\text{N}$   $44^{\circ}58'26''\text{E}$  and has an extent of approximately 1 km times 0.5 km. This feature shows persistently higher backscatter than its surroundings in many images, as exemplified in the left part of Figure 26. The second feature is the branching of the river Kwa in the Democratic Republic of the Congo, located at  $3^{\circ}3'0''\text{S}$   $16^{\circ}51'29''\text{E}$  (see right part of Figure 26). The river shows persistently lower backscatter than its surroundings. The geographical coordinates for feature 1 and 2 were manually recorded in, respectively, 28 and 21 images.

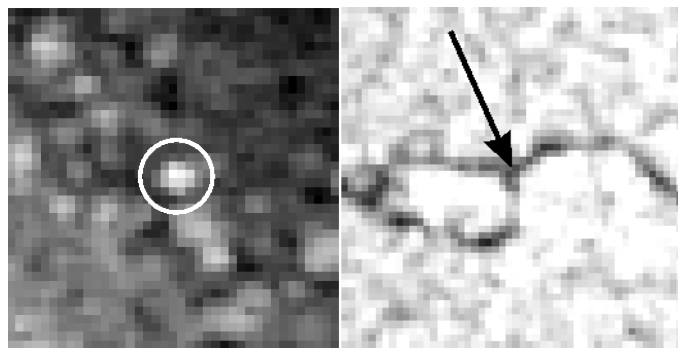


**Figure 26:** Example of image features used for assessing the geolocation accuracy. Left: detail of radar image with feature 1 (an industrial facility site in Saudi Arabia) encircled. Right: feature 2; branching of the river Kwa in Democratic Republic of the Congo.

	Mean relative error ( $^{\circ}$ )		Mean absolute error ( $^{\circ}$ )	
	Latitude	Longitude	Latitude	Longitude
Feature 1	39 m	239 m	258 m	269 m
Feature 2	120 m	342 m	127 m	486 m

**Table 4:** Geolocation accuracy for exemplary features.

Table 4 shows the result of the analysis for the two exemplary features. The mean relative error was calculated as the average deviation from the mean of the recorded coordinates in different images showing the example features. The mean absolute error correspond to the average deviation of the recorded coordinates in the geocoded images

from the geographical location of the features read from a map. The spatial resolution of the GM data is 1 km, the spatial sampling 500 m. Both the relative error among the images as well as the deviation from the true geographical coordinates of the features was calculated. Considering that the precision in the manual recording of the coordinates of the features were in the order of the pixel size, it was concluded that the accuracy of the geocoding is sub-pixel and that processing therefore can be performed on a pixel basis.

### 5.1.2. Radiometric Calibration

---

Change detection for surface soil moisture monitoring requires a good relative radiometric calibration of SAR images from both ascending and descending passes. Change detection requires that radiometric distortions in SAR images due to the topography are corrected to the best possible extent for achieving a good relative calibration. An exact absolute calibration would be of course desirable, but is not a pre-requisite for the proposed ASAR products.

A proper radiometric calibration of SAR images has to involve corrections for:

- scattering area: each output pixel is normalized for the actual illuminated area of each resolution cell, which may be different due to varying topography.
- antenna gain pattern: the effects of the variation of the antenna gain in range are corrected, taking into account the topography or a reference height.
- range spread loss: the received power must be corrected for the range distance changes from near to far range.

After the radiometric calibration there are still radiometric variations in  $\sigma^0$  caused by the local topography. Similar to geometric distortions, terrain induces radiometric distortion (Ulander 1996). Accurate SAR data calibration in areas with terrain variations can only be accomplished considering precise digital elevation models, precise position and altitude data of the sensor and the appropriate SAR geometry. It must however be noted that there are natural limitations in correcting SAR images radiometrically, depending on the orientation of the local terrain and the sensor look angle. If the slope angle is equal or higher than the incidence angle then layover is observed and the data is ambiguous and irrecoverable. Only if the slope angle of the terrain is well below the

incidence angle the real geometry and radiometry can be reconstructed (Holecz et al. 1993; Small et al. 1998).

Before images can be corrected radiometrically the backscatter signal has to be derived from the image digital number (DN), which is stored as 8 bit digital number, representing scaled amplitude of the backscattered signal. If the processor is correctly adjusted the radiometric calibration factor  $k$ , which is attached to each individual ASAR GM scene in the file header, gives a functional dependence between each pixel's DN value and the real backscatter according to (Rosich & Meadows 2004):

$$\sigma = k \cdot DN^2 \quad (\text{Eq. 5.3})$$

The basis formula for the radiometric calibration is the radar equation (Eq. 3.12). Important for a proper calibration is to determine the antenna elevation angle, the antenna azimuth angle, the local incidence angle in range and local incidence angle in azimuth. The first two allow correcting for the antenna gain, using the corresponding antenna diagrams, while the following two allow calculating the scattering area  $A$ . To determine above parameters one has to know the real antenna position, the real antenna pointing direction and the pixel position on the ground. In the space borne case, due to the stability of the satellite, ideal (processed) and real (actual) antenna position are the same, while actual antenna pointing is defined by the radar look angle (the antenna azimuth angle usually set to zero) and antenna depression angle. Concerning the derivation of the scattering area  $A$ , different methods can be used when an external DEM is available. Conventional SAR calibration methods have typically compensated for this local variation in “illumination area” by estimating the local area using the local incidence angle. Since such an estimate neglects the influence of azimuth variations, more complete models also include an azimuth term (Holecz et al. 1998). The most sophisticated models make use of the facets technique to account for heteromorphism in the illuminated terrain (Small et al. 1998).

The Envisat ASAR data acquired in Global Monitoring Mode were given least priority by ESA during calibration and validation activities. Therefore the in-flight performance of these data was unclear. Especially the radiometric properties as published before the launch of the sensor have not been update for a long time. Therefore a procedure was developed estimate the noise level in the data. This information is important for validating the retrieved surface soil moisture products and

accessing the possible errors sources of the change detection soil moisture retrieval algorithm.

Due to the high variability of C-band backscatter measurements over land there is no straight forward way for assessing the quality of the applied radiometric correction method on a spatially complete basis. However, the radiometric calibration of the sensor may be checked point wise for selected target classes characterized by very stable backscatter conditions and known backscatter characteristics. At C-band tropical rain forests with closed crown cover are known to be relatively stable targets. They represent volume scatterers characterized by high backscatter and low temporal variation. Therefore, tropical forests have been used as natural calibration sites for scatterometer and SAR measurements (Lecomte & Wagner 1998). The natural variations of the backscatter measurements is about 1 – 2 dB and may be the results of free water droplets in the vegetation canopy and other environmental effects. For volume scatterer the backscattering coefficient  $\sigma^0$  is expected to exhibit the following incidence angle dependency:

$$\sigma_{\text{linear}}^0 = \gamma \cos \theta \quad (\text{Eq. 5.4})$$

where  $\gamma$  is an alternative backscattering coefficient and  $\theta$  is the incidence angle. A comparison of Eq. 5.4 with actual GM measurements over two tropical forest sites is shown in Figure 27. As expected, one can observe that there is only little variation in radar backscatter over the incidence angle range of the ASAR GM data for the selected rain forest sites.

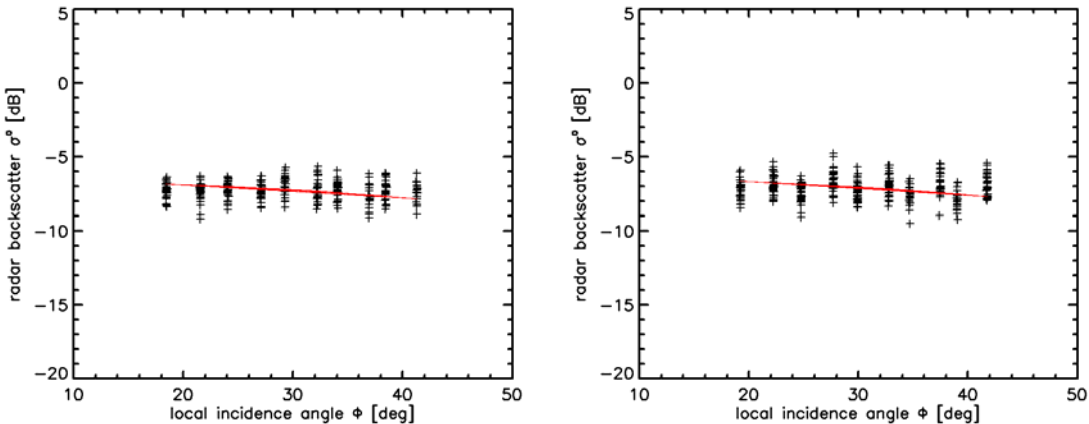


**Figure 27:** ASAR Global Monitoring mode backscatter observed over two tropical forest sites: 20.925°E, -2.525°S (left), 20.69°E, -3.79°S (right).

According to specifications the radiometric resolution of GM mode is equal or less than 1.6 dB (see Chapter 4.2.1.). To check if this specification is met in terms of the radiometric stability of the signal, the statistical properties of tropical forest backscatter were investigated using a simple noise model which considers actual backscatter measurement to be the result of natural variations and noise, including speckle and instrument noise. For retrieving geophysical parameters from the GM backscatter data, only the natural variation is of interest. The statistical noise model describes the measurements taken at one particular location as the result of the convolution of the natural backscatter variations (i.e. the "signal") and the noise:

$$PDF_{Measurement} = PDF_{Signal} \otimes PDF_{Noise} \quad (\text{Eq. 5.5})$$

where  $\otimes$  is the convolution operator,  $PDF_{Measurement}$  is the probability distribution function of the backscatter measurements made by ASAR GM mode, and  $PDF_{Signal}$  and  $PDF_{Noise}$  the probability distribution functions of the natural backscatter variation and the noise respectively. Assuming that the signal and the noise can be described by Gaussian distribution functions, also the resulting PDF of the measurements is a Gaussian with a standard deviation  $s_{Measurement}$  of

$$s_{Measurement}^2 = s_{Signal}^2 + s_{Noise}^2 \quad (\text{Eq. 5.6})$$

where  $s_{Signal}$  and  $s_{Noise}$  are the standard deviations of the signal and noise respectively. Using equation (8) the noise of GM measurements can be estimated when  $s_{Signal}$  is known.

To characterize the natural backscatter variation of tropical forest, spatial averages of radar backscatter time series measurements are calculated. The dependency of the radar backscatter on the local incidence angle has been removed during the local incidence angle normalization. The spatial averages for each backscatter acquisition date  $t$  for a test region covering an area of  $0.5^\circ \times 0.5^\circ$  are estimated using the formula:

$$\sigma_{reg}^0(30)(t) = \frac{1}{N} \sum_i^N \sigma_i^0(30)(t) \quad (\text{Eq. 5.7})$$

where  $\sigma_i^0(30)(t)$  is the local backscatter for a reference angle of  $30^\circ$ . The test region was chosen over the African tropical rain forest Figure 28. About 14.400 single measurements were used for each regional mean. By applying the spatial filtering, the noise inherent in the backscatter measurements is assumed to be averaged out. Therefore, only the natural variation of the backscatter remains in the regional

backscatter means. Thus, the natural variation was quantified using the standard deviation  $s_{Signal}$  of the regional mean time series. Then the noise was estimated from:

$$s_{Noise} = \sqrt{s_{Measurement}^2 - s_{Signal}^2} \quad (\text{Eq. 5.8})$$

where  $s_{Measurement}$  is the standard deviation for a single local backscatter time series.  $s_{Signal}$  was calculated for each local backscatter time series for all 14.400 location in the test region. The characteristic standard deviation of the noise,  $\langle s_{Signal} \rangle$ , was finally estimated from the mean of the 14.400 local standard deviations.

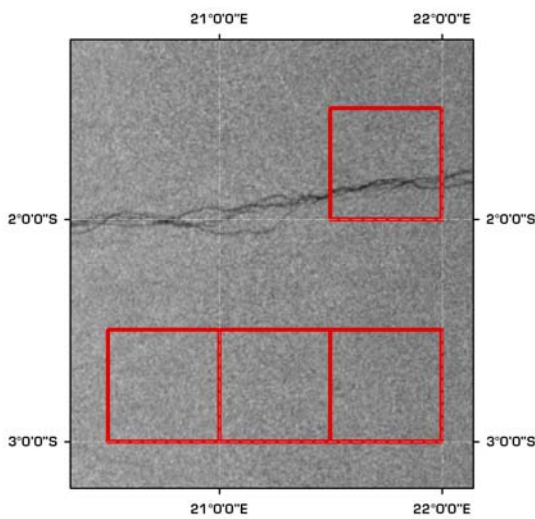


**Figure 28:** Tropical forest areas used for determining the noise and natural signal fluctuations of ASAR GM backscatter measurements.

### 5.1.3. Resampling of ASAR GM Data

Envisat ASAR GM data are acquired orbit-wise. Users are provided with single files, each containing one image acquisition. An image forms a two dimensional array of data. The smallest entity of an image acquisition is one individual picture element, also called pixel. Each pixel can be identified via its row and column number. During geocoding, a geographic coordinate (latitude/ longitude) was assigned to each pixel. Even though the sensor will pass over one location at fixed temporal intervals defined by the satellite repeat cycle, the geographic coordinates of image pixels of subsequent acquisitions over the same region will not perfectly coincide. Repeated observations of the Earth results in a large number of individual scenes each saved in a single image file. The analysis and product generation within the proposed change detection

approach is not performed on an image-by-image basis but on a time-series-basis for fixed geographic locations. Therefore it is necessary to define a fixed global grid and to resample the geocoded image data. After the resampling of the image data, a set of backscatter measurements is stored in a single file in a database for each grid point location. This also reduces read access to the hard disks, as only one file needs to be opened when querying backscatter measurements for one geographic location instead of opening a large number of images, calculating the nearest image pixel for a given grid location and retrieving the backscatter information.

For resampling the ASAR GM data a simple discrete global grid (DGG) based on the geographic coordinate system is used. The edges of the cells are defined by arcs of equal-angle increments of longitude and latitude (Sahr et al. 2003). Following the inherent resolution of the ASAR GM data, a sampling interval of 15 arcseconds, corresponding to a distance of about 500 m at the equator, was selected for the individual grid cell points. The chosen datum is WGS-84 and the origin was set to -180W/-90S. The grid was divided into blocks of  $0.5^\circ$  by  $0.5^\circ$  grid cells, resulting in 259.200 grid cells in 720 columns and 360 rows globally. Together with the backscatter measurements also the local incidence angle maps, which were generated as a by product during geocoding, are resampled to the regular grid too.

Each backscatter and local incidence angle image is resampled according to the defined regular grid. For each grid point, the closest image pixel is determined using the nearest neighbour resampling method. Due to the irregular sampling of the ASAR GM scenes, it is very unlikely that exactly one image pixel corresponds to one regular grid point location. Therefore the backscatter and local incidence angle values of the regular grid are retrieved from the irregular image grids using bilinear interpolation. After resampling, each individual grid cell point is represented as a binary data file in the data base. For each measurement a data triplet consisting of acquisition date/time, radar backscatter and local incidence angle is stored in the binary file. As new image scenes are processed, these binary data base files can be extended easily.

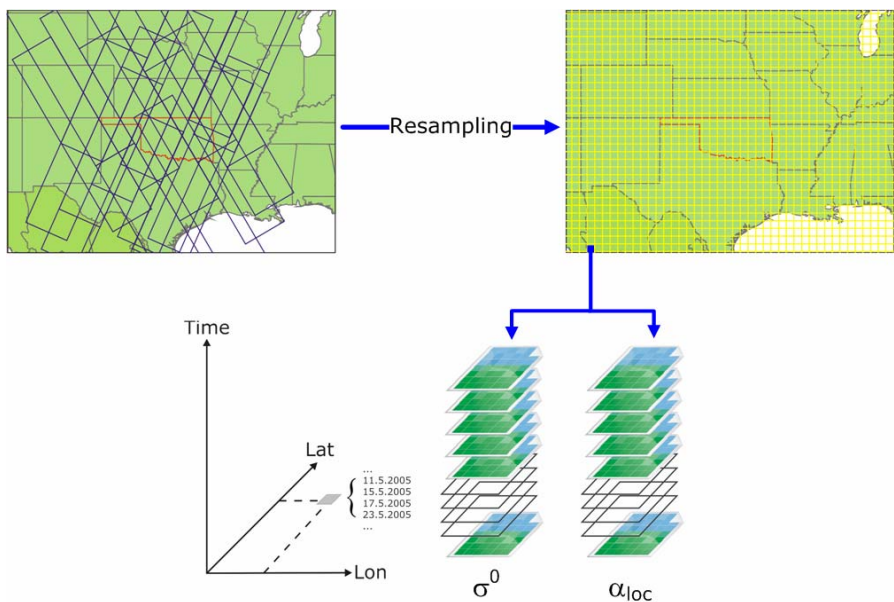


**Figure 29:** Illustration of the resampling procedure

#### 5.1.4. Local incidence normalization

Radar backscatter generally shows a strong dependency on the local incidence angle. This effect is more pronounced in SAR imagery covering large incidence angle ranges like airborne SAR or space-borne ScanSAR like ASAR GM data (Beaudoin et al. 1995; Lillesand & Kiefer 2000). For ASAR GM data obtained under different incidence angles, local incidence angle normalization is mandatory to allow qualitative and quantitative analysis as well as comparisons of backscatter characteristics between different acquisitions covering the same area or different range positions within one acquisition. Radar data acquired using the ScanSAR modes of the ENVISAT ASAR sensor are covering a much wider swath than conventional strip map mode SAR images like ERS-1/2 or ENVISAT ASAR Image Mode. ASAR GM data are acquired over an incidence angle range from 20° to 40°. This causes a typical, consistent decrease in image brightness from low local incidence angles in near range to high local incidence angles in far range (Figure 30). This decrease also depends on land cover. Different land cover classes show different degrees of angular dependency. Figure 31 shows the angular dependency of radar backscatter from local incidence angle for grassland area in Oklahoma. In Figure 32 the connection between radar backscatter and local incidence angle for coniferous forest is shown. For the grassland example, the dependency of radar backscatter on local incidence angle causes a decrease of up to 10 dB. For the

coniferous forest example, the influence of the local incidence angle causes a variation of 5 dB over the whole incidence angle range.

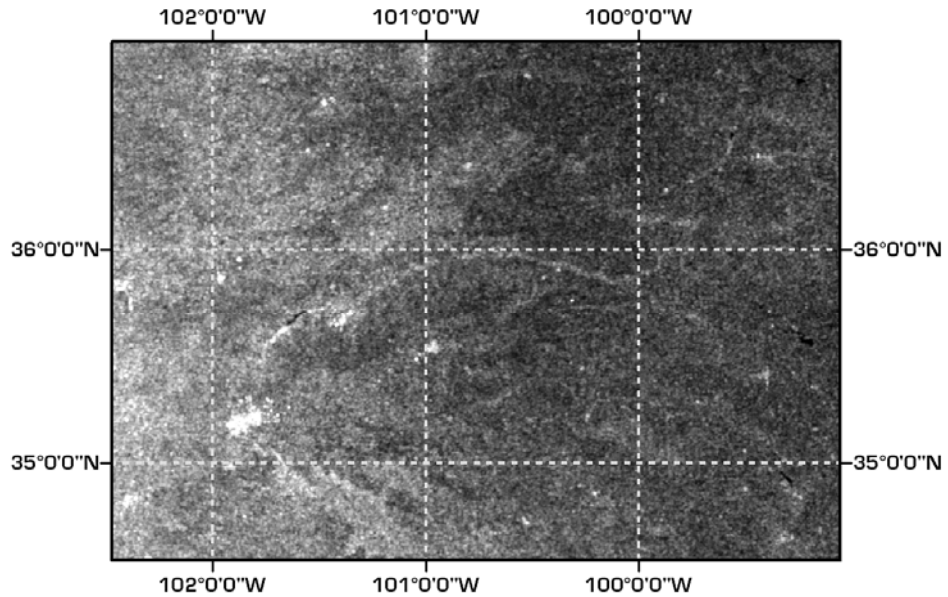


**Figure 30:** Change in image brightness due to angular dependency of Envisat ASAR GM data before normalization

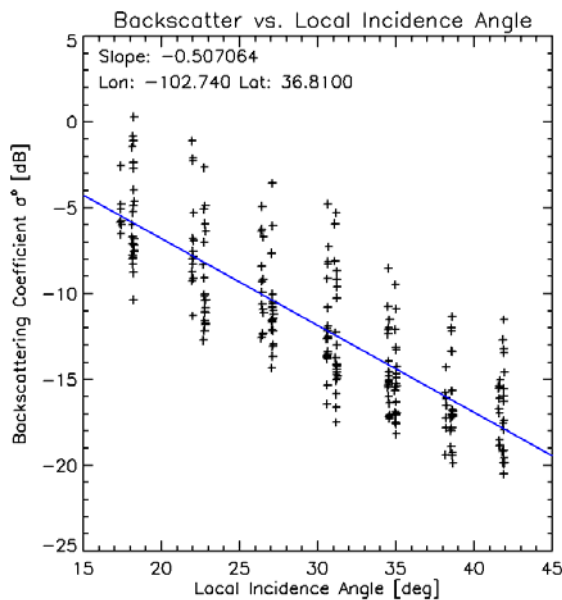


**Figure 31:** Angular dependency of radar backscatter before normalization Envisat ASAR GM for a grassland site in Oklahoma

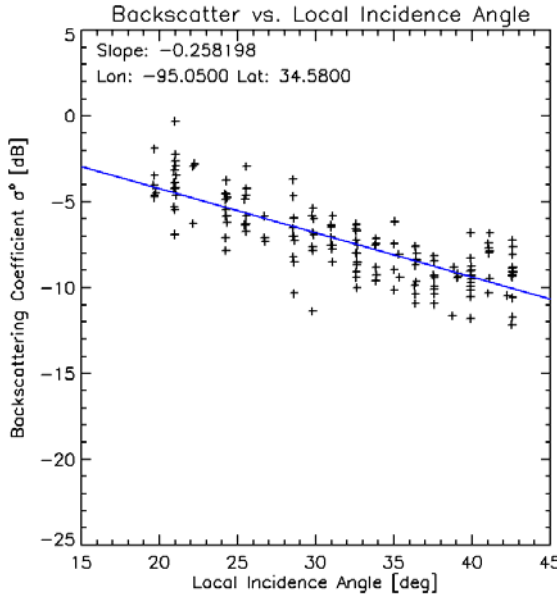


**Figure 32:** Angular dependency of radar backscatter before normalization of Envisat ASAR GM for a coniferous forest site in Oklahoma

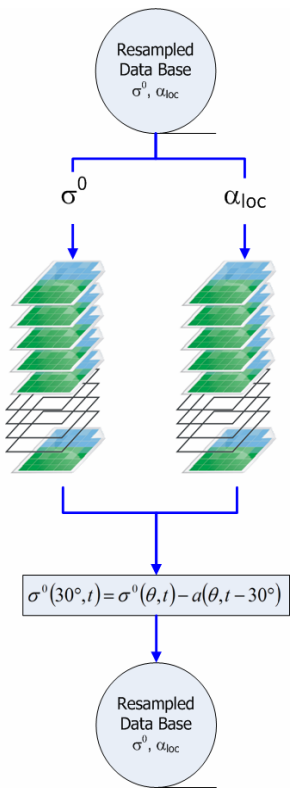


**Figure 33:** Multi-temporal pixel-by-pixel normalization procedure

Gauthier et al. (1998) are reporting variations in radar backscatter in ERS-1 SAR imagery acquired from ascending and descending orbits within 36 hours for a target under stable environmental conditions. The backscatter variation is mainly attributed to the sensitivity of radar backscattering coefficient to local incidence angle variations. A linear relationship between the radar backscattering coefficient and the local incidence angle is observed. A linear dependence of the radar backscattering coefficient is also documented for Radarsat data by Mäkynen et al. (2002) and for ERS scatterometer data by Frison & Mougin (1996). To remove the influence of local incidence angle on radar backscatter from ERS SAR, ERS scatterometer and RADARSAT data, linear models were fitted to the radar data to calculate backscatter values which are adjusted to predefined reference angles.

The angular dependency of radar backscatter is changing with surface roughness and scattering regime. Thus, it is closely related to land cover. The dielectrical and geometrical properties of the land cover changes with seasonal patterns

throughout the year for most parts of the world. Therefore a normalization procedure is required, which takes different land cover types and their temporal changes into account. To account for different land cover types and their temporal changes, the normalization procedure is based on multi-temporal data sets and is performed on a pixel-by-pixel basis defined by the single grid points of the regular grid. Each ASAR GM data set has been resampled to a regular grid (see Chapter 5.1.3.). During the geocoding process, a local incidence angle has been assigned to each radar backscatter measurement. For each grid point, a certain number of radar backscatter measurements acquired under different incidence angles are available (Figure 33).

Given the limited incidence angle range of ASAR GM, a linear model (Eq. 5.9) is sufficient to describe the incidence angle variation. All ASAR GM radar backscatter measurements are adjusted to a medium incidence angle of 30° using the formula:

$$\sigma^0(30^\circ, t) = \sigma^0(\theta, t) - \beta(\theta, t - 30^\circ) \quad (\text{Eq. 5.9})$$

where  $\sigma^0(30^\circ, t)$  is the normalized backscatter expressed in decibels,  $\sigma^0(\theta, t)$  is the uncorrected radar backscatter,  $\beta$  is the slope (unit decibels per degree) of the regression line of the linear model fitted to  $\sigma^0(\theta, t)$  time series data and  $\theta$  is the local incidence angle. Such a linear model has previously been used by (Champion 1996; Ezraty & Cavanie 1999; Sahebi et al. 2003; Kaleschke & Heygster 2004; Moran et al. 2004; Loew et al. 2006) for modeling the incidence angle dependency of  $\sigma^0$  observed in ASAR Wide Swath data.

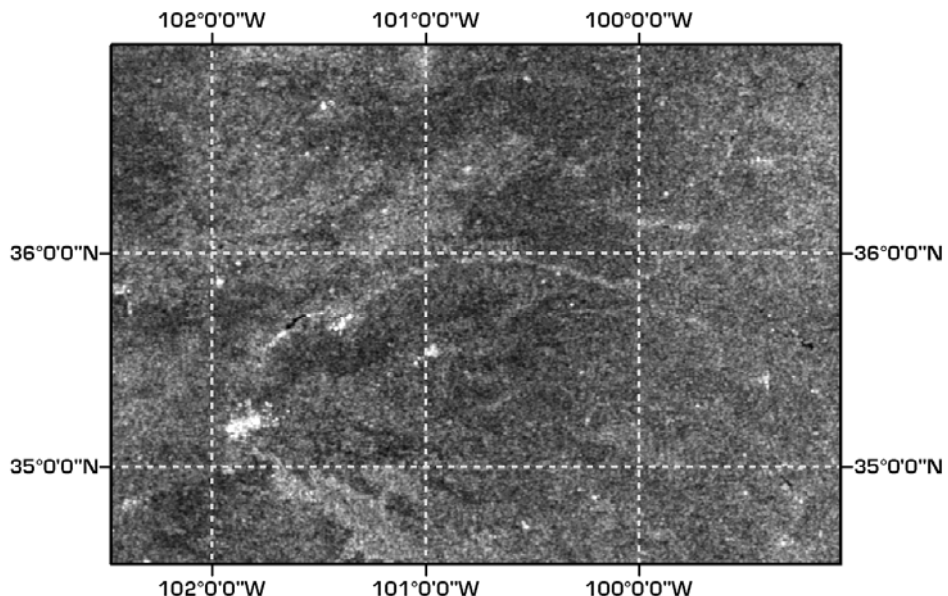


**Figure 34:** Removed change in image brightness due to angular dependency after normalization

Figure 34 illustrates the result of the local incidence angle normalization procedure. After normalization, the radar backscattering coefficient  $\sigma^0$  does not show any apparent influence of the local incidence angle. Radar image brightness shows a well balanced distribution. It is assumed, that the radar backscatter is now only influenced by terrain attributes. When looking at plots of radar backscatter vs. local incidence angle for the land cover classes used for Figure 31 and Figure 32, it can be seen that the angular dependency has been removed for grassland (Figure 35) as well as for coniferous forest (Figure 36).

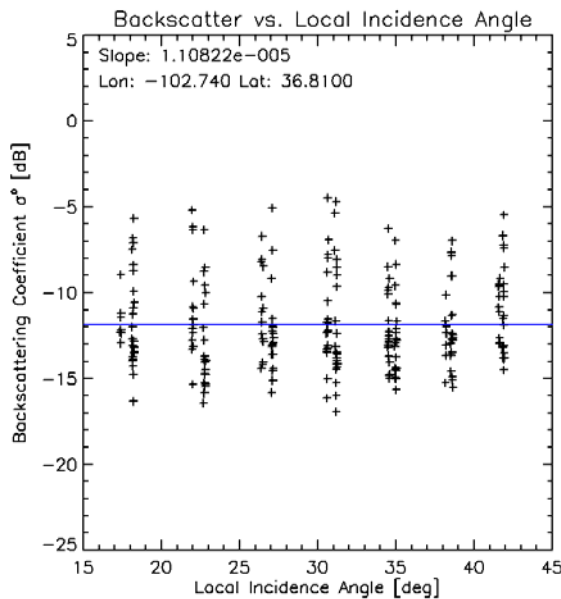


**Figure 35:** Angular dependency of radar backscatter after normalization of Envisat ASAR GM for a grassland site in Oklahoma

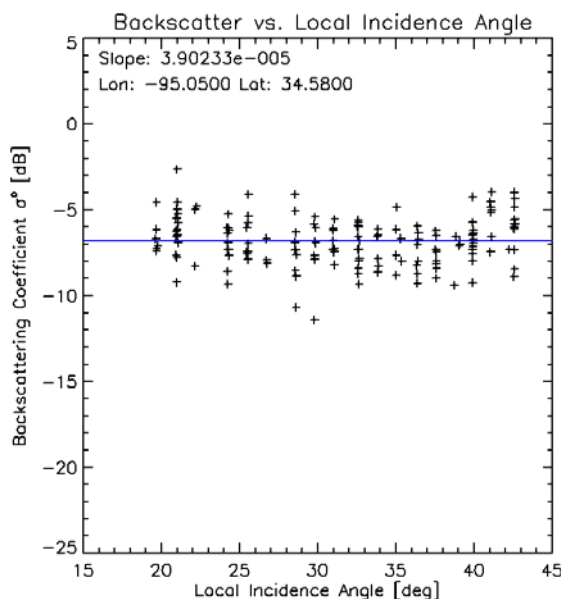


**Figure 36:** Angular dependency of radar backscatter after normalization of Envisat ASAR GM for a coniferous forest site in Oklahoma

## 5.2. Change Detection Surface Soil Moisture Retrieval Alortihm

---

The limitations of empirical and physically based backscatter models connected with the geometrical description of natural surfaces and the comprehensive input data amount (see Chapter 3.3.) prevent their applicability in regular operational soil moisture monitoring from current SAR data. Another reason is the low temporal resolution of past and current space-borne SAR sensors operating in strip-map mode, which is inadequate for observing a temporal highly variable parameter like soil moisture. On the other hand, scatterometers offer high temporal resolutions with up to 2 acquisitions per day at low spatial resolutions. Regardless of this fact, scatterometer data have been used for soil moisture extraction at continental and global scales.

### 5.2.1. Original ERS-1/2 Change Detection Soil Moisture Retrieval Algorithm

---

Recognizing the need for soil moisture information on continental to global scales, a change detection algorithm for retrieving soil moisture information from ERS-1/2 C-band scatterometer time-series data has been developed by Wagner et al. (1999a; 1999b; 1999c). The approach is based on the assumption that C-band microwave data are sensitive to soil moisture changes, which vary between wet and dry soil moisture conditions. These reference values represent radar backscatter at dry soil moisture conditions at wilting level ( $\sigma^0_{dry}$ ) and backscatter at wet soil moisture conditions at field capacity ( $\sigma^0_{wet}$ ).

$$m_s(t) = \frac{\sigma^0(\theta, t) - \sigma^0_{dry}(\theta, t)}{\sigma^0_{wet}(\theta, t) - \sigma^0_{dry}(\theta, t)} \quad (\text{Eq. 5.10})$$

The estimation of the two reference values is complicated by the fact, that radar backscatter also is influenced by the incidence angle and by vegetation biomass. Like it

is the case for soil moisture, an increase in biomass due to vegetation growth throughout the year leads to an increase in radar backscatter  $\sigma^0$  whereas an increasing incidence angle  $\theta$  leads to a decreasing radar backscatter  $\sigma^0$ . To account for these two unwanted influences, a number of processing steps are required before soil moisture retrieval. Here, the technical design of the ERS-1/2 scatterometer is exploited. The sensor is equipped with three antennas and therefore three independent measurements under different incidence angles are obtained during each acquisition. Therefore it is possible to describe the incidence angle dependency per acquisition and the following second order polynomial function was identified as a good approximation for describing radar backscatter:

$$\sigma^0(\theta, t) = \sigma^0(40, t) + \sigma'(40, t)(\theta - 40) + \frac{1}{2}\sigma''(40, t)(\theta - 40)^2 \quad (5.11)$$

with  $\sigma'$  being the first derivative of  $\sigma^0(\theta)$  also called slope, and  $\sigma''$  the second derivative of  $\sigma^0(\theta)$  also called curvature. If these parameters are estimated, the three individual measurements  $\sigma^0(\theta)$  can be averaged and extrapolated to a mean reference angle of  $40^\circ$  with:

$$\sigma^0(40) = \frac{1}{3} \sum_{i=1}^3 \sigma_i^0(\theta, t) - \sigma'(40, t)(\theta - 40) - \frac{1}{2}\sigma''(40, t)(\theta - 40)^2 \quad (5.12)$$

In a second step, the influence of vegetation on radar backscatter needs to be described, before soil moisture information can be derived. A characterization of the effects of growing vegetation on radar backscatter is based on the fact that backscatter may decrease or increase when vegetation grows, depending on whether the attenuation of the soil contribution is more important than the enhanced contribution from the vegetation canopy, or vice versa. Since the attenuation of the soil contribution is dominant at low incidence angles while canopy scattering dominates at higher incidence angles, an incidence angle called the “cross-over angle” at which both effects balance each other has been identified (Wagner et al. 1999a). This is illustrated in Figure 37, which shows the scatterometer model for a mixed grassland-agricultural area in Oklahoma ( $36.86^\circ\text{N}$ ,  $102.7^\circ\text{W}$ ). One can see that backscatter increases from winter to summer at higher incidence angles; while at lower incidence angles backscatter decreases. This is in agreement with vegetation models such as the Cloud Model introduced by (Ulaby & Attema 1978). Based on empirical studies for various climates and vegetation zones, the cross-over angles have been defined with  $\theta_{dry} = 25^\circ$  and  $\theta_{wet} =$

40. Just recently, setting  $\theta_{dry}$  to a value of  $25^\circ$  has been supported by findings of a study over a Sahelian test site in Mali by Baup et al. (2007).

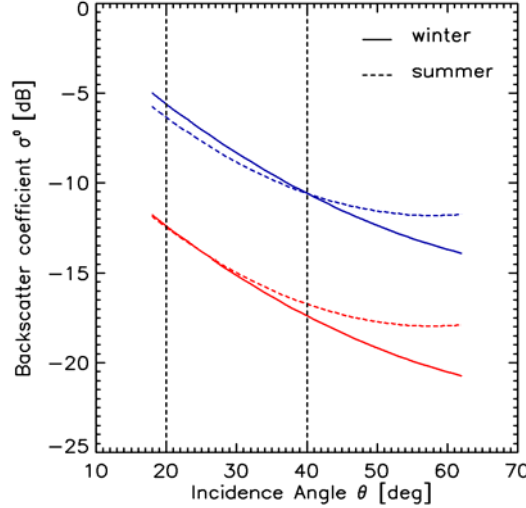


**Figure 37:** Dry (red) and wet (blue) backscatter reference curves for winter (solid line) and summer (dashed line) conditions. The model parameters were estimated from ERS scatterometer measurements (1991-2007) of a grassland region in Oklahoma ( $36.86^\circ\text{N}$ ,  $102.7^\circ\text{W}$ ). The two vertical lines indicate the incidence angle range of the ASAR GM ( $20$ - $40^\circ$ )

When vegetation grows, the slope  $\sigma'$  and the curvature  $\sigma''$  introduced in Eq. 5.6 will change. This annual variation of the slope  $\sigma'$  is described by the periodic function  $\Psi'(t)$  and the two parameters  $C'$  and  $D'$ , whereas the annual variation of the curvature  $\sigma''$  is described by the periodic function  $\Psi''(t)$  and the two parameters  $C''$  and  $D''$ . Once, these location specific variables have been defined, the reference backscatter  $\sigma_{dry}^0$  and  $\sigma_{wet}^0$  at dry and wet surface soil moisture conditions can be calculated (Wagner 1998; Scipal 2002):

$$\sigma_{dry}^0 = C_{dry}^0 - D' \Psi'(t)(\theta_{dry} - 40) - \frac{1}{2} D'' \Psi''(t)(\theta_{dry} - 40)^2 \quad (5.13)$$

with:

$$C_{dry}^0 = \sigma_{dry}^0(\theta_{dry}) - C'(\theta_{dry} - 40) - \frac{1}{2} C''(\theta_{dry} - 40)^2 \quad (5.14)$$

and:

$$\sigma_{wet}^0 = C_{wet}^0 - D' \Psi'(t)(\theta_{wet} - 40) - \frac{1}{2} D'' \Psi''(t)(\theta_{wet} - 40)^2 \quad (5.15)$$

with:

$$C_{wet}^0 = \sigma_{wet}^0(\theta_{wet}) - C'(\theta_{wet} - 40) - \frac{1}{2} C''(\theta_{wet} - 40)^2 \quad (5.16)$$

With the location specific, incidence angle and vegetation corrected reference backscatter values  $\sigma^0_{dry}$  and  $\sigma^0_{wet}$  it is then possible to scale each individual backscatter measurement between the dry and the wet reference and to derive a relative surface soil moisture value given in %.

The contribution of surface roughness to the backscattered signal is considered to be a constant parameter, which does not require separated treatment. As it has turned out, this is not completely true. This issue is connected with the design of the ERS scatterometer which is equipped with three antennas, one is oriented 45° forward, one perpendicular and one 45° backward relative to the satellite ground track. Whereas the incidence angle of the for- and backward oriented antenna are identical and thus the radar backscatter should be similar, the azimuth angle differs. It has turned out, that the backscatter difference between the measurements of the forward and backward oriented antennas is a function of the azimuth angle. Especially over desert areas with surface features with a pronounced directional alignment (e.g. sand dunes), the difference may become quite large and cause periodic noise-like signal variability. The initial version of the change detection surface soil moisture algorithm for ERS data was based on the assumption, that radar backscatter can be treated only as a function of soil moisture, vegetation cover and incidence angle only. Azimuthal effects were considered to have only a weak impact on radar backscatter (Scipal 2002). To account for the observed azimuthal effects, affected areas are masked out in the processed soil moisture product. A mathematical-physical description and a possible compensation of these azimuthal effects has been developed and is incorporated in the latest version of the retrieval algorithm, which also has been adapted for use with MetOp ASCAT data (Bartalis et al. 2006).

Another issue is connected to the estimation of the dry and wet references. Soil moisture is estimated by scaling individual backscatter measurements between a dry and a wet reference. This approach works well for most regions in the world. But it becomes problematic in regions characterized by a high variability of precipitation, e.g. barren land/sparsely vegetated land, shrublands, deserts. In such regions it is possible that saturated soil moisture conditions never have been observed within the period for which backscatter time series data are available. For such cases, a so called wet correction has been introduced in later versions of the ERS scatterometer soil moisture retrieval

approach. Within the wet correction, the wet reference values are increased, if saturated soil moisture conditions have not been observed for a distinct period of time.

The correction of the seasonal vegetation cover effects on radar backscatter as described above is based on the assumption that the vegetation phenology is the identical every year. This ignores natural variability of climate variables like precipitation or air temperature. Years with distinct anomalies in precipitation alter the development of the vegetation and therefore the correction of the vegetation cover effects as it is done within the ERS scatterometer change detection soil moisture retrieval approach cause an over- or undercompensation and thus to errors in the estimated soil moisture products.

---

### **5.2.2. Adapted Change Detection Soil Moisture Retrieval Algorithm for Envisat ASAR GM Data**

---

The change detection for ASAR GM data is based on the ERS-1/2 scatterometer approach described above. Due to the technical configuration of the ASAR sensor, which only allows its operation in exclusive modes together with multi-purpose character of the Envisat mission, some drawbacks need to be accepted and accounted for in the design of the change detection radar backscatter model. In the case of the ERS-1/2 scatterometer, modelling of phenological vegetation effects is possible due to the instrument's capability to acquire backscatter measurements at different incidence angles at the same time. Unfortunately, this is not the case for ASAR GM which acquires only one backscatter measurement at some incidence angle for a target during each overpass. Consequently, it is impossible to derive a slope value for each single acquisition and use the annual variation of the slope for biomass correction as it is done for the ERS scatterometer data. Nevertheless, from a temporal perspective the seasonal vegetation signal in C-band time series is much weaker than the soil moisture signal (Wagner et al. 1999a). Therefore the seasonal vegetation effects are neglected in a first approximation, i.e.  $\sigma^0_{dry}$  and  $\sigma^0_{wet}$  are assumed to be constant over the year. This assumption is supported by the exemplary plots in Figure 37. Within the incidence angle range covered by ASAR GM ( $20^\circ$ - $40^\circ$ ), changes in backscatter due to vegetation growth are in general much smaller than changes due to soil moisture. Additionally,

ASAR GM is commonly operated in HH polarization which penetrates vegetation better than VV polarization as used by the ERS scatterometer (Brown et al. 2003). The parameters  $\sigma_{dry}^0$  and  $S$  are now assumed to be constant in time because seasonal vegetation effects are expected to be weak for ASAR GM. Therefore, the following simplified change detection model is adapted for multi-temporal ASAR GM data:

$$\sigma^0(\theta, t) = \sigma_{dry}^0(30) + \beta(\theta - 30) + Sm_s(t) \quad (\text{Eq. 5.17})$$

$$S = \sigma_{wet}^0 - \sigma_{dry}^0 \quad (\text{Eq. 5.18})$$

Given the limited incidence angle range of ASAR GM, a linear model is sufficient to describe the incidence angle variation using the slope  $\beta$  of the regression line given in dB per degree for the relationship of  $\sigma^0$  and  $\theta$ . Such a linear model has previously been used by different researchers (Sahebi et al. 2003; Moran et al. 2004; Baup et al. 2007) for modeling the incidence angle dependency of  $\sigma^0$  observed in ASAR Wide Swath data.

Azimuthal effects like they were observed for the ERS scatterometer may also occur with ASAR GM data when combining ascending and descending orbits. Land cover patterns in Oklahoma are not expected to cause azimuthal effects. Consequently no correction of azimuthal effects is required.

A wrong estimation of wet references for regions with high precipitation variability like in the ERS scatterometer soil moisture retrieval algorithm is theoretically possible but this does not apply for the selected Oklahoma test site in the south-western part of the USA.

---

### 5.2.2.1. Estimation of Dry and Wet Reference

---

The estimation of the time-invariant dry and wet reference values,  $\sigma_{dry}^0$  and  $\sigma_{wet}^0$ , necessary for the inversion of the backscatter model (Eq. 5.12) to retrieve surface soil moisture from multi-temporal ASAR GM time series data is hampered by the high noise level in the ASAR GM data, which causes an artificial spreading of the backscatter measurements, and the variability of precipitation. The limited temporal and spatial coverage of the ASAR GM data does not necessarily guarantee that the wettest and driest surface soil moisture conditions for a particular location or test site area have been captured by on ASAR GM acquisition date. Following from this, relying only on

the minimum and maximum backscatter values observed at a location will not give good and robust estimates of the dry and wet references. To account for these problems, the estimation of the dry and wet references is based on the assumption that the probabilities of acquiring backscatter measurements during dry and wet surface soil moisture conditions is known. ERS-1/2 scatterometer data are available for the years 1992 to 2001 and the chance of missing the driest and wettest surface soil moisture conditions is minimized. The probabilities for the occurrence of dry and wet reference backscatter are called  $p_{dry}$  and  $p_{wet}$ . If  $N$  ASAR GM measurements were acquired over an area, then it is possible to calculate the number of measurements  $N_{dry}$  and  $N_{wet}$  taken under dry and wet surface soil moisture conditions.

$$N_{dry} = N \cdot p_{dry} \quad (\text{Eq. 5.19})$$

with

$$p_{dry} = \frac{N(m_s < 5\%)}{N_{ERS}} \quad (\text{Eq. 5.20})$$

where  $N(m_s < 5\%)$  represent the number of ERS scatterometer derived surface soil moisture values from an ascending ordered data set with a relative surface soil moisture lower than 5%. Similarly,  $N_{wet}$  is estimated using:

$$N_{wet} = N \cdot p_{wet} \quad (\text{Eq. 5.21})$$

with

$$p_{wet} = \frac{N(m_s > 95\%)}{N_{ERS}} \quad (\text{Eq. 5.22})$$

where  $N(m_s > 95\%)$  represent the number of ERS scatterometer derived surface soil moisture values from an ascending ordered data set with a relative surface soil moisture larger than 95%.

Because of the inherent noise of the ASAR GM backscatter measurements acquired during intermediate soil wetness conditions are to some extent mixed with measurements representing extreme dry or wet soil conditions. By averaging the  $N_{dry}$  lowest ASAR GM measurements and the  $N_{wet}$  highest ASAR GM measurements, reasonable estimates of  $\sigma_{dry}^0$  and  $\sigma_{wet}^0$  should be obtained:

$$\sigma_{dry}^0 \approx \frac{1}{N_{dry}} \sum_{i=1}^{N_{dry}} \sigma_i^0 \quad (\text{Eq. 5.23})$$

$$\sigma_{wet}^0 \approx \frac{1}{N_{wet}} \sum_{i=1}^{N_{wet}} \sigma_i^0 \quad (\text{Eq. 5.24})$$

The probabilities  $p_{dry}$  and  $p_{wet}$  depend on the climatic conditions and on characteristics of the land surface (soil type, vegetation, etc.). For an arid environment one expects e.g. that  $p_{dry}$  is high and  $p_{wet}$  very low. For a more humid environment the changes of acquiring measurements during wet reference conditions increases and decrease for dry conditions. Based on the long-term soil moisture archive from the ERS scatterometer these two probabilities can be estimated. Because the scatterometer derived probabilities are only available at 50 km scale, the values need to be interpolated to the ASAR GM 1 km grid. The estimation of these probabilities and the interpolation to 1 km is obviously not meaningful in areas where it is not possible to observe a soil moisture signal, i.e. in tropical rain forest, ever-dry desert areas, and rocky areas. Therefore land cover data are used to mask out these areas.

### 5.2.2.2. Surface Soil Moisture Retrieval

Once, the model parameters  $\sigma_{dry}^0, \sigma_{wet}^0$  and  $S$  respectively have been estimated, surface soil moisture is retrieved from normalized ASAR GM backscatter measurements for each grid point and for each individual acquisition date. To do so, the multi-temporal backscatter model is inverted to retrieve surface soil moisture information:

$$m_s(t) = \frac{\sigma^0(30, t) - \sigma_{dry}^0(30)}{S} \quad (5.25)$$

For characterizing the temporal agreement, the ASAR GM retrieved soil moisture time series are compared to the in-situ and ERS scatterometer soil moisture data over the MESONET stations. The following statistical measures are calculated for each of the three time series pairs for each MESONET station: correlation coefficient ( $R$ ), the *BIAS*, and the standard deviation ( $SD$ ).

$$r = \frac{\sum_{i=1}^n (x_i - \bar{x})(y_i - \bar{y})}{\sqrt{\frac{1}{n} \sum_{i=1}^n (x_i - \bar{x})^2 \cdot \frac{1}{n} \sum_{i=1}^n (y_i - \bar{y})^2}} \quad (\text{Eq. 5.26})$$

The *BIAS* between two soil moisture datasets  $x$  and  $y$  is given by:

$$BIAS = \frac{1}{M} \sum_{j=1}^M (y(t_j) - x(t_j)) \quad (\text{Eq. 5.27})$$

where M is the number of concurrent measurements at times  $t_j$ . The standard SD deviation is calculated using the formula:

$$SD = \sqrt{\frac{1}{M-1} \sum_{j=1}^M (y(t_j) - x(t_j) - BIAS)^2} \quad (\text{Eq. 5.28})$$

### 5.2.3. Calculation of the Retrieval Error

The relative surface soil moisture  $m_s$  is extracted from ASAR GM time series data using the proposed inverted change detection backscatter model (Eq. 5.20). Thus, the soil moisture  $m_s$  is a function of the model parameters and can be written as:

$$m_s = \frac{\sigma^0 - \sigma_{dry}^0 - \beta(\theta - 30^\circ)}{\sigma_{wet}^0 - \sigma_{dry}^0} = f(\sigma^0, \beta, \theta, \sigma_{wet}^0, \sigma_{dry}^0) \quad (5.29)$$

The estimated surface soil moisture  $m_s$  will contain errors caused by noise in the ASAR GM backscatter data  $\sigma^0$  as well as by estimation errors during the determination of the dry and wet references  $\Delta\sigma_{dry}^0, \Delta\sigma_{wet}^0$  and the normalization of the influences of the local incidence angle  $\theta$  using the slope  $\beta$  for characterizing the relation between radar backscatter and local incidence angle.

An isolated treatment of each parameter may ignore the mutual influences of the errors in the individual parameters on the overall retrieval error in the soil moisture  $m_s$ . Assuming that the errors of the model parameters follow a Gaussian distribution, then the principles of Gaussian error propagation can be applied to determine the retrieval error of the soil moisture model  $\Delta m_s$  and to assess the impact of the errors in the individual model parameters on the retrieval error  $\Delta m_s$  (Gottwald 1995; Taylor 1997). According to the principles of the Gaussian error propagation law, the error  $\Delta y$  in  $y$  as a function of:

$$y = f(x_1, x_2, \dots, x_n) \quad (5.30)$$

can be estimated using the formula:

$$\Delta y = \sqrt{\sum_{i=1}^n \left( \frac{\partial y}{\partial x_i} \Delta x_i \right)^2} = \sqrt{\left( \frac{\partial y}{x_1} \Delta x_1 \right)^2 + \left( \frac{\partial y}{x_2} \Delta x_2 \right)^2 + \dots + \left( \frac{\partial y}{x_n} \Delta x_n \right)^2} \quad (5.31)$$

When applying this general formulation to the change detection soil moisture retrieval approach, the retrieval error  $\Delta m_s$  is derived as the sum of the individual errors using the expression:

$$\Delta m_s = \sqrt{\left( \frac{\partial f}{\partial \sigma^0} \Delta \sigma^0 \right)^2 + \left( \frac{\partial f}{\partial \beta} \Delta \beta \right)^2 + \left( \frac{\partial f}{\partial \sigma_{dry}^0} \Delta \sigma_{dry}^0 \right)^2 + \left( \frac{\partial f}{\partial \sigma_{wet}^0} \Delta \sigma_{wet}^0 \right)^2} \quad (5.32)$$

with  $\frac{\partial f}{\partial \sigma^0}$ ,  $\frac{\partial f}{\partial \beta}$ ,  $\frac{\partial f}{\partial \sigma_{dry}^0}$ ,  $\frac{\partial f}{\partial \sigma_{wet}^0}$  being the partial derivates for each parameter of the

inverted change detection radar backscatter model.

The partial derivates of the model parameters are:

$$\frac{\partial f}{\partial \sigma^0} = \frac{1}{S} \text{ with } S = \sigma_{wet}^0 - \sigma_{dry}^0 \quad (5.33, 5.34)$$

$$\frac{\partial f}{\partial \beta} = -\frac{\theta - 30}{S} \quad (5.35)$$

$$\frac{\partial f}{\partial \sigma_{dry}^0} = \frac{-1(\sigma_{wet}^0 - \sigma_{dry}^0) - (\sigma^0 - \beta(\theta - 30) - \sigma_{dry}^0)(-1)}{(\sigma_{wet}^0 - \sigma_{dry}^0)^2} \quad (5.36)$$

$$= \frac{\sigma^0 - \beta(\theta - 30) - \sigma_{wet}^0}{(\sigma_{wet}^0 - \sigma_{dry}^0)^2} \quad (5.37)$$

$$= -\frac{1}{S} \cdot \frac{\sigma^0 - \beta(\theta - 30) - \sigma_{dry}^0 - (\sigma_{wet}^0 - \sigma_{dry}^0)}{S} \quad (5.38)$$

$$= \frac{1}{S} (m_s - 1) \quad (5.39)$$

$$\frac{\partial f}{\partial \sigma_{wet}^0} = \frac{\partial}{\partial \sigma_{wet}^0} (\sigma^0 - \beta(\theta - 30) - \sigma_{dry}^0)(\sigma_{wet}^0 - \sigma_{dry}^0)^{-1} \quad (5.40)$$

$$= -1(\sigma^0 - \beta(\theta - 30) - \sigma_{dry}^0)(\sigma_{wet}^0 - \sigma_{dry}^0)^{-1} \quad (5.41)$$

$$= \frac{\sigma^0 - \beta(\theta - 30) - \sigma_{dry}^0}{(\sigma_{wet}^0 - \sigma_{dry}^0)^2} \quad (5.42)$$

$$= -\frac{1}{S} m_s \quad (5.43)$$

With the partial derivates of the model parameters, the retrieval error  $\Delta m_s$  can be calculated using the formula:

$$\Delta m_s \approx \sqrt{\left(\frac{\Delta \sigma^0}{S}\right)^2 + \left(\frac{(\theta - 30)\Delta \beta}{S}\right)^2 + \left(\frac{(m_s - 1)\Delta \sigma_{dry}^0}{S}\right)^2 + \left(\frac{m_s \Delta \sigma_{wet}^0}{S}\right)^2} \quad (5.46)$$

with:

$$S = \sigma_{wet}^0 - \sigma_{dry}^0 \quad (5.47)$$

While the noise of the ASAR GM backscatter measurements  $\Delta \sigma_{dry}^0$  is known beforehand (see Chapter 6.1.), the errors of the model parameters are unknown. They are defined based on theoretical considerations on potential error sources for each model parameter. Here, four error sources need to be named:

- Error source 1: The temporal coverage and the irregular temporal sampling interval of the ASAR GM data over the four seasons with their distinct phenological and climatologic characteristics.
- Error source 2: Raw data by the data provider and data pre-processing may have introduced errors in the geometrically and radiometrically corrected, incidence angle normalized radar backscatter data
- Error source 3: The method for deriving the model parameters  $\beta$ ,  $\sigma_{dry}^0$  and  $\sigma_{wet}^0$  gives estimates of the parameters, which may contain errors.
- Error source 4: Neglecting seasonal vegetation cover effects due to the limited number of data in the radar backscatter time series can lead to seasonally varying errors. As the model parameters are derived from time series data irrespective of their acquisition date, errors due to neglecting

seasonal vegetation cover effects are, if present, contained in all model parameters.

Based on these considerations, it is assumed that due to vegetation phenology the slope parameter  $\beta$  in particular introduces a high relative error in the range of 10%. Also, the errors  $\Delta\sigma^0_{dry}$  and  $\Delta\sigma^0_{wet}$  are assumed to be 10 % relative to the observed dynamic range of the backscatter measurements, i.e.  $\Delta\sigma^0_{dry} = \Delta\sigma^0_{wet} = 0.1S$ .

# **Chapter 6**

## **Results and Discussion**

---

In this chapter, the results of the doctoral thesis are presented. First the estimated of the noise level of the ASAR GM data are exposed as important prerequisite for the later discussion of the results of the surface soil moisture retrieval using the proposed change detection algorithm. Model parameters and their spatial patterns are shown using maps and plots. References to the physiographic features of Oklahoma (see Chapter 4.1.) are intended to provide an understanding of the observed spatial patterns. The extracted relative surface soil moisture with their spatial and temporal patterns is presented using summarizing figures and tables. More detailed tables and figures can be found in the appendix. The results are discussed in the context of the objectives of this doctoral thesis and recent research. To validate the observed temporal patterns of relative GM surface soil moisture, *in-situ* soil moisture measurements of the Oklahoma Mesonet and ERS-1/2 scatterometer derived relative surface soil moisture data are used as a basis for comparison. Different statistical measures are calculated to quantify the quality of the retrieved relative surface soil moisture data.

### **6.1. Estimated Noise Level of ASAR GM Data**

---

As reliable information on the radiometric properties of the ASAR GM data have not been published so far, a method for accessing the results of the radiometric calibration as implemented in the processing chain, has been developed and set up. Four test sites over the African rain forest with a dimension of  $0.5^\circ \times 0.5^\circ$  each were analyzed. Time series of ASAR GM data for every single point of the 14.400 points within each test site were used to derive the test statistics. Table 5 shows that the estimated noise level of the ASAR GM measurements is about 1.2 dB.

Test region	UL/LR of test region (lon, lat [decimal degrees])	$S_{natural}$	$\langle S_{noise} \rangle$
1	20.5°E, 2.5°S / 21°E, 3°S	0.30 dB	1.18 dB
2	21.5°E, 1.5°S / 22°E, 2°S	0.36 dB	1.19 dB
3	21°E, 2.5S / 21.5° E, 3°S	0.31 dB	1.19 dB
4	21.5°E, 2.5°S / 22°E, 3°S	0.28 dB	1.18 dB
<b>Estimated noise level:</b>			1.185 dB

Table 5: Standard deviations of natural backscatter variation  $s_{Signal}$  and noise  $s_{Noise}$ . For an overview of the location of the test regions see also Figure 24; numbering top down and left to right.

Considering that the expected sensitivity of  $\sigma^0$  to soil moisture changes is in the order of 4 – 8 dB for grass- and agricultural areas, depending on the phenological state, the noise of GM backscatter measurement is relatively high. This is important information for the development of the experimental soil moisture product, as one can expect only a few soil moisture classes. Additionally, regions with a low signal-to-noise-ratio are masked out, as the backscatter signal variations caused by soil moisture are effectively masked by the high noise level.

The relatively high noise is caused by the low bandwidth of the ASAR when operated in GM mode. The selection of the low bandwidth during sensor design is a trade-off between geometric/radiometric resolution and temporal resolution. A duty cycle of nearly 100% for ASAR GM at a medium spatial resolution of 1 km is achieved at the cost of radiometric resolution. Compared to this, the ERS scatterometer has a very high radiometric resolution of 0.15 dB – but for 50 km footprints only.

## 6.2. Spatial Patterns

### 6.2.1. Model parameters

Maps of the backscatter model parameters dry reference  $\sigma^0_{dry}$ , slope  $\beta$  and sensitivity  $S$  have been generated for the Oklahoma test site and are presented and discussed in the following.

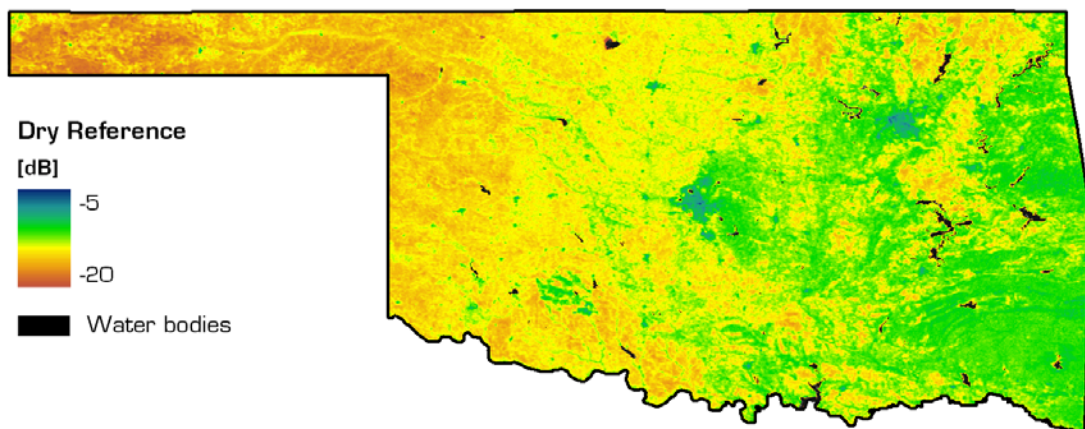


**Figure 38:** Backscatter model parameter dry reference  $\sigma_{dry}^0$  extracted from ASAR GM time series

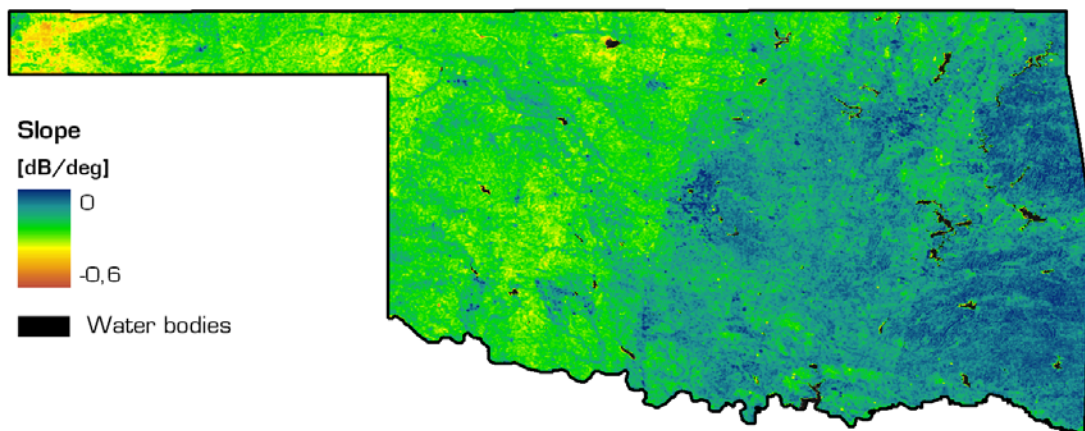


**Figure 39:** Backscatter model parameter slope  $\beta$  (in dB/deg) extracted from ASAR GM time series

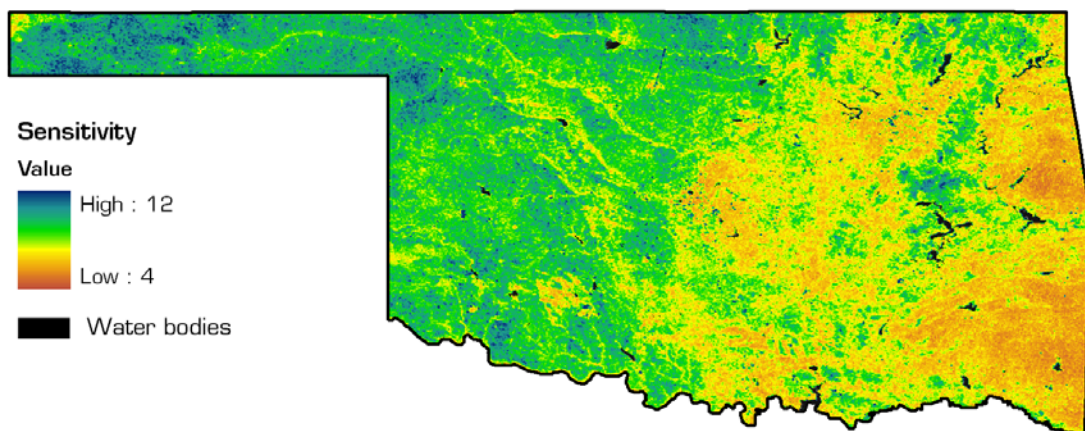


**Figure 40:** Backscatter model parameter sensitivity  $S$  (in dB) extracted from ASAR GM time series

The dry reference  $\sigma^0_{dry}$  (Figure 38) represents the backscatter conditions for dry surface soil moisture conditions. Dry reference values of -8 to -12 dB in the southeast decrease towards the northwest, where values of -14 to -18 dB are present. The lowest dry reference values in the order of -16 to -20 dB are found in the panhandle.

The spatial distribution of the slope values  $\beta$  (Figure 39) also shows a clear trend from east to west. The highest values can be found in the east where they vary around -0.05 dB/deg. Towards the northwest they are gradually decreasing to values of 0.3 to 0.35 dB/deg; minimum slope values can be found in the westernmost part of the panhandle.

The spatial plot of the sensitivity values (Figure 40) show spatial patterns similar to the other two model parameters. Low sensitivities around 5 dB can be found for the eastern part of Oklahoma. Similar to the other two parameters, the sensitivity changes towards the west. High sensitivities around 10 dB are mapped for the central and the western part with highest values of  $\geq 11$  in the western part of the panhandle.

The spatial patterns of the model parameters reflect the physiographic conditions of Oklahoma. When looking at the three model parameter maps, linear structures mainly oriented in east-west direction can be observed. These structures usually follow topographic features. These phenomena are most pronounced in the central and western part of Oklahoma. They can be identified as valleys, where model parameters differ significantly from their neighbourhood. Valley bottoms usually show wetter soil moisture conditions than the neighbouring area outside the valleys. Due to these soil moisture conditions, valleys are also often characterized by specific land cover features, e.g. trees and/or bushes compared to grassland or agricultural areas outside the river valleys. All together, this leads to radar backscatter conditions which result in the clearly distinguishable linear structures. The overall spatial patterns in the model parameter maps reflect the spatial distribution of land cover features (Figure 19, chapter 4.3.4.) to a large amount. A summarizing overview of typical model parameter values for the main land cover classes is given in the Figures 36-38. For this comparative presentation of the land cover specific model parameter values, boxplots have been prepared. Boxplots, or box-and-whisker diagrams, show a summary of the smallest value of the statistic, lower quartile Q1, the median Q2, the upper quartile Q3 and the largest value of the statistic. The distinct difference between the classes grassland/cultivated and forest is clearly recognizable in all three boxplots. Bearing the

area percentages of the main land cover classes in mind (see Chapter 4.3.4, Figure 19), the discussion of the spatial distribution of the model parameters will focus on the classes' grasslands/cultivated areas and forests.

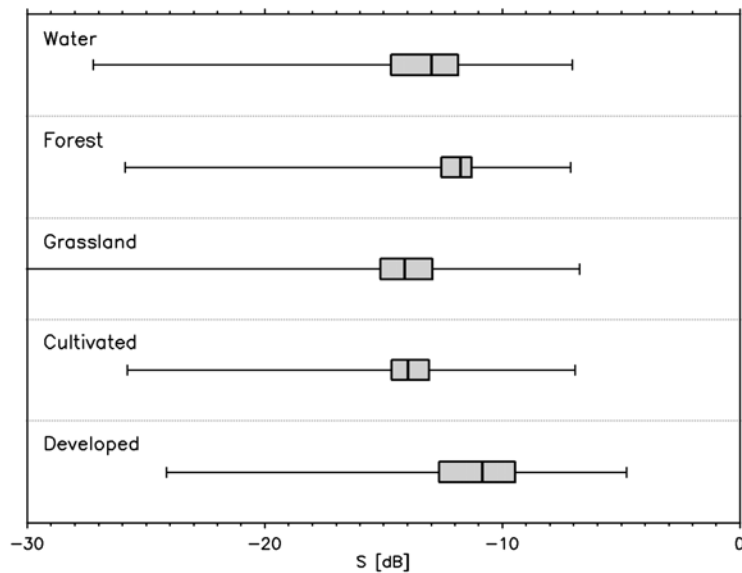


**Figure 41:** Box plot showing the dry reference  $\sigma_{dry}^0$  for main land cover classes

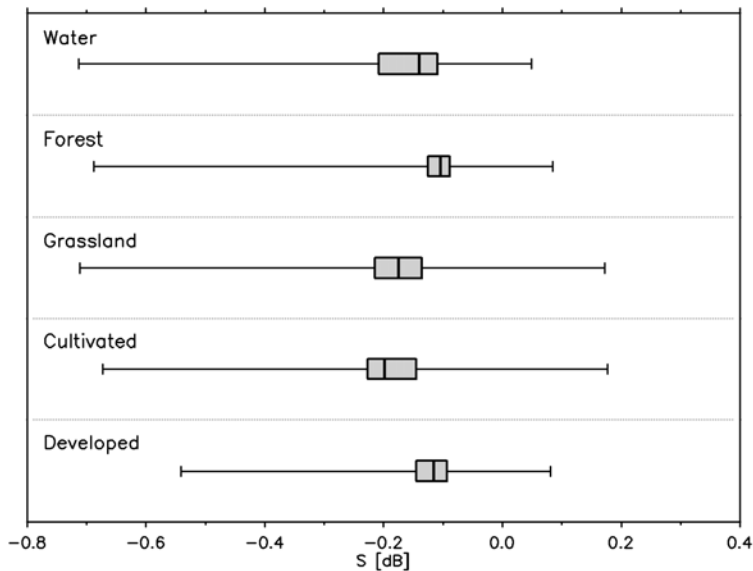


**Figure 42:** Box plot showing the slope  $\beta$  for main land cover classes

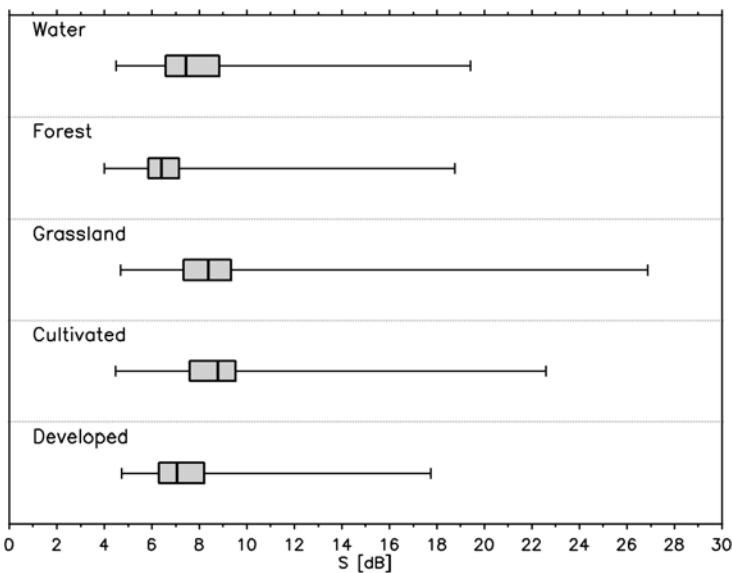


**Figure 43:** Box plot showing sensitivity  $S$  for main land cover classes

The eastern part of Oklahoma is mainly covered by forests, whereas the western part is dominated by grasslands. Here, low dry reference values are typically found, whereas higher dry reference values are mainly found in forested areas in the south-eastern part of Oklahoma. Also slope values are low, which means steep, for grassland areas and tend to increase for forest areas, approaching 0 dB/deg. This points to a negligible incidence angle dependency for forests in the eastern part of Oklahoma. Radar theory describing the fundamental relation between radar backscattering from vegetated surfaces and the incidence angle gives an explanation for this finding (see Chapter 3.3.). With increasing vegetation density, the transmissivity of the vegetation layer covering the soil surface is decreasing. Backscatter from the underlying soil surface decreases in favour of volume scattering from the vegetation canopy. Volume scattering from dense vegetation is almost uniformly distributed over a wide range of incidence angles. Therefore for densely vegetated areas the slope is less steep than for sparsely vegetated surfaces (Wagner et al. 1999b). Sensitivity is high, where the dry reference and the slope values are low. This is the case for the western part of Oklahoma with grassland as dominating land cover class. This is in agreement with radar theory, after which also signal components from the underlying soil surface contributes to radar backscatter from grasslands and cultivated areas. Seasonal precipitation patterns manifest in the range of soil moisture controlled backscatter and typical backscatter levels for dry and wet surface soil moisture conditions can be

derived for each grid point over these regions. Towards the east, sensitivity decreases, while dry reference and slope are increasing. Following the explanations from above, surface soil moisture related signal contribution become less pronounced for forest covered areas, as volume scattering signal contribution dominates backscatter from these regions. Consequently, only a low sensitivity is observed.

In the map of the slope parameter, diagonal stripes can be observed. Stripes are running from northeast to southwest or northwest to southeast. These are artefacts introduced by the individual ASAR GM acquisitions taken during either descending or ascending orbits. With values~0.01 dB/deg, they are comparably small and have a much weaker effect on the retrieved surface soil moisture than other error sources (see Chapter 6.4.). It was observed that these striping effects tend to get less pronounced with increasing number of ASAR GM data for the observed region. Therefore it is assumed that these effects will almost disappear for Oklahoma with regular updates of ASAR GM the time series data base.

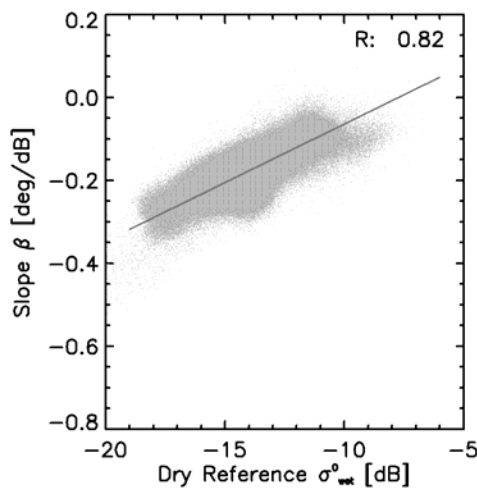


**Figure 44:** Slope  $\beta$  vs. Dry Reference  $\sigma_{\text{wet}}^0$

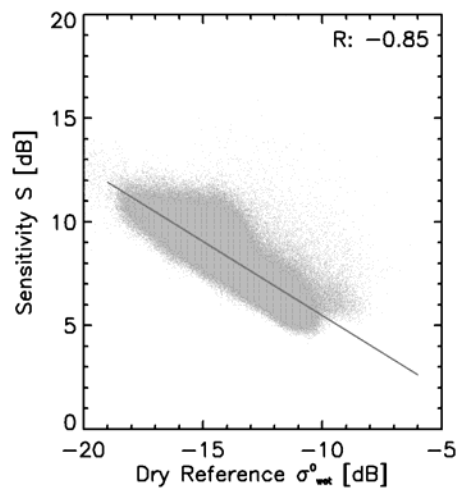


**Figure 45:** Sensitivity  $S$  vs. Dry Reference  $\sigma_{\text{wet}}^0$

The observations made for the spatial variation of the three model parameters are supported by scatterplots of the model parameters. The relation of dry reference values and slope values is characterized by a positive linear correlation – increasing dry reference values are followed by increasing slope values (Figure 44). A negative linear correlation was detected for the comparison of the sensitivity  $S$  and the dry reference

$\sigma^{\theta}_{wet}$  (Figure 45), where high sensitivities correspond to low dry reference values and vice versa. The relation between the sensitivity  $S$  and the slope  $\beta$  is also described by a negative linear correlation coefficient (Figure 46), where high sensitivity values are found for low slope values.

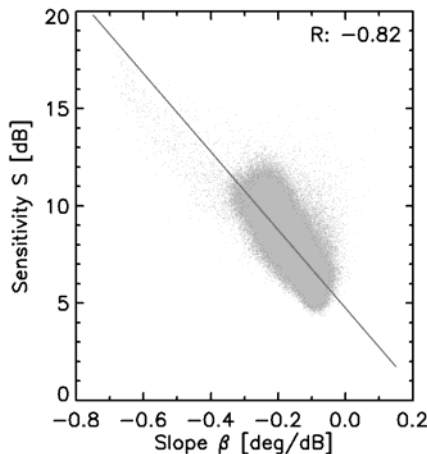


**Figure 46:** Sensitivity  $S$  vs. Slope  $\beta$

---

### 6.2.2. Relative Surface Soil Moisture

---

Relative surface soil moisture time series extracted from ASAR GM data as well as from ERS scatterometer data have been mapped for the Oklahoma test site. As an example a sequence of relative surface soil moisture is shown in Figure 47 for five consecutive acquisitions in June 2006. The visual comparison of the soil moisture products from the two sensors reveals similar spatial distribution of areas of high and low surface soil moisture. The surface soil moisture patterns mostly are a reflection of the precipitation history. The strip-like areas of high relative surface soil moisture which covering Oklahoma from the North to the South are mainly caused by advective precipitation and moving frontal systems. The sequence of surface soil moisture maps in Figure 47 shows the transition from very dry surface soil moisture conditions to nearly saturated soil moisture conditions.

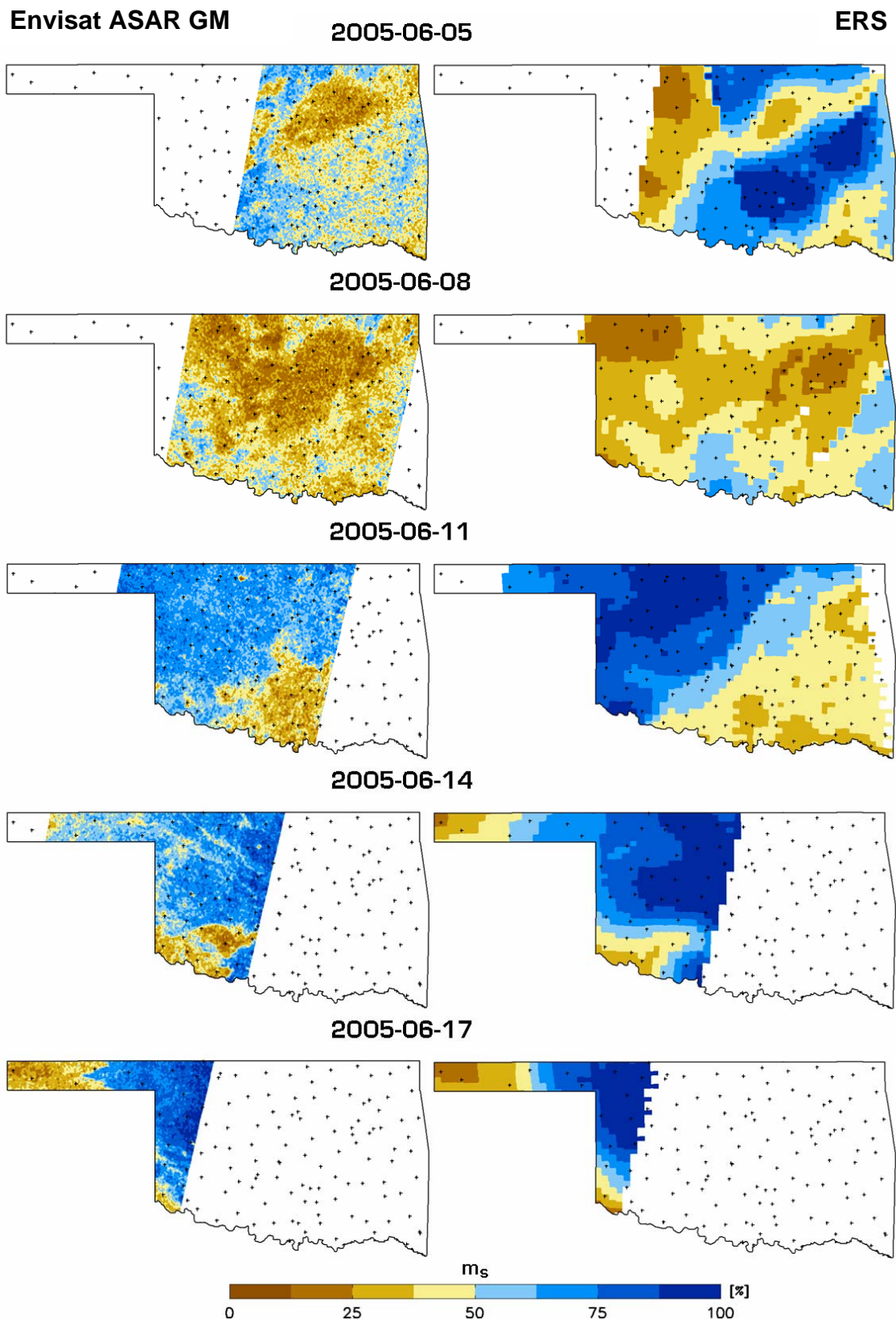


**Figure 47:** Relative surface soil moisture maps of Oklahoma extracted from ERS-1/2 scatterometer (right) and ASAR GM data (left) for a sequence of consecutive acquisitions in June 2005

The most striking difference in the comparative presentation of the remotely sensed soil moisture from ERS-1/2 scatterometer and ASAR GM data is their spatial resolution. The maps of the ERS-1/2 scatterometer derived surface soil moisture appear much smoother than the maps based on ASAR GM backscatter data and suggest clearly discernable areas of uniform surface soil moisture conditions. The ASAR GM surface soil moisture maps show, that this is not the case. Large areas of a specific surface soil moisture class can be interspersed with other moisture classes indeed. The grainy appearance of the ASAR GM surface soil moisture maps is also a result of the much higher noise level of the ASAR GM backscatter measurements. Even though, the ASAR GM based surface soil moisture maps have been resampled from the original spatial resolution of 1 km to now 3 km, the grainy effect could be further reduced by applying filters at the cost of detail.

A comparison of the spatial patterns of the remotely sensed relative surface soil moisture to *in-situ* soil moisture point measurements would only be possible when the *in-situ* soil moisture measurements gathered at the stations of the Oklahoma Mesonet are spatially interpolated. This is not regarded to be a meaningful analysis, as such a spatial interpolation completely ignores physiographic conditions, which govern soil moisture and precipitation patterns in nature (see Chapter 2.3.).

### **6.3. Temporal Patterns of Surface Soil Moisture**

---

The validation of the temporal patterns of the remotely sensed ASAR GM soil moisture data was carried out using *in-situ* soil moisture measurements from 75 stations of the Oklahoma Mesonet. ASAR GM acquisition dates with snow covered or frozen surface conditions were excluded from the validation. For this purpose, meteorological data were used, and all acquisition dates with a minimum temperature  $<1^{\circ}\text{C}$  were removed from the data sets before performing the validation. Compared to ERS-1/2 scatterometer data, the ASAR GM data are characterized by a relatively high noise level. According to the technical specifications the radiometric accuracy of the ASAR GM data is 1.2 dB. To account for this noise, the ASAR GM soil moisture at the Oklahoma Mesonet measurement stations were averaged over a 3 x 3 pixel window corresponding to a 3 x 3 km region centred on the geographic location of individual measurement stations. Therefore, the spatial resolution of the ASAR GM soil moisture

used during validation is 3 km. For comparisons of ASAR GM soil moisture to ERS scatterometer derived soil moisture, the ASAR GM soil moisture was reduced to 50 km spatial resolution.

For validating the temporal agreement of the ASAR GM soil moisture time series data, the statistical measures correlation, bias and standard deviation (see Chapter 5.2.4.) have been calculated for the following combinations of the validation data sets:

- (1) ERS scatterometer derived surface soil moisture at 50 km spatial resolution and *in-situ* soil moisture
- (2) ASAR GM derived surface soil moisture resampled to 3 km spatial resolution and *in-situ* soil moisture
- (3) ASAR GM derived surface soil moisture resampled to 50 km spatial resolution and *in-situ* soil moisture
- (4) ERS scatterometer derived surface soil moisture at 50 km spatial resolution and ASAR GM derived surface soil moisture resampled to 3 km spatial resolution
- (5) ERS scatterometer derived surface soil moisture at 50 km spatial resolution and ASAR GM derived surface soil moisture resampled to 50 km spatial resolution

An introductory remark on the apparent differences in the spatial scale between the *in-situ* point measurements from the Oklahoma Mesonet typically representing an areas of up to 100 m<sup>2</sup>, ASAR GM derived surface soil moisture integrated over a 3 km x 3 km region and ERS scatterometer derived surface soil moisture for an area of 50 km x 50 km is required. It seems to be not very meaningful to compare data acquired at these different spatial scales, but it is nevertheless possible. Temporal patterns of soil moisture and the relation between large scale and small scale components of spatial soil moisture patterns (see chapter 2.3.) allows to relate *in-situ* point measurements to areal estimates of soil moisture and vice versa. Observations of *in-situ* soil moisture measurements showed, that spatial soil moisture patterns are similar over different spatial scales and tend to persist in time. Consequently, point time-series *in-situ* soil moisture measurements are often highly correlated with the mean soil moisture content over an area, e.g. a catchment. This observation has been picked up by the temporal stability concept, introduced by Vauchaud et al. (1985), which allows the identification of an area representative *in-situ* measurement station, that shows a similar absolute value and a comparable temporal evolution of *in-situ* soil moisture as the area averaged

values. This one station allows conclusions on the overall soil moisture conditions in a specific area and helps to simplify planning of *in-situ* soil moisture measurement networks. This concept has been inverted and adapted for ASAR Wide Swath Mode data by Wagner et al. (2008) to estimate local scale soil moisture from areal remotely sensed soil moisture estimates.

Time-series plots showing the temporal evolution of the ASAR GM and ERS scatterometer derived soil moisture in comparison to *in-situ* soil moisture, which were generated for the 75 Oklahoma Mesonet measurement stations (see Fig. A.1 - A.75 in the Appendix), give a first visual impression of the performance of the ASAR GM change detection backscatter model and its ability to map temporal soil moisture patterns. As soil moisture is highly variable in the temporal domain, only ERS and ASAR sensor measurements have been taken into account, which were acquired within a +/- 2 hours time frame. An exemplary plot is given in Figure 48 for the station "LAHO". The lower part of the figure (Fig. 42b) shows the concurrent FWI values representing the *in-situ* soil moisture measurements of the Oklahoma Mesonet. From the plot, it can be seen that the temporal evolution of the two remotely sensed soil moisture datasets agree reasonably well with the *in-situ* soil moisture measurements, even though the transitions from dry to wet are in general more pronounced in the FWI data. A similar behaviour can be observed for other stations too.

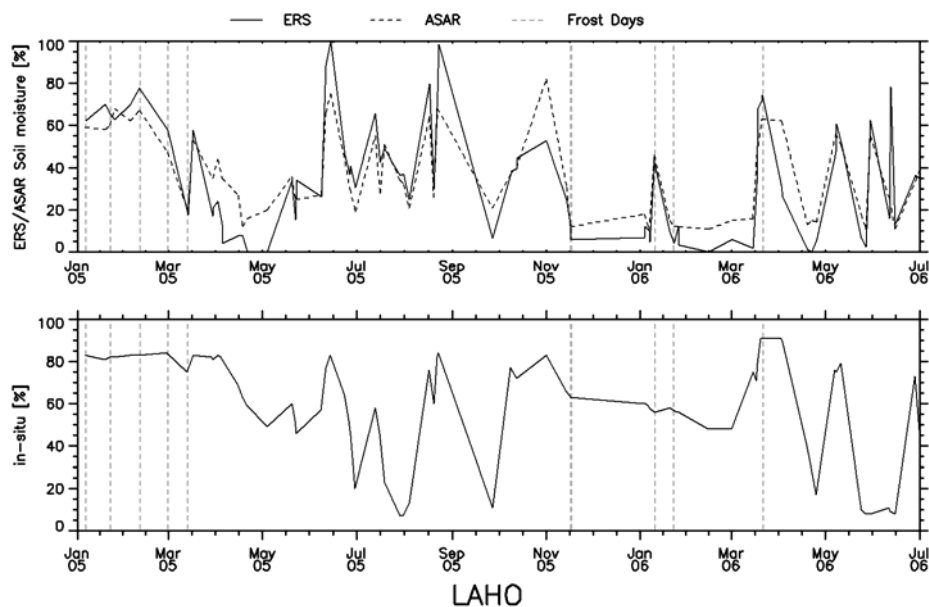


**Figure 48:** Soil moisture time series from ASAR GM (solid line) and ERS scatterometer (dashed line) (top) and in-situ measurements (bottom) at the MESONET station LAHO for the period January 2005 to July 2006.

To characterize the temporal agreement of the remotely sensed ASAR GM surface soil moisture data with the validation data sets, the statistical measures correlation, bias and standard deviation have been calculated for all five data combinations and for each of the 75 Oklahoma Mesonet stations. Tables with all results of the comparisons can be found in the appendix B in Table B.2 to B.16. For a comparative presentation of the validation results, again boxplots are used. For each pair of validation data, they show a summary of the smallest value of the statistic, lower quartile Q1, the median Q2, the upper quartile Q3 and the largest value of the statistic.

The boxplot in Figure 49 gives an overview of the results of the correlation analysis for the five data combinations. The correlation found for the comparison of the remotely sensed soil moisture data of the ERS and the ASAR sensor and the *in-situ* measurements show results which were expected from other previous studies, which compared *in-situ* soil moisture and coarse resolution remotely sensed soil moisture products (Crow & Zhan 2007; Wagner et al. 2007b; Owe et al. 2008). Apart from the absolute correlation results, the correlation results calculated for the ERS - *in-situ* data combination and the two ASAR – *in-situ* data combinations shows the performance of the ASAR sensor operated in GM mode compared to the ERS scatterometer. The results of the correlation between the  $m_{s-ERS}$  at 50 km and the *in-situ* soil moisture are very similar to the results of the correlation between the  $m_{s-ASAR}$  at 50 km and the *in-situ* soil moisture. A slightly lower correlation was calculated for the comparison of the  $m_{s-ASAR}$  at 3 km and the *in-situ* soil moisture data, although the scale difference between the 3 km spatial resolution of the ASAR data and the *in-situ* measurement data is much smaller than for the ERS data at a spatial resolution of 50 km. From the error analysis it is concluded (see Chapter 6.3.) that the main reason for this can be found in the higher noise level of the ASAR GM data. In the case of the ASAR data, the noise level was reduced with the reduction of the spatial resolution from the original 1 km to the 50 km spatial resolution and therefore the results of the correlation analysis of the  $m_{s-ERS}$  at 50 km and  $m_{s-ASAR}$  at 50 km are very similar. Additionally the neglect of seasonal vegetation cover effects in the change detection backscatter model also contributes to the weaker performance of  $m_{s-ASAR}$  at 3 km when compared to the two soil moisture products at coarser spatial resolutions. On the other hand, the performance of the  $m_{s-ASAR}$  at 3 km is in an acceptable range and the differences to the two remotely sensed soil moisture products at 50 km spatial resolution

are within suitable limits. As the suitability of ERS scatterometer for surface soil moisture data retrieval has been proven in a number of studies, the comparison of the remotely sensed ERS and ASAR soil moisture products reveals information of the usability of the ASAR GM data for surface soil moisture retrieval. The comparison of  $m_s$ -ASAR at 50 km and  $m_s$ -ERS gives high correlations. The considerably lower correlation between  $m_s$ -ASAR at 3 km and  $m_s$ -ERS can also be addressed to the aforementioned higher noise level of the ASAR data. However, the good correlations between the surface soil moisture products from the two sensors and especially the high correlation between  $m_s$ -ASAR and  $m_s$ -ERS at 50 km shows, that the ASAR GM data contain relevant information for surface soil moisture retrieval.

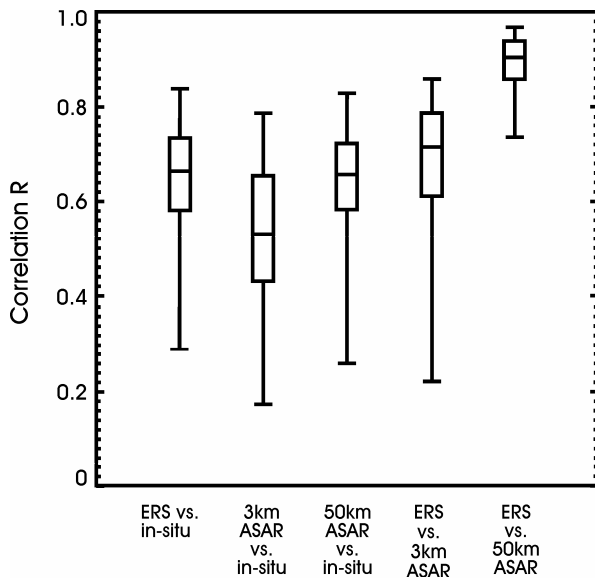


**Figure 49:** Correlation  $R$  between remotely sensed soil moisture derived from ERS scatterometer and ASAR GM backscatter measurements for 75 Oklahoma Mesonet stations:  $m_s$ -ERS vs. in-situ,  $m_s$ -ASAR at 3 km vs. in-situ,  $m_s$ -ASAR at 50 km vs. in-situ,  $m_s$ -ERS at 50 km vs.  $m_s$ -ASAR at 3 km and  $m_s$ -ERS at 50 km vs.  $m_s$ -ASAR at 50 km

In Figure 50 the results for the calculation of the BIAS is shown. The most apparent feature in the boxplot is the small BIAS calculated for the cross-comparison of the two remotely sensed relative surface soil moisture data sets. In both cases, the combination of  $m_s$ -ERS at 50 km and  $m_s$ -ASAR at 3 km and  $m_s$ -ERS at 50 km and  $m_s$ -ASAR at 50 km, the median of BIAS is positive and close to zero. That means that  $m_s$  derived from the ASAR GM data is slightly higher than the  $m_s$  values derived from the ERS scatterometer data. Compared to this, there is a considerable BIAS for the comparisons of  $m_s$  derived from ERS scatterometer and ASAR GM data. In the three cases, the  $m_s$

values consistently underestimated the *in-situ* measurements. These results are similar to the results of other studies where also large differences between the absolute levels of soil moisture data sets derived either from remote sensing or models.

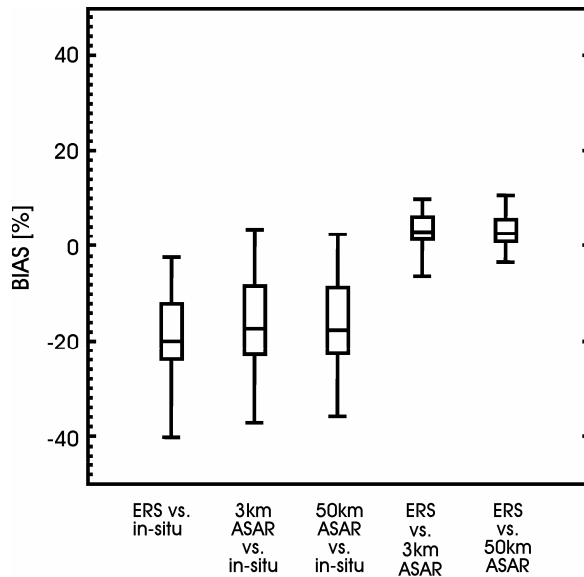


**Figure 50:** BIAS between remotely sensed soil moisture derived from ERS scatterometer and ASAR GM backscatter measurements for 75 Oklahoma Mesonet stations:  $m_{s\text{-}ERS}$  vs.  $m_{s\text{-}in-situ}$ ,  $m_{s\text{-}ASAR}$  at 3 km vs.  $m_{s\text{-}in-situ}$ ,  $m_{s\text{-}ASAR}$  at 50 km vs.  $m_{s\text{-}in-situ}$ ,  $m_{s\text{-}ERS}$  at 50 km vs.  $m_{s\text{-}ASAR}$  at 3 km and  $m_{s\text{-}ERS}$  at 50 km vs.  $m_{s\text{-}ASAR}$  at 50 km

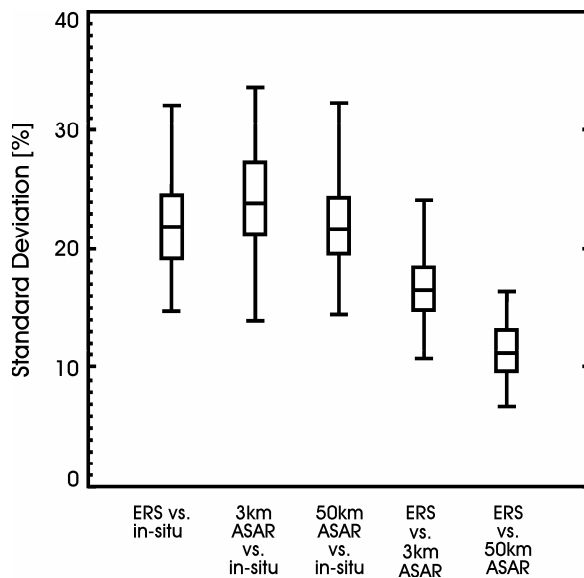


**Figure 51:** Standard deviation between remotely sensed soil moisture derived from ERS scatterometer and ASAR GM backscatter measurements for 75 Oklahoma Mesonet stations:  $m_{s\text{-}ERS}$  vs.  $m_{s\text{-}in-situ}$ ,  $m_{s\text{-}ASAR}$  at 3 km vs.  $m_{s\text{-}in-situ}$ ,  $m_{s\text{-}ASAR}$  at 50 km vs.  $m_{s\text{-}in-situ}$ ,  $m_{s\text{-}ERS}$  at 50 km vs.  $m_{s\text{-}ASAR}$  at 3 km and  $m_{s\text{-}ERS}$  at 50 km vs.  $m_{s\text{-}ASAR}$  at 50 km

The standard deviations derived from the comparison of the five different validation data combinations are given in Figure 51. The standard deviations obtained for the five validation data combinations reflect the results of the correlation analysis but mirrored. The smallest standard deviations were found for the  $m_{s\text{-}ERS}$  at 50 km vs.  $m_{s\text{-}ASAR}$  at 50 km combination which showed the best correlations and the highest standard deviation for the comparison of  $m_{s\text{-}ASAR}$  at 3 km with the *in-situ* soil moisture measurements for which the lowest correlation have been calculated.

A comparison of the correlation  $R$  between  $m_{s\text{-}ASAR}$  at 3 km and the *in-situ* soil moisture measurements with land cover patterns shows that there exists no distinct relation in the spatial distribution of stations with certain correlation values and specific land cover classes (Figure 52). There is no spatial clustering of either high or low  $R$  values observable. From the grassland dominated western part of Oklahoma to the forest covered south-eastern part of the state, either high or medium or low correlations can be observed. Thus, the correlation  $R$  at neighbouring stations can vary substantially. The same applies to the spatial distribution of the BIAS (Figure 53) and standard deviation values (Figure 54) derived from the comparison of  $m_{s\text{-}ASAR}$  at 3 km with *in-situ* soil moisture measurements at the Mesonet stations. Also in this case, the spatial distribution of the statistics does not follow a systematic scheme.

Based on this observation it can be said, that the change detection approach used for soil moisture retrieval works well for different land cover classes. The model parameters dry reference, slope and sensitivity can account for the spatial distribution of different land cover features and vegetation patterns. This is a remarkable fact, as natural grasslands and cultivated farm lands differ in their vegetation phenology. This can be seen as a proof that neglecting seasonal vegetation effects in the soil moisture retrieval procedure does not cause significant retrieval errors and are a valid simplification.

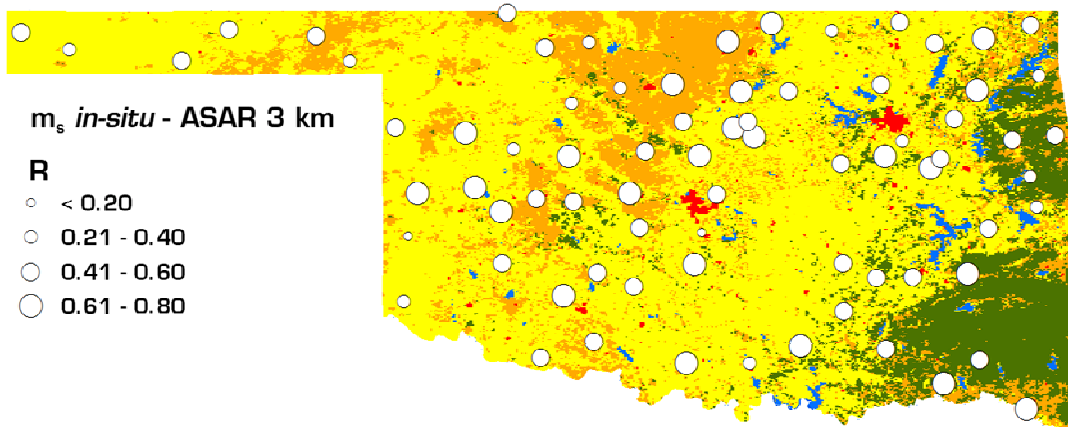


**Figure 52:** Spatial distribution of correlation  $R$  between ms-ASAR at 3 km and in-situ soil moisture for 75 Oklahoma Mesonet stations

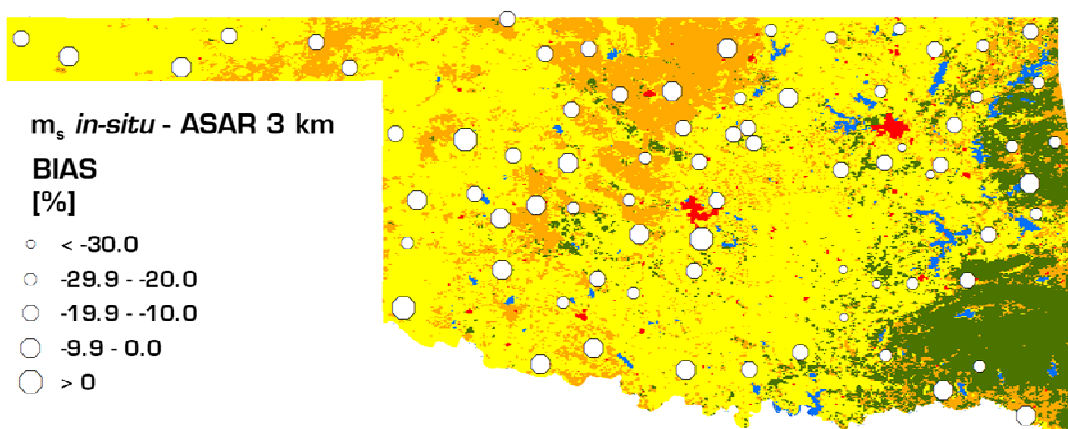


**Figure 53:** Spatial distribution of BIAS between ms-ASAR at 3 km and in-situ soil moisture for 75 Oklahoma Mesonet stations

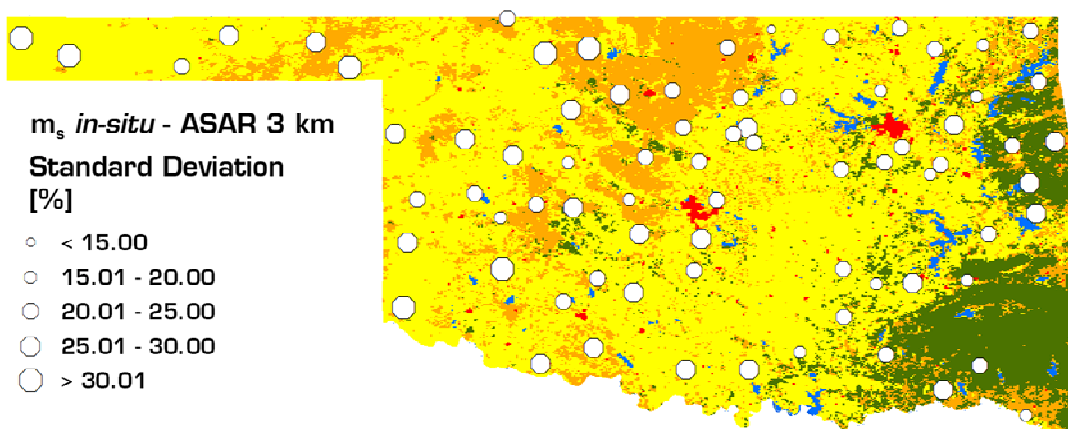


**Figure 54:** Spatial distribution of Standard Deviation between ms-ASAR at 3 km and in-situ soil moisture for 75 Oklahoma Mesonet stations

## 6.4. Retrieval Error

According to the principles of Gaussian error propagation, the overall retrieval error  $\Delta m_s$  is estimated as the sum of the partial derivates of the parameters of the inverted change detection backscatter model Eq. 5.46 for two scenarios (see Table 6). The retrieval error for the surface soil moisture estimates based on the theoretical considerations made on the error sources has been calculated for two scenarios: for completely dry and for completely wet surface soil moisture conditions. The values for the model parameters used within this calculation are listed in Table 6.

Parameter	Scenario 1	Scenario 2
$\Delta \sigma^0$	12 dB	12 dB
$\Delta \sigma^0$	10%	10%
$\Delta \sigma^0$	10%	10%
$\Delta \beta$	10%	10%
$m_s$	0%	100%

*Table 6: Settings for calculating model uncertainty*

The retrieval error has been calculated for every grid point of the ASAR GM radar backscatter time series data base. A map showing the spatial distribution of the retrieval error over Oklahoma is shown in Figure 55.

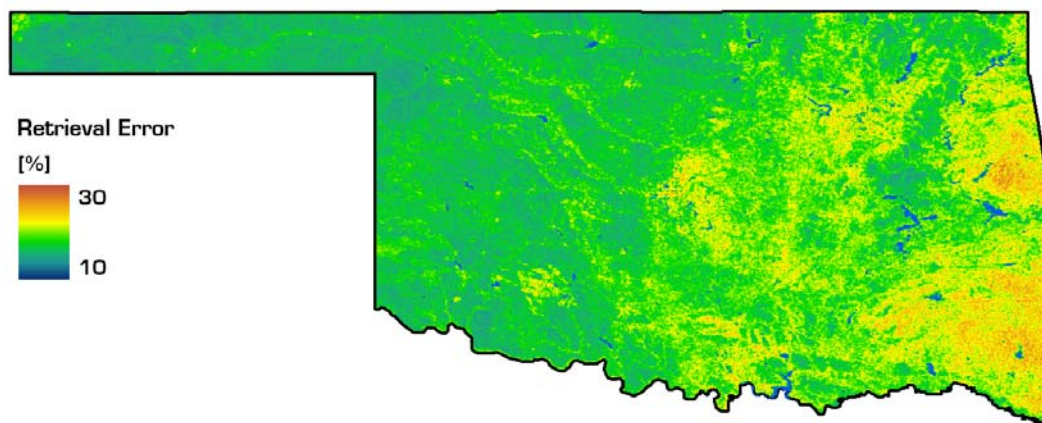


*Figure 55: Soil moisture retrieval error  $\Delta m_s$  [%]*

The map of the retrieval error  $\Delta m_s$ , mirrors the spatial patterns found for the slope parameter  $\beta$  and the sensitivity S. In general, a high retrieval error can be observed over Oklahoma. The eastern part of Oklahoma covered by denser vegetation is characterized by higher retrieval errors of >20% than the western part of the state with values around 15%, where grasslands and agricultural lands prevail.

When analyzing Eq. 5.46, it can be said, that changes in the model parameters slope  $\beta$ , dry and wet references  $\sigma^0_{dry}$  and  $\sigma^0_{wet}$ , even when the setting to rather high values, cause only little change in the retrieval error for a given sensitivity S at small ( $\theta = 20^\circ$ ) or large ( $\theta = 40^\circ$ ) incidence angles and at completely dry ( $m_s = 0$ ) or saturated ( $m_s = 1$ ) surface soil moisture conditions. In any case, the noise  $\Delta\sigma^0$  in the radar backscatter data has the largest influence on the retrieval error. Therefore the estimation of the retrieval error can also be reduced to a simpler formulation:

$$\Delta m_s = \frac{\Delta\sigma^0}{S} \cdot 100\% \quad (6.1)$$

Now, the retrieval error  $\Delta m_s$  can be regarded as function of the sensitivity S for a given backscatter noise level  $\Delta\sigma^0$ .

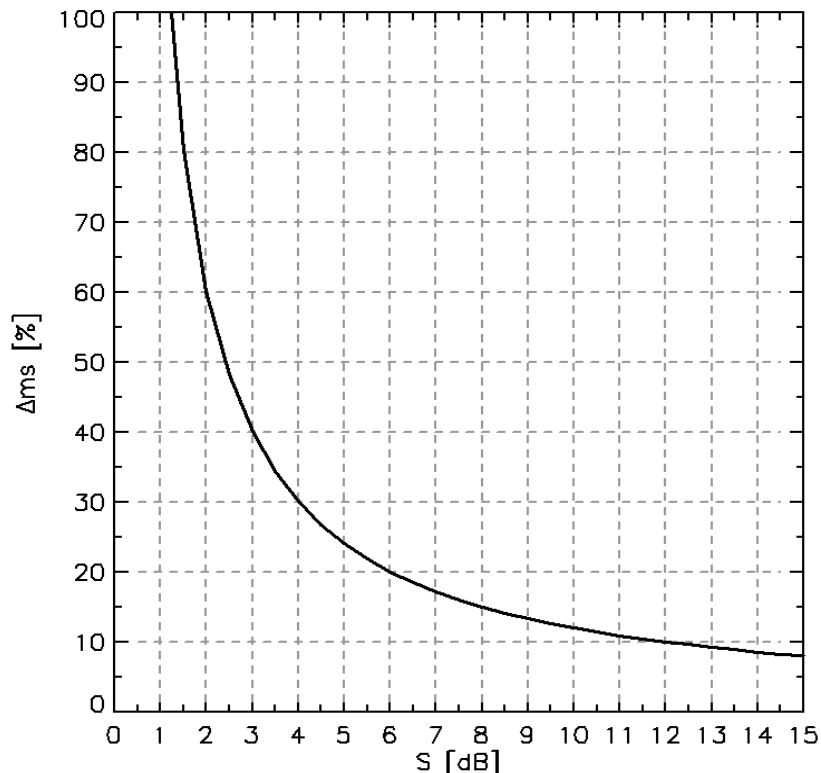


**Figure 56:** Retrieval error  $\Delta m_s$  as a function of the sensitivity S for given noise  $\Delta\sigma^0$  in radar backscatter

Even though the slope parameter  $\beta$  is not contained in Eq. 6.1, it is still accounted for, as areas covered by denser vegetation typically are characterized by high negative slope values and low sensitivities (see also Figure 39 & Figure 40). Therefore a low sensitivity as observed for densely vegetated areas will lead to a high retrieval error. From Figure 56 it can be seen, that a sensitivity  $S \geq 6$  dB is required to reach a relative error  $\Delta ms \leq 20\%$ . For comparison,  $\Delta\sigma^0$  of the ERS scatterometer is mostly in the range from about 0.15 – 0.3 dB depending on land cover and azimuthal effects, which means that a much lower sensitivity is required in order to reach a comparable accuracy of the soil moisture estimates. This dependency on the noise level in the backscatter data is illustrated in Figure 57, shows the relation between sensitivity and retrieval error for noise levels from 0 dB to 2 dB.

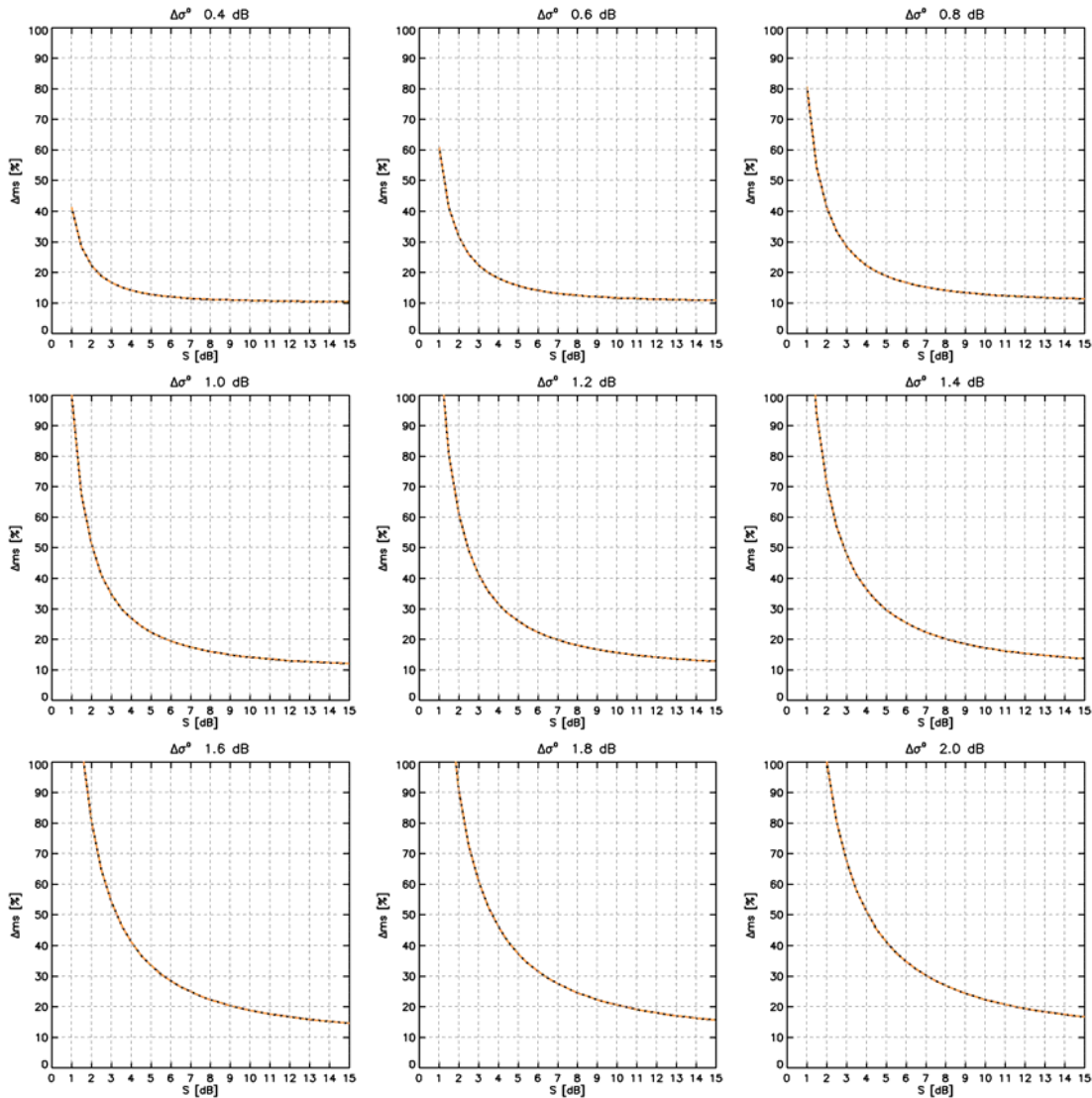


Figure 57: Model uncertainty  $\Delta ms$  in relation to the sensitivity  $S$  for different values of  $\Delta\sigma^0$

When comparing the results of the retrieval error estimation with the standard deviations calculated for the  $m_{s\text{-ASAR}}$  at 3 km-in-situ soil moisture combination, it must be recognized that the estimated retrieval error slightly underestimates the real conditions. This can be addressed to the scaling problem, which needs to be taken into account, when comparing areal estimates of surface soil moisture at 3 km and 50 km with the *in-situ* soil moisture point measurements. Furthermore, errors of the *in-situ* measurements caused by errors related to the measurement principle and the soil moisture sensors used as well as errors connected to the conversion of absolute soil moisture to unitless relative FWI soil moisture values also contribute to the real error. If soil hydraulic properties would be known, the real error based on the comparison of the remotely sensed  $m_{s\text{-ASAR}}$  at 3 km and the *in-situ* soil moisture measurements could be calculated for every grid point of the remotely sensed time series data base and mapped for the Oklahoma test site.

The absolute error of the soil moisture estimates could theoretically be calculated, if the true value of the surface soil moisture is known. Unfortunately this is not the case as the soil moisture measurements also contain systematic and random errors which can not be quantified. Therefore a calculation of the absolute error can be performed when assuming that the two datasets, the estimated relative surface soil moisture and the *in-situ* soil moisture measurements are characterized by comparable absolute errors. Based on this assumption, the standard error ( $SE$ ) can be estimated from the standard deviation ( $SD$ ) between the two data sets according to Eq. 5.28 with  $SE=SD/\sqrt{n}$  with  $n=2$ . The observed standard deviation for the comparison of  $m_{s\text{-ASAR}}$  at 3 km and the *in-situ* soil moisture varies between approx. 15% and 35%, which corresponds to a standard error of  $\approx 10.6\%$  to  $\approx 24.7\%$ . Depending on soil texture and porosity, a soil can contain different amounts of water. A loamy soil for example may contain a maximum of approx.  $0.4 \text{ m}^3 \cdot \text{m}^{-3}$  of water. Using the standard errors found for the comparison of  $m_{s\text{-ASAR}}$  at 3 km and the *in-situ* soil moisture, the real error of the remotely sensed soil moisture in units of volumetric soil moisture can be derived. The real error of the remotely sensed soil moisture in case for the loamy soil is in the range of 10.6% of  $0.04 \text{ m}^3 \cdot \text{m}^{-3}$  with  $\approx 0.04 \text{ m}^3 \cdot \text{m}^{-3}$  to 24.7% of  $0.4 \text{ m}^3 \cdot \text{m}^{-3}$  with  $\approx 0.09 \text{ m}^3 \cdot \text{m}^{-3}$ . This is in good agreement with previous studies, where similar values absolute errors were found (Pellarin et al. 2006; Crow & Zhan 2007; de Jeu et al. 2008).

# **Chapter 7**

## **Conclusions and Outlook**

---

### **7.1. Conclusions**

---

Soil moisture has been identified as an important variable in the Earth's hydrologic, energy and carbon cycle. Routine measurements of soil moisture at continental to global scales are not feasible. Remote sensing offers the possibility of regular acquisition of areal data. Active space-borne sensors operating in the microwave region of the electromagnetic spectrum are regarded as optimum tools for soil moisture monitoring. Recognizing the non-availability of operational soil moisture retrieval algorithms for spatial high resolution SAR data and motivated by the achievements made with a soil moisture change detection algorithm for ERS-1/2 scatterometer data, a change detection algorithm was developed, implemented and validated within this thesis. The work was based on a comprehensive archive of ASAR GM data. An automatic processing chain has been set up for geometric correction, radiometric calibration, incidence angle normalization and resampling from irregular image format to regular gridded time series format. The soil moisture change detection algorithm originally developed for ERS-1/2 scatterometer data was adapted for use with ASAR GM data. The model parameters dry reference, slope and sensitivity have been estimated and relative surface soil moisture data were generated for the Oklahoma test site. The results were validated using *in-situ* soil moisture data from the Oklahoma Mesonet and ERS-1/2 scatterometer derived relative surface soil moisture. Good agreement between ASAR GM relative surface soil moisture and both *in-situ* soil moisture measurements and ERS-1/2 scatterometer derived soil moisture was observed. The direct comparison of the results shows that the surface soil moisture extracted from ERS-1/2 scatterometer data performs slightly better than the data derived from ASAR GM. As the main source of error, the noise of the ASAR GM data with a value of 1.2 dB has been identified. Due to the ScanSAR imaging principle, the radiometric accuracy of the ASAR GM data with 1.2 dB is low

when compared to scatterometers like the ERS-1/2 or the MetOp ASCAT, which deliver data with a radiometric resolution of at least 0.3 dB. Therefore spatial averaging is recommended to account for the noise level in the ASAR GM data to some degree. Even so, the ASAR GM data offer surface soil moisture data with much more details than the ERS-1/2 scatterometer data and still keeping the capability of the scatterometer data to map temporal surface soil moisture trends.

The validation of the remotely sensed soil moisture extracted from ASAR GM data has proven that neglecting seasonal vegetation cover effects can be regarded as a valid assumption. The three model parameters are able to describe the spatial land cover and vegetation patterns. Nevertheless, the observed and quantified retrieval errors can be addressed - besides the noise level of the ASAR GM data as main error source - to the simplifying assumption on the influence of vegetation. With an increasing spatial coverage it can be possible to further reduce the retrieval error by incorporating a description of seasonal vegetation cover effects in the backscatter model by introducing a seasonally varying slope parameter  $\beta$ , which better accounts for the influences of the vegetation phenology on radar backscatter.

This leads directly to a disadvantage of the ASAR sensor. Due to the multi-purpose character of the Envisat mission, the ASAR modes were designed as exclusive modes. The sensor can be operated in conventional strip-map mode or in one of the two ScanSAR modes at one time. Even though the ASAR GM was laid out as so called background mission with a potential daily coverage of 35%, only an irregular temporal coverage was achieved for ASAR GM data, as the imaging modes of the ASAR sensor have been designed as exclusive modes. For some regions like the central and western part of Europe, only a very small number of ASAR GM data have been acquired, because a large number of data orders for acquisitions in image mode or WS needed to be satisfied. Therefore it would be beneficial for soil moisture retrieval using change detection approaches that future missions, which are intended to yield data from regional to global scales, solely focus on ScanSAR data. Such time series data sets would perfectly fill in the gap between temporal high resolution scatterometers and spatial high resolution SAR's.

The results as presented in this doctoral thesis show that ASAR GM data can be used for an operational soil moisture monitoring system. For operational applications of ASAR GM data, improvements of the data dissemination procedures are recommended.

Operational data processing and product generation requires easy and fast access to the data, especially if a near-real-time service is aspired. Therefore the EO data should be made accessible via rolling archives without tedious data ordering tools which require manual user input.

In the present study, the influence of the vegetation has been neglected. As it has turned out, this assumption worked well for the selected test site. It must be admitted that this does not guarantee from itself the easy transferability to other test sites in other vegetation zones with different climatologic conditions. To test the validity and the applicability of the proposed soil moisture retrieval approach, further studies are necessary. First results obtained for the southern African continent suggest that this is possible (Bartsch et al. 2006; Wagner et al. 2007c). Developing and validating soil moisture retrieval algorithms essentially require reference data. The main problem here is the non-availability of long-term *in-situ* soil moisture measurement networks for different climate and vegetation zones. Existing networks are too much dependent on the commitment of single persons/institutions and/or funding through national or international sources. From a researchers point of view it would be highly appreciated, if space agencies would actively support the setting up and operation of validation in different Earth regions.

According to the initial research questions raised in Chapter 1.2. it can be concluded that the ASAR GM data are potentially suited for use in pre-operational soil moisture monitoring applications. The big advantage of the ASAR GM derived relative surface soil moisture data is their much higher level of detail when compared to the ERS-1/2 scatterometer derived surface soil moisture maps. This allows mapping surface soil moisture patterns, which are not visible in scatterometer derived soil moisture maps – simply because of the substantial difference in spatial resolution of the two sensor concepts. The disadvantage of the ASAR GM data is their relatively high noise level, which has been identified as the main source of error. The reason for this can be found in the design of the ASAR GM mode measurement principle which is a compromise between temporal resolution and radiometric accuracy. Degrading the ASAR GM data from its original spatial resolution of 1 km to 3 km can compensate this deficiency to some degree. Due to technological limitations connected to the ScanSAR technique, the temporal resolution of ScanSAR data as offered by the ASAR sensor will never be comparable to the temporal resolution of scatterometers.

## 7.2. Outlook

---

The importance of soil moisture as a land surface parameter that links the global energy, water and carbon cycle has been emphasised by the rising awareness of climate change. The fourth assessment report of the IPCC stressed the value of soil moisture as an land surface parameter required for climate and carbon flux models and their evaluation (IPCC 2007). The Global Climate Observing System (GCOS), an institution founded in 1992 to support the World Climate Programme, the Intergovernmental Panel on Climate Change (IPCC) and the United Nations Framework Convention on Climate Change (UNFCCC), lists soil moisture as an emerging climate variable. In recent a report of the Terrestrial Observation Panel for Climate to the steering committee of GCOS, it was endorsed that soil moisture should be added to the list of the essential climate variables (ECV's), as it is important for the initialization of climate models and the assessment of climate feedbacks (GCOS 2008b). The steering committee supports the development of soil moisture as an ECV and encourages space agencies to consider the implementation of soil moisture observations from space in their activities (GCOS 2008a). The necessity of incorporating soil moisture in future Earth observation missions is underlined by a recent technical paper edited by the IPCC, where it has been stated that '*many hydrometeorological variables e.g., streamflow, soil moisture and actual evapotranspiration, are inadequately measured*' (IPCC 2008).

It is generally agreed upon that *in-situ* soil moisture measurements at continental to global scales is not feasible due to organisational and financial reasons. The exploitation of the unique sensitivity of radiation from the microwave region of the electromagnetic spectrum to surface soil moisture content makes microwave remote sensing methods to the tool of choice. Within the microwave remote sensing community, soil moisture retrieval has been a research issue for the last 30 years. But still, this topic is and will be an objective of Earth observation missions. An overview of current and planned missions related to soil moisture is given in Figure 58. Even this list of 22 missions in this overview is not complete, e.g. the MetOp satellite series with the current MetOp-1 satellite and its ASCAT sensor is missing.

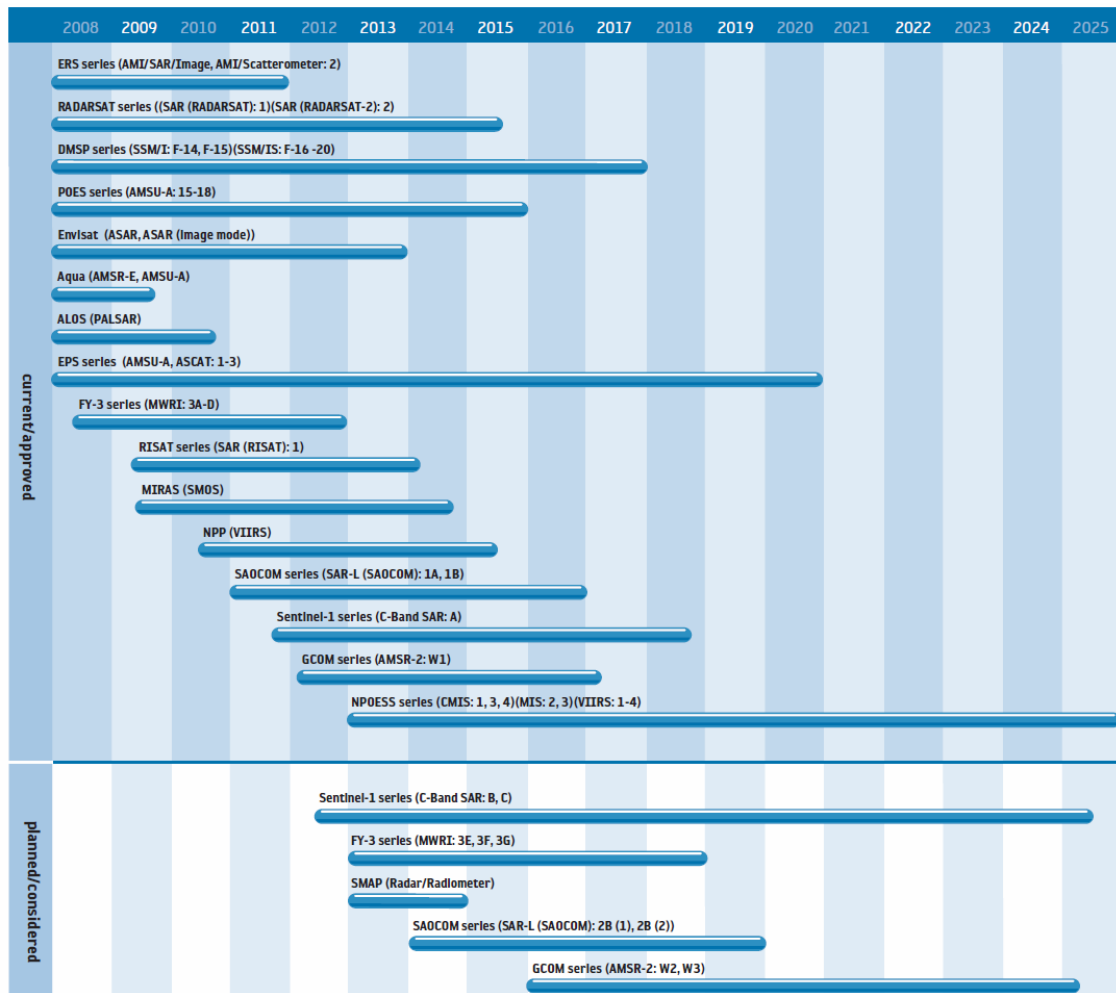


Figure 58: Selected current and planned Earth observation missions related to soil moisture (ESA 2008)

The European Space Agency started activities in active radar remote sensing with the launch of the ERS-1 satellite carrying the active microwave instrument (AMI) in 1991. Since then data are acquired on a global level at various spatial and temporal scales. In 2009, the Envisat satellite as the follow-up mission of ERS-2 will enter its seventh year in orbit. The Envisat mission will be replaced by the Sentinel program with the launch of the first satellite Sentinel-1 in 2011. Like its predecessors ERS-1/2 and Envisat, it will carry a C-band SAR sensor, which will offer four acquisition modes: 1) an conventional strip-map mode with a swath width of 80 km and a spatial resolution of 5 m x 5 m, 2) an interferometric wide swath mode with a swath width of 250 km and a spatial resolution of 5 m x 20 m, 3) an extra wide swath mode covering a swath of 400 km at a spatial resolution of 25 m x 100 m and 4) a low data rate wave mode. With the Sentinel program ESA will guarantee the continuity of their time series data bases of global radar backscatter measurements.

Only very recently, soil moisture retrieval reached a level of maturity which allows operational applications. On 18<sup>th</sup> December 2008, the European Organisation for the Exploitation of Meteorological Satellites (EUMETSAT) announced that the ASCAT soil moisture service was declared operational (<http://www.eumetsat.int/Home/Main/Media/Features/708786>). The ASCAT sensor is a C-band scatterometer operated by EUMETSAT, which supplements ERS-1/2 C-band scatterometer data. The sensor is carried by the first out of three satellite of the MetOp program, which is intended to deliver data for the next fifteen years. The ASCAT sensor offers C-band backscatter time series data at an improved spatial temporal resolution. The coexistence of scatterometers with high temporal resolutions and ScanSAR systems with much higher spatial resolutions gives the opportunity to combine the advantages of both sensor designs. Great potential lays in the combined exploitation of temporal high resolution and spatial high resolution microwave remote sensing data using downscaling approaches.

## **REFERENCES**

---

---

- Adam, D. (2002): Gravity measurement: Amazing grace. *Nature* 416: 10-11.
- Altese, E., Bolognani, O., Mancini, M., Troch, P.A. (1996): Retrieving soil moisture over bare soil from ERS-1 synthetic aperture radar data: sensitivity analysis based on a theoretical surface scattering model and field data. *Water Resources Research* 32(3): 653-661.
- Anderson, J., Hardy, E., Roach, J., Witmer, R. (1976). A land use and land cover classification system for use with remote sensor data.
- Arnell, N. W. (1999): Climate change and global water resources. *Global Environmental Change* 9: S31-S49.
- Arya, L. M., Paris, J. F. (1981): A physicoempirical model to predict the soil moisture characteristic from particle-size distribution and bulk density data. *Soil Sci. Soc. Am. J.* 45: 1023-1030.
- Attema, E., Desnos, Y.-L., Duchossois, G. (2000): Synthetic Aperture Radar in Europe: ERS, Envisat, and Beyond. *Johns Hopkins APL Technical Digest* 21(1): 155-161.
- Baghdadi, N., Zribi, M. (2006): Evaluation of radar backscatter models IEM, OH and DUBOIS using experimental observations. *Int. J. Rem. Sens.* 27(18-20): 3831-3852.
- Bamler, R., Eineder, M. (1996): ScanSAR Processing Using Standard High Precision SAR Algorithms. *IEEE Trans. Geosci. Rem. Sens.* 34(1): 212-218.
- Barsch, H., Billwitz, K., Bork, H.-R. (2000): Arbeitsmethoden in Phsiogeographie und Geoökologie. Gotha, Klett-Perthes.
- Bartalis, Z., Wagner, W., Naeimi, V., Hasenauer, S., Scipal, K., Bonekamp, H., Figa, J., Anderson, C (2007): Initial soil moisture retrievals from the METOP-A Advanced Scatterometer (ASCAT). *Geophysical Research Letters* 34: L20401.
- Bartalis, Z., Scipal, K., Wagner, W. (2006): Azimuthal Anisotropy of Scatterometer Measurements Over Land. *IEEE Trans. Geosci. Rem. Sens.* 44(8): 2083-2092.
- Bartsch, A., Scipal, K., Wolski, P., Pathe, C., Sabel, D., Wagner, W. (2006): Microwave remote sensing of hydrology in southern Africa. 2nd Göttingen GIS & Remote Sensing Days: Global Change Issues in Developing and Emerging Countries, 4-6 October 2006

- Basara, J. B., Crawford, T. M. (2000): Improved Installation Procedures for Deep-Layer Soil Moisture Measurements. *Journal of Atmospheric and Oceanic Technology* 17(6): 879-884.
- Bastiaanssen, W. G. M. (1999): The use of remote sensing to improve irrigation water management in developing countries. 18th EARSeL Symposium on Operational Remote Sensing for Sustainable Development, Enschede, The Netherlands, 11-14 May 1998
- Baup, F., Mougin, E., de Rosnay, P., Timouk, F., Chêneré, I. (2007): Surface soil moisture estimation over the AMMA Sahelian site in Mali using ENVISAT/ASAR data. *Rem. Sens. Environ.* 109: 473-481.
- Beaudoin, A., Stussi, N., Troufleau, D., Desbois, N., Piet, L., Deshayes, M. (1995): On the use of ERS-1 SAR data over hilly terrain: Necessity of radiometric corrections for thematic applications. IGARSS'95.2179-2182
- Berger, M., Kerr, Y., Font, J., Wigneron, J.-P., Calvet, J.-C., Saleh, K., Lopez-Baeza, E., Simmonds, L., Ferrazzoli, P., van den Hruk, B., Waldteufel, P., Petitcolin, F., van de Griend, A., Attema, E., Rast, M. (2003): Measuring the Moisture in the Earth's Soil - Advancing the Science with ESA's SMOS Mission. *ESA bulletin* 115: 40-45.
- Bindlish, R., Barros, A. P. (2000): Multifrequency Soil Moisture Inversion from SAR Measurements with the Use of IEM. *Rem. Sens. Environ.* 71: 67-88.
- Bindlish, R., Barros, A. P. (2001): Parameterization of vegetation backscatter in radar-based, soil moisture estimation. *Rem. Sens. Environ.* 76: 130-137.
- Bindlish, R., Jackson, T.J., Wood, E., Gao, H., Starks, P., Bosch, D., Lakshmi, V. (2003): Soil moisture estimates from TRMM Microwave Imager observations over the Southern United States. *Rem. Sens. Environ.* 85: 507-515.
- Birdsall, S.S., Florin, J. (1992): Regional Landscapes of the United States and Canada., Wiley & Sons.
- Blöschl, G., Sivapalan, M. (1995): Scale issues in hydrological modelling - a review. *Hydrological Processes* 9: 251-290.
- Brady, N. C., Weil, R. R. (1996): The Nature and Properties of Soils. Upper Saddle River, New Jersey, Prentice-Hall, Inc.
- Brisco, B., Brown, R. J. (1998): Agricultural Applications With Radar. *Principles and Applications of Imaging Radar*. F. M. Henderson and A. J. Lewis. New York, Wiley & Sons.

- Brock, F. V., Crawford, K. C., Elliott, R. L., Cuperus, G. W., Stadler, S., Johnson, H. L., Eilts, M. D. (1995): The Oklahoma Mesonet: A Technical Overview. *Journal of Atmospheric and Oceanic Technology* 12(1): 5-19.
- Brown, S. C. M., Quegan, S., Morrison, K., Bennett, J. C., Cookmartin, G. (2003): High-Resolution Measurements of Scattering in Wheat Canopies - Implications for Crop Parameter Retrieval. *IEEE Trans. Geosci. Rem. Sens.* 41(7): 1602-1610.
- Brown, S.C.M., Quegan, S., Morrison, K., Bennett, J. C., Cookmartin, G. (2003): High-Resolution Measurements of Scattering in Wheat Canopies - Implications for Crop Parameter Retrieval. *IEEE Transactions on Geoscience and Remote Sensing* 41(7): 1602-1610.
- Buttafuoco, G., Castrignanò, A., Busoni, E., Dimase, A. c. (2005): Studying the spatial structure evolution of soil water content using multivariate geostatistics. *Journal of Hydrology* 311: 202-218.
- Ceballos, A., Scipal, K., Wagner, W., Martinez-Fernandez, J. (2005): Validation of ERS scatterometer-derived soil moisture data in the central part of the Duero Basin, Spain. *Hydrological Processes* 19: 1549-1566.
- Chauhan, N. S., Miller, S., Ardanuy, P. (2003): Spaceborne soil moisture estimation at high resolution: a microwave-optical/IR synergistic approach. *Int. J. Rem. Sens.* 24(22): 4599-4622.
- Chi, T., Sarabandi, K. (2000): Electromagnetic Scattering from Short Branching Vegetation. *IEEE Trans. Geosci. Rem. Sens.* 38(2): 911-925.
- Commission for Environmental Cooperation (1997): Ecological Regions of North America: Towards a Common Perspective. Montreal, Quebec.
- Crapolicchio, R., Lecomte, P. (2005): The ERS-2 scatterometer mission: events and long-loop instrument and data performances-. ENVISAT & ERS Symposium, 6-10 September 2004, Salzburg, Austria.SP-572, CDROM
- Crow, W., Zhan, X. (2007): Continental-Scale Evaluation of Remotely Sensed Soil Moisture Products. *IEEE Geoscience and Remote Sensing Letters* 4(3): 451-455.
- Crowley, J. W., Mitrovica, J. X., Bailey, R. C., Tamisiea, M. E., Davis, J. L. (2007): Annual variations in water storage and precipitation in the Amazonas Basin. *J Geod* DOI 10.1007/ss00190-007-0153-1.
- Cumming, I., Guo, Y., Wong, F. (1997): A Comparison of Phase-Preserving Algorithms for Burst-Mode SAR Data Processing. *Proc. IGARSS'97*: 731-733.

Curlander, J. C., McDonough, R. N. (1991): Synthetic Aperture Radar. Systems and Signal Processing. New York, Chichester, Brisbane, Wiley.

Curran, P. J. (1985): Principles of Remote Sensing.

Curran, P. J. (2001): Remote sensing: Using the spatial domain. *Environment and Ecological Statistics* 8: 331-344.

D'Urso, G., Minacapilli, M. (2006): A semi-empirical approach for surface soil water content estimation from radar data without a-priori information on surface roughness. *Journal of Hydrology* 321: 297-310.

Daughtry, c. S. T., Ranson, K. J., Biehl, L. L. (1991): C-band backscattering from corn canopies. *Int. J. Rem. Sens.* 12(5): 1097-1109.

Davidson, M. W. J., Le Toan, T., Mattia, F., Satalino, G., Manninen, T., Borgeaud, M. (2000): On the Characterization of Agricultural Soil Roughness for Radar Remote Sensing Studies. *IEEE Trans. Geosci. Rem. Sens.* 38(2): 630-640.

de Jeu, R., Wagner, W., Holmes, T., Dolman, A. J., van de Giesen, N. C., Friesen, J. (2008): Global Soil Moisture Patterns Observed by Space Borne Microwave Radiometers and Scatterometers. *Surveys in Geophysics* DOI 10.1007/s10712-008-9044-0.

Desnos, Y.-L., Buck, C., Guijarro, J., Suchail, J.-L., Torres, R., Attema, E. (2000): ASAR - Envisat's Advanced Synthetic Aperture Radar. Building on ERS Achievements towards Future Watch Missions. *ESA bulletin* 102: 91-100.

Dobson, M. C., Ulaby, F. T. (1998): Mapping Soil Moisture Distribution With Imaging Radar. *Principles and Applications of Imaging Radar*. F. M. Henderson and A. J. Lewis. New York, Wiley & Sons.

Dobson, M. C., Ulaby, F. T., Pierce, L. E. (1995): Land-Cover Classification and Estimation of Terrain Attributes Using Synthetic Aperture Radar. *Rem. Sens. Environ.* 51: 199-214.

Douville, H., Chauvin, F. (2000): Relevance of soil moisture for seasonal climate predictions: a preliminary study. *Climate Dynamics* 16: 719-736.

Drusch, M., Wood, E., Gao, H., Thiele, A. (2004): Soil moisture retrieval during the Southern Great Plains Hydrologic Experiment 1999: a comparison between experimental remote sensing data and operational products. *Water Resources Research* 40(W02504): doi:10.1029/2003WR002441.

Dubayah, R., Wood, E.F., Lavallée, D. (1997): Multiscaling Analysis in Distributed Modelling and Remote Sensing: An Application Using Soil Moisture. *Scale in Remote*

- Sensing and GIS.* D. A. Quattrochi and M. F. Goodchild. Boca Raton, London, New York, Washington, D.C., Lewis Publishers.
- Dubois, P. C., van Zyl, J., Engman, E. T. (1995): Measuring Soil Moisture with Imaging Radars. *IEEE Trans. Geosci. Rem. Sens.* 33(4): 915-926.
- Ellis, S., Mellor, A. (1995): Soils and environment. London, Routledge.
- Engman, E. T. (1994): The potential of SAR in hydrology. *Proc. IGARSS'94:* 283-285.
- Engman, E. T. (1995): Recent Advances in remote sensing in hydrology. *Reviews of Geophysics* 33(S1): 967-976.
- Engman, E. T. (2000): Soil moisture. *Remote Sensing in Hydrology and Water Management.* G. A. Schultz and E. T. Engman. Berlin, Springer: 197-216.
- Engman, E. T., Chauhan, N.S. (1995): Status of Microwave Soil Moisture Measurements with Remote Sensing. *Rem. Sens. Environ.* 51: 189-198.
- Entekhabi, D., Njoku, E. G., Houser, P., Spencer, M., Doiron, T., Yunjin, Kim, Smith, J., Girard, R., Belair, S., Crow, W., Jackson, T. J., Kerr, Y. H., Kimball, J. S., Koster, R., McDonald, K. C., O'Neill, P. E., Pultz, T., Running, S. W., Jiancheng, Shi, Wood, E., van Zyl, J. (2004): The hydrosphere State (hydros) Satellite mission: an Earth system pathfinder for global mapping of soil moisture and land freeze/thaw. *IEEE Trans. Geosci. Rem. Sens.* 42(10): 2184-2195.
- Entekhabi, D., Rodriguez-Iturbe, I., Castelli, F. (1995): Mutual interaction of soil moisture state and atmospheric processes. *Journal of Hydrology* 184: 3-17.
- Entekhabi, D., Rodriguez-Iturbe, I., Castelli, F. (1996): Mutual interaction of soil moisture state and atmospheric processes. *Journal of Hydrology* 184: 3-17.
- Entin, J.K., Robock, A., Vinnikov, K. Y., Hollinger, S.E., Liu, S., Namkhai, A. (1999): Temporal and spatial scales of observed soil moisture variations in the extratropics. *J. Geophys. Res.* 105(D9): 11865-11877.
- Entin, J.K., Robock, A., Vinnikov, K. Y., Hollinger, S.E., Liu, S., Namkhai, A. (2000): Temporal and spatial scales of observed soil moisture variations in the extratropics. *J. Geophys. Res.* 105(D9): 11865-11877.
- ESA (1998): European Space Agency/ESTEC: ENVISAT-1: Mission & System Summary. Noordwijk, The Netherlands.
- ESA (1998b): Envisat ASAR Science Applications. *ESA SP 1225.*
- ESA (2008): CEOS Earth Observation Handbook. *ESA SP-1315.*

- Famiglietti, J. s., Rudnicki, J. W., Rodell, M. (1998): Variability in surface moisture content along a hillslope transect: Rattlesnake Hill, Texas. *Journal of Hydrology* 210: 259-281.
- Frison, P.-L., Mougin, E. (1996): Use of ERS-1 Wind Scatterometer Data over Land Surfaces. *IEEE Trans. Geosci. Rem. Sens.* 34(2): 550-560.
- Fung, A. K. (1994): Microwave scattering and emission models and their applications. Boston, Artech House.
- Gauthier, Y., Bernier, M., Fortin, J.-P. (1998): Aspect and incidence angle sensitivity in ERS-1 SAR data. *Int. J. Rem. Sens.* 19(10): 2001-2006.
- GCOS (2008a). Future Climate Change Research and Observations: GCOS, WCRP and IGBP Learning from the IPCC Fourth Assessment Report. GCOS-117, WCRP-127, IGBP Report No. 58.
- GCOS (2008b). Report of the Sixteenth Session of the WMO-IOC-UNEP-ICSU Steering Committee for GCOS. GCOS-124.
- Gleick, P. H. (1996): Water resources. *Encyclopedia of Climate and Weather*. S. H. Schneider. New York, Oxford University Press. 2: 817-823.
- Gottwald, S. (Ed.) (1995): Meyers kleine Enzyklopädie Mathematik. Mannheim, Leipzig, Wien, Zürich, Meyers Lexikonverl.
- Grayson, R., Blöschl, G. (2000): Spatial Processes, Organisation and Patterns. *Spatial Patterns in Catchment Hydrology*. R. Grayson and G. Blöschl. New York, Cambridge University Press.
- Grayson, R., Blöschl, G. (2001): Spatial Processes, Organisation and Patterns. *Spatial patterns in catchment hydrology: observations and modelling*. R. Grayson and G. Blöschl, Cambridge University Press.
- Grayson, R., Western, A.W., Chiew, F. H. S., Blöschl, G. (1997): Preferred states in spatial soil moisture patterns: Local and nonlocal controls. *Water Resources Research* 33(12): 2897-2908.
- Guijarro, J., Auriol, A., Costes, M., Jayles, C., Vincent, P. (2000): MWR and DORIS - Supporting Envisat's Radar Altimetry Mission. *ESA bulletin* 106: 41-46.
- Hallikainen, M. T., Ulaby, F. T., Dobson, M. C., El-Rayes, M. A., Wu, I.-K. (1985): Microwave Dielectric Behavior of Wet Soil - Part I: Empirical Models and Experimental Observations. *IEEE Trans. Geosci. Rem. Sens.* GE-23(1): 25-34.

- Hillel, D. (1982): Introduction to Soil Physics. San Diego, Academic Press.
- Holecz, F., Freeman, A., van Zyl, J. (1993): Topographic effects on the antenna gain pattern correction. IGARSS'95.587-589
- Holecz, F., Freeman, A., van Zyl, J. (1995): Topographic effects on the antenna gain pattern correction. IGARSS'95.587-589
- Holecz, F., Pasquali, P., Moreira, A., Nüesch, D. (1998): Rigorous Radiometric Calibration of Airborne AeS-1 InSAR Data. *Proc IGARSS'98, IEEE International* 5: 2442-2444.
- Holzner, J., Bamler, R. (2002): Burst-Mode and ScanSAR Interferometry. *IEEE Trans. Geosci. Rem. Sens.* 40(9): 1917-1934.
- Huete, A. R. (2004): Remote sensing of soils and soil processes. *Remote Sensing for Natural Resources Management and Environmental Monitoring: Manual of Remote Sensing*. S. Ustin, John Wiley & Sons. 4: 1-48.
- Illston, B. G., Basara, J. B., Crawford, K. C. (2004b): Seasonal to Interannual Variations of Soil Moisture measured in Oklahoma. *Int. J. Climatology* 24: 1883-1896.
- Illston, B. G., Caldwell, J. C., Bodnar, s. G. (2004a): Representativeness of Soil Moisture Conditions in Central Oklahoma During the Enhanced Drying Phase. American Meteorological Society - 18th Conference on Hydrology; Jan 11-15, Seattle, Washington
- IPCC (2001). Climate Change 2001: Impacts, Adaptation, and Vulnerability. Contribution of Working Group II to the Third Assessment Report of the Intergovernmental Panel on Climate Change.
- IPCC (2007). Climate Change 2007: The Physical Basis. Contribution of Working Group I to the fourth Assessment Report of the Intergovernmental Panel in Climate Change [Solomon, S., D. Qin, M. Manning, Z. Chen, M. Marquis, K.B. Averyt, M. Tignor and H.L. Miller (eds.)]. Cambridge University Press, Cambridge, United Kingdom and New York, NY, USA, 996 pp.
- IPCC (2008). Climate Change and Water. [Bates, B.C., Kundzewicz, Z. W., Wu, S., Palutikof, J. P. (eds.)]. Technical Paper of the Intergovernmental Panel on Climate Change, IPCC Secretariat, Geneva, 210 pp.
- Jackson, T. J., Schmugge, T. J., Engman, E. T. (1996): Remote sensing applications to hydrology: soil moisture. *Hydrological Sciences - Journal des Sciences Hydrologiques* 41(4): 517-530.
- Jones, S. B., Wraith, J. M., Or, D. (2002): Time domain reflectrometry measurement principles and applications. *Hydrological Processes* 16: 141-153.

- Kerr, Y. H. (2007): Soil moisture from space: Where are we? *Hydrogeology Journal* 15(1): 117-120.
- KNMI EARS Team (2007). ERS Scatterometer Product User Manual. KNMI-publicatie 212e; De Bilt, The Netherlands.
- Koorevaar, P., Menelik, G., Dirksen, C. (1999): Elements of soil physics. Amsterdam, Elsevier.
- Kraus, K., Schneider, W. (1988): Fernerkundung. Band 1. Physikalische Grundlagen und Aufnahmetechniken. Bonn, Ferd. Dümmlers.
- Leckie, D. G., Ranson, K. J. (1998): Forestry Applications Using Imaging Radar. *Principles and Applications of Imaging Radar*. F. M. Henderson and A. J. Lewis. New York, Wiley & Sons.
- Lecomte, P., Wagner, W. (1998): ERS Wind Scatterometer Commissioning and in-flight Calibration. Workshop on Emerging Scatterometer Applications: From Research to Operations, ESTEC, Noordwijk, The Netherlands, 5-7 October 1998, *ESA-SP-424*
- Lewis, A. J., Henderson, F. M., Holcomb, D. W. (1998): Radar Fundamentals: The Geoscience Perspective. *Principles and Applications of Imaging Radar*. F. M. Henderson and A. J. Lewis. New York, Wiley & Sons.
- Li, D., Mausel, P., Brondízio, E., Moran, E. (2004): Change detection techniques. *Int. J. Rem. Sens.* 25(12): 2365-2407.
- Lichtenegger, J. (1996): The contribution of ERS SAR to monitoring of hilly and mountainous regions. Proc. of the 4th International Symposium on High Mountain Remote Sensing Cartography, Karlstadt, August 19-29, Sweden, *The University of Karlstadt, Research Report 97:3*
- Lillesand, T. M., Kiefer, R. W. (2000): Remote Sensing and Image Interpretation. New York, Chichester, Weinheim, Wiley.
- Liu, X., Ma, H., Sun, W. (2006): Study on the geolocation algorithm of space-borne SAR image. *Advances in Machine VISION, Image Processing and Pattern Analysis* 4153: 270-280.
- Löffler, E. (1994): Geographie und Fernerkundung. Stuttgart, B. G. Teubner.
- Macelloni, G., Nesti, G., Pampaloni, P., Sigismondi, S., Tarchi, D., Lolli, S. (2000): Experimental Validation of Surface Scattering and Emission Models. *IEEE Trans. Geosci. Rem. Sens.* 38(1): 459-469.

- Mäkynen, M. P., Manninen, T., Similä, M. H., Karvonen, J. A., Hallikainen, M. T. (2002): Incidence Angle Dependence of the Statistical Properties of C-Band HH-Polarization Backscattering Signatures of the Baltic Sea Ice. *IEEE Trans. Geosci. Rem. Sens.* 40(12): 2593-2609.
- Manninen, T. (2003): Multiscale surface roughness description for scattering modelling of bare soil. *Physica A* 319: 535-551.
- Martyn, P., Williams, J., Nicoll, J., Guritz, r., Bicknell, T. (1999): Calibration of the Radarsat SWB processor at the Alaska SAR Facility. *Proceedings of the IGARSS 1999*: 2355-2359.
- Mattia, F., Satalino, G., Dente, L., Pasquariello, G. (2006): Using A Priori Information to Improve Soil Moisture Retrieval From ENVISAT ASAR AP Data in Semiarid Regions. *IEEE Trans. Geosci. Rem. Sens.* 44(4): 900-912.
- McKnight, T.L. (1992): Regional Geography of the United States and Canada. Englewood Cliffs, New Jersey, Prentice Hall.
- Meier, E., Frei, U., Nüesch, D. (1993): Precise Terrain corrected Geocoded Images. *SAR processing: data and systems*. G. Schreier. Karlsruhe, Wichmann: 435.
- Melillo, J. M., Steudler, P. A., Aber, J. D., Newkirk, K., Lux, H., Bowles, F. P., Catricala, C., Magill, A., Ahrens, T., Morrisseau, S. (2002): Soil Warming and Carbon-Cycle Feedbacks to the Climate. *Science* 298(5601): 2173-2176.
- Minier, C. (2005). ENVISAT-1 Products Specifications Volume 16: Auxiliary Data Files.
- Moeremans, B., Dautrebande, S. (1998): Use of ERS SAR interferometric coherence and PRI images to evaluate crop height and soil moisture to identify crops. *Proc. EUROPTO Conf. on Rem. Sens. for Agriculture, Ecosystems and Hydrology, Barcelona, Spain*: 9-19.
- Moeremans, B., Dautrebande, S. (2000): Soil moisture evaluation by means of multi-temporal ERS SAR PRI images and interferometric coherence. *Journal of Hydrology* 234: 162-169.
- Mohanty, B. P., Skaggs, T. H. (2001): Spatio-temporal evolution and time-stable characteristics of soil moisture within remote sensing footprints with varying soil, slope, and vegetation. *Adv. Water Res.* 24: 1051-1067.
- Moran, M. S., McElroy, S., Watts, J. M., Peters-Lidar, C. D. (2006): Radar remote sensing for estimation of surface soil moisture at the watershed scale. *Modelling and Remote Sensing Applied in Agriculture (US and Mexico)*. C. W. Richardson, A. S. Baez-Gonzalez and M. Tiscareno, INIFAP Publ. Mexico: 91-106.

- Moran, M. S., Peters-Lidar, C. D., Watts, J. M., McElroy, S. (2004): Estimating soil moisture at the watershed scale with satellite-based radar and land surface models. *Can. J. Remote Sensing* 30(5): 805-826.
- Njoku, E. G., Entekhabi, D. (1996): Passive microwave remote sensing of soil moisture. *Journal of Hydrology* 184: 101-129.
- Njoku, E. G., Jackson, T. J., Lakshmi, V., Chan, T. K., Nghiem, S. V. (2003): Soil moisture retrieval from AMSR-E. *IEEE Transactions on Geoscience and Remote Sensing* 41(2): 215-229.
- Oh, Y., Sarabandi, K., Ulaby, F. T. (1992): An Empirical Model and an Inversion Technique for Radar Scattering from Bare Soil Surfaces. *IEEE Trans. Geosci. Rem. Sens.* 30(2): 370-381.
- Oldak, A., Jackson, T. J., Starks, P., Elliot, R. (2003): Mapping near-surface soil moisture on regional scale using ERS-'' SAR data. *Int. J. Rem. Sens.* 24(22): 4579-4598.
- Olmstedt, C. (1993). Scientific SAR User's Guide. Alaska SAR Facility ASF-SD-003.
- Owe, M., de Jeu, R., Holmes, T. (2008): Multisensor historical climatology of satellite-derived global land surface moisture. *Journal of Geophysical Research* 113(F1): DOI: 10.1029/2007JF000769.
- Paterson, J.H. (1994): North America. A Geography of the United States and Canada. New York, Oxford, Oxford University Press.
- Pellarin, T., Calvet, J.-C., Wagner, W. (2006): Evaluation of ERS scatterometer soil moisture products over a half-degree region in southwestern France. *Geophysical Research Letters* 33(17): DOI: 10.1029/2006GL027231.
- Pietroniro, A., Prowse, T. D. (2002): Applications of remote sensing in hydrology. *Hydrological Processes* 16: 1537-1541.
- Porporato, A., D'Odorico, P., Laio, F., Rodriguez-Iturbe, I. (2003): Hydrologic controls on soil carbon and nitrogen cycles. I. Modelling scheme. *Adv. Water Res.* 26: 45-58.
- Quesney, A., Le Hégarat-Mascle, S., Taconet, O., Vidal-Madjar, D., Wigneron, J., Loumagne, C., Normand, M. (2000): Estimation of watershed soil moisture index from ERS/SAR data. *Rem. Sens. Environ.* 72: 290-303.
- Raju, S., Chanzy, A., Wigneron, J., Calvet, J., Kerr, Y., Laguerre, L. (1995): Soil moisture and temperature profile effects on microwave emission at low frequencies. *Rem. Sens. Environ.* 54: 85-97.

- Raney, R.K. (1998): Radar Fundamentals: Technical Perspective. *Principles and Applications of Imaging Radar*. F. M. Henderson and A. J. Lewis. New York, Wiley & Sons.
- Rees, W. G. (2001): Physical Principles of Remote Sensing. Cambridge, Cambridge University Press.
- Robock, A., Vinnikov, K.Y., Srinivasan, G., Entin, J.K., Hollinger, S.E., Speranskaya, N.A., Liu, S., Namkhai, A. (2000): The Global Soil Moisture Data Bank. *Bull. Amer. Meteorol. Soc.* 81: 1281-1299.
- Rombach, M., Demicran, A., Mauser, W. (1993): Correlation between soil moisture and the backscattering coefficient. *Proc. 2nd ERS-1 Symp. on Space at the Service of our Environment, Hamburg, Germany*: 861-864.
- Ropelewski, C. F., Yarosh, E. S. (1998): The Observed Mean Annual Cycle of Moisture Budgets over the Central United States (1973-92). *Journal of Climate* 11(9): 2180-2190.
- Rosich, B., Meadows, P. (2004). Absolute Calibration of ASAR Level 1 Products Generated with PF-ASAR. Technical Note ENVI-CLVL-EOPG-TN-03-0010. ESA. Frascati, Italy.
- Roth, A., Craubner, A., Hügel, T. (1993): Standard Geocoded Ellipsoid Corrected images. *SAR processing: data and systems*. G. Schreier. Karlsruhe, Wichmann: 435.
- Sahebi, M. R., Bonn, F., Gwyn, G. H. J. (2003): Estimation of the moisture content of bare soil from RADARSAT-1 SAR using simple empirical models. *Int. J. Rem. Sens.* 24(12): 2575-2582.
- Sahr, K., White, D., Kimerling, A. J. (2003): Geodesic Discrete Global Grid Systems. *Cartography and Geographic Information Science* 30(2): 121-134.
- Satalino, G., Mattia, F., Davidson, M. W. J., Le Toan, T., Pasquariello, G., Borgeaud, M. (2002): On Current Limits of Soil Moisture Retrieval From ERS-SAR Data. *IEEE Trans. Geosci. Rem. Sens.* 40(11): 2438-2447.
- Schanda, E. (1986): Physical fundamentals of remote sensing. Berlin, Springer.
- Scheffer, F., Schachtschabel, P. (1998): Lehrbuch der Bodenkunde. Stuttgart, Enke.
- Schiermeier, Q. (2008): A Long Dry Summer. *Nature* 452: 270-273.
- Schmugge, T. J., Jackson, T. J., McKim, H. L. (1980): Survey of Methods for Soil Moisture Determination. *Water Resources Research* 16(6): 961-979.

- Schneider, J. M., Fisher, D. K., Elliott, R. L., Brown, G. O., Bahrmann, C. P. (2003): Spatiotemporal Variations in Soil Water: First Results from the ARM SGP CART Network. *Journal of Hydrology* 4: 106-120.
- Scipal, K. (2002): Global soil moisture retrieval from ERS scatterometer data. *PhD dissertation, Vienna Univ. of Technology, Austria.*
- Shannon, M. A., Bohn, P. W., Elimelech, M., Georgiadis, J. G., Mariñas, B. J., Mayes, A. M. (2008): Water under Pressure. *Nature* 452: 269.
- Shea, D. J., Worley, S. J., Stern, I. R., Hoar, T. J. (1994). An Introduction to Atmospheric and Oceanographic Data. NCAR Technical Note 404+1A. Boulder, Colorado, National Center for Atmospheric Research. Boulder, Colorado.
- Shoshany, M., Svoray, T., Curran, P. J., Foody, G. M., Perevolotsky, A. (2000): The relationship between ERS-2 SAR backscatter and soil moisture: generalization from a humid to semi-arid transect. *Int. J. Rem. Sens.* 21(11): 2337-2343.
- Singh, A. (1989): Digital change detection techniques using remotely sensed data. *Int. J. Rem. Sens.* 10(6): 989-1003.
- Small, D., Holecz, F., Meier, E., Nüesch, D. (1998): Absolute radiometric correction in rugged terrain: a plea for integrated radar brightness. *Proc IGARSS'98, IEEE International* 1: 330-332.
- Srivastava, S. K., Hawkins, R. K., Banik, B. T., Adamovic, M., Gray, R., Murnaghan, K., Lukowski, T. I., Jefferies, W. C. (2001): Radarsat-1 image quality and calibration - A continuing success. *Adv. Space Res.* 28(1): 99-108.
- Su, Z., Troch, P.A., de Trco, F.P. (1997): Remote sensing of bare soil moisture using EMAC/ESAR data. *Int. J. Rem. Sens.* 18(10): 2105-2124.
- Taylor, J. R. (1997): An Introduction to Error Analysis: The Study of Uncertainties in Physical Measurements. Sausalito, Univ Science Books.
- Thoma, D. P., Moran, M. S., Bryant, R., Rahman, M., Holifield-Collins, C.D., Skrivin, S., Sano, E. E., Slocum, K. (2006): Comparison of four models to determine surface soil moisture from C-band radar imagery in a sparsely vegetated semiarid landscape. *Water Resources Research* 42.
- Tipler, P. A., Mosca, G. (2004): Physik für Wissenschaftler und Ingenieure. München, Heidelberg, Elsevier, Spektrum Akad. Verl.
- Titz, S. (2005): Wie wird der nächste Sommer? *Spektrum der Wissenschaft* August 2008: 48-52.

- Topp, G.C. (2003): State of the art of measuring soil water content. *Hydrological Processes* 17: 2993-2996.
- U.S. Census Bureau Population Division (2007). Annual Estimates of the Population for the United States, Regions, and Puerto Rico: April 1, 2007 (NST-EST2007-01).
- Ulaby, F. T., Attema, E. (1978): Vegetation modeled as a water cloud. *Radio Science* 13(2): 357-364.
- Ulaby, F. T., Dubois, P. C., van Zyl, J. (1996): Radar mapping of surface soil moisture. *Journal of Hydrology* 184: 57-84.
- Ulaby, F. T., Moore, B., Fung, A. K. (1982): Microwave Remote Sensing - Active and Passive, Vol. II: Radar Remote Sensing and Surface Scattering and Emission Theory. Norwood, Artech House.
- Ulaby, F. T., Moore, R. K., Fung, A. K. (1986): Microwave Remote Sensing - Active and Passive, Vol. III: From Theory to Applications. Norwood, Artech House.
- Ulaby, F. T., Sarabandi, K., McDonald, K., Whitt, M., Dobson, M. C. (1990): Michigan Microwave Canopy Scattering Model (MIMICS). *Int. J. Rem. Sens.* 11(7): 1223-1253.
- Ulander, L. M. H. (1996): Radiometric Slope Correction of Synthetic-Aperture Radar Images. *IEEE Trans. Geosci. Rem. Sens.* 34(5): 1115-1122.
- USDA United States Department of Agriculture (1999): Soil Taxonomy. A Basic System of Soil Classification for Making and Interpreting Soil Surveys.
- Vauchaud, G., Passerat de Silans, A., Balabanis, P., Vauclin, M. (1985): Temporal Stability of Spatially Measured Soil Water Probability Density Function. *Soil Sci. Soc. Am. J.* 49: 822-828.
- Verhoest, N. E. C., Lievens, H., Wagner, W., Alvarez-Mozos, J., Moran, M. S., Mattia, F. (2008): On the Soil Roughness Parameterization Problem in Soil Moisture Retrieval of Bare Soil Surfaces from Synthetic Aperture Radar. *Sensors* 8: DOI: 10.3390/s8074213.
- Verstraeten, W. W., Veroustraete, F., van der Sande, C. J., Grootaers, I., Feyen, J. (2006): Soil moisture retrieval using thermal inertia determined with visible and thermal spaceborne data, validated for European forests. *Rem. Sens. Environ.* 101: 299-314.
- Vinnikov, K. Y., Robock, A., Speranskaya, N. A., Schlosser, C. A. (1996): Scales of temporal and spatial variability of midlatitude soil moisture. *J. Geophys. Res.* 101(D3): 7163-7174.
- Vörösmarty, C. J. (2002): Global water assessment and potential contributions from Earth Systems Science. *Aquat. Sci.* 64: 328-351.

- Wagner, W. (1998): Soil Moisture Retrieval from ERS Scatterometer Data. *PhD dissertation, Vienna Univ. of Technology, Austria.*
- Wagner, W., Blöschl, G., Pampaloni, P., Calvet, J.-C., Bizzarri, B., Wigneron, J.-P., Kerr, Y. (2007a): Operational readiness of microwave remote sensing of soil moisture for hydrologic applications. *Nordic Hydrology* 38(1): 1-20.
- Wagner, W., Lemoine, G., Borgeaud, M., Rott, H. (1999a): A Study of Vegetation Cover Effects on ERS Scatterometer Data. *IEEE Trans. Geosci. Rem. Sens.* 37(2): 938-948.
- Wagner, W., Lemoine, G., Rott, H. (1999b): A Method for Estimating Soil Moisture from ERS Scatterometer and Soil Data. *Rem. Sens. Environ.* 70: 191-207.
- Wagner, W., Naemi, V., Scipal, K., de Jeu, R., Martinez-Fernandez, J. (2007b): Soil moisture from operational meteorological satellites. *Hydrogeology Journal* 15(1): 121-131.
- Wagner, W., Pathe, C., Doubkova, M., Sabel, D., Bartsch, A., Hasenauer, S., Blöschl, G., Scipal, K., Martinez-Fernandez, J., Löw, A. (2008): Temporal stability of soil moisture and radar backscatter observed by the Advanced Synthetic Aperture Radar (ASAR). *Sensors* 8: 1174-1197.
- Wagner, W., Pathe, C., Sabel, D., Bartsch, A., Künzer, C., Scipal, K. (2007c): Experimental 1 km soil moisture products from ENVISAT ASAR for Southern Africa. *Proceed. of Envisat Symposium 2007.*
- Wagner, W., Scipal, K., Pathe, C., Gerten, D., Lucht, W., Rudolf, B. (2003): Evaluation of the agreement between the first global remotely sensed soil moisture data with model and precipitation data. *J. Geophys. Res. Atmos.* 108(D19): 4611, DOI10.1029/2003JD003663.
- Wagner, W., Scipal, K., Pathe, C., Gerten, D., Lucht, W., Rudolf, B. (2003): Evaluation of the agreement between the first global remotely sensed soil moisture data with model and precipitation data. *Journal of Geophysical Research* 108(D19, 4611): doi:10.1029/2003JD003663.
- Walker, J. P. (1999). Estimating Soil Moisture Profile Dynamics from Near-Surface Soil Moisture Measurements and Standard Meteorological Data. Dissertation. Department of Civil Surveying and Environmental Engineering, University of Newcastle, New South Wales, Australia: 767 p.
- Walker, J. P., Willgoose, G. R., Kalma, J. D. (2004b): In situ measurement of soil moisture: a comparison of techniques. *Journal of Hydrology* 293(1-4): 85-99.
- Walker, J.P., Houser, P.R., Willgoose, G. R. (2004a): Active microwave remote sensing for soil moisture measurement: a field evaluation using ERS-2. *Hydrological Processes* 18(11): 1975-1997.

- Weimann, A., von Schönermark, M., Schuhmann, A., Jorn, P., Gunter, R. (1998): Soil moisture estimation with ERS-1 SAR in the East German loess soil area. *Int. J. Rem. Sens.* 19: 237-243.
- Weimann, A., von Schönermark, M., Schuhmann, A., Jorn, P., Gunter, R. (1998): Soil moisture estimation with ERS-1 SAR in the East German loess soil area. *Int. J. Rem. Sens.* 19(2): 237-243.
- Wen, J., Su, Z. (2003): A time series based method for estimating relative soil moisture with ERS wind scatterometer data. *Geophysical Research Letters* 30(7): doi:10.1029/2002GL016557.
- Western, A.W., Blöschl, G. (1999): On the spatial scaling of soil moisture. *Journal of Hydrology* 217: 203-224.
- Wickel, A. J., Jackson, T. J., Wood, E. (2001): Multitemporal monitoring of soil moisture with RADARSAT SAR during the 1997 Southern Great Plains hydrology experiment. *Int. J. Rem. Sens.* 22(8): 1571-1583.
- Wild, A. (1993): Soils and the environment: an introduction. New York, Cambridge University Press.
- Wong, F., Stevens, D., Cumming, I. (1997): Phase-Preserving Processing of ScanSAR Data with a Modified Range Doppler Algorithm. *Proc. IGARSS'97*: 725-727.
- Woodhouse, I. H. (2006): Introduction to Microwave Remote Sensing. Boca Raton, London, New York, Taylor & Francis.
- Woods, A.J., Omernik, J.M., Butler, J.M., Ford, J.G., Henley, J.E., Hoagland, B.W., Arndt, D.S., Moran, B.S. (2005): Ecoregions of Oklahoma (color poster with map, descriptive text, summary tables, and photographs).
- Zazueta, F. S., Xin, J. (1994): Soil Moisture Sensors. *Bulletin 292, Florida Cooperative Extension Service, Institute of Food and Agricultural Sciences, University of Florida*.
- Zegelin, S. (1996): Soil Moisture Measurement. Workshop on Field Measurement Techniques in Hydrology, Corpus Christi College, Clayton
- Zink, M., Buck, C., Suchail, J.-L., Torres, R., Bellini, A., Closa, J., Desnos, Y.-L., Rosich, B. (2001): The Radar Imaging Instrument and Its Applications: ASAR. *ESA bulletin* 106: 46-55.
- Zribi, M., Baghdadi, N., Holah, N., Fafin, O. (2005): New methodology for soil surface moisture estimation and its application to ENVISAT-ASAR multi-incidence data inversion. *Rem. Sens. Environ.* 96: 485-496.

# **APPENDIX:**

## **TABLES**

**Table A.1: Correlation R between  $m_s$ -ERS at 50 km and in-situ soil moisture at 75 Oklahoma Mesonet stations**

Station ID	R	Station ID	R
ACME	0.722446	MEDI	0.746926
ALV2	0.492322	MIAM	0.728911
APAC	0.617444	MINC	0.693085
ARD2	0.706427	MRSH	0.610917
ARNE	0.604920	NEWK	0.618569
BEAV	0.546185	NOWA	0.737833
BESS	0.833470	NRMN	0.731497
BIXB	0.378326	PAWN	0.690299
BLAC	0.657727	PERK	0.664596
BOIS	0.377550	PORT	0.611180
BREC	0.775692	PRYO	0.792180
BRIS	0.489175	PUTN	0.373217
BUTL	0.701183	REDR	0.508897
CALV	0.389141	RING	0.680754
CAMA	0.658264	SALL	0.704810
CENT	0.632626	SKIA	0.632789
CHER	0.290125	SLAP	0.678223
CHEY	0.705617	SPEN	0.745101
CLOU	0.719552	STIG	0.679939
COOK	0.673216	STIL	0.632647
COPA	0.711884	STUA	0.632589
ELRE	0.683804	TAHL	0.577904
ERIC	0.482835	TISH	0.778702
FAIR	0.563422	VINI	0.790492
FORA	0.607530	WALT	0.741745
GOOD	0.647549	WASH	0.764690
GRA2	0.641382	WATO	0.617019
GUTH	0.611241	WEAT	0.664398
HASK	0.780562	WEST	0.702498
HECT	0.839217	WILB	0.762922
HINT	0.414862		
HOBA	0.584433		
HOLL	0.561004		
HOOK	0.618751		
HUGO	0.720217		
IDAB	0.757592		
INOL	0.731496		
JAYX	0.643163		
KENT	0.536877		
KING	0.528923		
LAHO	0.336416		
LANE	0.695025		
MARE	0.671215		
MAYR	0.558661		
MCAL	0.747673		

**Table A.2: Correlation R between  $m_s$ -ASAR at 3 km and in-situ soil moisture at 75 Oklahoma Mesonet stations**

Station ID	R	Station ID	R
ACME	0.465989	MEDI	0.663593
ALV2	0.455964	MIAM	0.521112
APAC	0.549907	MINC	0.571518
ARD2	0.338129	MRSH	0.568627
ARNE	0.547684	NEWK	0.725744
BEAV	0.480435	NOWA	0.580448
BESS	0.787061	NRMN	0.175002
BIXB	0.381542	PAWN	0.582102
BLAC	0.640823	PERK	0.634383
BOIS	0.261607	PORT	0.488814
BREC	0.702773	PRYO	0.717112
BRIS	0.516269	PUTN	0.332796
BUTL	0.684022	REDR	0.627366
CALV	0.495414	RING	0.717508
CAMA	0.620700	SALL	0.389296
CENT	0.531486	SKIA	0.476361
CHER	0.291306	SLAP	0.380390
CHEY	0.727637	SPEN	0.512871
CLOU	0.529641	STIG	0.592588
COOK	0.299140	STIL	0.433123
COPA	0.506344	STUA	0.555212
ELRE	0.677912	TAHL	0.519754
ERIC	0.180478	TISH	0.724741
FAIR	0.366034	VINI	0.675783
FORA	0.385442	WALT	0.528687
GOOD	0.520445	WASH	0.600955
GRA2	0.557464	WATO	0.725148
GUTH	0.649951	WEAT	0.575575
HASK	0.707884	WEST	0.418864
HECT	0.728318	WILB	0.754322
HINT	0.404601		
HOBA	0.426915		
HOLL	0.336700		
HOOK	0.511393		
HUGO	0.653531		
IDAB	0.681736		
INOL	0.599403		
JAYX	0.393457		
KENT	0.508175		
KING	0.492070		
LAHO	0.345417		
LANE	0.539333		
MARE	0.651098		
MAYR	0.576084		
MCAL	0.491643		

**Table A.3: Correlation R between  $m_s$ -ASAR at 50 km and in-situ soil moisture at 75 Oklahoma Mesonet stations**

Station ID	R	Station ID	R
ACME	0.662378	MEDI	0.787411
ALV2	0.519851	MIAM	0.659002
APAC	0.628533	MINC	0.696855
ARD2	0.653924	MRSH	0.610280
ARNE	0.567511	NEWK	0.640781
BEAV	0.503983	NOWA	0.719859
BESS	0.828895	NRMN	0.751500
BIXB	0.412659	PAWN	0.688046
BLAC	0.687127	PERK	0.735300
BOIS	0.258683	PORT	0.585874
BREC	0.777450	PRYO	0.777820
BRIS	0.574824	PUTN	0.412871
BUTL	0.781491	REDR	0.555476
CALV	0.449220	RING	0.735134
CAMA	0.689431	SALL	0.703757
CENT	0.609550	SKIA	0.625744
CHER	0.360249	SLAP	0.657039
CHEY	0.686863	SPEN	0.628768
CLOU	0.632036	STIG	0.672229
COOK	0.618073	STIL	0.704601
COPA	0.637505	STUA	0.628271
ELRE	0.693953	TAHL	0.590993
ERIC	0.456736	TISH	0.730783
FAIR	0.582838	VINI	0.769178
FORA	0.587091	WALT	0.752744
GOOD	0.617005	WASH	0.742295
GRA2	0.655877	WATO	0.677803
GUTH	0.687970	WEAT	0.671728
HASK	0.731148	WEST	0.662831
HECT	0.790457	WILB	0.719498
HINT	0.469529		
HOBA	0.624515		
HOLL	0.526197		
HOOK	0.572138		
HUGO	0.697540		
IDAB	0.756954		
INOL	0.704253		
JAYX	0.642942		
KENT	0.484528		
KING	0.551239		
LAHO	0.456431		
LANE	0.606622		
MARE	0.699707		
MAYR	0.551991		
MCAL	0.728723		

**Table A.4:** Correlation R between  $m_{s\text{-ERS}}$  at 50 km and  $m_{s\text{-ASAR}}$  at 3 km at 75 Oklahoma Mesonet stations

Station ID	R	Station ID	R
ACME	0.659692	MEDI	0.610279
ALV2	0.787634	MIAM	0.388572
APAC	0.806887	MINC	0.667961
ARD2	0.427192	MRSH	0.761959
ARNE	0.772390	NEWK	0.786485
BEAV	0.707856	NOWA	0.747962
BESS	0.818925	NRMN	0.222314
BIXB	0.570898	PAWN	0.737111
BLAC	0.736309	PERK	0.696089
BOIS	0.852400	PORT	0.685423
BREC	0.821918	PRYO	0.706714
BRIS	0.570808	PUTN	0.796732
BUTL	0.818200	REDR	0.785314
CALV	0.396534	RING	0.753024
CAMA	0.770332	SALL	0.389614
CENT	0.508909	SKIA	0.526051
CHER	0.543497	SLAP	0.748187
CHEY	0.812345	SPEN	0.486235
CLOU	0.623986	STIG	0.714256
COOK	0.468918	STIL	0.468108
COPA	0.701967	STUA	0.653993
ELRE	0.732343	TAHL	0.597636
ERIC	0.687876	TISH	0.773956
FAIR	0.675233	VINI	0.757822
FORA	0.590269	WALT	0.691808
GOOD	0.858922	WASH	0.651138
GRA2	0.791572	WATO	0.841658
GUTH	0.776161	WEAT	0.847532
HASK	0.792737	WEST	0.552384
HECT	0.735143	WILB	0.742187
HINT	0.816461		
HOBA	0.796682		
HOLL	0.633895		
HOOK	0.723235		
HUGO	0.676475		
IDAB	0.742087		
INOL	0.701478		
JAYX	0.528147		
KENT	0.771426		
KING	0.829618		
LAHO	0.765138		
LANE	0.609752		
MARE	0.707830		
MAYR	0.792953		
MCAL	0.600856		

**Table A.5:** Correlation  $R$  between  $m_{s\text{-ERS}}$  at 50 km and  $m_{s\text{-ASAR}}$  at 50 km at 75 Oklahoma Mesonet stations

Station ID	R	Station ID	R
ACME	0.7224	MEDI	0.7469
ALV2	0.4923	MIAM	0.7289
APAC	0.6174	MINC	0.6931
ARD2	0.7064	MRSH	0.6109
ARNE	0.6049	NEWK	0.6186
BEAV	0.5462	NOWA	0.7378
BESS	0.8335	NRMN	0.7315
BIXB	0.3783	PAWN	0.6903
BLAC	0.6577	PERK	0.6646
BOIS	0.3776	PORT	0.6112
BREC	0.7757	PRYO	0.7922
BRIS	0.4892	PUTN	0.3732
BUTL	0.7012	REDR	0.5089
CALV	0.3891	RING	0.6808
CAMA	0.6583	SALL	0.7048
CENT	0.6326	SKIA	0.6328
CHER	0.2901	SLAP	0.6782
CHEY	0.7056	SPEN	0.7451
CLOU	0.7196	STIG	0.6799
COOK	0.6732	STIL	0.6326
COPA	0.7119	STUA	0.6326
ELRE	0.6838	TAHL	0.5779
ERIC	0.4828	TISH	0.7787
FAIR	0.5634	VINI	0.7905
FORA	0.6075	WALT	0.7417
GOOD	0.6475	WASH	0.7647
GRA2	0.6414	WATO	0.6170
GUTH	0.6112	WEAT	0.6644
HASK	0.7806	WEST	0.7025
HECT	0.8392	WILB	0.7629
HINT	0.4149		
HOBA	0.5844		
HOLL	0.5610		
HOOK	0.6188		
HUGO	0.7202		
IDAB	0.7576		
INOL	0.7315		
JAYX	0.6432		
KENT	0.5369		
KING	0.5289		
LAHO	0.3364		
LANE	0.6950		
MARE	0.6712		
MAYR	0.5587		
MCAL	0.7477		

**Table A.6: BIAS between  $m_s$ -ERS at 50 km and in-situ soil moisture at 75 Oklahoma Mesonet stations**

Station ID	BIAS [%]	Station ID	BIAS [%]
ACME	-27.5610	MEDI	-25.2930
ALV2	-17.6616	MIAM	-18.0893
APAC	-17.5996	MINC	-6.63459
ARD2	-14.7912	MRSH	-16.6048
ARNE	-19.4773	NEWK	-35.0480
BEAV	-22.8719	NOWA	-9.24058
BESS	-5.20618	NRMN	-4.11376
BIXB	-38.1005	PAWN	-11.6471
BLAC	-9.90941	PERK	-16.9723
BOIS	-12.7763	PORT	-17.4288
BREC	-6.76872	PRYO	-22.9728
BRIS	-19.1713	PUTN	-23.9856
BUTL	-20.1922	REDR	-25.1095
CALV	-39.7766	RING	-5.94425
CAMA	-3.57918	SALL	-22.9391
CENT	-34.8931	SKIA	-23.8189
CHER	-22.0497	SLAP	-19.3525
CHEY	-16.1979	SPEN	-21.5013
CLOU	-29.3168	STIG	-16.7644
COOK	-8.65068	STIL	-13.1556
COPA	-23.6853	STUA	-29.6607
ELRE	-26.3745	TAHL	-20.7311
ERIC	-31.7617	TISH	-11.1425
FAIR	-20.5492	VINI	-23.3746
FORA	-34.3745	WALT	-10.2902
GOOD	-12.7556	WASH	-18.2083
GRA2	-15.1186	WATO	-8.92402
GUTH	-20.6886	WEAT	-1.95685
HASK	-34.0198	WEST	-25.7695
HECT	-11.1342	WILB	-19.7236
HINT	-29.3813		
HOBA	-7.49548		
HOLL	-5.42922		
HOOK	-21.1197		
HUGO	-14.7724		
IDAB	-11.9096		
INOL	-18.9607		
JAYX	-23.4258		
KENT	-22.7638		
KING	-25.9785		
LAHO	-21.8415		
LANE	-31.7813		
MARE	-23.4555		
MAYR	-18.9679		
MCAL	-22.7303		

**Table A.7: BIAS between  $m_s$ -ASAR at 3 km and in-situ soil moisture at 75 Oklahoma Mesonet stations**

Station ID	BIAS [%]	Station ID	BIAS [%]
ACME	-22.5053	MEDI	-21.1818
ALV2	-12.3061	MIAM	-17.8750
APAC	-13.1875	MINC	-8.24299
ARD2	-12.3647	MRSH	-18.0575
ARNE	-17.0645	NEWK	-28.4737
BEAV	-17.3025	NOWA	-13.6517
BESS	-0.166667	NRMN	1.83529
BIXB	-36.6203	PAWN	-8.56250
BLAC	-5.55000	PERK	-12.7033
BOIS	-5.18103	PORT	-17.1047
BREC	-0.887755	PRYO	-21.2683
BRIS	-16.3913	PUTN	-19.2000
BUTL	-11.3238	REDR	-20.8478
CALV	-36.4524	RING	-3.86239
CAMA	3.46218	SALL	-28.0145
CENT	-31.1429	SKIA	-27.5000
CHER	-15.0787	SLAP	-12.1944
CHEY	-9.77451	SPEN	-17.1650
CLOU	-26.3187	STIG	-17.9767
COOK	-6.63889	STIL	-11.7816
COPA	-27.8590	STUA	-30.3492
ELRE	-20.9216	TAHL	-21.4699
ERIC	-27.4000	TISH	-10.5301
FAIR	-16.8387	VINI	-23.0488
FORA	-27.4507	WALT	-1.45192
GOOD	-6.62832	WASH	-17.1786
GRA2	-4.61856	WATO	-6.71591
GUTH	-19.0899	WEAT	-0.0808082
HASK	-31.5730	WEST	-23.9722
HECT	-18.4225	WILB	-15.2706
HINT	-23.0000		
HOBA	-2.69318		
HOLL	3.84783		
HOOK	-11.8295		
HUGO	-6.78652		
IDAB	-6.61176		
INOL	-19.1728		
JAYX	-27.1000		
KENT	-14.7658		
KING	-23.1919		
LAHO	-18.9186		
LANE	-28.5652		
MARE	-17.4000		
MAYR	-14.1848		
MCAL	-20.5632		

**Table A.8: BIAS between  $m_s$ -ASAR at 50 km and in-situ soil moisture at 75 Oklahoma Mesonet stations**

Station ID	BIAS [%]	Station ID	BIAS [%]
ACME	-22.3571	MEDI	-17.3023
ALV2	-11.0408	MIAM	-18.4444
APAC	-9.71250	MINC	-5.38947
ARD2	-12.3176	MRSH	-13.5402
ARNE	-12.4405	NEWK	-30.1915
BEAV	-16.7521	NOWA	-8.64474
BESS	-1.97222	NRMN	-1.09756
BIXB	-34.6835	PAWN	-7.21519
BLAC	-5.17500	PERK	-13.8427
BOIS	-3.02586	PORT	-18.7531
BREC	-4.08163	PRYO	-21.9024
BRIS	-18.2805	PUTN	-20.9625
BUTL	-14.8161	REDR	-20.5185
CALV	-34.5000	RING	-4.25287
CAMA	-0.485437	SALL	-25.2899
CENT	-32.7262	SKIA	-26.7848
CHER	-15.9205	SLAP	-12.0297
CHEY	-9.14706	SPEN	-17.6591
CLOU	-27.6333	STIG	-19.8718
COOK	-9.80282	STIL	-10.8506
COPA	-25.7949	STUA	-30.6935
ELRE	-22.6477	TAHL	-17.6988
ERIC	-26.9778	TISH	-8.66216
FAIR	-16.0215	VINI	-26.3699
FORA	-35.3000	WALT	-4.63736
GOOD	-5.62832	WASH	-16.0119
GRA2	-5.01031	WATO	-5.47674
GUTH	-16.6977	WEAT	-2.11236
HASK	-33.1235	WEST	-23.6620
HECT	-11.9143	WILB	-14.3614
HINT	-27.8750		
HOBA	-1.15909		
HOLL	2.61446		
HOOK	-14.1774		
HUGO	-9.17241		
IDAB	-8.85882		
INOL	-18.1625		
JAYX	-25.6282		
KENT	-11.8829		
KING	-22.2588		
LAHO	-19.5349		
LANE	-30.2326		
MARE	-21.5349		
MAYR	-13.3370		
MCAL	-19.8333		

**Table A.9:** BIAS between  $m_{s\text{-ERS}}$  at 50 km and  $m_{s\text{-ASAR}}$  at 3 km at 75 Oklahoma Mesonet stations

Station ID	BIAS [%]	Station ID	BIAS [%]
ACME	5.00784	MEDI	4.11122
ALV2	5.37147	MIAM	1.55517
APAC	4.22567	MINC	-1.51635
ARD2	2.17046	MRSH	-1.45263
ARNE	1.31649	NEWK	6.57434
BEAV	5.06013	NOWA	-4.41110
BESS	2.03024	NRMN	5.94906
BIXB	1.47654	PAWN	3.14322
BLAC	4.35941	PERK	4.26905
BOIS	7.21107	PORT	0.324148
BREC	5.88097	PRYO	1.70453
BRIS	2.78000	PUTN	5.01381
BUTL	8.86843	REDR	4.26166
CALV	3.02668	RING	2.08186
CAMA	7.13003	SALL	-5.00263
CENT	3.40861	SKIA	-4.20580
CHER	6.21773	SLAP	6.61614
CHEY	6.42334	SPEN	4.33624
CLOU	3.25017	STIG	-0.876048
COOK	2.01179	STIL	1.18521
COPA	-4.17370	STUA	0.391415
ELRE	5.12693	TAHL	-0.738813
ERIC	8.90336	TISH	0.592194
FAIR	3.71049	VINI	0.325806
FORA	6.54658	WALT	7.64494
GOOD	6.12727	WASH	1.13545
GRA2	9.94153	WATO	2.20811
GUTH	1.59871	WEAT	1.87605
HASK	2.44681	WEST	1.79723
HECT	-6.28846	WILB	4.45296
HINT	6.61146		
HOBA	4.80229		
HOLL	9.27705		
HOOK	9.18712		
HUGO	7.98586		
IDAB	5.36198		
INOL	-0.156057		
JAYX	-3.67424		
KENT	7.99801		
KING	2.92184		
LAHO	2.92290		
LANE	4.00792		
MARE	6.05547		
MAYR	3.18851		
MCAL	2.13724		

**Table A.10:** BIAS between  $m_{s\text{-ERS}}$  at 50 km and  $m_{s\text{-ASAR}}$  at 50 km at 75 Oklahoma Mesonet stations

Station ID	BIAS [%]	Station ID	BIAS [%]
ACME	5.99051	MEDI	7.29949
ALV2	6.54319	MIAM	0.782258
APAC	7.80592	MINC	2.39152
ARD2	2.50767	MRSH	3.06461
ARNE	4.98533	NEWK	5.24305
BEAV	5.82355	NOWA	-0.378403
BESS	2.03024	NRMN	2.38283
BIXB	3.43904	PAWN	4.43477
BLAC	4.73441	PERK	3.27902
BOIS	9.55021	PORT	-1.41763
BREC	2.68709	PRYO	1.07039
BRIS	0.673516	PUTN	2.56554
BUTL	3.41139	REDR	4.64742
CALV	4.07924	RING	2.16120
CAMA	2.90923	SALL	-2.34549
CENT	1.46543	SKIA	-3.01381
CHER	5.50237	SLAP	6.37660
CHEY	7.05080	SPEN	2.32096
CLOU	1.76454	STIG	-3.13592
COOK	-0.621847	STIL	2.26475
COPA	-2.10959	STUA	-0.883799
ELRE	3.21235	TAHL	3.03227
ERIC	8.93494	TISH	1.81050
FAIR	4.52770	VINI	-2.49994
FORA	-0.429746	WALT	5.75796
GOOD	7.12727	WASH	2.35898
GRA2	9.86072	WATO	3.97104
GUTH	3.74325	WEAT	0.142549
HASK	0.298917	WEST	1.90954
HECT	-0.450329	WILB	5.00328
HINT	1.08047		
HOBA	6.33638		
HOLL	7.72227		
HOOK	7.02582		
HUGO	5.47115		
IDAB	2.90960		
INOL	0.684236		
JAYX	-2.52989		
KENT	10.8809		
KING	2.82132		
LAHO	2.30662		
LANE	0.796465		
MARE	1.72888		
MAYR	4.51330		
MCAL	2.68134		

**Table A.11:** Standard deviation SD between  $m_s$ -ERS at 50 km and in-situ soil moisture at 75 Oklahoma Mesonet stations

Station ID	SD [%]	Station ID	SD [%]
ACME	22.7256	MEDI	21.7846
ALV2	30.1948	MIAM	19.0760
APAC	22.6804	MINC	22.7418
ARD2	21.3213	MRSH	22.3308
ARNE	24.5497	NEWK	18.7752
BEAV	27.0786	NOWA	19.0668
BESS	16.7184	NRMN	17.9993
BIXB	24.3710	PAWN	20.6212
BLAC	23.8899	PERK	21.7861
BOIS	31.0242	PORT	22.7009
BREC	19.9603	PRYO	16.7111
BRIS	25.2655	PUTN	27.4670
BUTL	22.5861	REDR	25.5069
CALV	25.0416	RING	26.0854
CAMA	24.4532	SALL	18.9375
CENT	20.0353	SKIA	16.3573
CHER	32.0891	SLAP	23.3178
CHEY	24.3066	SPEN	19.4209
CLOU	17.7464	STIG	19.6462
COOK	19.2230	STIL	25.1666
COPA	18.5201	STUA	19.5852
ELRE	19.0898	TAHL	21.3950
ERIC	23.2644	TISH	16.6794
FAIR	24.4917	VINI	14.7934
FORA	19.8911	WALT	23.2245
GOOD	21.4483	WASH	19.0785
GRA2	23.4257	WATO	23.9458
GUTH	22.4949	WEAT	21.0370
HASK	15.5271	WEST	19.4239
HECT	16.8413	WILB	19.3593
HINT	29.4981		
HOBA	27.5641		
HOLL	27.1714		
HOOK	24.6285		
HUGO	23.4555		
IDAB	16.7446		
INOL	22.0614		
JAYX	20.0503		
KENT	30.6744		
KING	23.5174		
LAHO	30.3363		
LANE	18.8997		
MARE	20.8651		
MAYR	24.0960		
MCAL	20.6069		

**Table A.12:** Standard deviation SD between  $m_s$ -ASAR at 3 km and in-situ soil moisture at 75 Oklahoma Mesonet stations

Station ID	SD [%]	Station ID	SD [%]
ACME	29.2382	MEDI	24.8890
ALV2	30.7422	MIAM	23.8244
APAC	24.1824	MINC	25.6213
ARD2	29.0733	MRSH	23.2946
ARNE	25.4630	NEWK	14.0734
BEAV	27.3287	NOWA	22.9273
BESS	18.4154	NRMN	29.0578
BIXB	21.4370	PAWN	23.2089
BLAC	24.3258	PERK	22.4403
BOIS	33.5840	PORT	24.3967
BREC	22.9216	PRYO	19.0140
BRIS	24.4787	PUTN	27.8124
BUTL	23.0641	REDR	21.8757
CALV	21.3510	RING	25.0246
CAMA	25.3841	SALL	25.1177
CENT	21.5133	SKIA	19.5570
CHER	30.2937	SLAP	30.2743
CHEY	23.9256	SPEN	24.8892
CLOU	21.6666	STIG	20.9902
COOK	25.0100	STIL	29.3164
COPA	23.2137	STUA	18.8749
ELRE	18.4893	TAHL	21.1004
ERIC	27.2842	TISH	18.4089
FAIR	27.6532	VINI	17.6551
FORA	22.8516	WALT	29.4318
GOOD	23.4860	WASH	23.6241
GRA2	25.5854	WATO	19.9931
GUTH	21.0247	WEAT	23.1118
HASK	15.1814	WEST	25.4337
HECT	20.5730	WILB	19.6501
HINT	28.4631		
HOBA	30.8621		
HOLL	31.8161		
HOOK	26.0703		
HUGO	25.6508		
IDAB	19.0013		
INOL	25.9180		
JAYX	24.8889		
KENT	31.4136		
KING	22.3920		
LAHO	27.8746		
LANE	22.2431		
MARE	20.8811		
MAYR	23.4492		
MCAL	26.8496		

**Table A.13: Standard deviation SD between  $m_s$ -ASAR at 50 km and in-situ soil moisture at 75 Oklahoma Mesonet stations**

Station ID	SD [%]	Station ID	SD [%]
ACME	25.0477	MEDI	23.0090
ALV2	28.9086	MIAM	21.0512
APAC	21.6592	MINC	22.6346
ARD2	23.9877	MRSH	21.7372
ARNE	25.0457	NEWK	15.1411
BEAV	26.9949	NOWA	20.4879
BESS	17.2887	NRMN	18.9428
BIXB	18.6682	PAWN	21.5178
BLAC	23.5994	PERK	20.7243
BOIS	32.2944	PORT	22.5818
BREC	20.4242	PRYO	19.3592
BRIS	22.2463	PUTN	23.5041
BUTL	21.9097	REDR	22.4839
CALV	21.4436	RING	26.9518
CAMA	24.7310	SALL	19.6380
CENT	19.6336	SKIA	15.4045
CHER	28.3744	SLAP	24.2122
CHEY	25.7760	SPEN	23.4133
CLOU	20.4980	STIG	19.3822
COOK	18.0465	STIL	24.1572
COPA	20.5106	STUA	17.7548
ELRE	17.5021	TAHL	19.7470
ERIC	21.9933	TISH	19.5849
FAIR	22.9205	VINI	14.9680
FORA	16.3586	WALT	24.6173
GOOD	20.6662	WASH	21.1338
GRA2	22.3726	WATO	21.3573
GUTH	20.3181	WEAT	19.4553
HASK	14.6111	WEST	21.5764
HECT	22.3372	WILB	22.8017
HINT	25.9997		
HOBA	25.5972		
HOLL	27.8895		
HOOK	24.3708		
HUGO	26.7317		
IDAB	18.2738		
INOL	25.0516		
JAYX	21.0590		
KENT	31.9399		
KING	19.7750		
LAHO	24.2534		
LANE	20.4771		
MARE	19.5987		
MAYR	23.7132		
MCAL	24.1081		

**Table A.14:** Standard deviation SD between  $m_{s\text{-ERS}}$  at 50 km and  $m_{s\text{-ASAR}}$  at 3 km at 75 Oklahoma Mesonet stations

Station ID	SD [%]	Station ID	SD [%]
ACME	18.7356	MEDI	19.4695
ALV2	14.8421	MIAM	21.9262
APAC	14.1127	MINC	18.1876
ARD2	22.0278	MRSH	14.9809
ARNE	14.4830	NEWK	14.0747
BEAV	17.8522	NOWA	17.3704
BESS	15.7919	NRMN	24.1809
BIXB	19.5537	PAWN	14.9108
BLAC	15.3807	PERK	16.1285
BOIS	10.8407	PORT	17.4000
BREC	15.6021	PRYO	16.5778
BRIS	20.4056	PUTN	14.9307
BUTL	14.3105	REDR	14.7130
CALV	22.0493	RING	16.0448
CAMA	14.9224	SALL	22.5157
CENT	20.6233	SKIA	18.0489
CHER	21.1182	SLAP	17.7684
CHEY	13.1261	SPEN	18.3444
CLOU	16.0722	STIG	16.7104
COOK	23.2659	STIL	21.8139
COPA	15.5978	STUA	18.0536
ELRE	17.1166	TAHL	18.5561
ERIC	17.1826	TISH	13.4453
FAIR	17.5786	VINI	15.0208
FORA	20.6074	WALT	17.7344
GOOD	15.4032	WASH	18.3960
GRA2	15.6989	WATO	13.5434
GUTH	14.4153	WEAT	13.7958
HASK	15.1073	WEST	19.2174
HECT	15.3128	WILB	14.9878
HINT	14.6981		
HOBA	16.1414		
HOLL	17.8636		
HOOK	17.9598		
HUGO	15.8942		
IDAB	14.7939		
INOL	17.5872		
JAYX	18.4148		
KENT	13.7113		
KING	14.5688		
LAHO	17.1451		
LANE	18.0475		
MARE	16.6421		
MAYR	13.9890		
MCAL	17.9157		

**Table A.15:** Standard deviation SD between  $m_{s\text{-ERS}}$  at 50 km and  $m_{s\text{-ASAR}}$  at 50 km at 75 Oklahoma Mesonet stations

Station ID	SD [%]	Station ID	SD [%]
ACME	11.4034	MEDI	12.0986
ALV2	10.3576	MIAM	14.2372
APAC	9.44824	MINC	9.13107
ARD2	14.3240	MRSH	8.01796
ARNE	8.44693	NEWK	10.4748
BEAV	8.75852	NOWA	11.9420
BESS	11.0398	NRMN	13.2688
BIXB	15.7856	PAWN	10.7813
BLAC	8.43795	PERK	11.2837
BOIS	6.86166	PORT	13.1601
BREC	9.23397	PRYO	14.1605
BRIS	12.0811	PUTN	9.98306
BUTL	9.68424	REDR	11.1048
CALV	13.8375	RING	12.9439
CAMA	10.3253	SALL	14.4955
CENT	12.7750	SKIA	10.8815
CHER	10.7288	SLAP	9.03774
CHEY	9.62337	SPEN	12.9781
CLOU	13.6399	STIG	14.6411
COOK	16.4901	STIL	12.1816
COPA	10.7273	STUA	14.5404
ELRE	8.92413	TAHL	15.9540
ERIC	9.68342	TISH	11.5816
FAIR	10.1053	VINI	12.2383
FORA	12.7506	WALT	9.72522
GOOD	8.50356	WASH	12.7651
GRA2	9.23705	WATO	10.8211
GUTH	11.8315	WEAT	9.67412
HASK	13.7137	WEST	14.8041
HECT	13.3706	WILB	13.0557
HINT	9.80872		
HOBA	10.8858		
HOLL	10.5021		
HOOK	9.32436		
HUGO	12.6995		
IDAB	12.8824		
INOL	14.7322		
JAYX	14.5802		
KENT	7.66045		
KING	10.7493		
LAHO	10.7650		
LANE	12.4163		
MARE	12.1038		
MAYR	9.42522		
MCAL	13.1882		

## **APPENDIX:**

## **FIGURES**

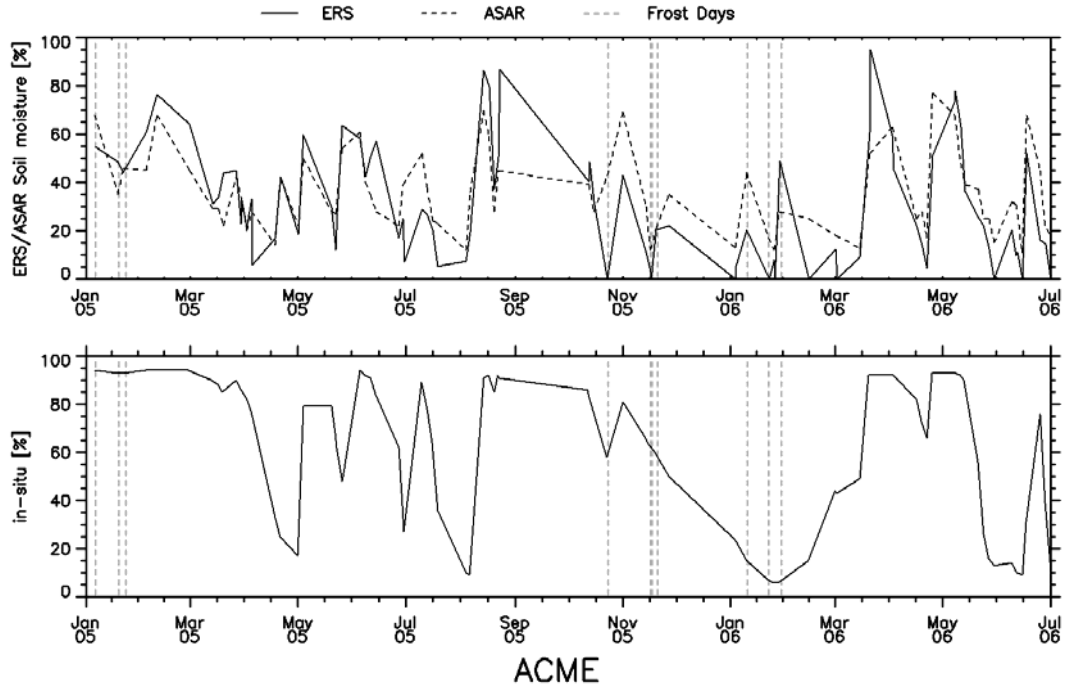


**Figure B 1:** Soil moisture time series from ASAR GM (solid line) and ERS scatterometer (dashed line) (top) and in-situ measurements (bottom) at the MESONET station ACME for the period January 2005 to July 2006.

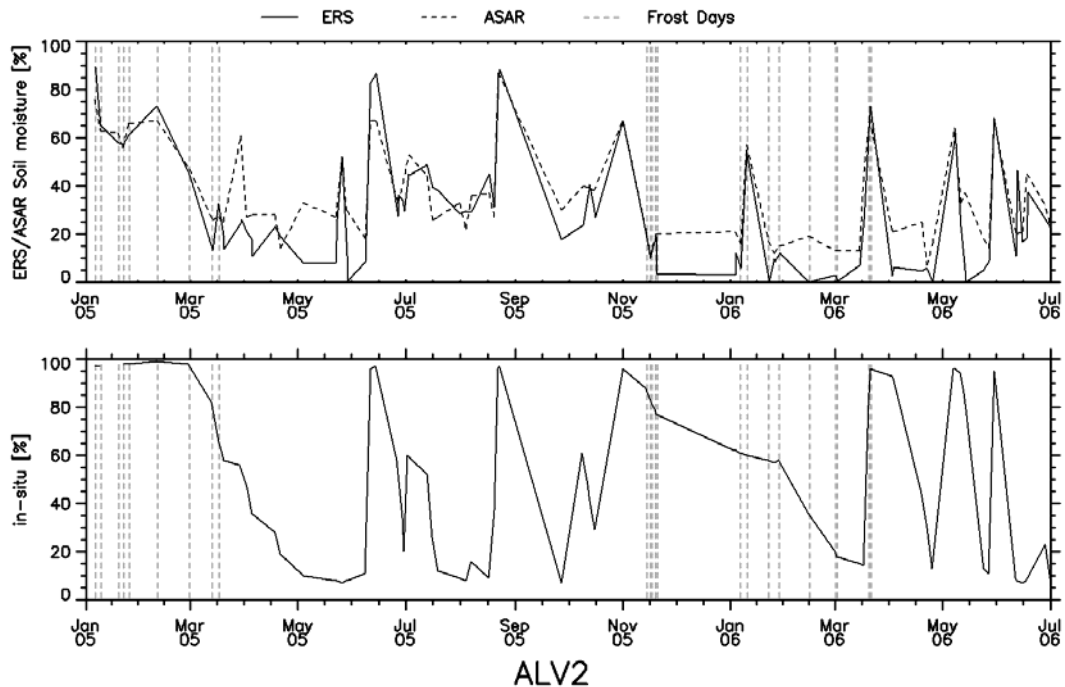


**Figure B 2:** Soil moisture time series from ASAR GM (solid line) and ERS scatterometer (dashed line) (top) and in-situ measurements (bottom) at the MESONET station ALV2 for the period January 2005 to July 2006.

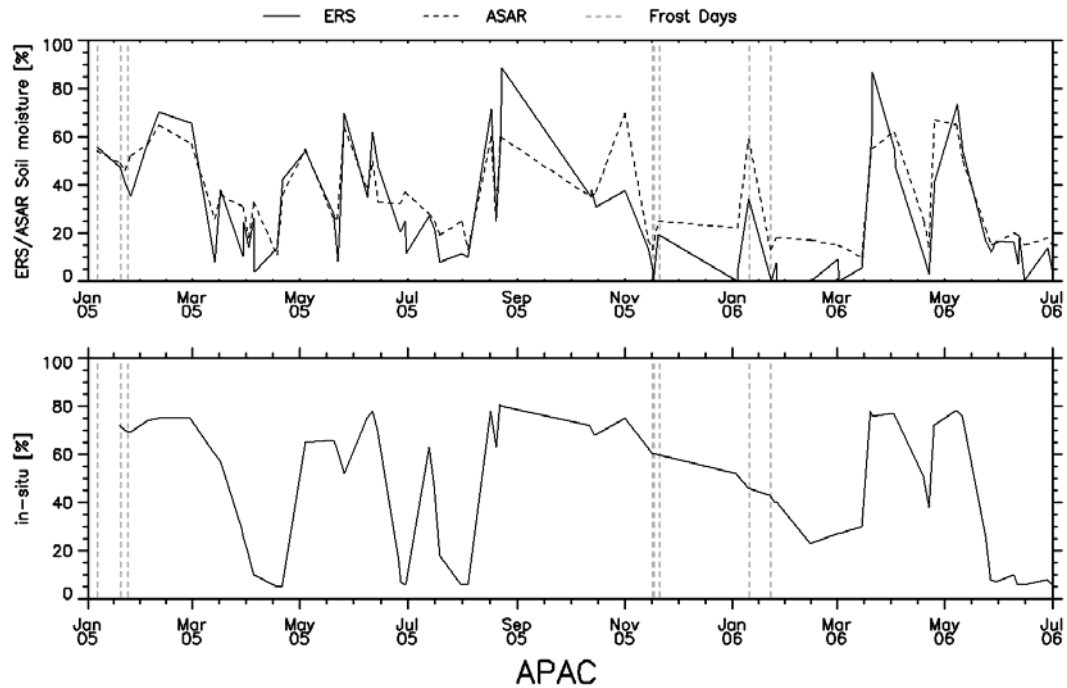


**Figure B 3:** Soil moisture time series from ASAR GM (solid line) and ERS scatterometer (dashed line) (top) and in-situ measurements (bottom) at the MESONET station APAC for the period January 2005 to July 2006.

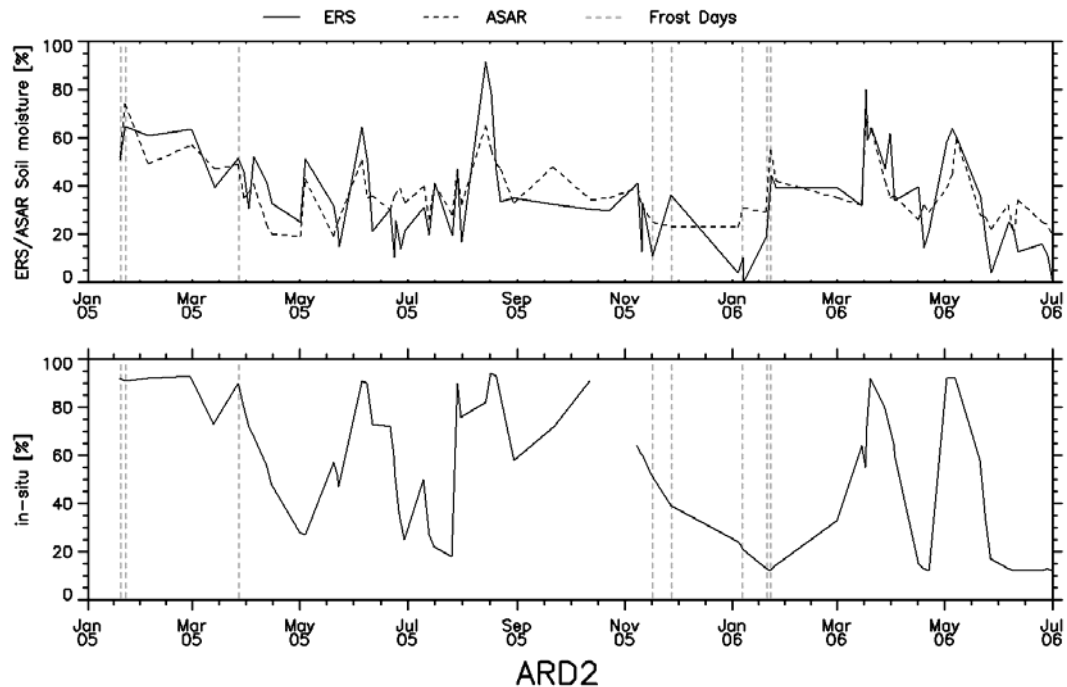


**Figure B 4:** Soil moisture time series from ASAR GM (solid line) and ERS scatterometer (dashed line) (top) and in-situ measurements (bottom) at the MESONET station ARD2 for the period January 2005 to July 2006.

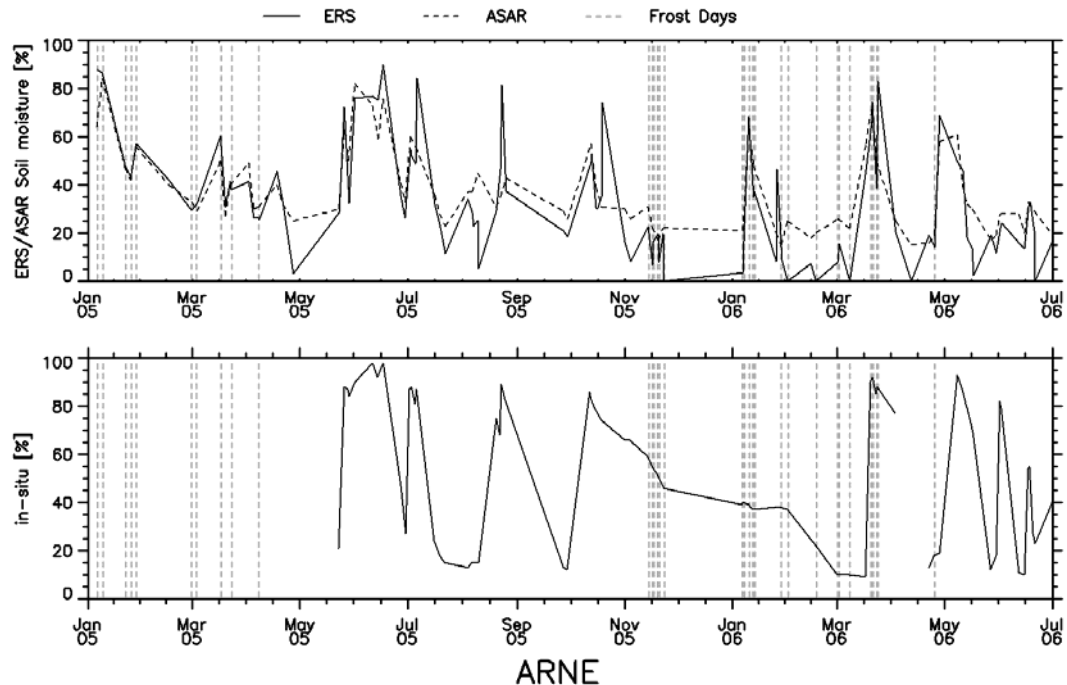


**Figure B 5:** Soil moisture time series from ASAR GM (solid line) and ERS scatterometer (dashed line) (top) and in-situ measurements (bottom) at the MESONET station ARNE for the period January 2005 to July 2006.

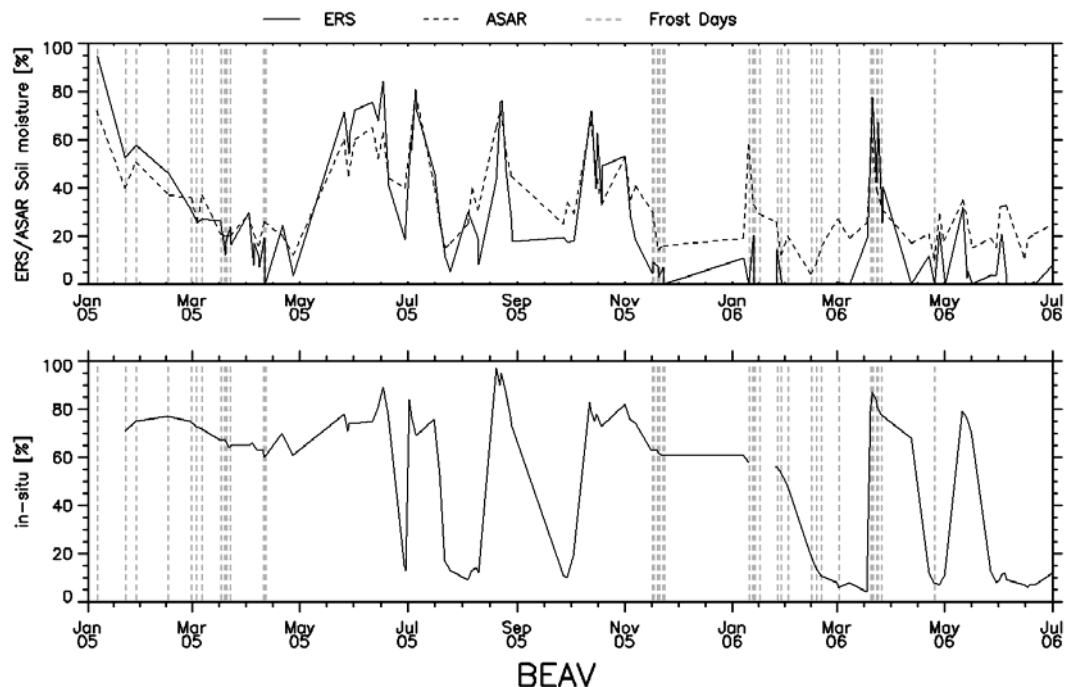


**Figure B 6:** Soil moisture time series from ASAR GM (solid line) and ERS scatterometer (dashed line) (top) and in-situ measurements (bottom) at the MESONET station BEAV for the period January 2005 to July 2006.

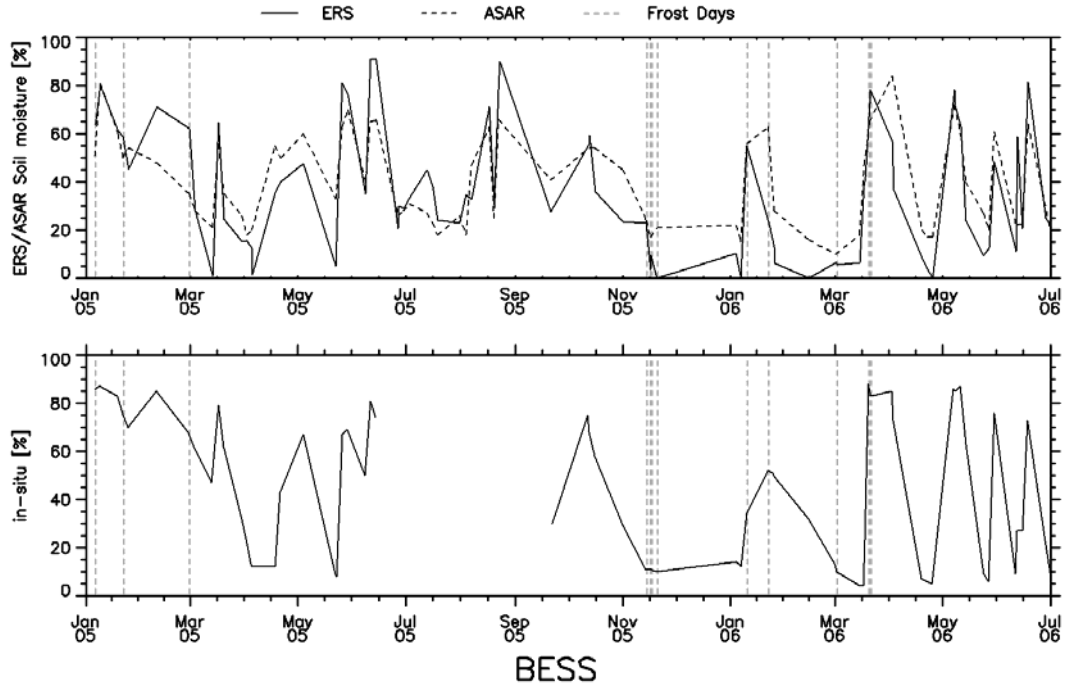


**Figure B 7:** Soil moisture time series from ASAR GM (solid line) and ERS scatterometer (dashed line) (top) and in-situ measurements (bottom) at the MESONET station BESS for the period January 2005 to July 2006.

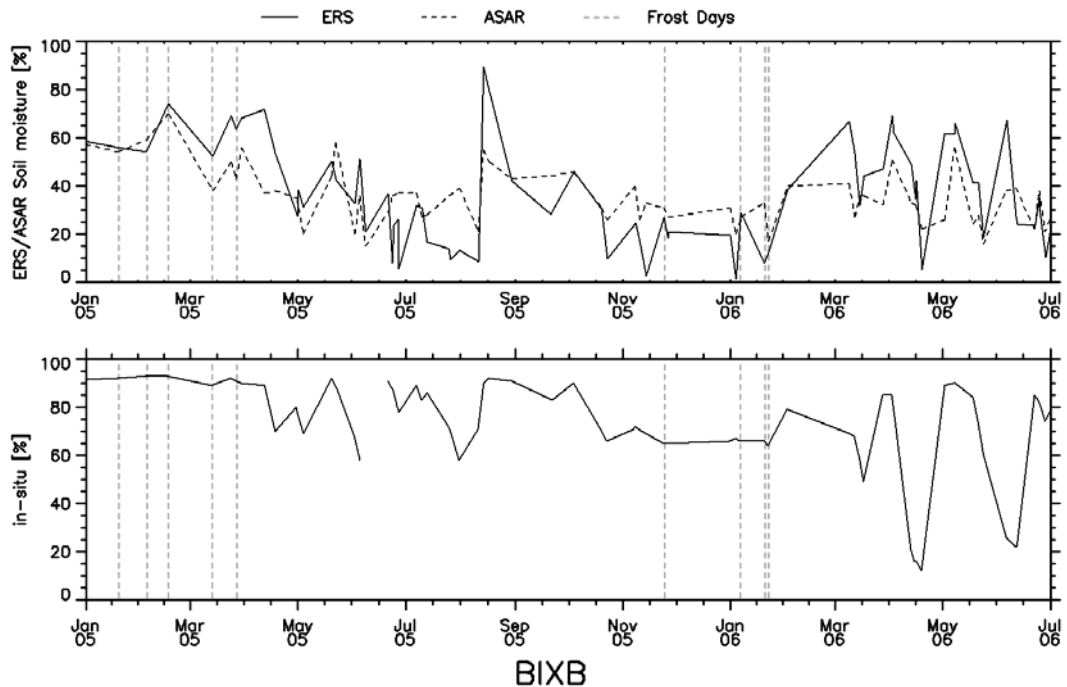


**Figure B 8:** Soil moisture time series from ASAR GM (solid line) and ERS scatterometer (dashed line) (top) and in-situ measurements (bottom) at the MESONET station BIXB for the period January 2005 to July 2006.

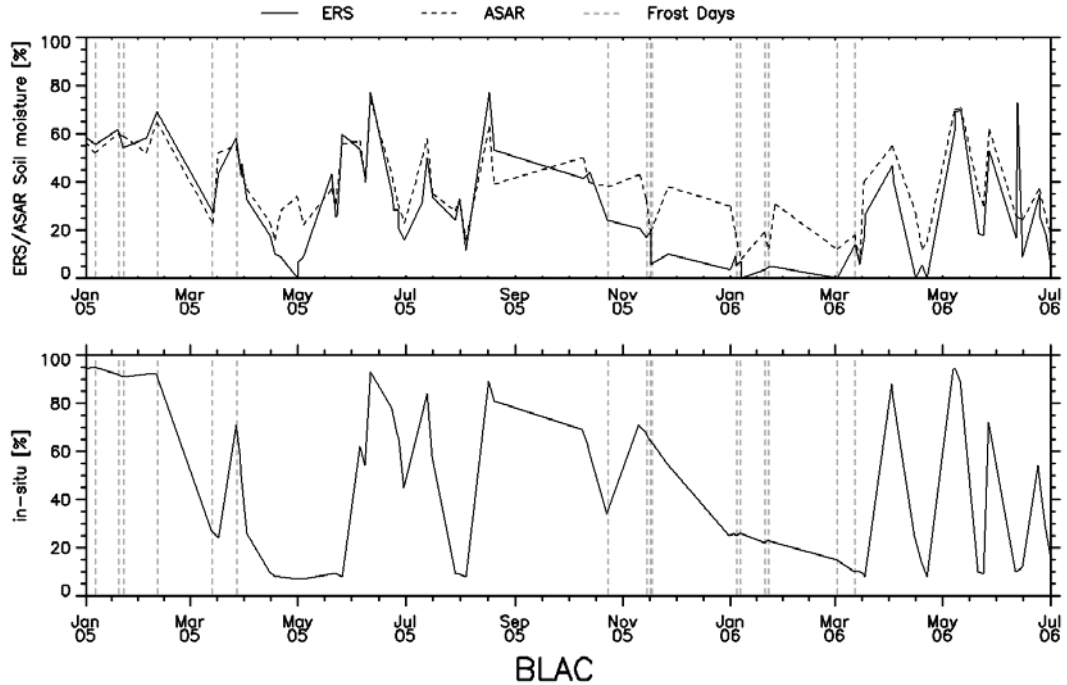


**Figure B 9:** Soil moisture time series from ASAR GM (solid line) and ERS scatterometer (dashed line) (top) and in-situ measurements (bottom) at the MESONET station BLAC for the period January 2005 to July 2006.

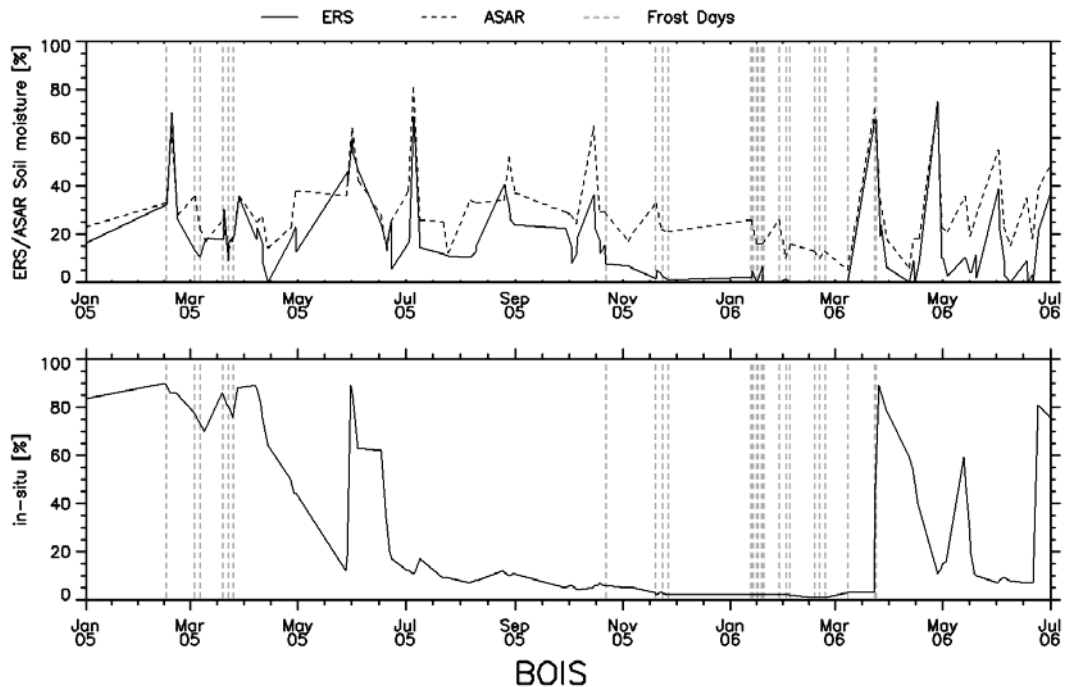


**Figure B 10:** Soil moisture time series from ASAR GM (solid line) and ERS scatterometer (dashed line) (top) and in-situ measurements (bottom) at the MESONET station BOIS for the period January 2005 to July 2006.

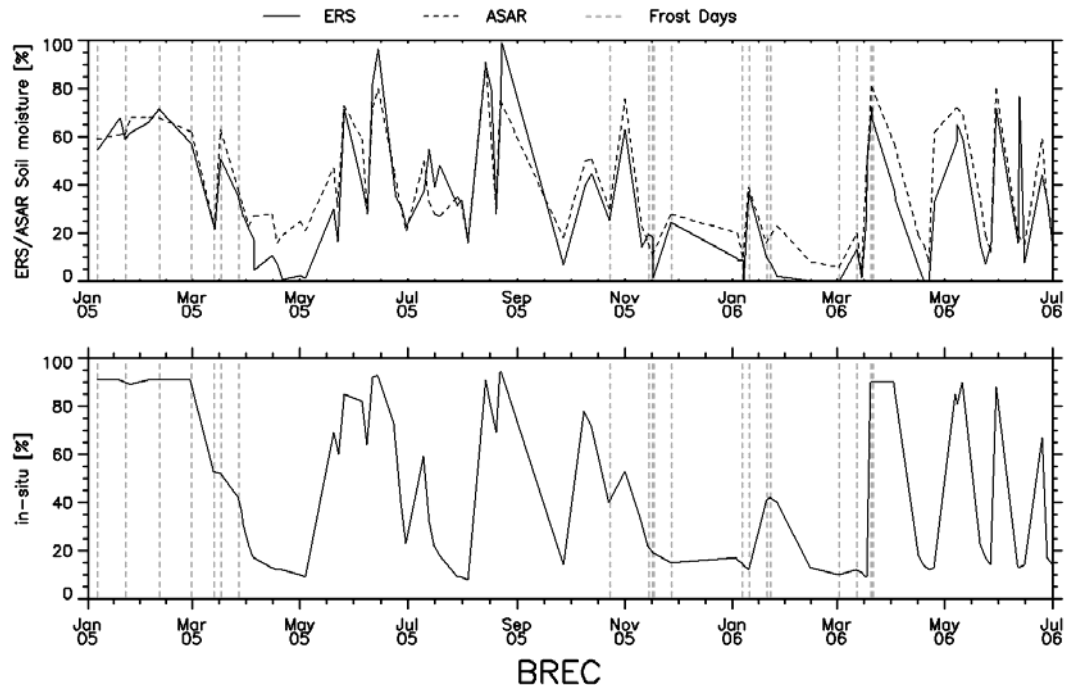


**Figure B 11:** Soil moisture time series from ASAR GM (solid line) and ERS scatterometer (dashed line) (top) and in-situ measurements (bottom) at the MESONET station BREC for the period January 2005 to July 2006.

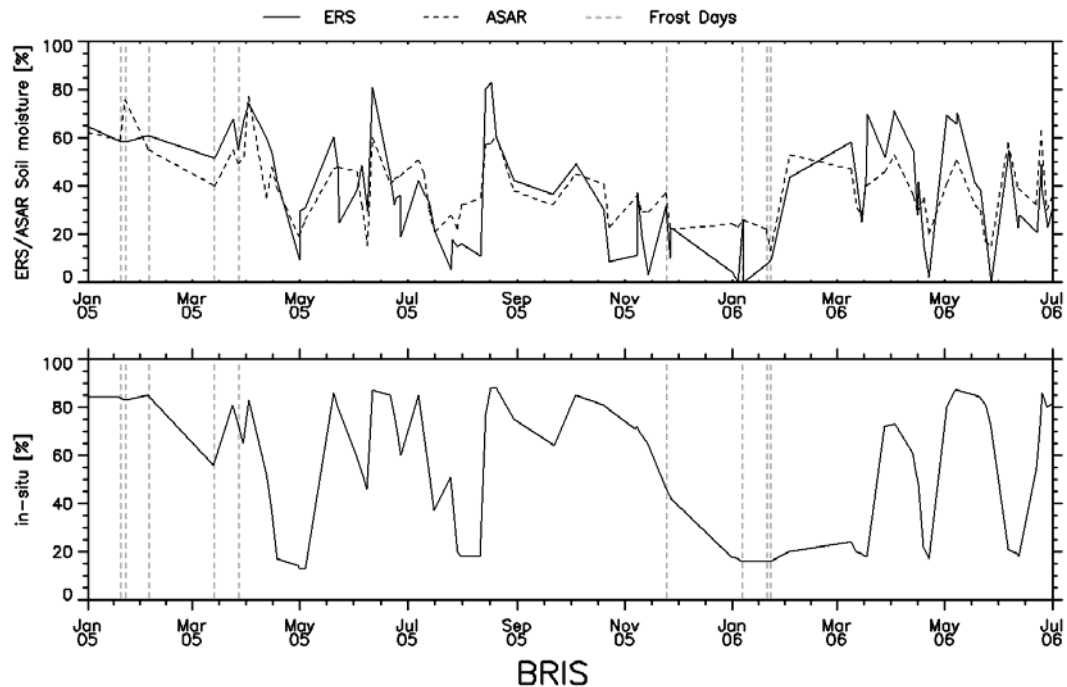


**Figure B 12:** Soil moisture time series from ASAR GM (solid line) and ERS scatterometer (dashed line) (top) and in-situ measurements (bottom) at the MESONET station BRIS for the period January 2005 to July 2006.

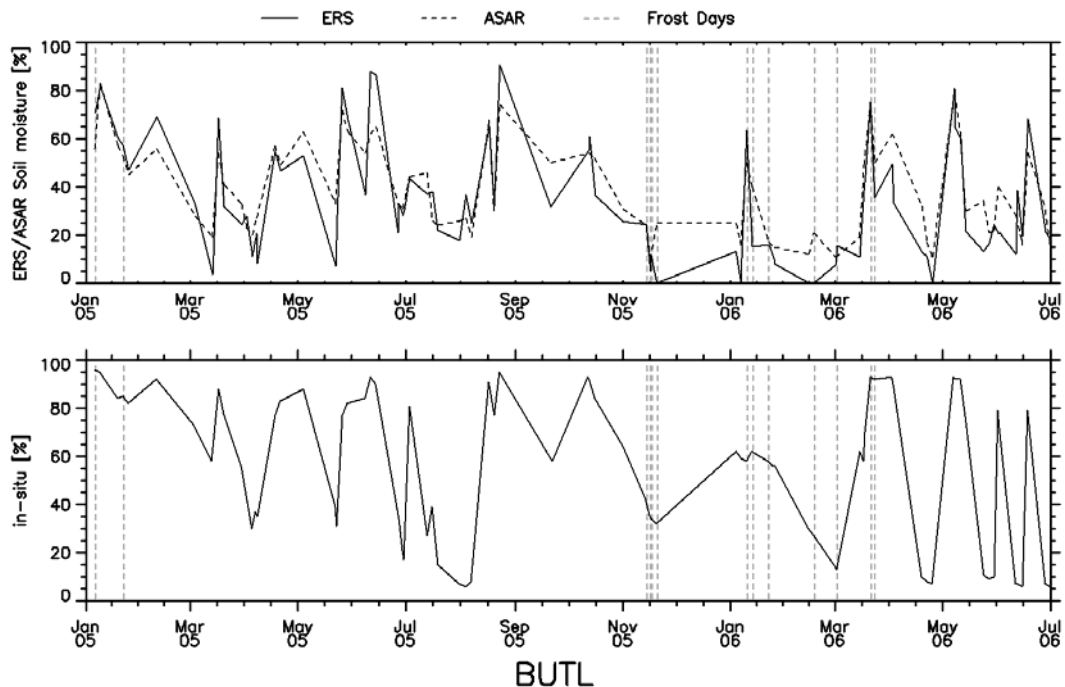


**Figure B 13:** Soil moisture time series from ASAR GM (solid line) and ERS scatterometer (dashed line) (top) and in-situ measurements (bottom) at the MESONET station BUTL for the period January 2005 to July 2006.

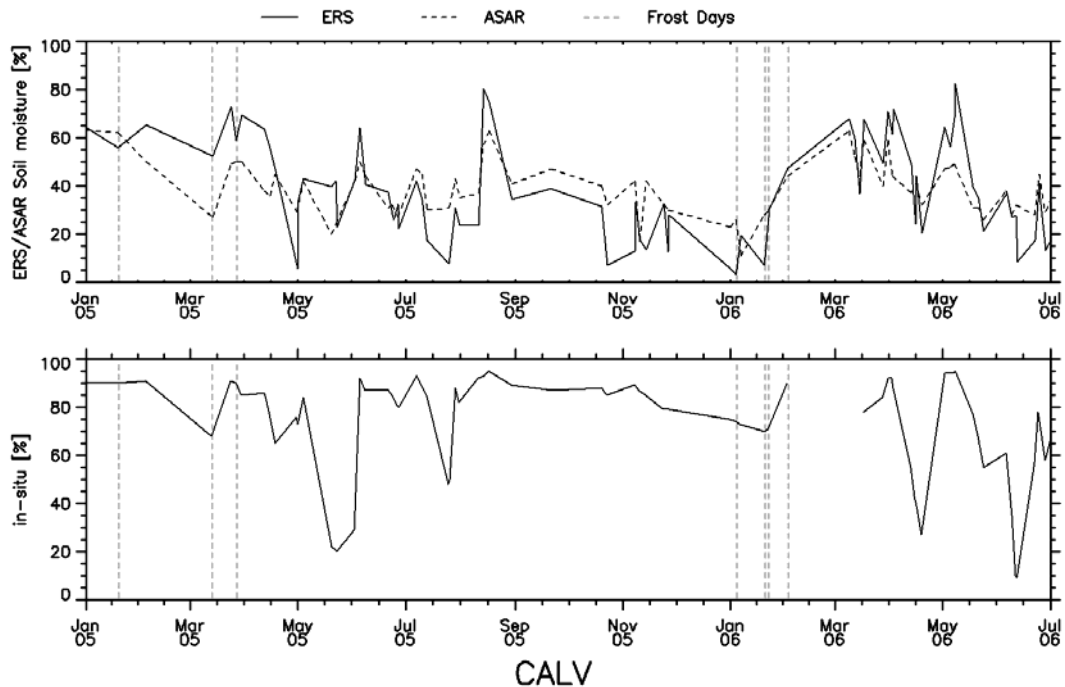


**Figure B 14:** Soil moisture time series from ASAR GM (solid line) and ERS scatterometer (dashed line) (top) and in-situ measurements (bottom) at the MESONET station CALV for the period January 2005 to July 2006.

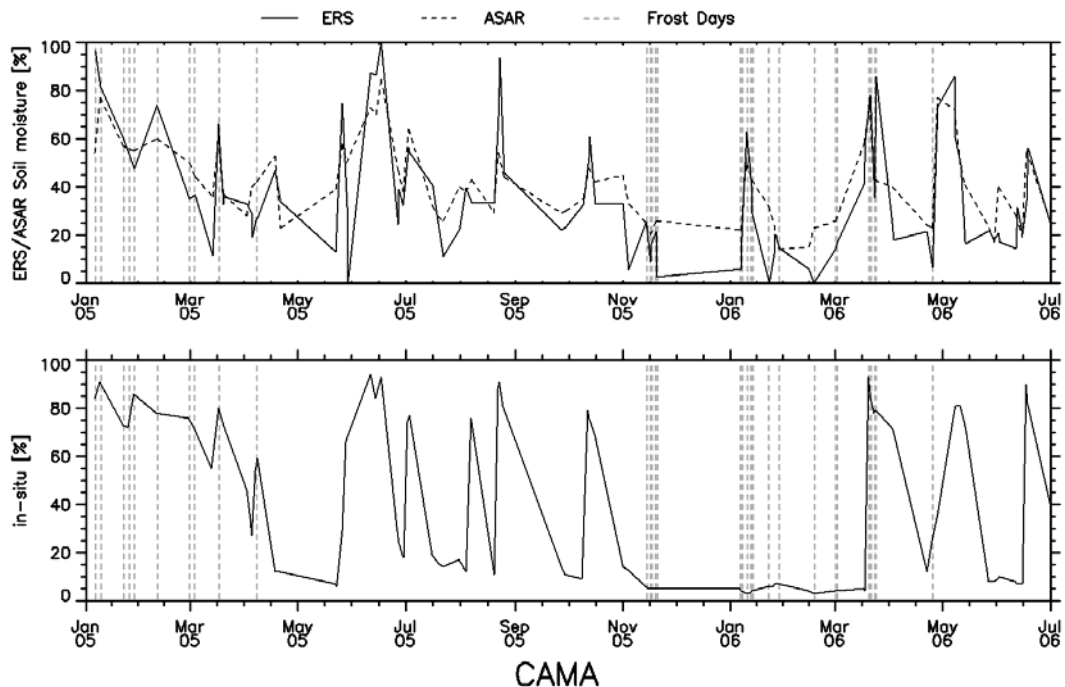


**Figure B 15:** Soil moisture time series from ASAR GM (solid line) and ERS scatterometer (dashed line) (top) and in-situ measurements (bottom) at the MESONET station CAMA for the period January 2005 to July 2006.

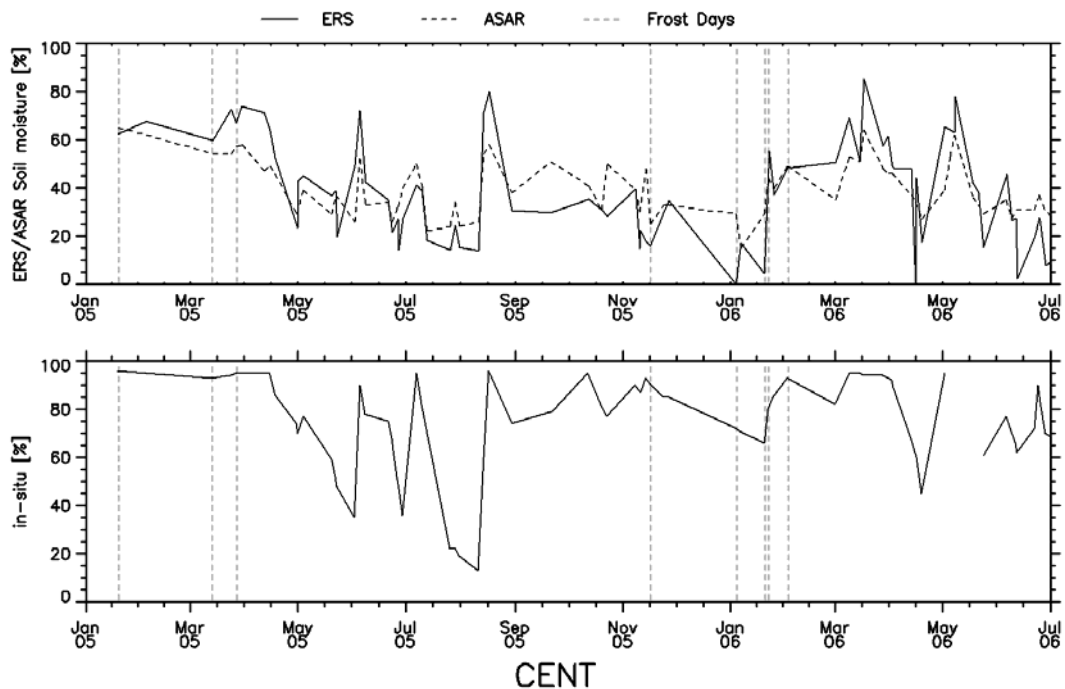


**Figure B 16:** Soil moisture time series from ASAR GM (solid line) and ERS scatterometer (dashed line) (top) and in-situ measurements (bottom) at the MESONET station CENT for the period January 2005 to July 2006.

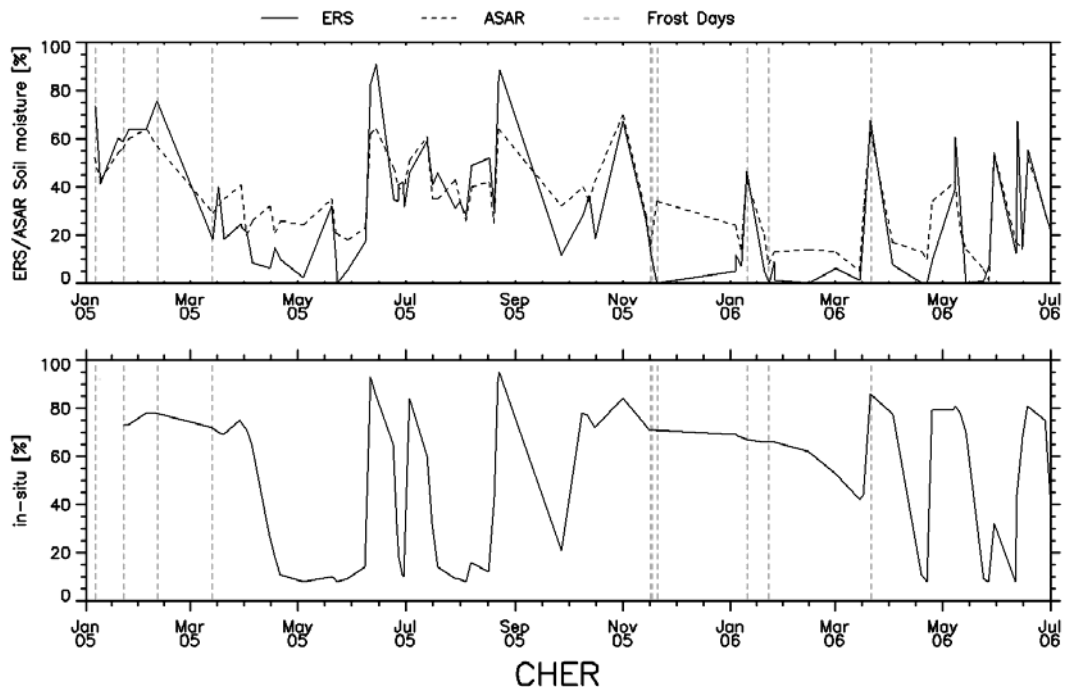


**Figure B 17:** Soil moisture time series from ASAR GM (solid line) and ERS scatterometer (dashed line) (top) and in-situ measurements (bottom) at the MESONET station CHER for the period January 2005 to July 2006.

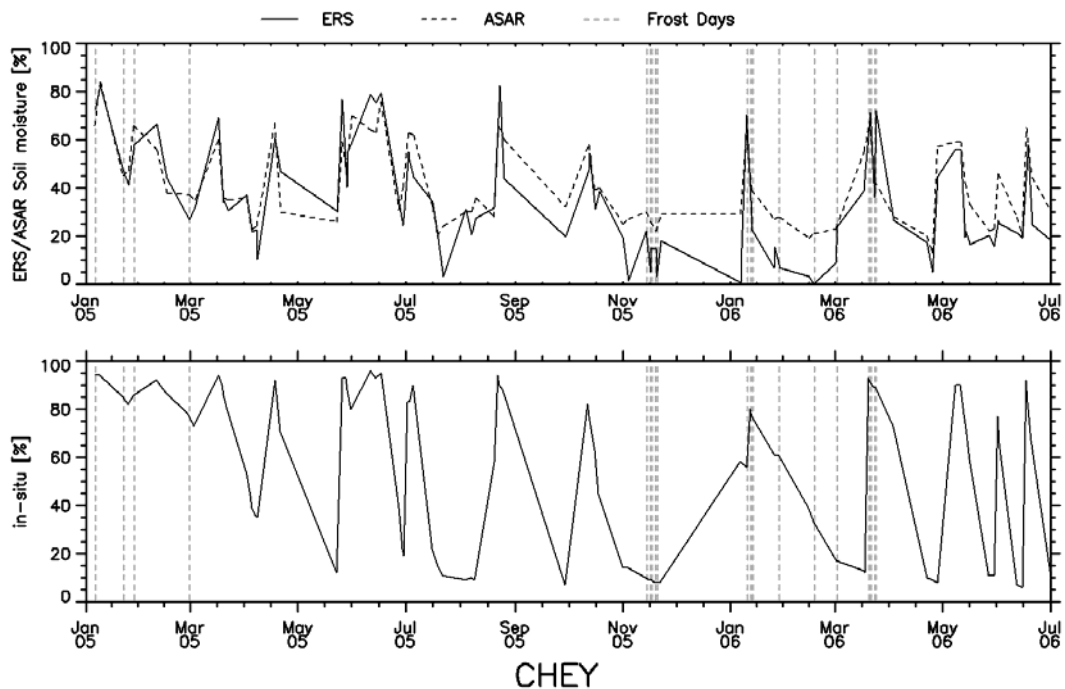


**Figure B 18:** Soil moisture time series from ASAR GM (solid line) and ERS scatterometer (dashed line) (top) and in-situ measurements (bottom) at the MESONET station CHEY for the period January 2005 to July 2006.

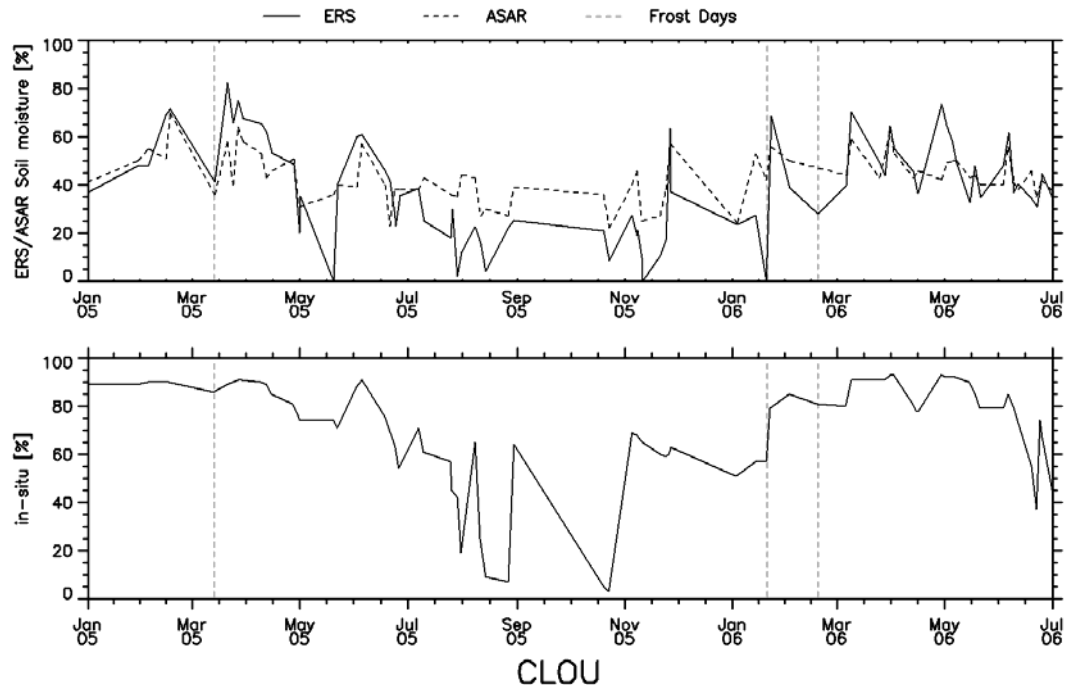


**Figure B 19:** Soil moisture time series from ASAR GM (solid line) and ERS scatterometer (dashed line) (top) and in-situ measurements (bottom) at the MESONET station CLOU for the period January 2005 to July 2006.

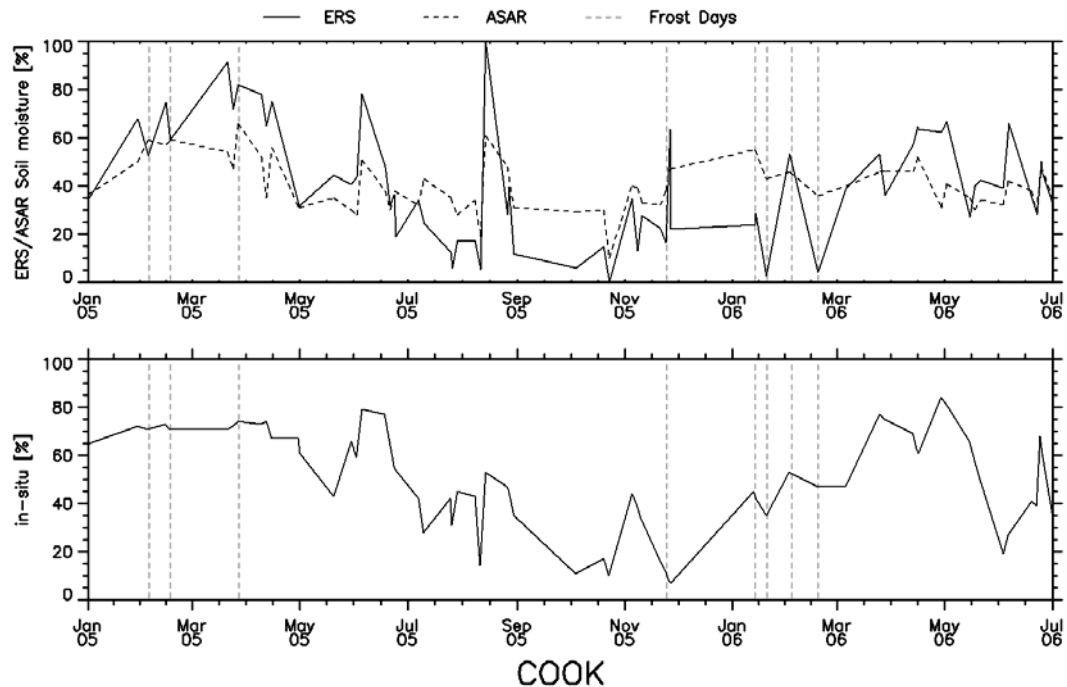


**Figure B 20:** Soil moisture time series from ASAR GM (solid line) and ERS scatterometer (dashed line) (top) and in-situ measurements (bottom) at the MESONET station COOK for the period January 2005 to July 2006.

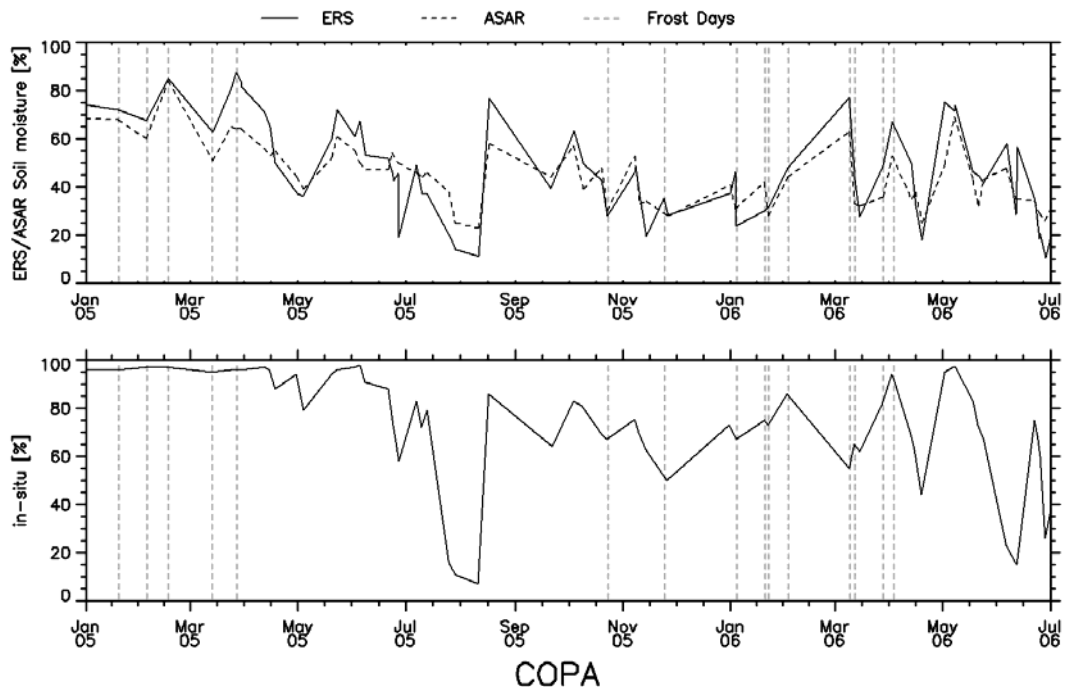


**Figure B 21:** Soil moisture time series from ASAR GM (solid line) and ERS scatterometer (dashed line) (top) and in-situ measurements (bottom) at the MESONET station COPA for the period January 2005 to July 2006.

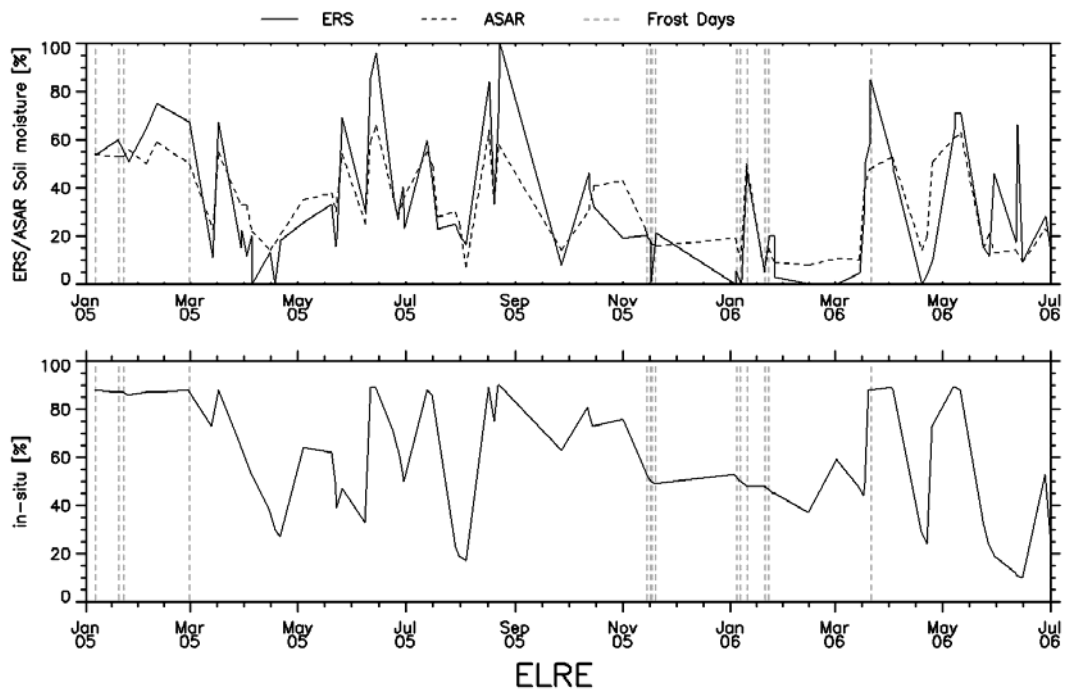


**Figure B 22:** Soil moisture time series from ASAR GM (solid line) and ERS scatterometer (dashed line) (top) and in-situ measurements (bottom) at the MESONET station ELRE for the period January 2005 to July 2006.

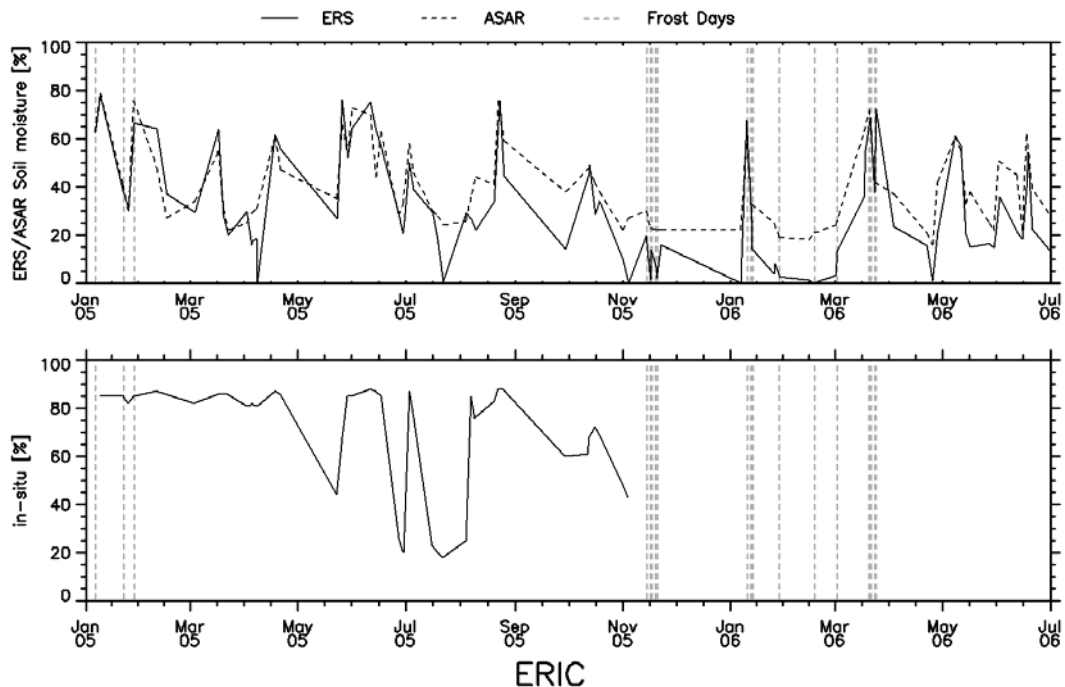


**Figure B 23:** Soil moisture time series from ASAR GM (solid line) and ERS scatterometer (dashed line) (top) and in-situ measurements (bottom) at the MESONET station ERIC for the period January 2005 to July 2006.

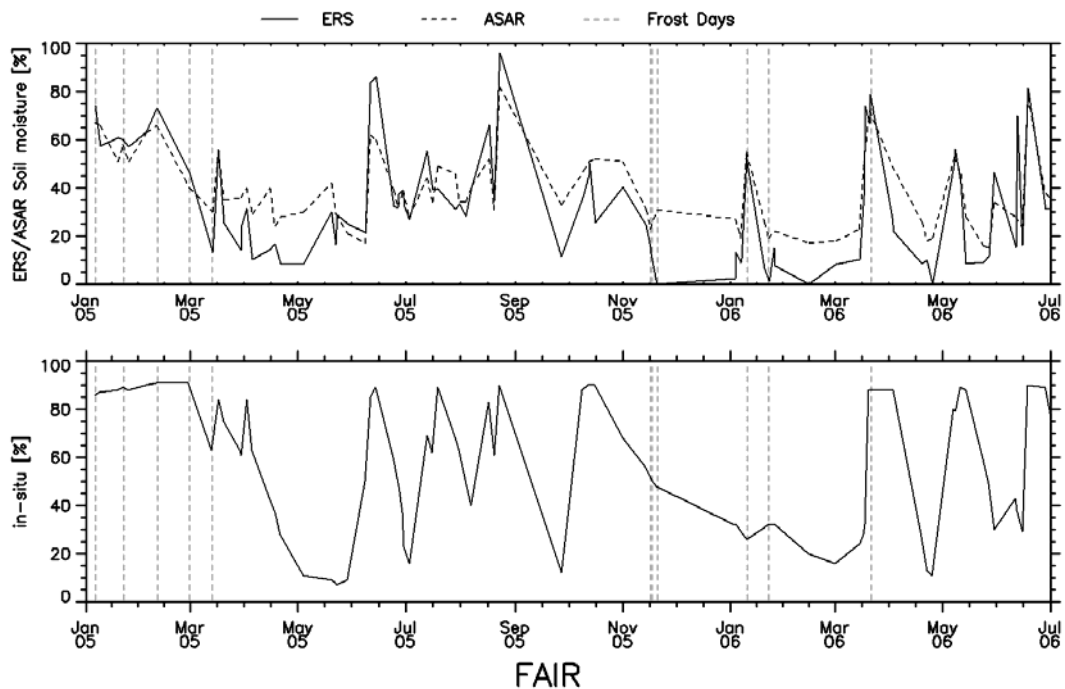


**Figure B 24:** Soil moisture time series from ASAR GM (solid line) and ERS scatterometer (dashed line) (top) and in-situ measurements (bottom) at the MESONET station FAIR for the period January 2005 to July 2006.

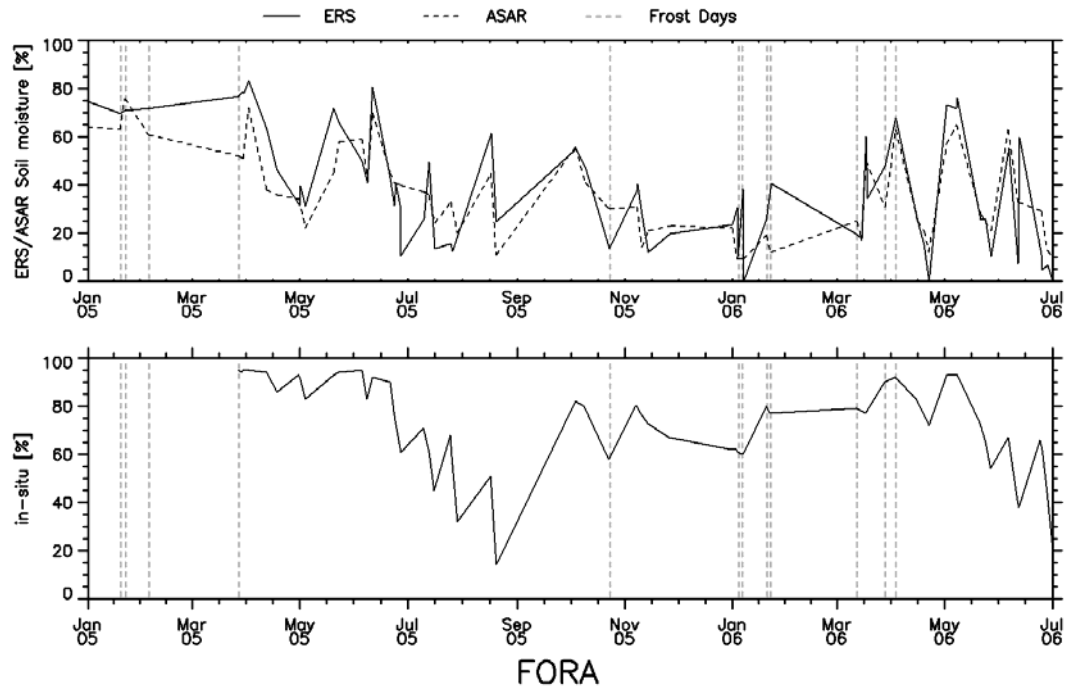


**Figure B 25:** Soil moisture time series from ASAR GM (solid line) and ERS scatterometer (dashed line) (top) and in-situ measurements (bottom) at the MESONET station FORA for the period January 2005 to July 2006.

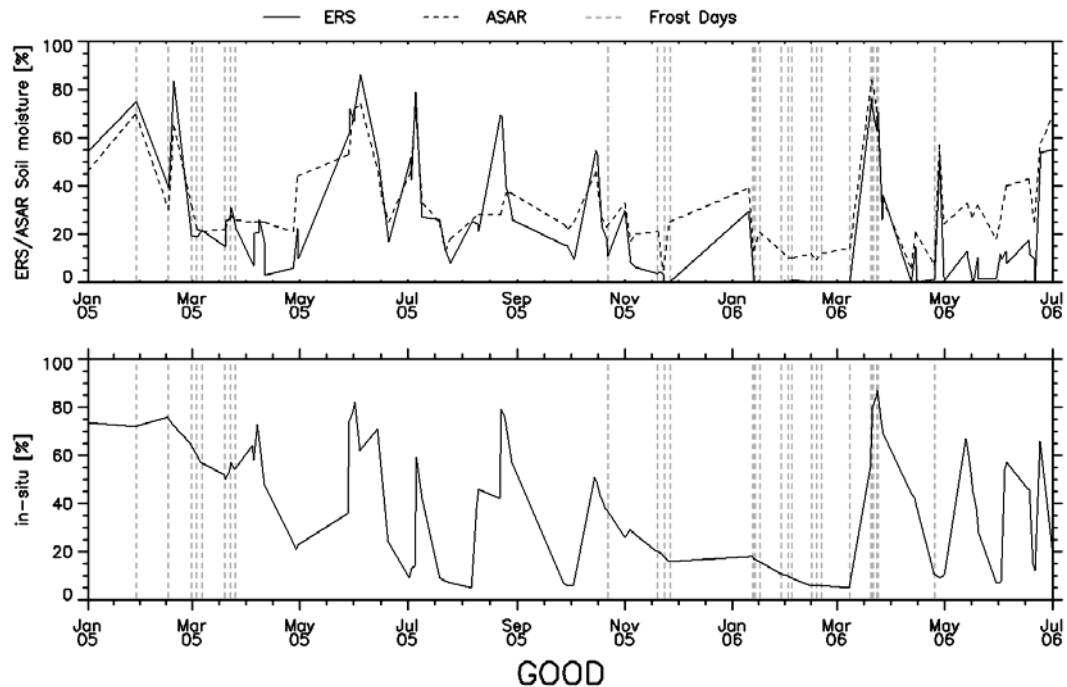


**Figure B 26:** Soil moisture time series from ASAR GM (solid line) and ERS scatterometer (dashed line) (top) and in-situ measurements (bottom) at the MESONET station GOOD for the period January 2005 to July 2006.

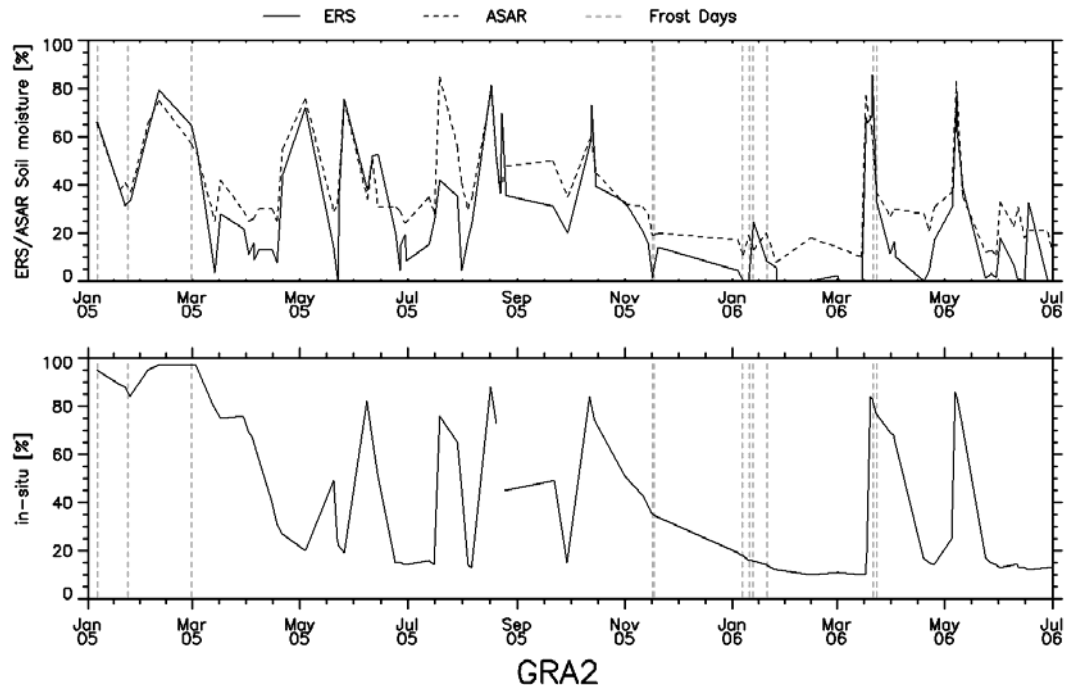


**Figure B 27:** Soil moisture time series from ASAR GM (solid line) and ERS scatterometer (dashed line) (top) and in-situ measurements (bottom) at the MESONET station GRA2 for the period January 2005 to July 2006.

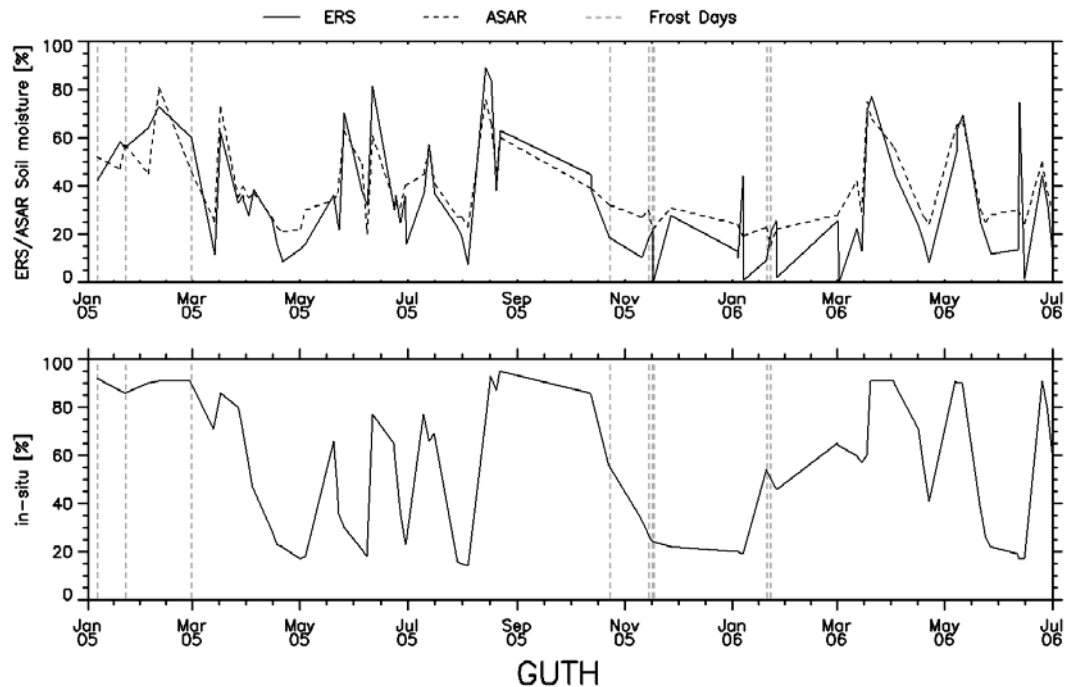


**Figure B 28:** Soil moisture time series from ASAR GM (solid line) and ERS scatterometer (dashed line) (top) and in-situ measurements (bottom) at the MESONET station GUTH for the period January 2005 to July 2006.

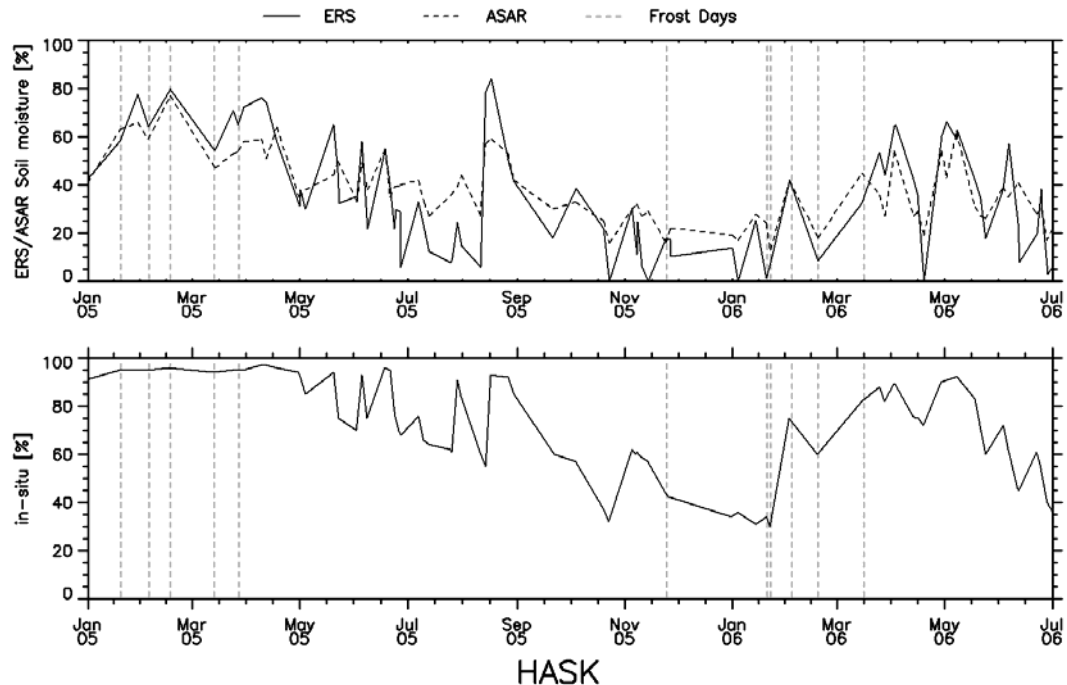


**Figure B 29:** Soil moisture time series from ASAR GM (solid line) and ERS scatterometer (dashed line) (top) and in-situ measurements (bottom) at the MESONET station HASK for the period January 2005 to July 2006.

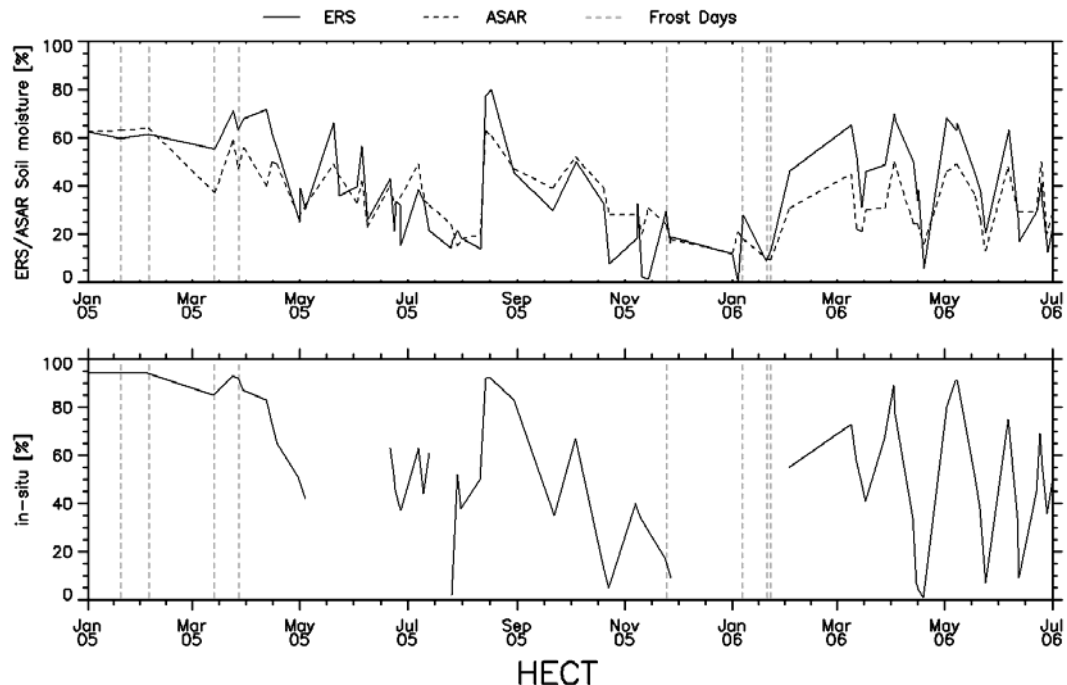


**Figure B 30:** Soil moisture time series from ASAR GM (solid line) and ERS scatterometer (dashed line) (top) and in-situ measurements (bottom) at the MESONET station HECT for the period January 2005 to July 2006.

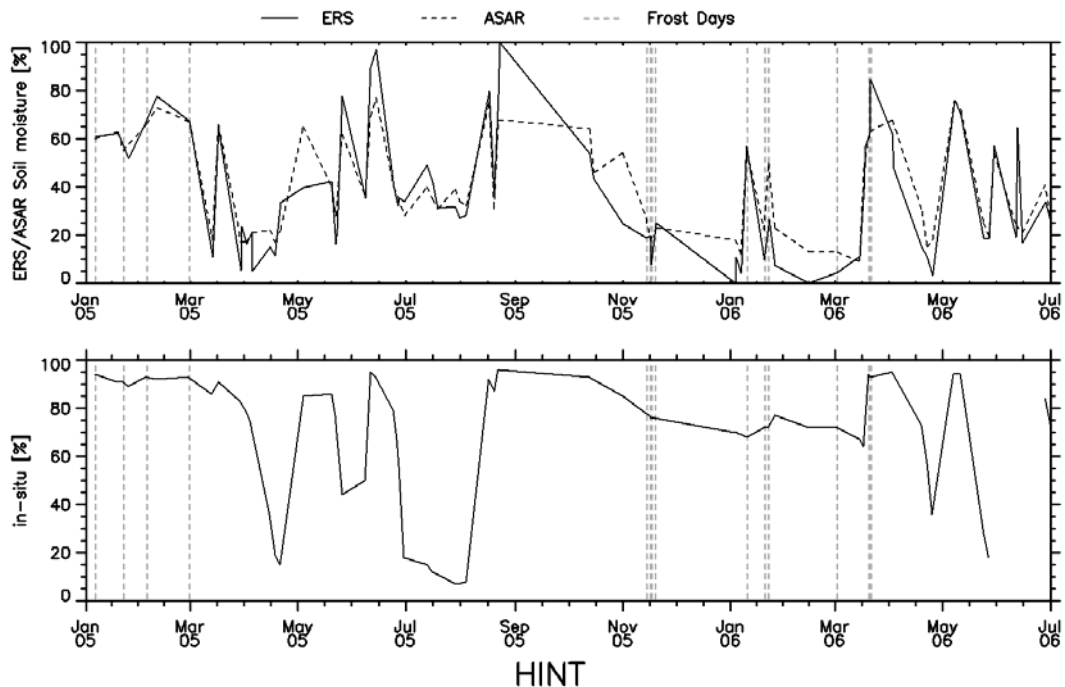


**Figure B 31:** Soil moisture time series from ASAR GM (solid line) and ERS scatterometer (dashed line) (top) and in-situ measurements (bottom) at the MESONET station HINT for the period January 2005 to July 2006.

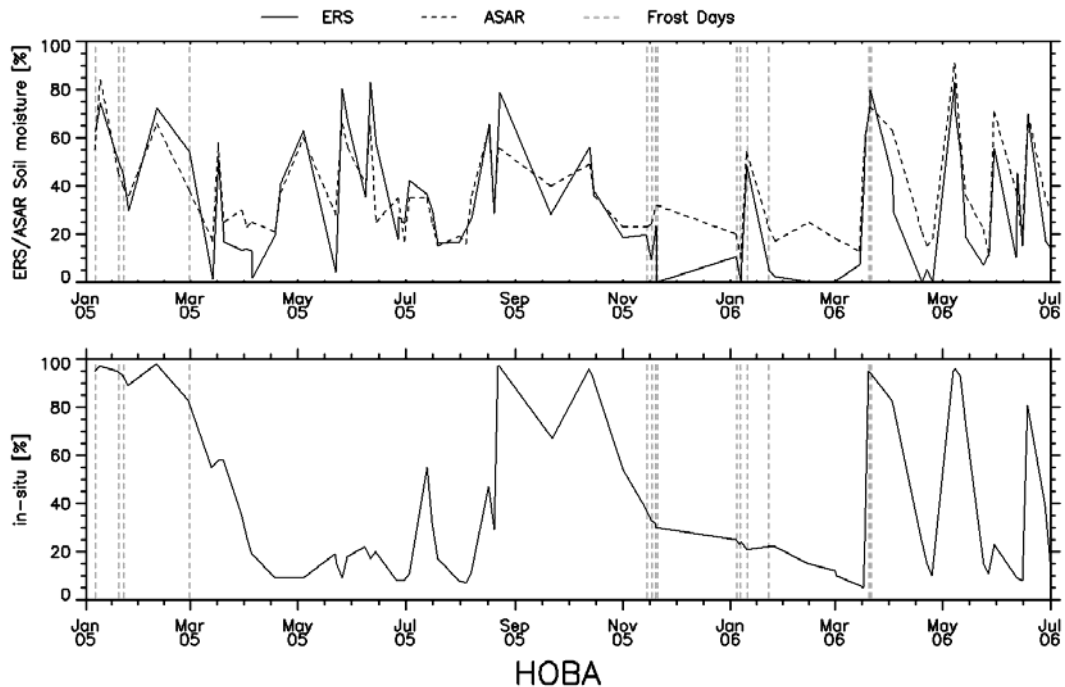


**Figure B 32:** Soil moisture time series from ASAR GM (solid line) and ERS scatterometer (dashed line) (top) and in-situ measurements (bottom) at the MESONET station HOBA for the period January 2005 to July 2006.

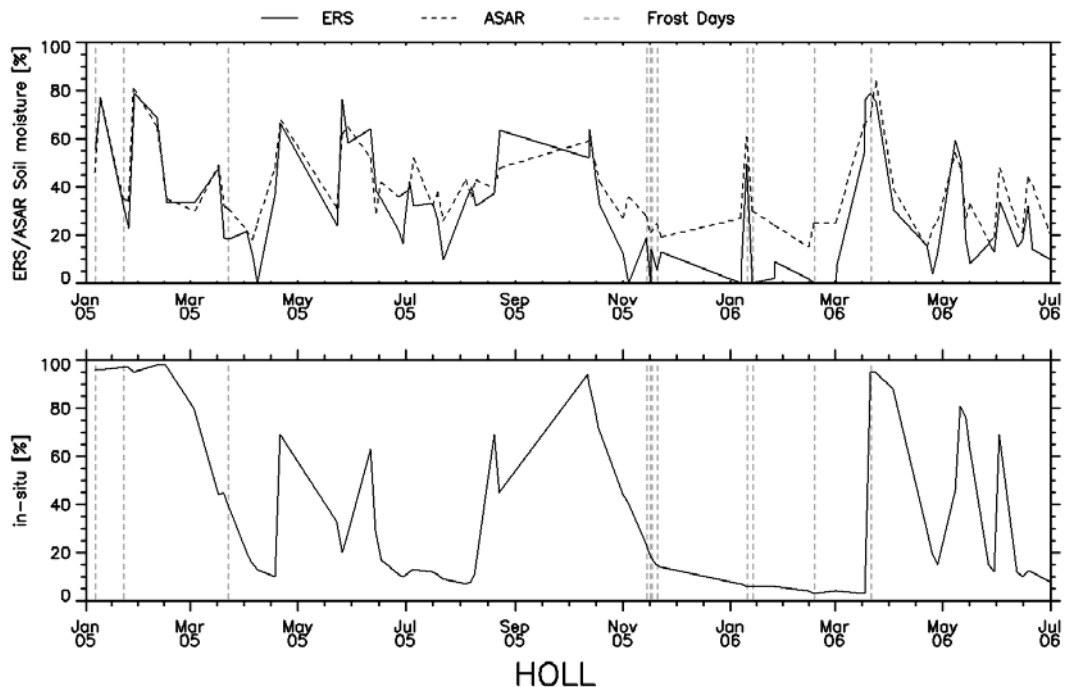


**Figure B 33:** Soil moisture time series from ASAR GM (solid line) and ERS scatterometer (dashed line) (top) and in-situ measurements (bottom) at the MESONET station HOLL for the period January 2005 to July 2006.

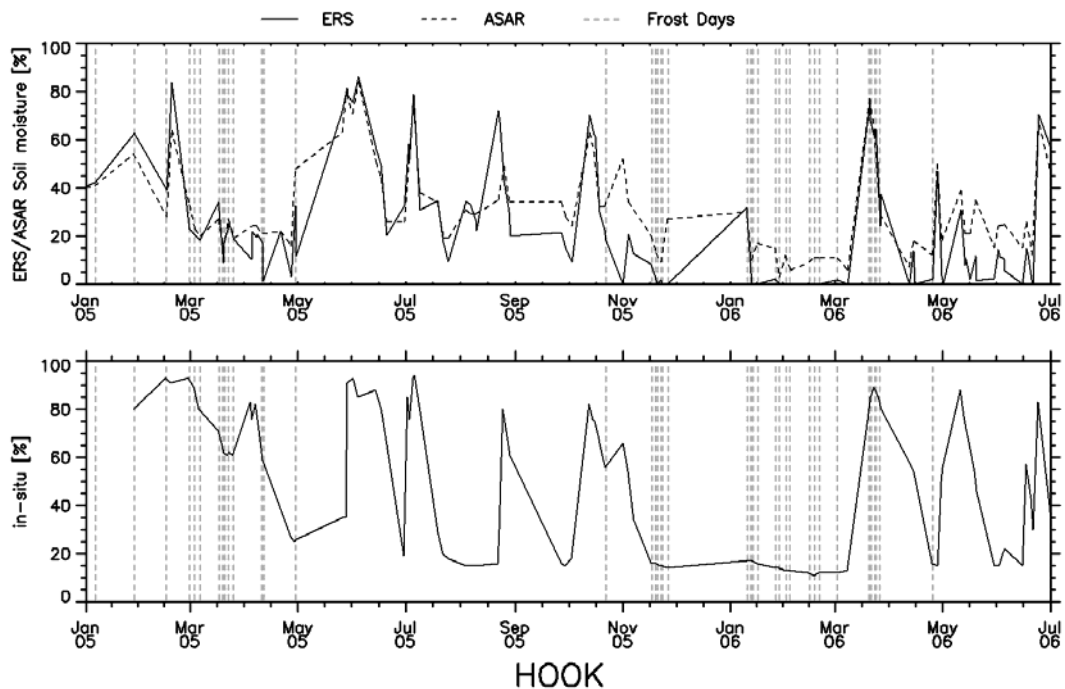


**Figure B 34:** Soil moisture time series from ASAR GM (solid line) and ERS scatterometer (dashed line) (top) and in-situ measurements (bottom) at the MESONET station HOOK for the period January 2005 to July 2006.

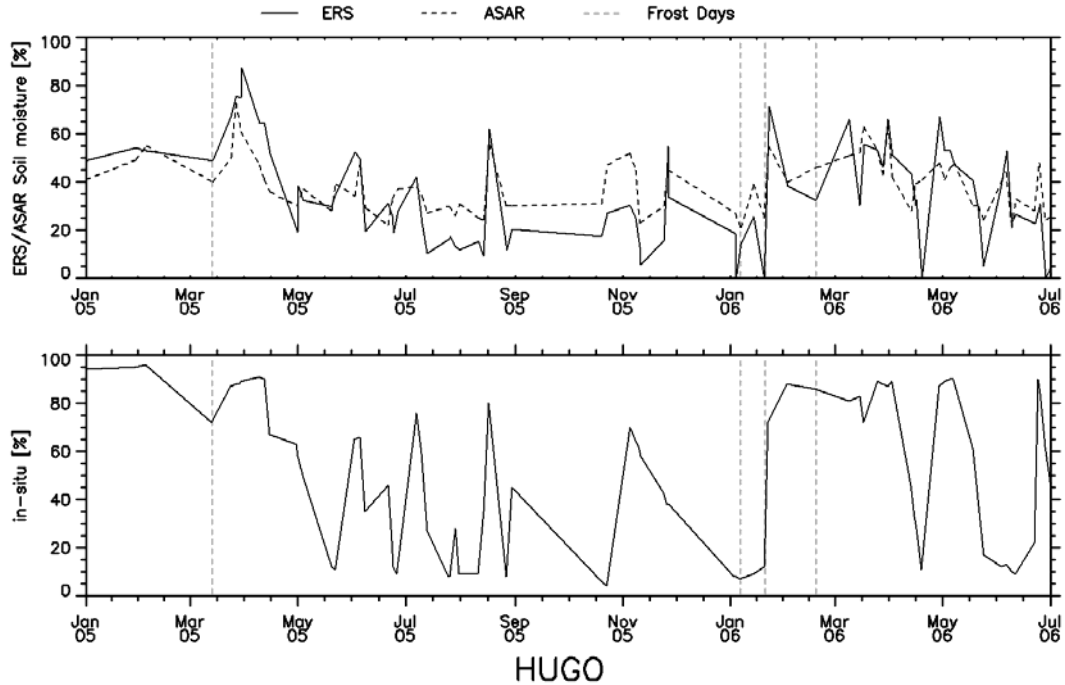


**Figure B 35:** Soil moisture time series from ASAR GM (solid line) and ERS scatterometer (dashed line) (top) and in-situ measurements (bottom) at the MESONET station HUGO for the period January 2005 to July 2006.

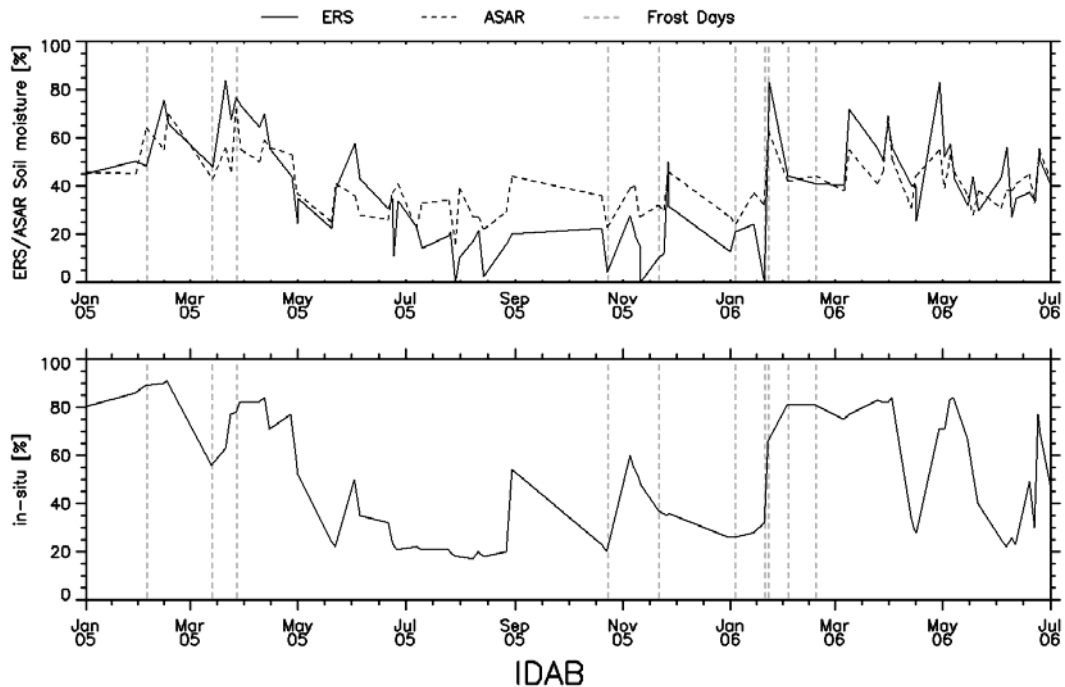


**Figure B 36:** Soil moisture time series from ASAR GM (solid line) and ERS scatterometer (dashed line) (top) and in-situ measurements (bottom) at the MESONET station IDAB for the period January 2005 to July 2006.

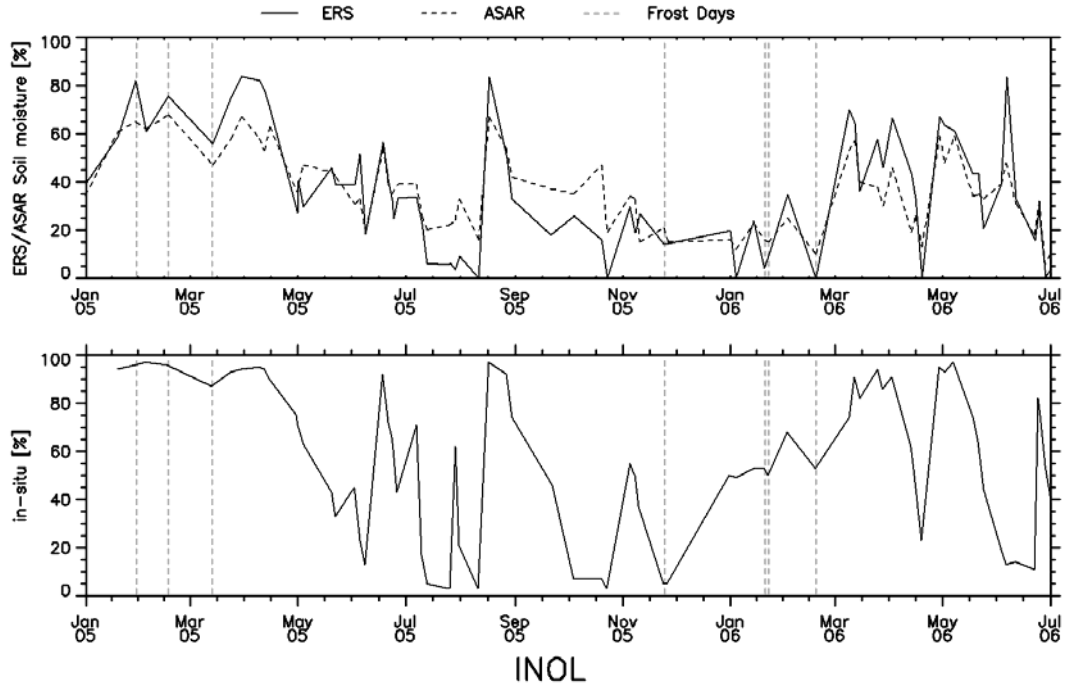


**Figure B 37:** Soil moisture time series from ASAR GM (solid line) and ERS scatterometer (dashed line) (top) and in-situ measurements (bottom) at the MESONET station INOL for the period January 2005 to July 2006.

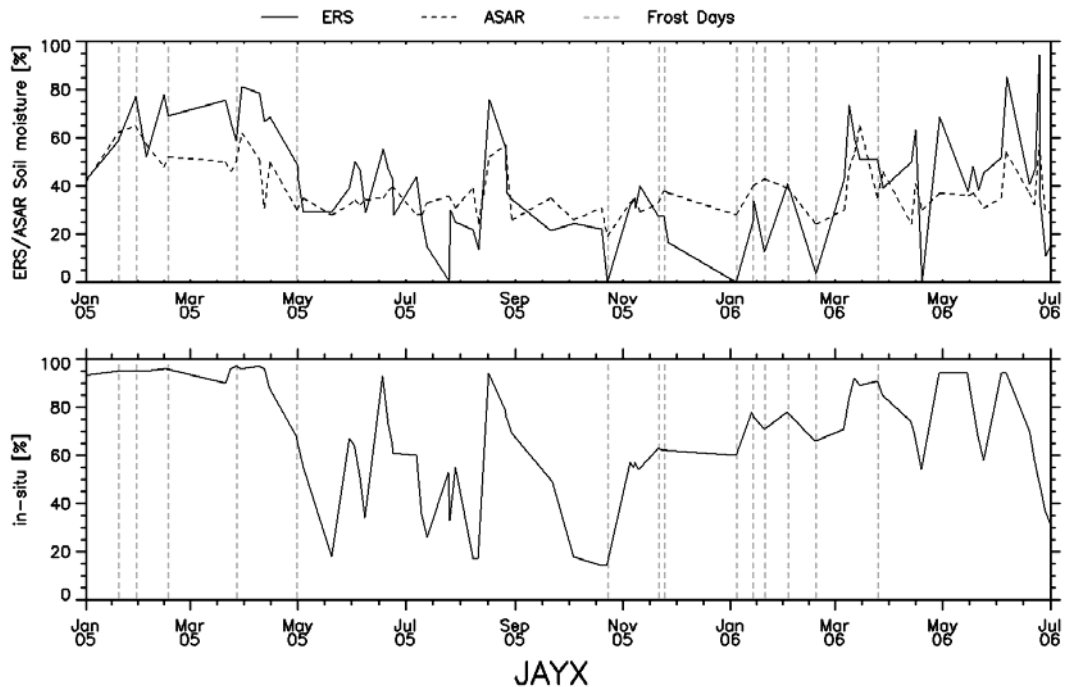


**Figure B 38:** Soil moisture time series from ASAR GM (solid line) and ERS scatterometer (dashed line) (top) and in-situ measurements (bottom) at the MESONET station JAYX for the period January 2005 to July 2006.

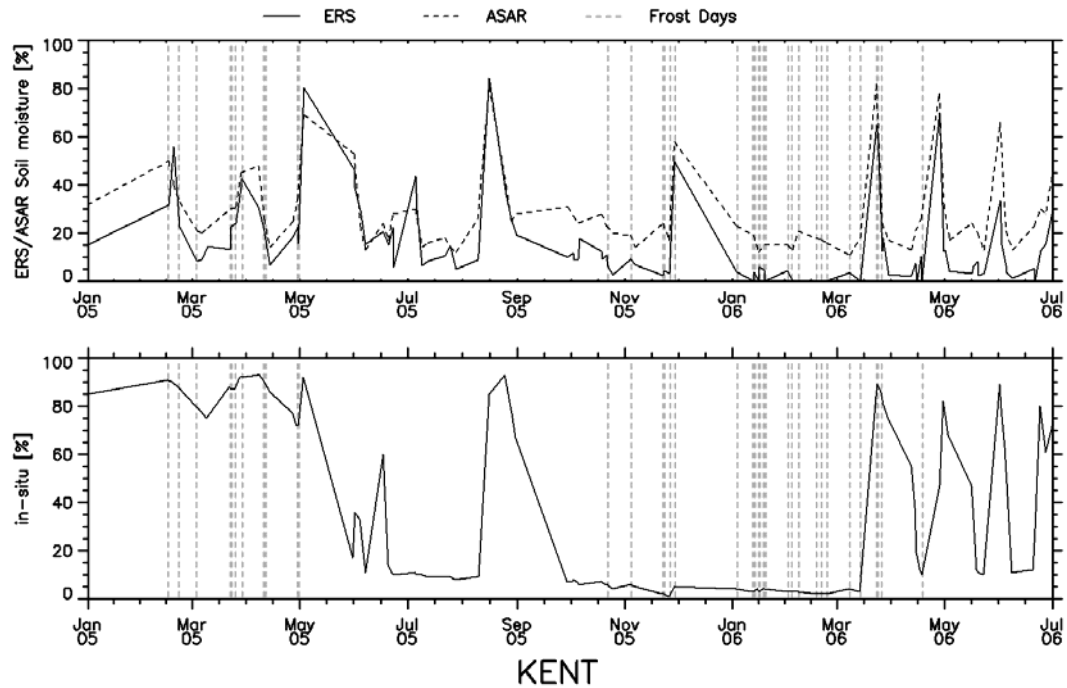


**Figure B 39:** Soil moisture time series from ASAR GM (solid line) and ERS scatterometer (dashed line) (top) and in-situ measurements (bottom) at the MESONET station KENT for the period January 2005 to July 2006.

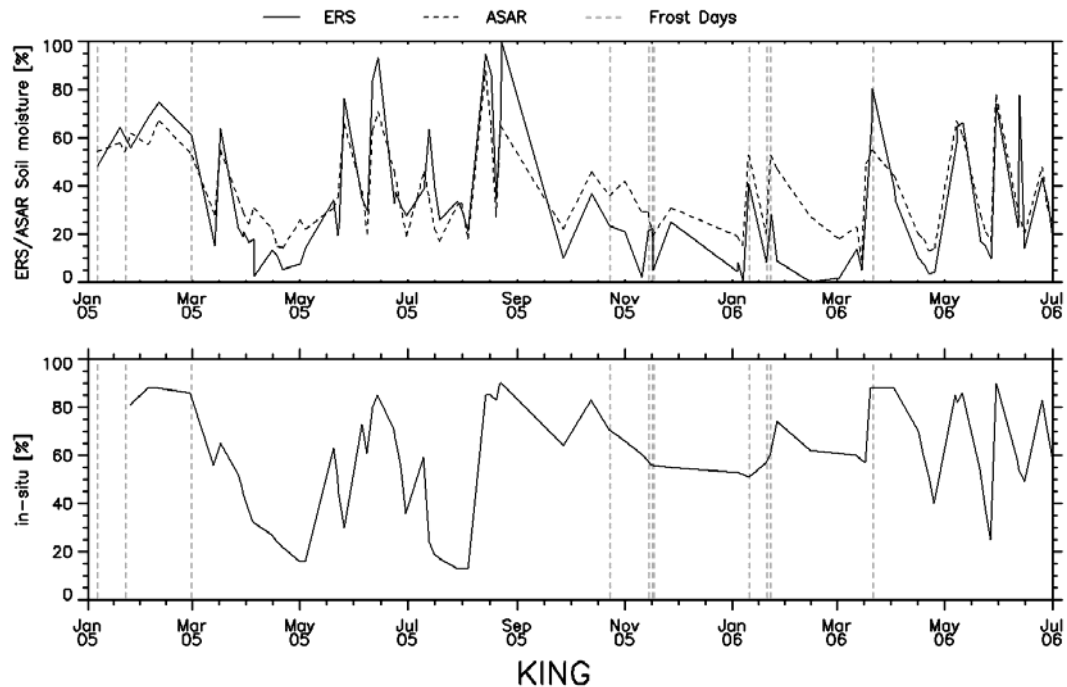


**Figure B 40:** Soil moisture time series from ASAR GM (solid line) and ERS scatterometer (dashed line) (top) and in-situ measurements (bottom) at the MESONET station KING for the period January 2005 to July 2006.

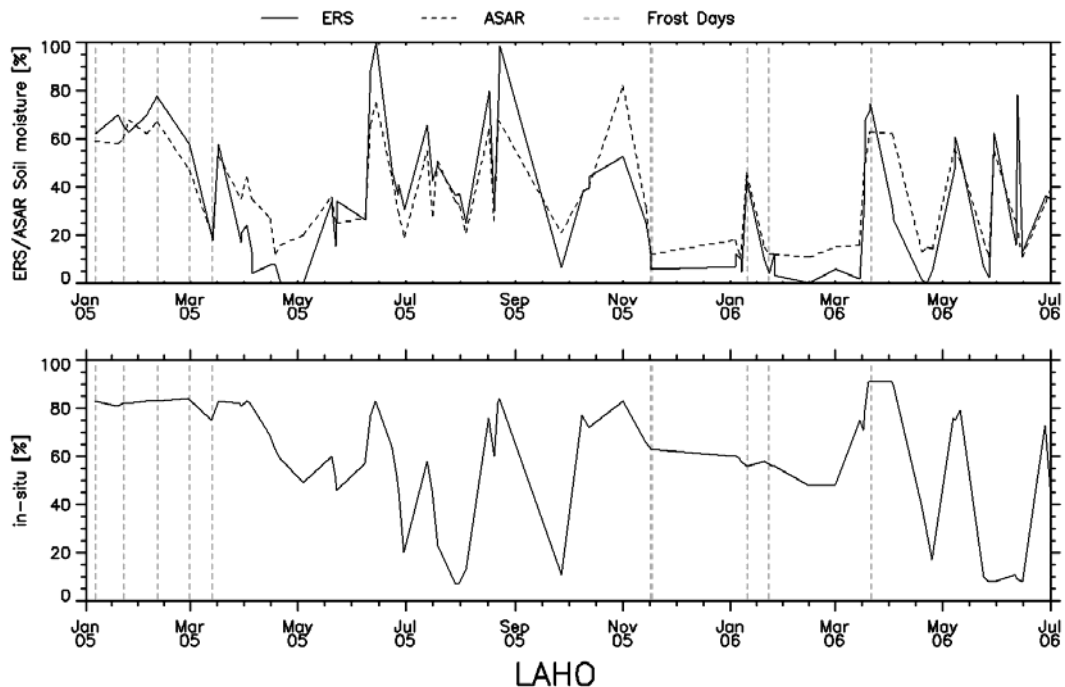


**Figure B 41:** Soil moisture time series from ASAR GM (solid line) and ERS scatterometer (dashed line) (top) and in-situ measurements (bottom) at the MESONET station LAHO for the period January 2005 to July 2006.

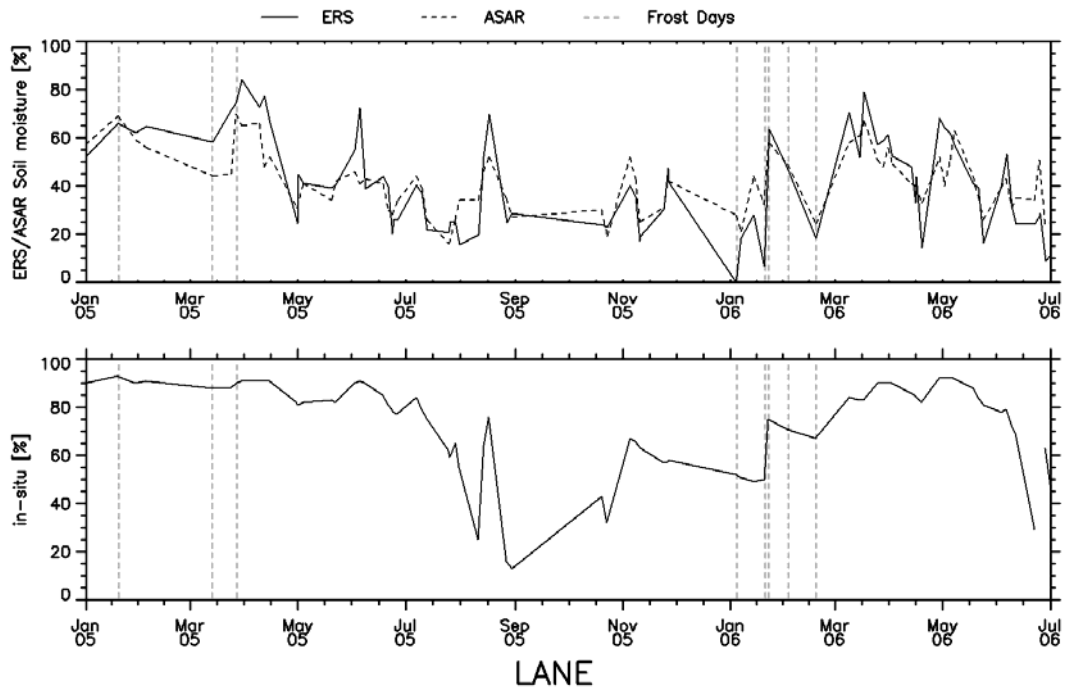


**Figure B 42:** Soil moisture time series from ASAR GM (solid line) and ERS scatterometer (dashed line) (top) and in-situ measurements (bottom) at the MESONET station LANE for the period January 2005 to July 2006.

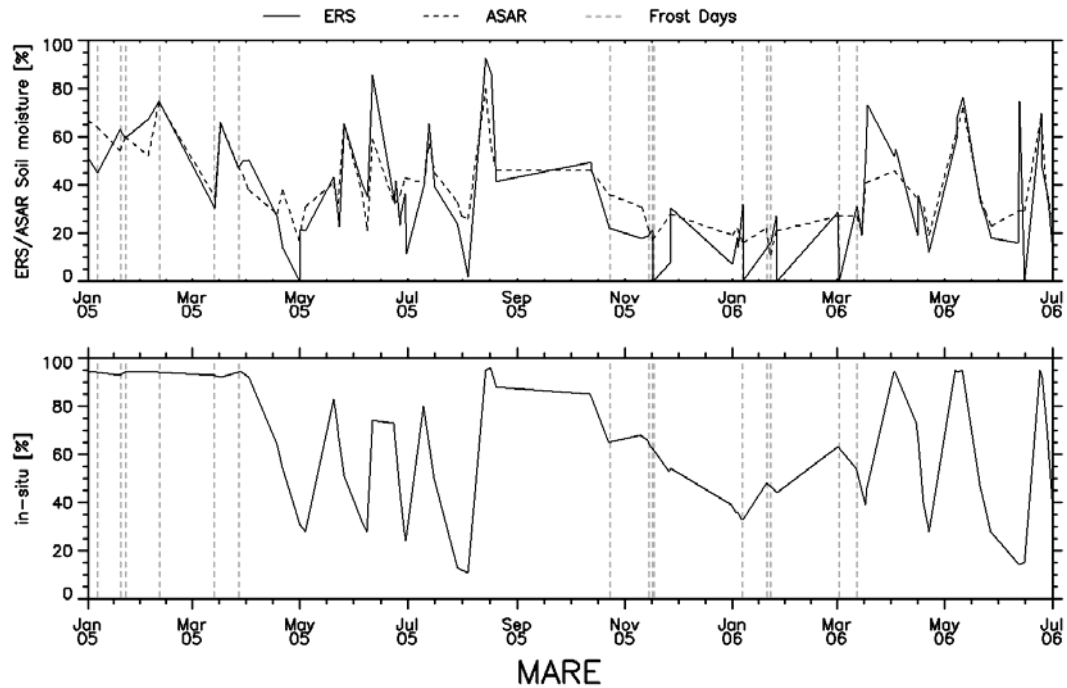


**Figure B 43:** Soil moisture time series from ASAR GM (solid line) and ERS scatterometer (dashed line) (top) and in-situ measurements (bottom) at the MESONET station MARE for the period January 2005 to July 2006.

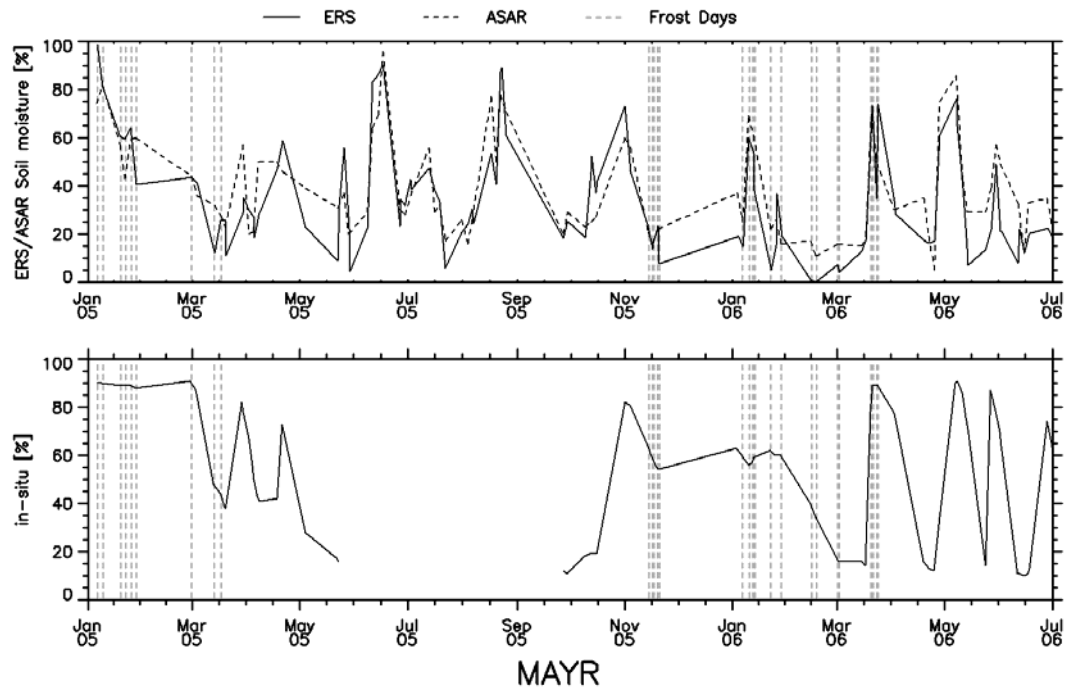


**Figure B 44:** Soil moisture time series from ASAR GM (solid line) and ERS scatterometer (dashed line) (top) and in-situ measurements (bottom) at the MESONET station MAYR for the period January 2005 to July 2006.

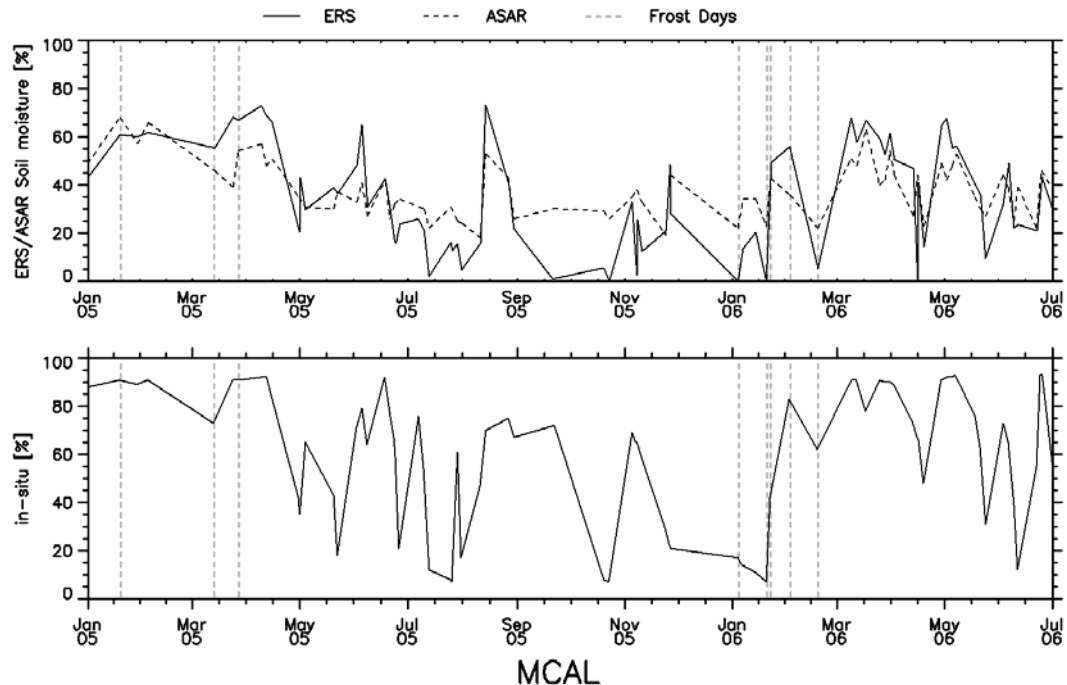


**Figure B 45:** Soil moisture time series from ASAR GM (solid line) and ERS scatterometer (dashed line) (top) and in-situ measurements (bottom) at the MESONET station MCAL for the period January 2005 to July 2006.

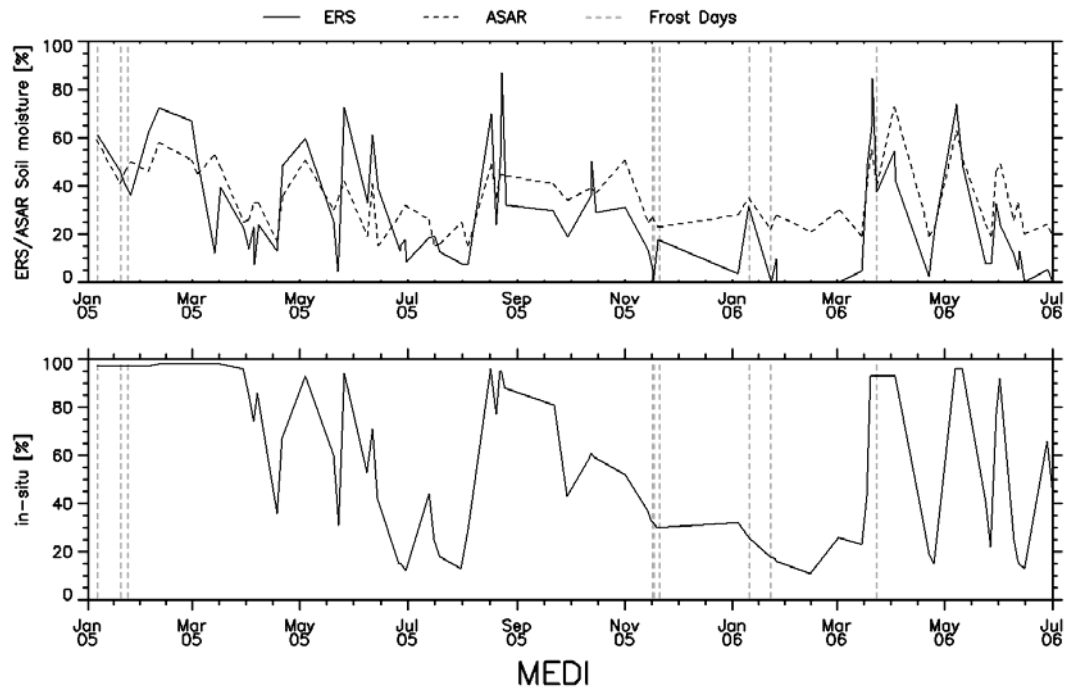


**Figure B 46:** Soil moisture time series from ASAR GM (solid line) and ERS scatterometer (dashed line) (top) and in-situ measurements (bottom) at the MESONET station MEDI for the period January 2005 to July 2006.

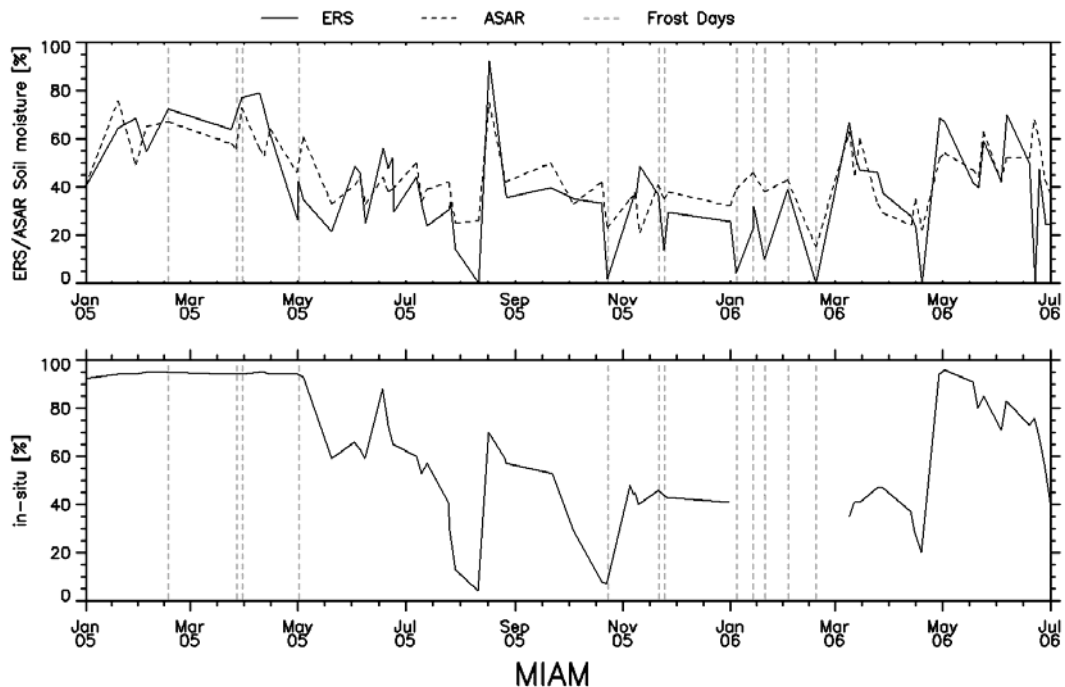


**Figure B 47:** Soil moisture time series from ASAR GM (solid line) and ERS scatterometer (dashed line) (top) and in-situ measurements (bottom) at the MESONET station MIAM for the period January 2005 to July 2006.

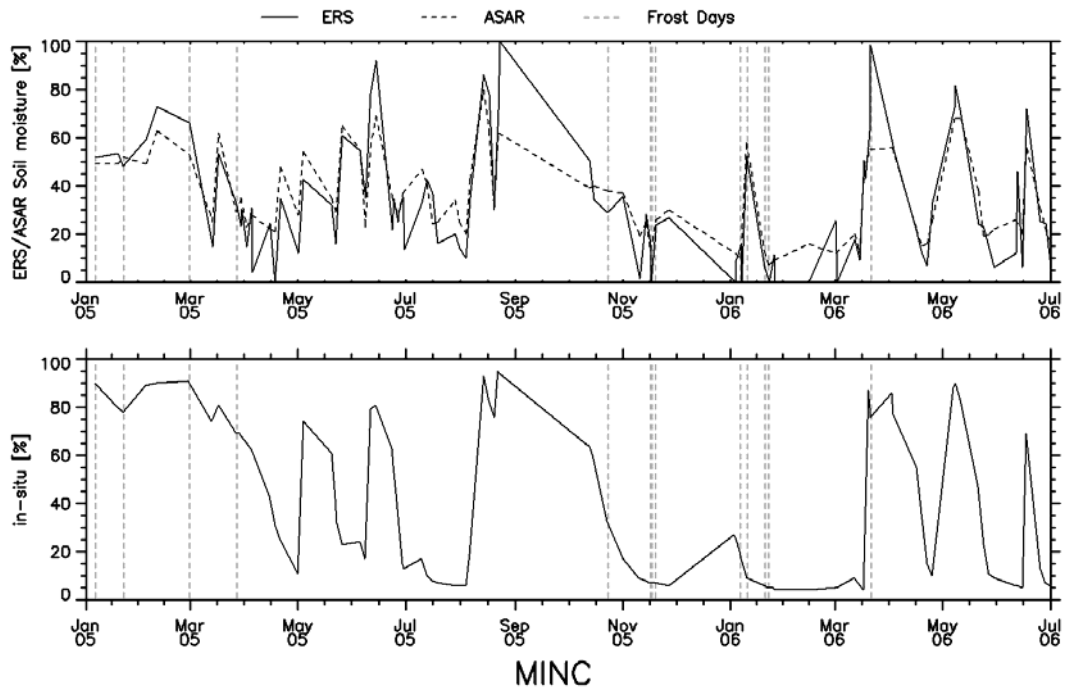


**Figure B 48:** Soil moisture time series from ASAR GM (solid line) and ERS scatterometer (dashed line) (top) and in-situ measurements (bottom) at the MESONET station MINC for the period January 2005 to July 2006.

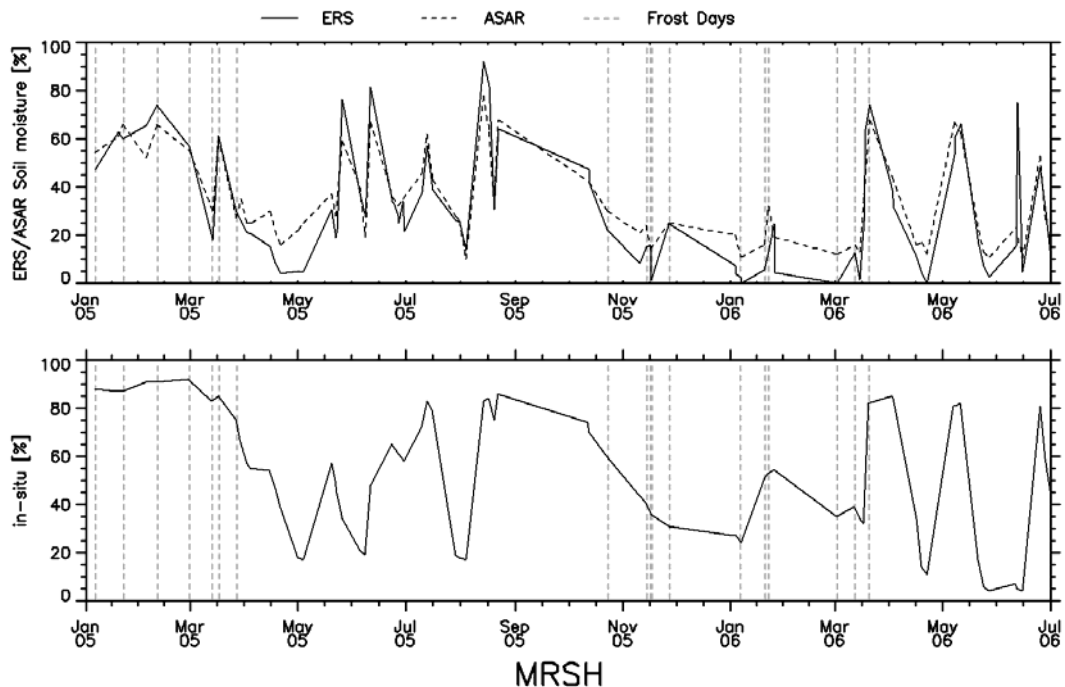


**Figure B 49:** Soil moisture time series from ASAR GM (solid line) and ERS scatterometer (dashed line) (top) and in-situ measurements (bottom) at the MESONET station MRSH for the period January 2005 to July 2006.

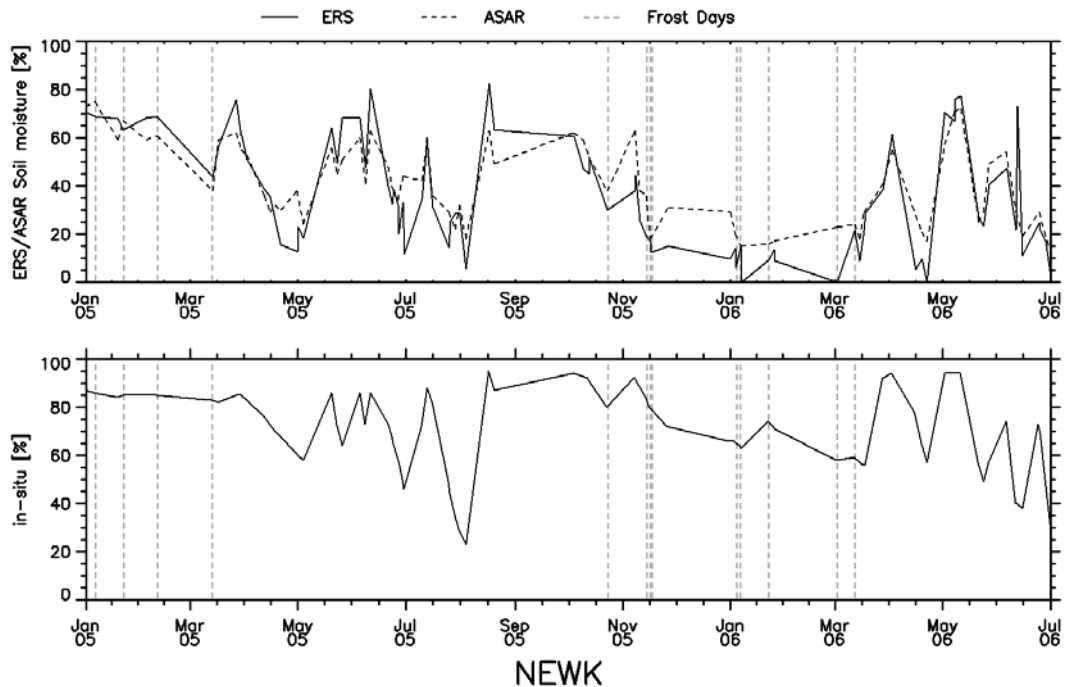


**Figure B 50:** Soil moisture time series from ASAR GM (solid line) and ERS scatterometer (dashed line) (top) and in-situ measurements (bottom) at the MESONET station NEWK for the period January 2005 to July 2006.

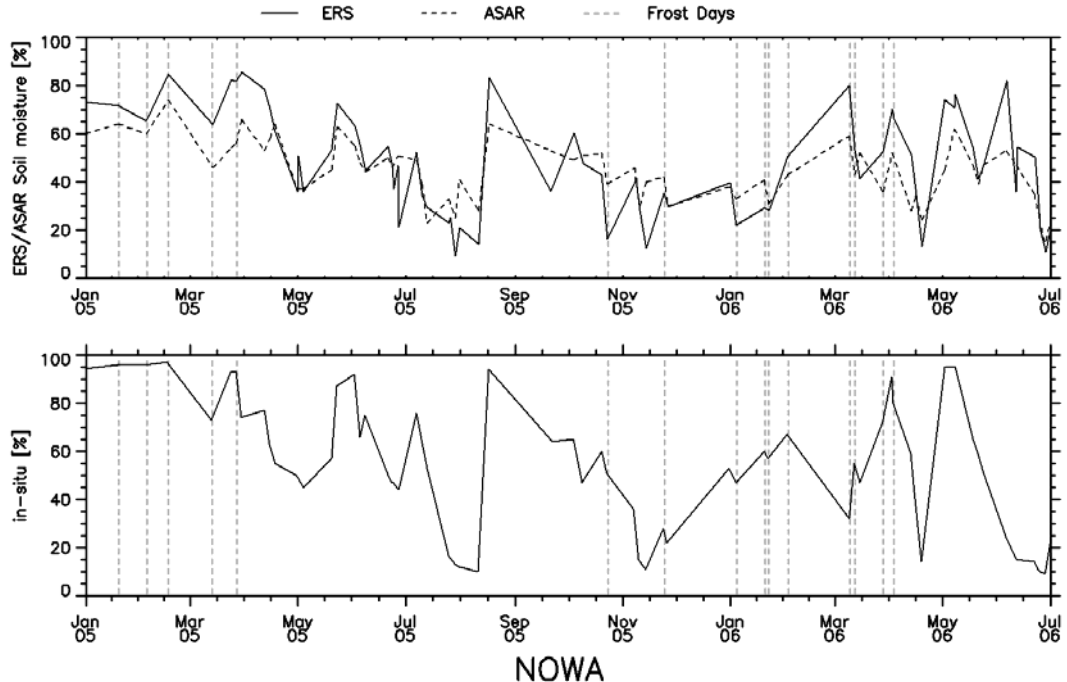


**Figure B 51:** Soil moisture time series from ASAR GM (solid line) and ERS scatterometer (dashed line) (top) and in-situ measurements (bottom) at the MESONET station NOWA for the period January 2005 to July 2006.

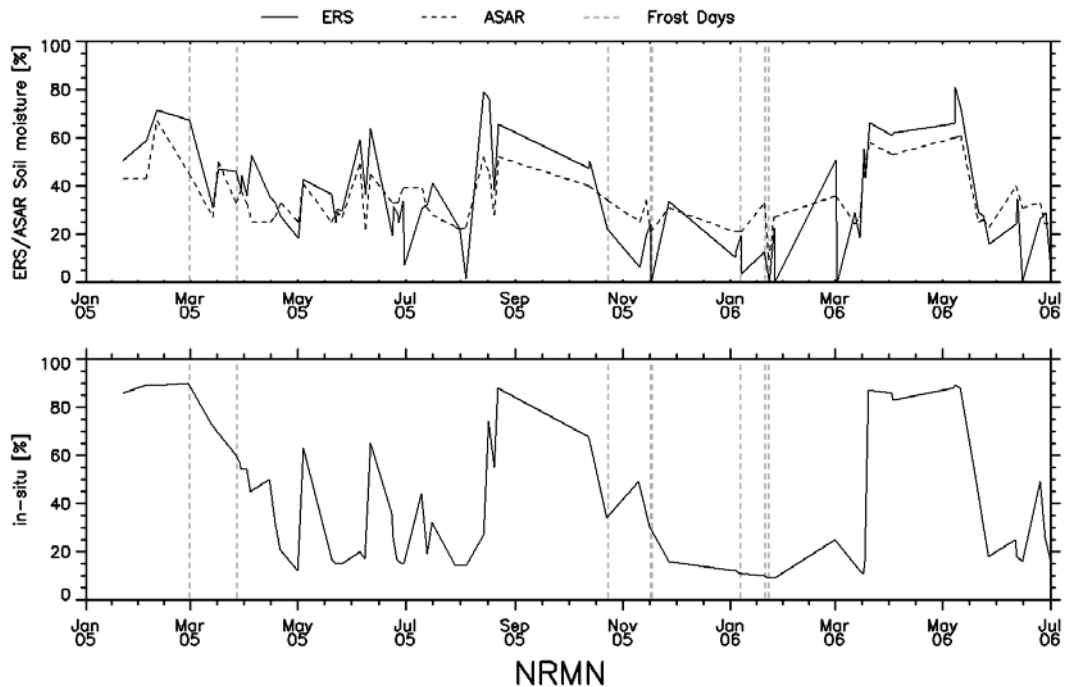


**Figure B 52:** Soil moisture time series from ASAR GM (solid line) and ERS scatterometer (dashed line) (top) and in-situ measurements (bottom) at the MESONET station NRMN for the period January 2005 to July 2006.

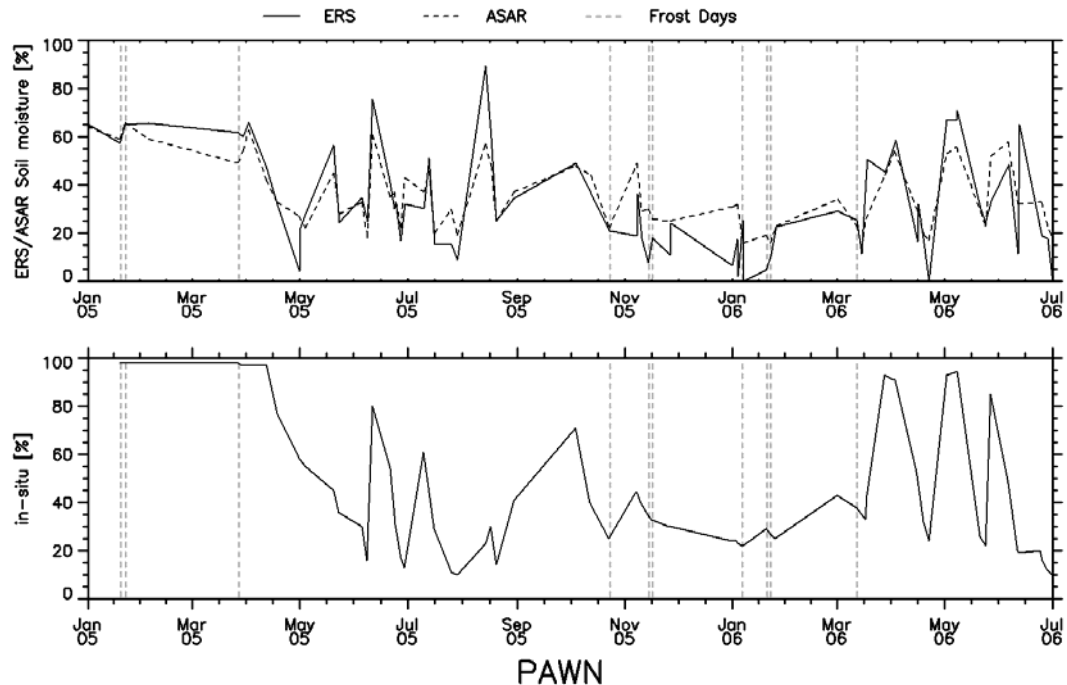


**Figure B 53:** Soil moisture time series from ASAR GM (solid line) and ERS scatterometer (dashed line) (top) and in-situ measurements (bottom) at the MESONET station PAWN for the period January 2005 to July 2006.

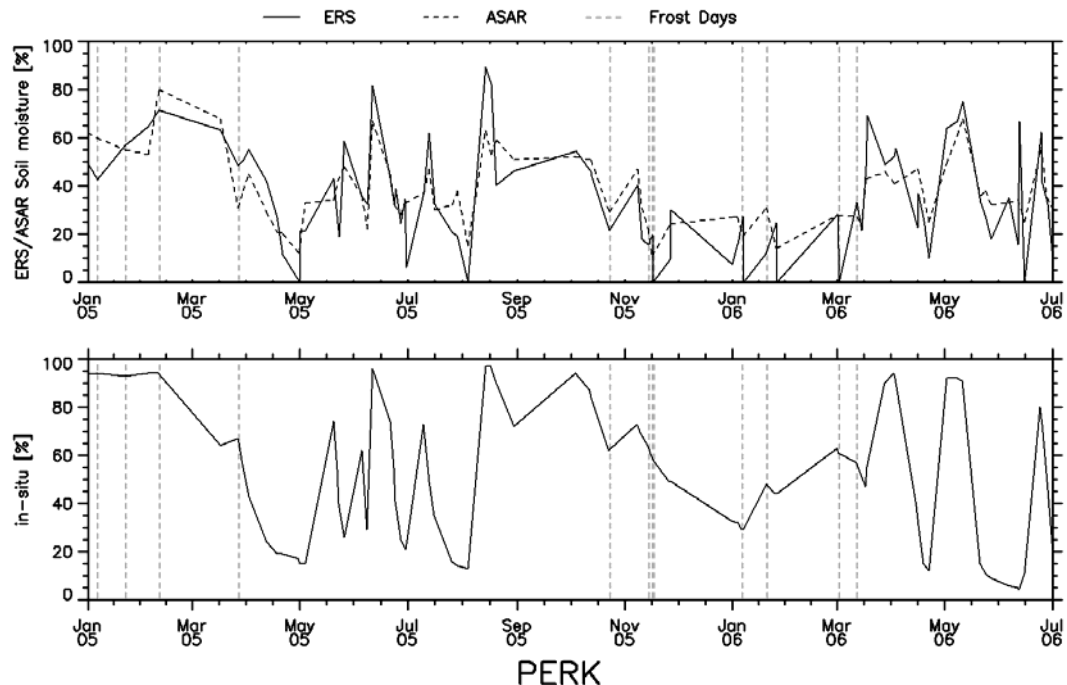


**Figure B 54:** Soil moisture time series from ASAR GM (solid line) and ERS scatterometer (dashed line) (top) and in-situ measurements (bottom) at the MESONET station PERK for the period January 2005 to July 2006.

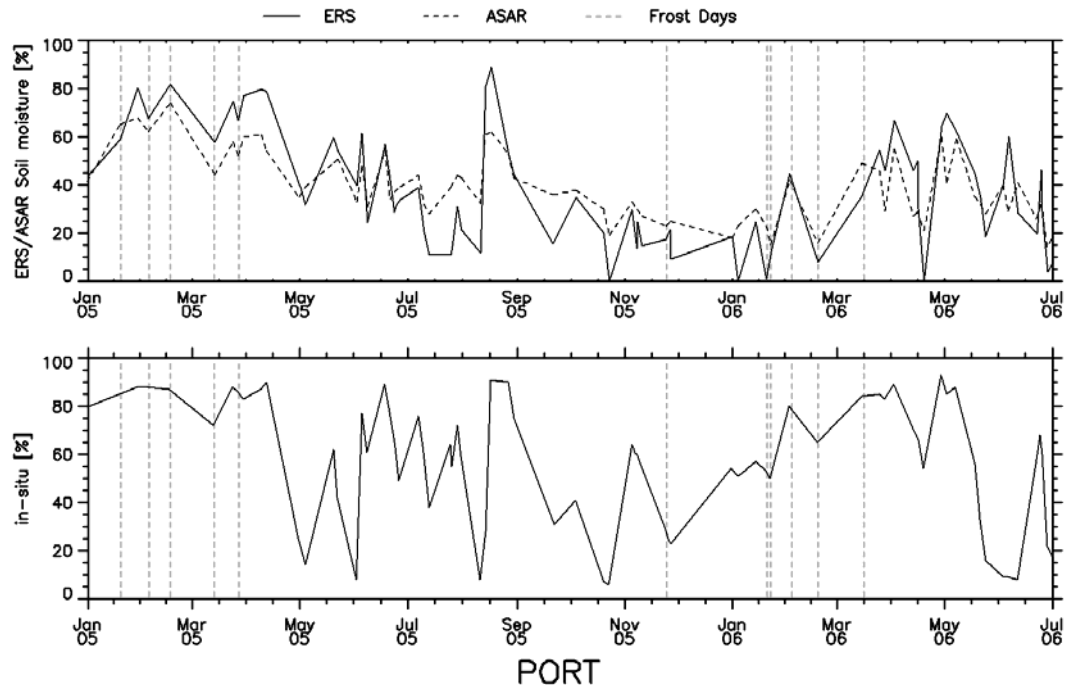


**Figure B 55:** Soil moisture time series from ASAR GM (solid line) and ERS scatterometer (dashed line) (top) and in-situ measurements (bottom) at the MESONET station PORT for the period January 2005 to July 2006.

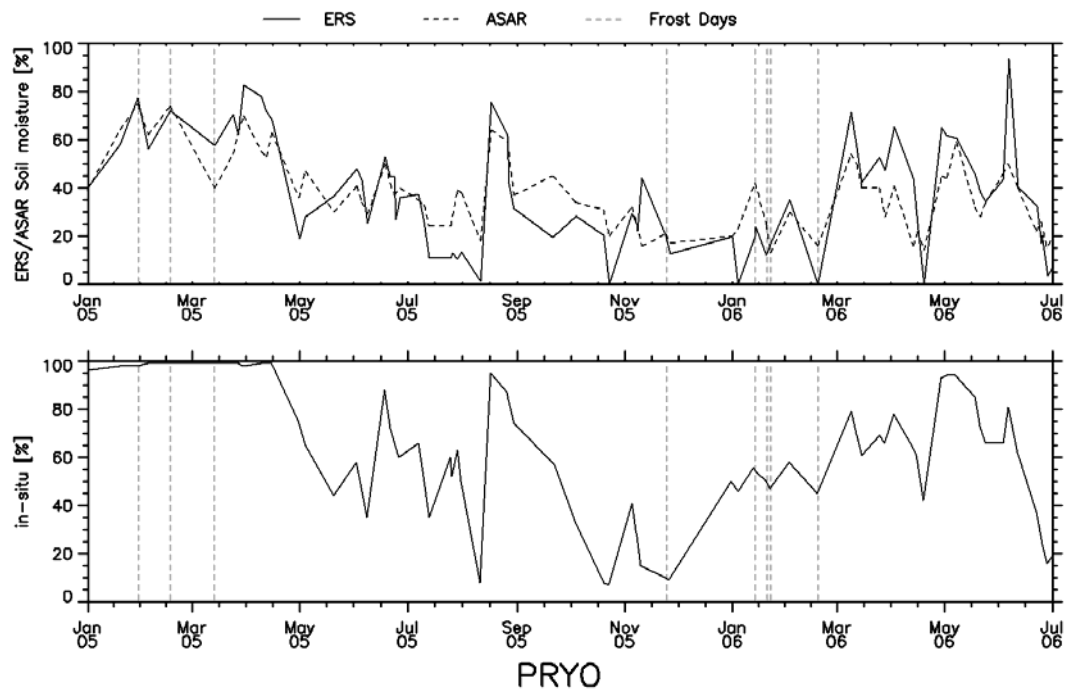


**Figure B 56:** Soil moisture time series from ASAR GM (solid line) and ERS scatterometer (dashed line) (top) and in-situ measurements (bottom) at the MESONET station PYRO for the period January 2005 to July 2006.

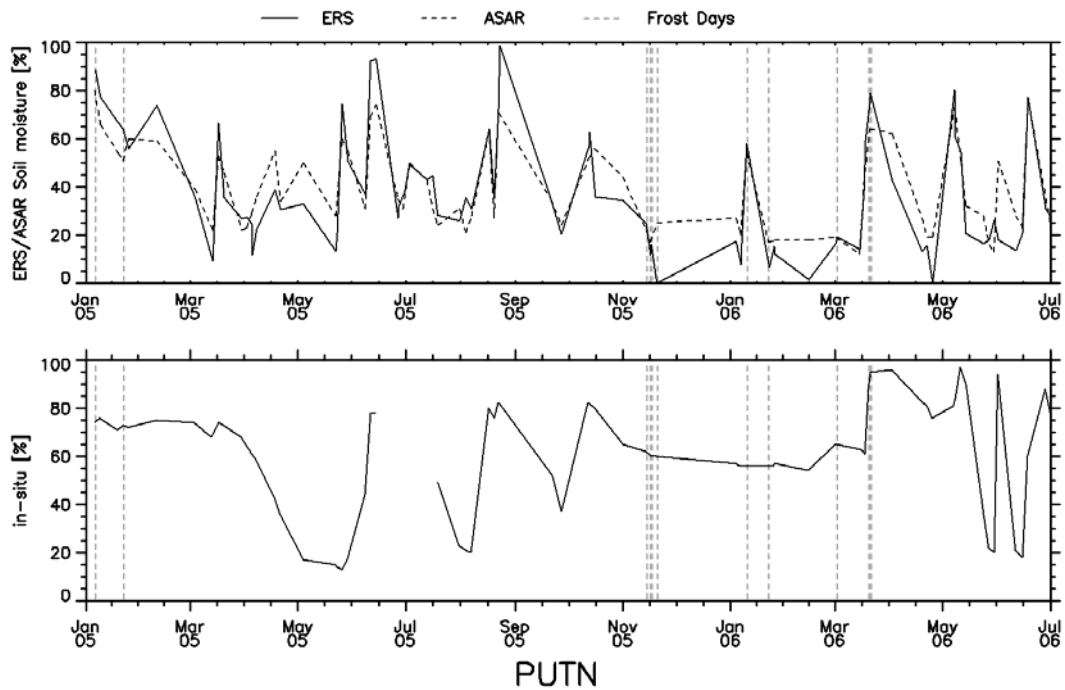


**Figure B 57:** Soil moisture time series from ASAR GM (solid line) and ERS scatterometer (dashed line) (top) and in-situ measurements (bottom) at the MESONET station PUTN for the period January 2005 to July 2006.

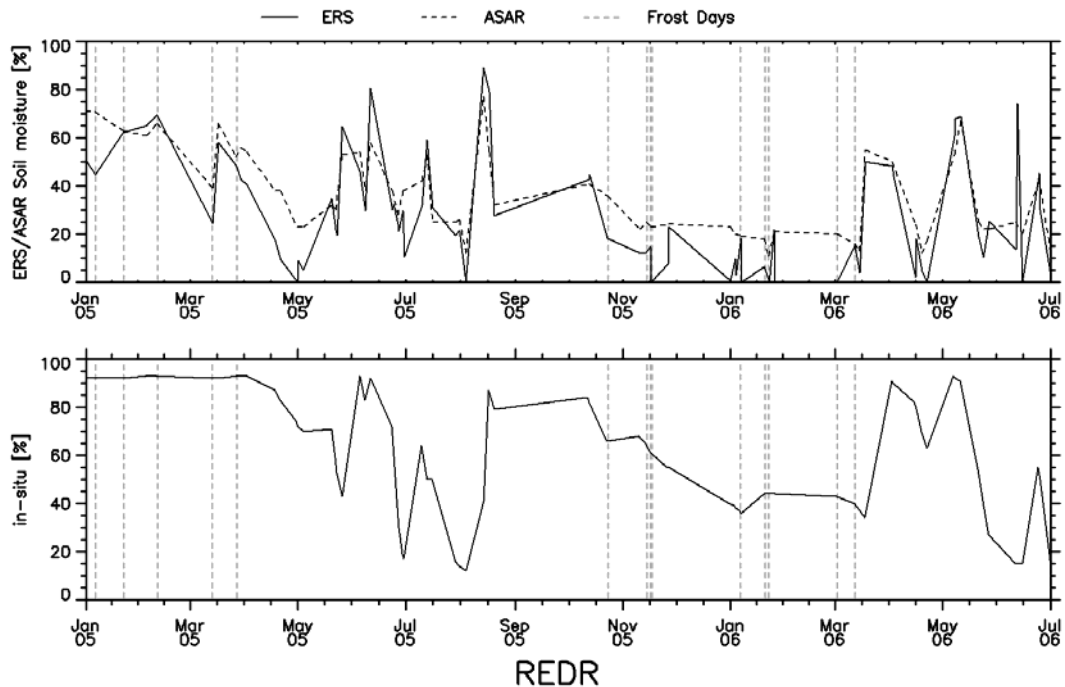


**Figure B 58:** Soil moisture time series from ASAR GM (solid line) and ERS scatterometer (dashed line) (top) and in-situ measurements (bottom) at the MESONET station REDR for the period January 2005 to July 2006.

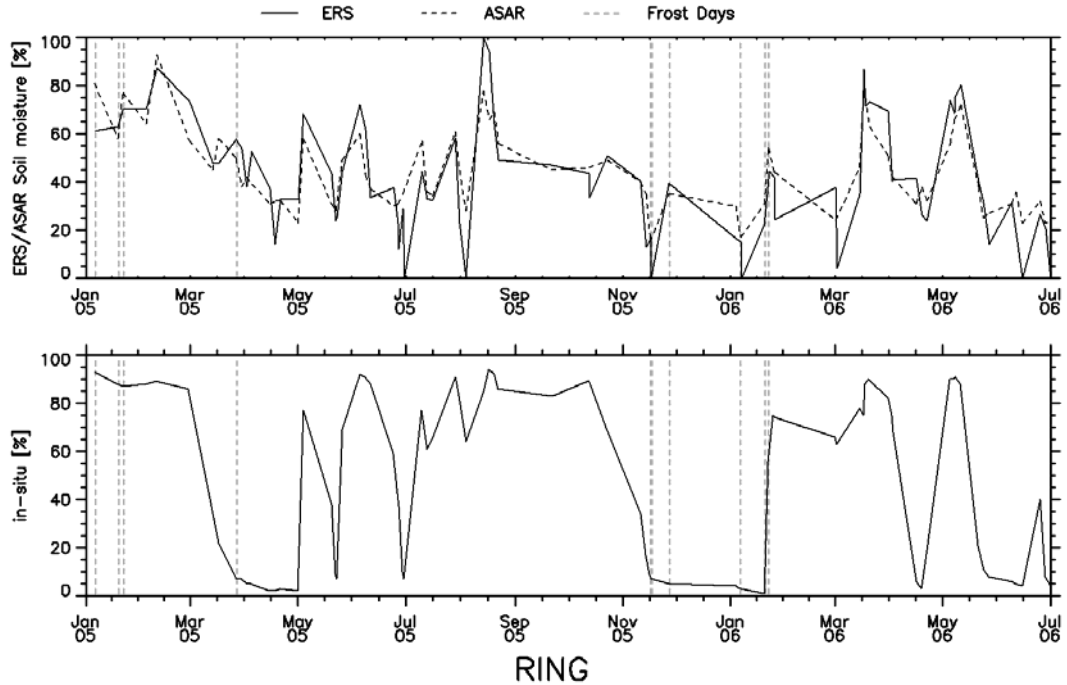


**Figure B 59:** Soil moisture time series from ASAR GM (solid line) and ERS scatterometer (dashed line) (top) and in-situ measurements (bottom) at the MESONET station RING for the period January 2005 to July 2006.

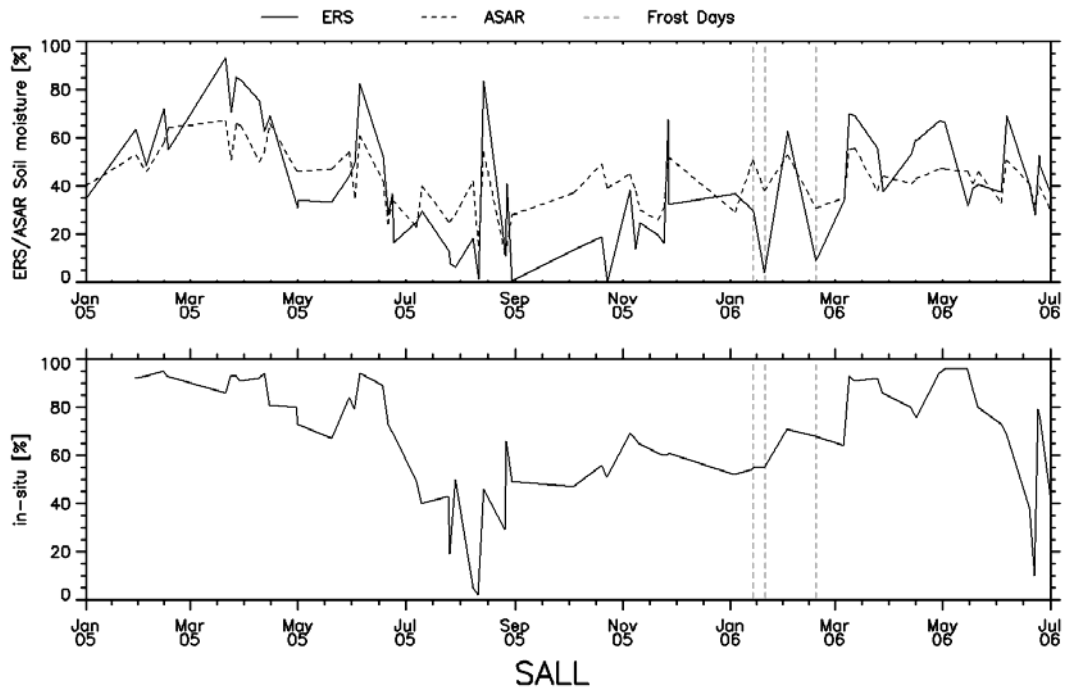


**Figure B 60:** Soil moisture time series from ASAR GM (solid line) and ERS scatterometer (dashed line) (top) and in-situ measurements (bottom) at the MESONET station SALL for the period January 2005 to July 2006.

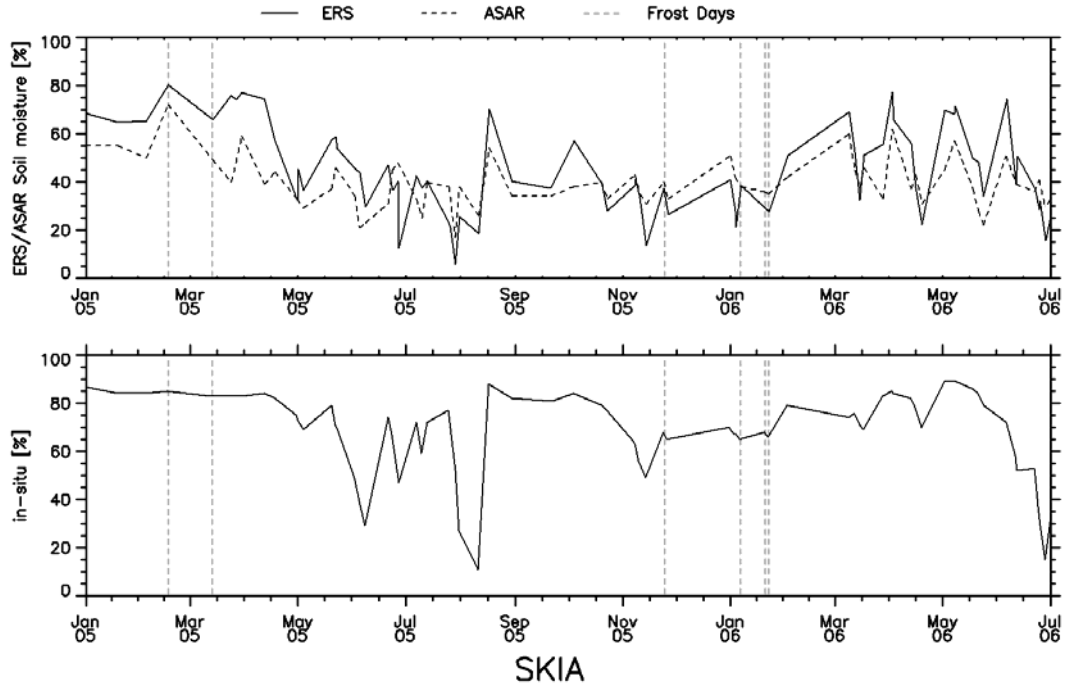


**Figure B 61:** Soil moisture time series from ASAR GM (solid line) and ERS scatterometer (dashed line) (top) and in-situ measurements (bottom) at the MESONET station SKIA for the period January 2005 to July 2006.

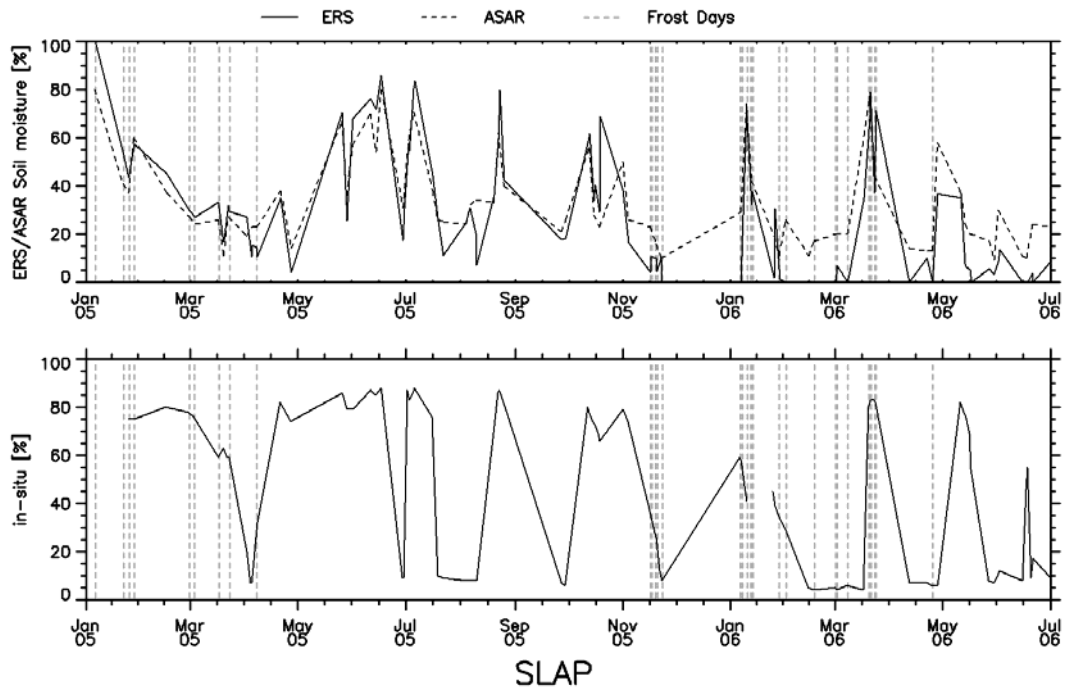


**Figure B 62:** Soil moisture time series from ASAR GM (solid line) and ERS scatterometer (dashed line) (top) and in-situ measurements (bottom) at the MESONET station SLAP for the period January 2005 to July 2006.

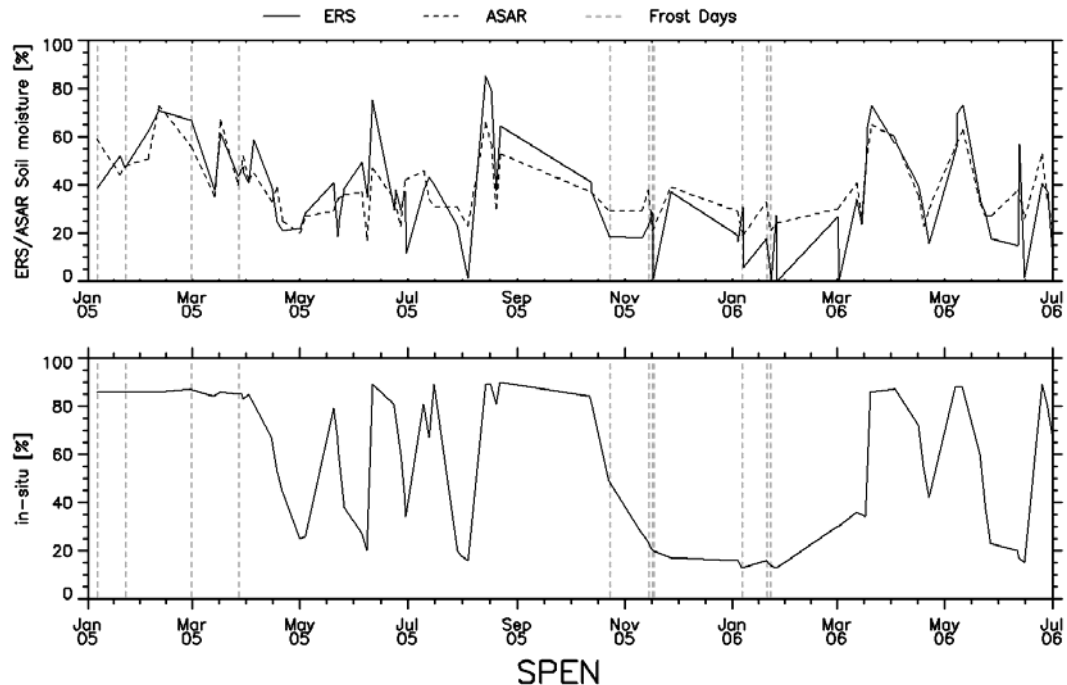


**Figure B 63:** Soil moisture time series from ASAR GM (solid line) and ERS scatterometer (dashed line) (top) and in-situ measurements (bottom) at the MESONET station SPEN for the period January 2005 to July 2006.

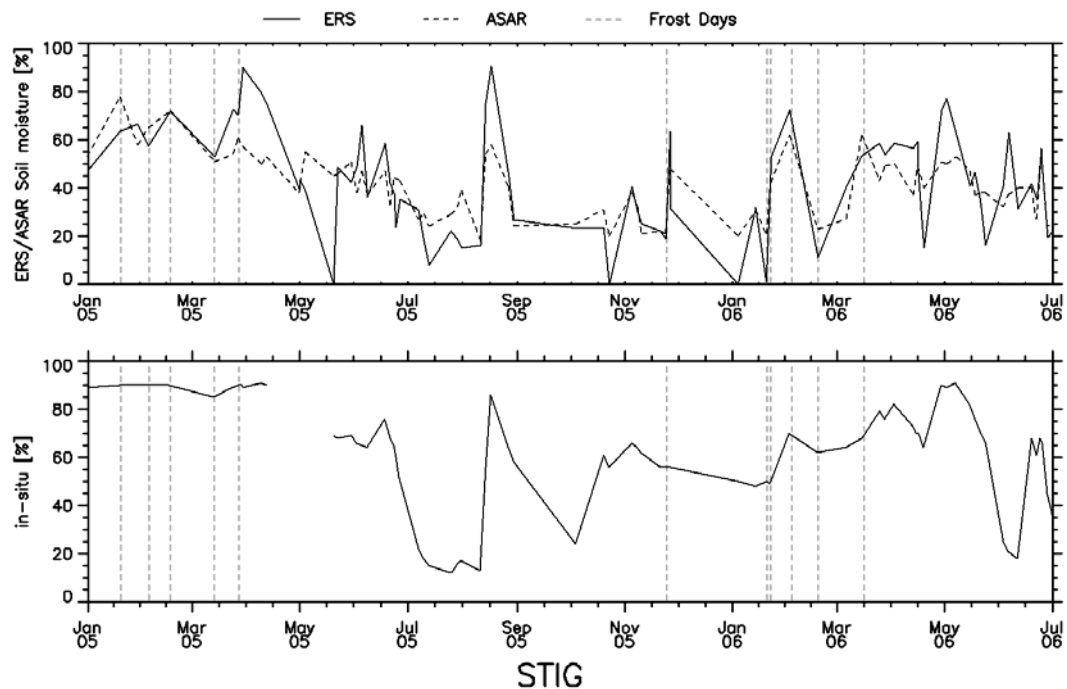


**Figure B 64:** Soil moisture time series from ASAR GM (solid line) and ERS scatterometer (dashed line) (top) and in-situ measurements (bottom) at the MESONET station STIG for the period January 2005 to July 2006.

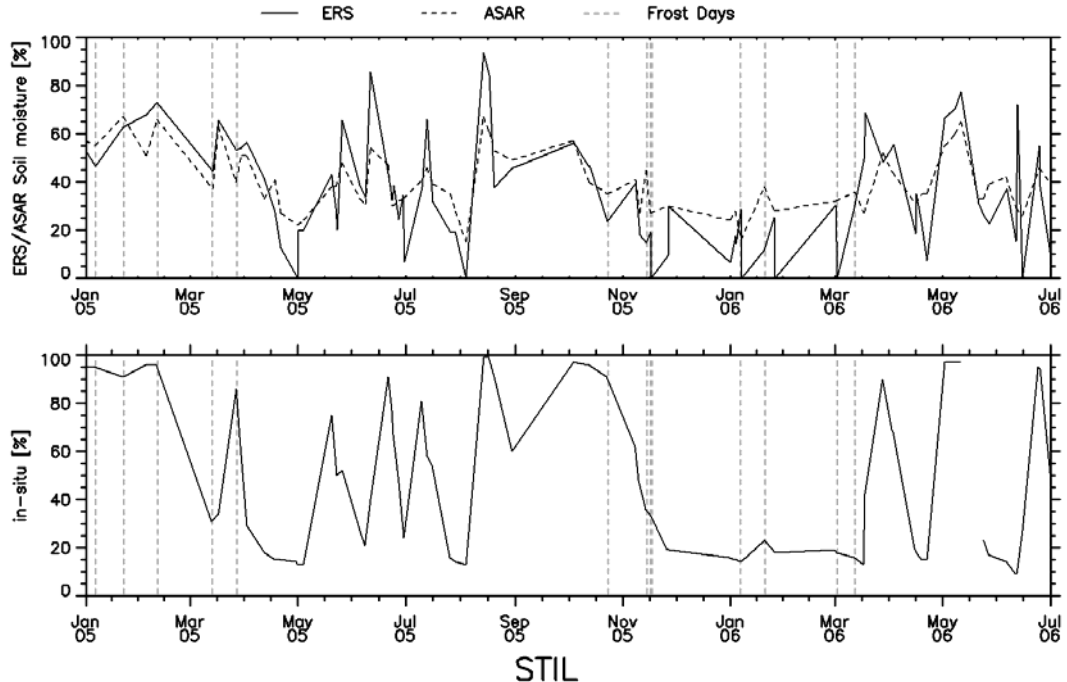


**Figure B 65:** Soil moisture time series from ASAR GM (solid line) and ERS scatterometer (dashed line) (top) and in-situ measurements (bottom) at the MESONET station STIL for the period January 2005 to July 2006.

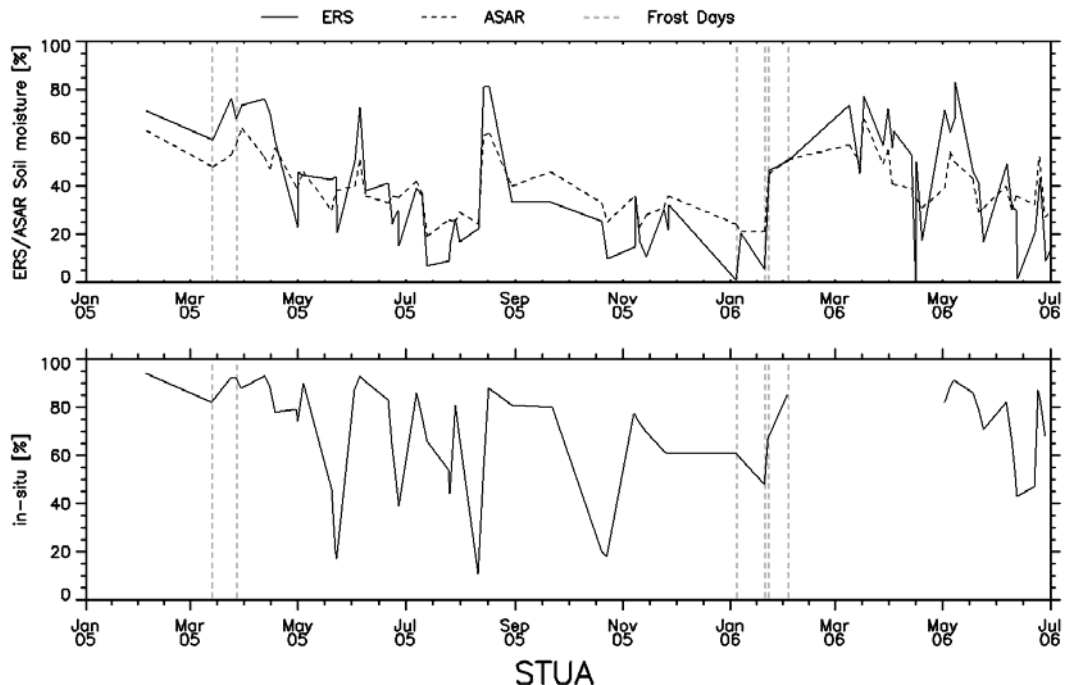


**Figure B 66:** Soil moisture time series from ASAR GM (solid line) and ERS scatterometer (dashed line) (top) and in-situ measurements (bottom) at the MESONET station STUA for the period January 2005 to July 2006.

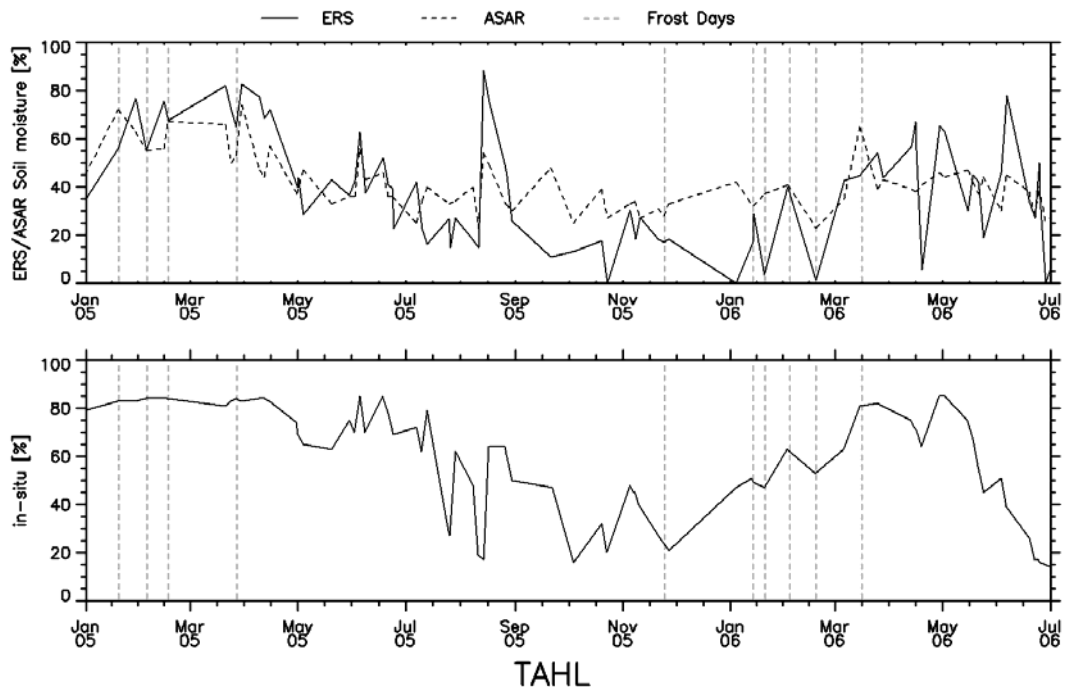


**Figure B 67:** Soil moisture time series from ASAR GM (solid line) and ERS scatterometer (dashed line) (top) and in-situ measurements (bottom) at the MESONET station TAHL for the period January 2005 to July 2006.

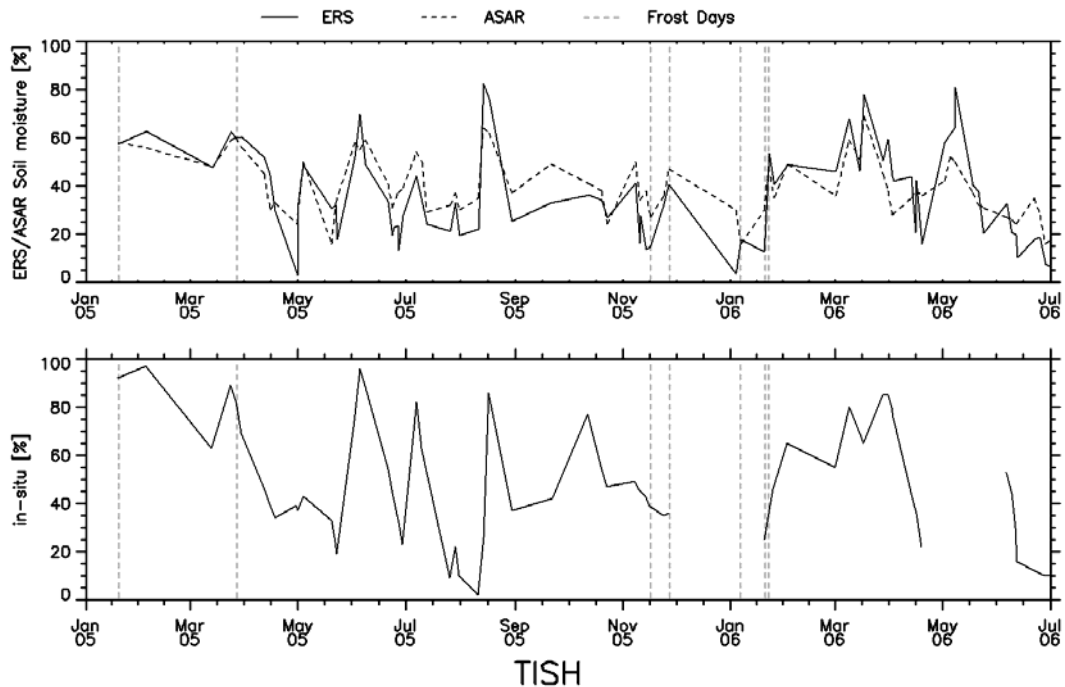


**Figure B 68:** Soil moisture time series from ASAR GM (solid line) and ERS scatterometer (dashed line) (top) and in-situ measurements (bottom) at the MESONET station TISH for the period January 2005 to July 2006.

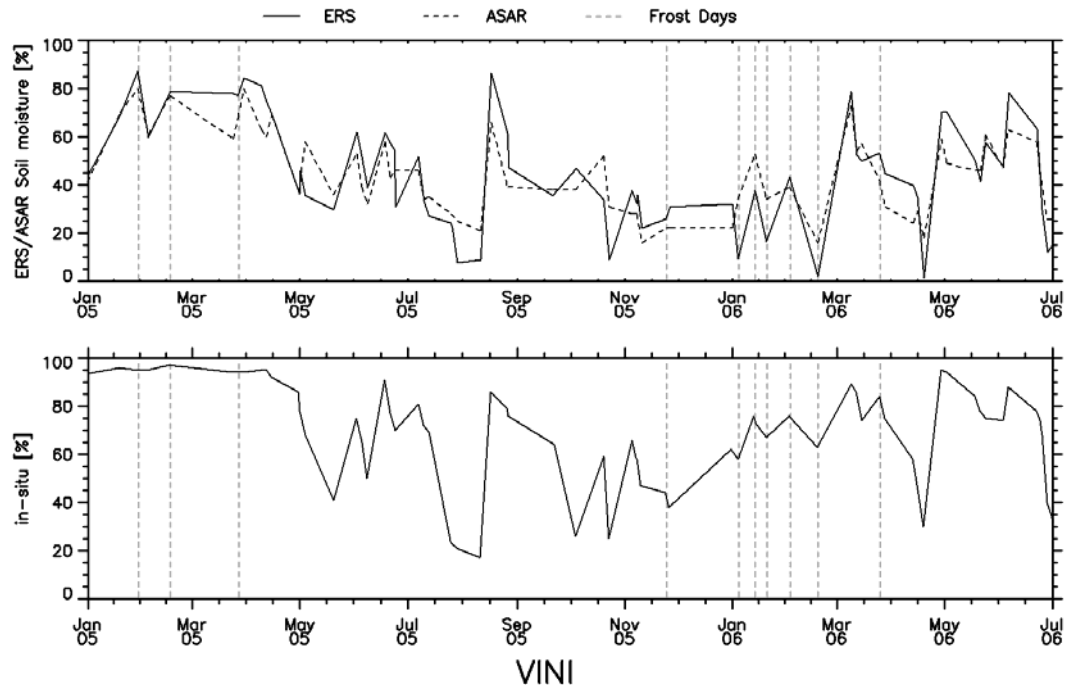


**Figure B 69:** Soil moisture time series from ASAR GM (solid line) and ERS scatterometer (dashed line) (top) and in-situ measurements (bottom) at the MESONET station VINI for the period January 2005 to July 2006.

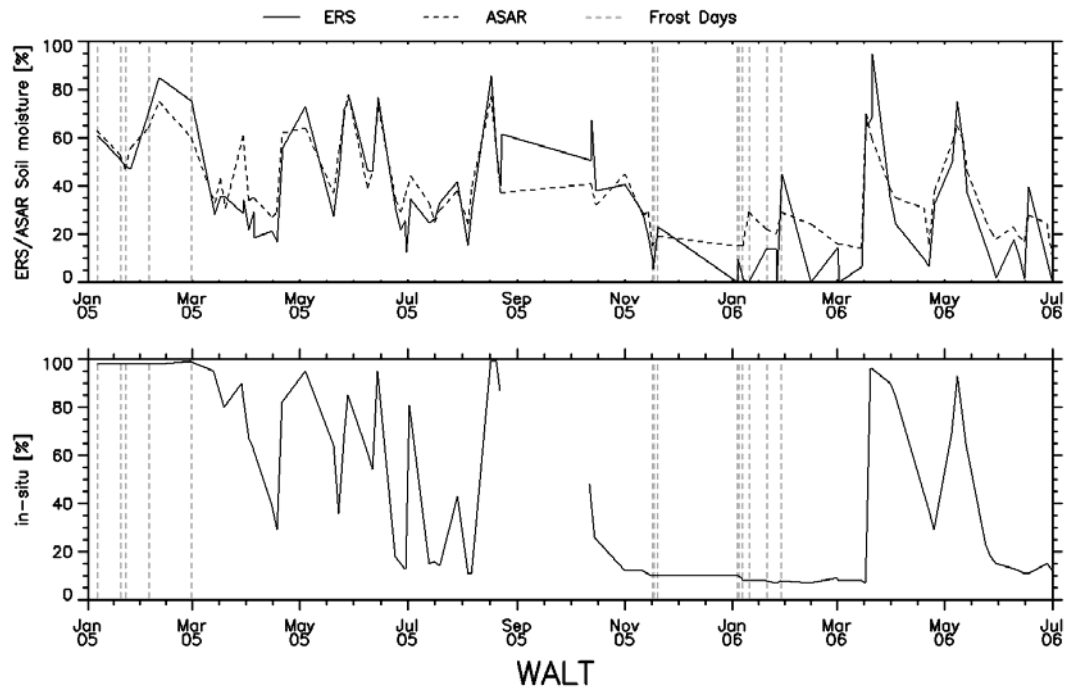


**Figure B 70:** Soil moisture time series from ASAR GM (solid line) and ERS scatterometer (dashed line) (top) and in-situ measurements (bottom) at the MESONET station WALT for the period January 2005 to July 2006.

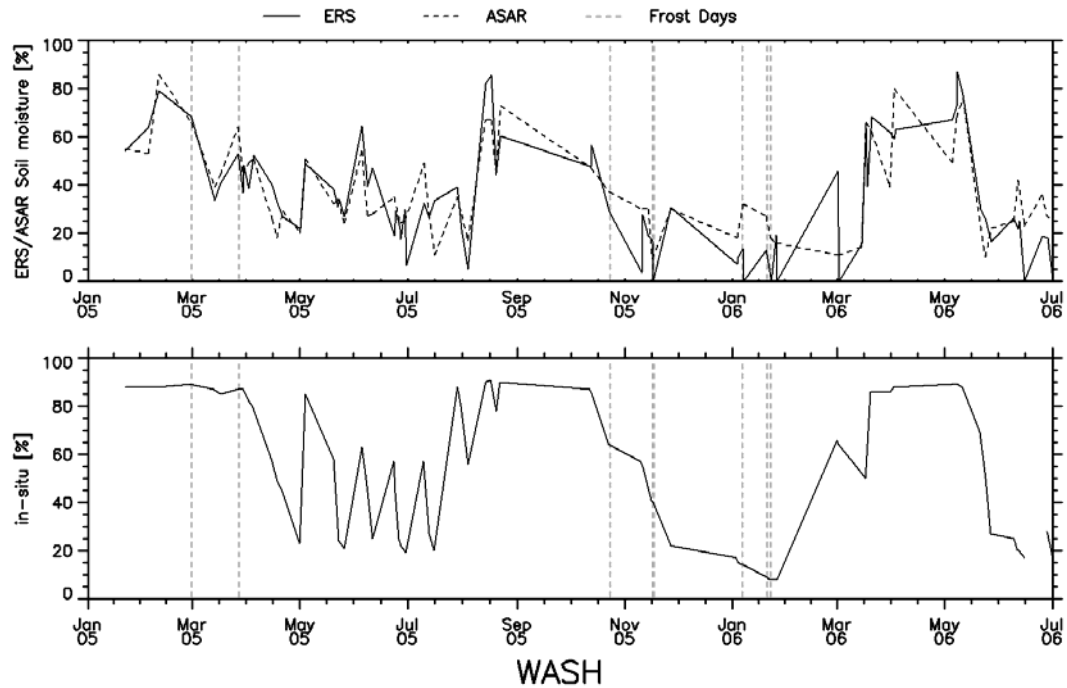


**Figure B 71:** Soil moisture time series from ASAR GM (solid line) and ERS scatterometer (dashed line) (top) and in-situ measurements (bottom) at the MESONET station WASH for the period January 2005 to July 2006.

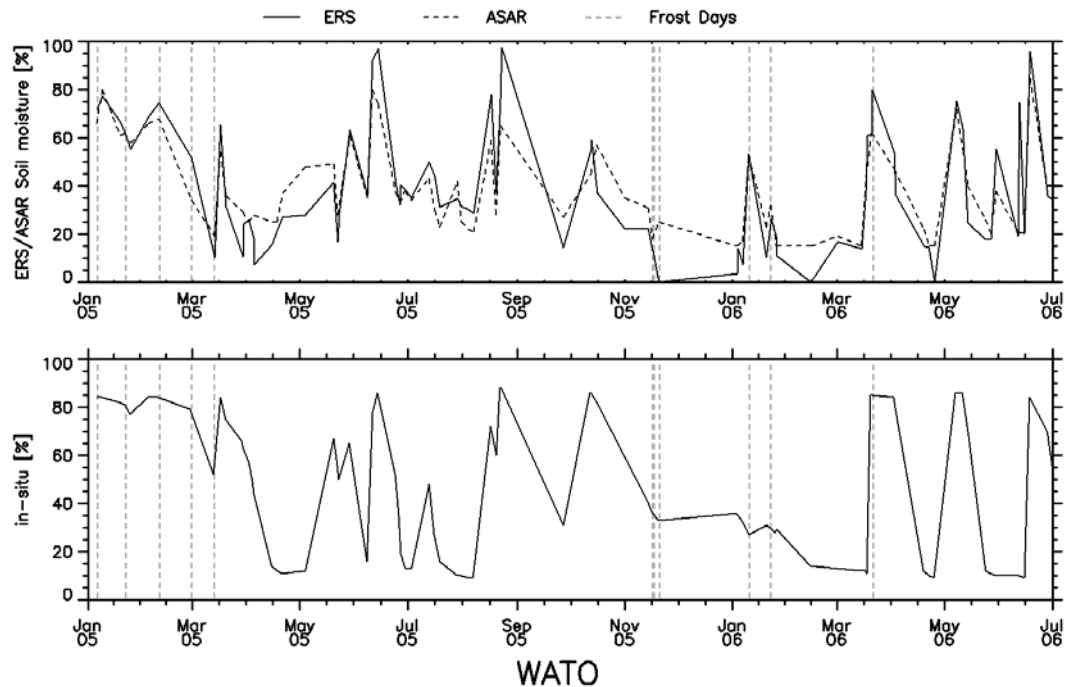


**Figure B 72:** Soil moisture time series from ASAR GM (solid line) and ERS scatterometer (dashed line) (top) and in-situ measurements (bottom) at the MESONET station WATO for the period January 2005 to July 2006.

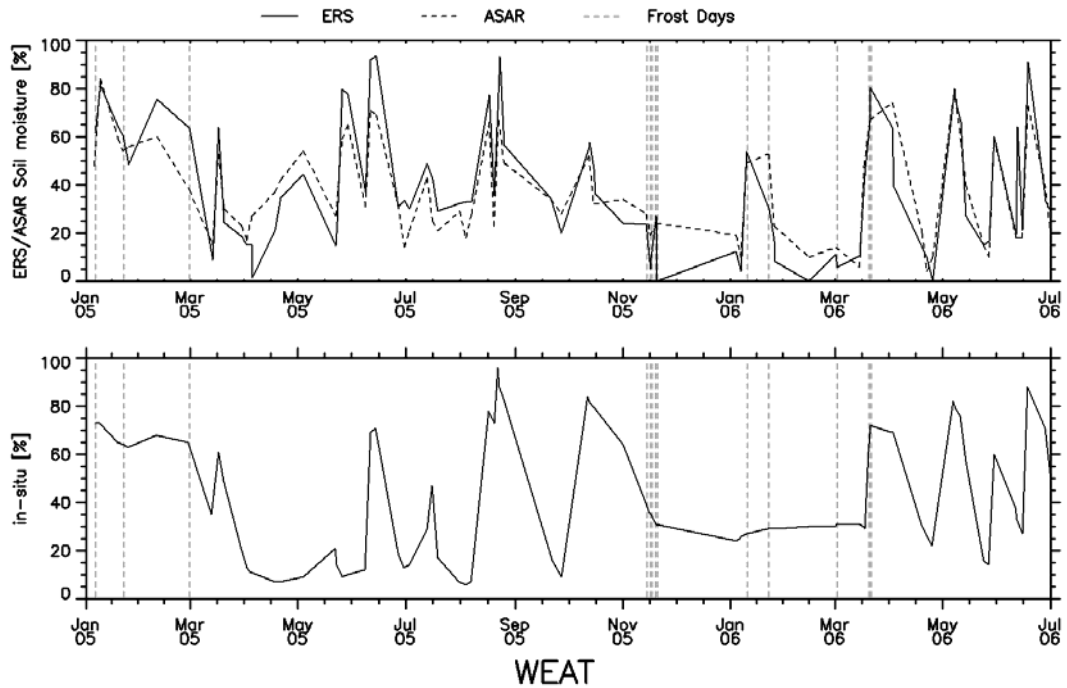


**Figure B 73:** Soil moisture time series from ASAR GM (solid line) and ERS scatterometer (dashed line) (top) and in-situ measurements (bottom) at the MESONET station WEAT for the period January 2005 to July 2006.

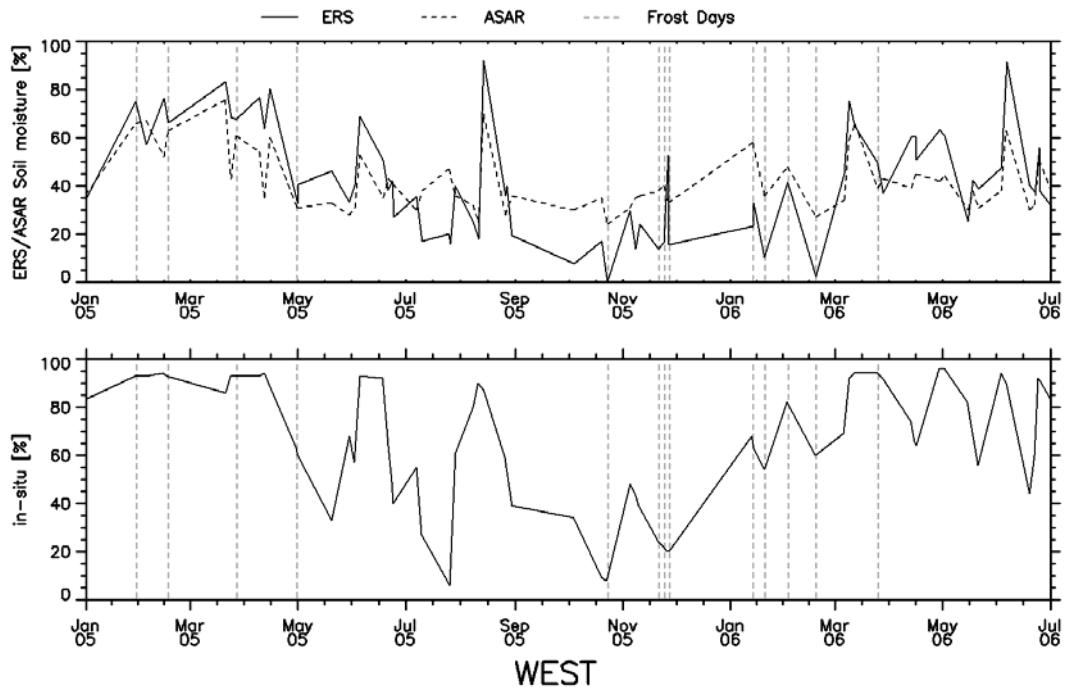


**Figure B 74:** Soil moisture time series from ASAR GM (solid line) and ERS scatterometer (dashed line) (top) and in-situ measurements (bottom) at the MESONET station WEST for the period January 2005 to July 2006.

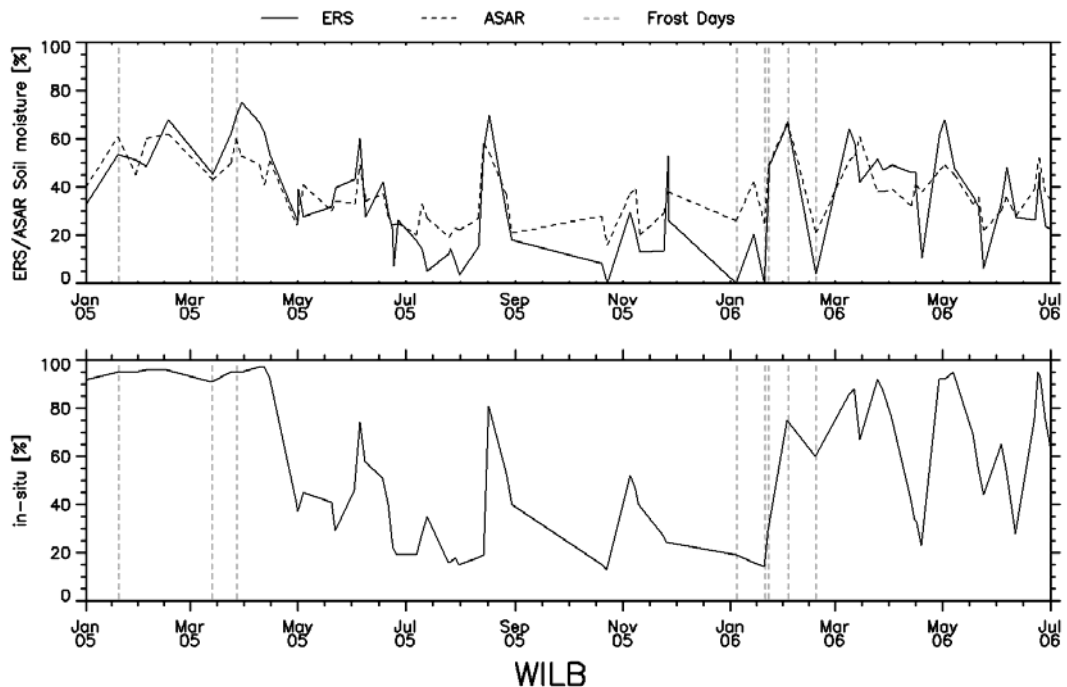


**Figure B 75:** Soil moisture time series from ASAR GM (solid line) and ERS scatterometer (dashed line) (top) and in-situ measurements (bottom) at the MESONET station WILB for the period January 2005 to July 2006.

# **Curriculum Vitae**

---

---

Name:	Carsten Pathe
Date of Birth	5th March 1976
Place of Birth:	Poessneck
Nationality:	Germany
8/82-7/86	Primary School
9/86-7/90	Grammar School
9/90-6/94	Comprehensive Secondary School
6/94	School leaving exam (Abitur)
8/94-10/95	Civilian Service
10/95 - 06/2002	Study of Geography at the Friedrich-Schiller-University, Jena, Germany Study of Regional Planning at the Bauhaus-University, Weimar, Germany
06/2002	Diploma examination, title of the diploma thesis: "Influence of Diurnal Variations of Surface Wetness on Classification of Agricultural Crops Using Multi-Parametric E-SAR Data With Respect to Future TerraSAR Applications."
08/2002 - present	Research assistant at the Institute of Photogrammetry and Remote Sensing (I.P.F.) at the University of Technology, Vienna

### University Placements

03/2000 - 05/2000	German Remote Sensing Data Center at the German Aerospace Center (DLR DFD) in Oberpfaffenhofen, Germany
06/2000 - 07/2000	Center for Environmental Research (UFZ) in Leipzig, Germany

### Relevant Experience

03/97 - 06/97	Student Assistant at the Thuringian Regional Office for the Environment (TLUG), Jena, Germany
01/98 - 03/2000, 09/2000 - 12/2001	Student Assistant at the Institute for Geography, Department of Geoinformatics, Hydrology and Modelling, Friedrich-Schiller-University Jena, Germany

## Relevant Publications

C. Pathe, W. Wagner, D. Sabel, M. Doubkova, J. B. Basara: “*Using ENVISAT ASAR Global Mode for Surface Soil Moisture Retrieval over Oklahoma, USA*”; IEEE Trans. Geosci. Rem. Sens., (2008) DOI 10.1109/TGRS.20082004711

C. Pathe, A. Bartsch, D. Sabel, M. Doubkova, W. Wagner (in preparation): “*SHARE: Soil Moisture for Hydrometeorologic applications in the SADC (Southern African Development Community) Region*” Proceedings of the Open Science Conference on “Africa and Carbon Cycle: the CarboAfrica project”, 25-27 November 2008, Accra, Ghana

C. Pathe, W. Wagner, D. Sabel, Z. Bartalis, M. Doubkova, V. Naeimi, J. Basara (in preparation): “*Scatterometer and ScanSAR Soil Moisture observations of the contiguous United States*” Proceedings of the 2009 IEEE Radar Conference. Radar: From Science to Systems, 4-8 May 2009, Pasadena, California, USA